Hybrid and Pseudo-Cascaded Active Noise Control Applied to Headphones

Von der Fakultät für Elektrotechnik
der Helmut-Schmidt-Universität / Universität der Bundeswehr Hamburg
zur Erlangung des akademischen Grades eines Doktor-Ingenieurs
genehmigte

DISSERTATION
vorgelegt von

Piero Iared Rivera Benois

aus Santiago de Chile, Chile
Hamburg 2020

Gutachter:	Univ.-Prof. Dr.-Ing. habil. Udo Zölzer Helmut-Schmidt-Universität, Universität der Bundeswehr Hamburg
	Univ.-Prof. Dr.-Ing. Delf Sachau Helmut-Schmidt-Universität, Universität der Bundeswehr Hamburg
Vorsitzender:	Univ.-Prof. Dr. phil. nat. Bernd Klauer Helmut-Schmidt-Universität, Universität der Bundeswehr Hamburg
Tag der Disputation:	14.12.2020

Acknowledgments

This thesis was written during my time as research assistant at the Department of Signal Processing and Communications of the Helmut-Schmidt-University / University of the Federal Armed Forces Hamburg, Germany. I would like to take this opportunity to express my gratitude to the numerous people who have accompanied me during this journey.

First of all, I would like to thank my supervisor Prof. Udo Zölzer, who gave me the opportunity to embark on the thrilling journey of research. His guidance and his confidence in my work gave me the best possible environment to develop as a researcher. I would also like to thank my co-supervisor Prof. Delf Sachau and his team for introducing me into the topic of active noise control. Furthermore, I would like to thank the chairman of the supervisory board Prof. Bernd Klauer and his team for the dynamic collaboration during the more practical part of my research.

Special thanks goes to my working colleagues in the Department of Signal Processing and Communications. Lars Urbansky, for showing me the funny side of German humor (yes, there is one). Etienne Gerat, for being so curious about my ideas and building prototypes with me. Patrick Nowak, for his sincere friendship, fruitful discussions and long yet enjoyable measurement hours in the laboratory. Purbaditya Bhattacharya, Guillaume Larnaudie de Ferrand, André Kelm and Carlos de Obaldía for making our collective memories so great.

Last but not least, I would like to thank my partner Veatriki for her love and advice. Without her support this work would not have been possible.

Piero Rivera Benois

Abstract

The subject of this dissertation is the active control of acoustical noise by means of headphones. The contribution to the research field entails three novel control structures and the optimization of their parameters. These control structures combine simultaneously the three classical control schemes, namely the feedforward, the minimum variance and the internal model control schemes, into one system. This is achieved without requiring additional microphones or loudspeakers. The optimization of the controller parameters is performed in two stages. First, the minimum variance and the internal model controllers are co-optimized while subject to the stability, performance, and controller gain constraints developed in this work. Second, based on these optimized parameters and the novel control structure to be used, the feedforward controller is optimized. This can be done offline for a fixed controller implementation, by following a Wiener controller derivation. Alternatively, the optimization can be done online based on the implementation of an adaptive controller. To achieve this goal the Modified Normalized Filtered-x LMS algorithm is integrated into the novel control structures in a way that requires a minimum of memory and computational resources.

The fixed controllers are evaluated by means of simulations of an ANC headphones prototype subject to an ipsilateral single-source free-field excitation. From the results it is concluded that, if the impulse response of the feedforward controller is as long as the one of the primary path, then the performance of the novel control structure is the same as the one of a classical feedforward scheme. However, if the impulse response of the feedforward controller is shorter than the one of the primary path, the minimum variance and internal model controllers significantly increase the attenuation in the low frequencies. Moreover, at the same time the

detrimental waterbed effect produced by the feedback controllers is compensated by the feedforward controller. Thus, the novel control structures achieve a better performance.

The adaptive controllers are evaluated by means of measurements done with an ANC headphones prototype under ipsilateral and contralateral single-source stochastic noise excitation. It is found that, under ipsilateral excitation the results achieved in the simulations can be corroborated. However, it is also found that the attenuation performance is subject to deterioration, if the impulse response of the estimated secondary path is not sufficiently long. Under a contralateral excitation the performance of the novel control structures is shown to be subject to an additive noise introduced by the feedforward controller in the low frequencies. Nevertheless, it is also found that the performance of the minimum variance and internal model controllers combined together achieve a comparable performance to the one achieved under an ipsilateral excitation. Hence, if the shortcomings of the adaptive feedforward controller can be solved in the future, the improved performance of the novel structures could also be achieved for contralateral excitation scenarios.

Contents

Glossary

In this glossary the mathematical operators, functions, symbols and abbreviations used in this work are introduced. The symbols which are used once and defined directly in their sections are omitted. The elements are arranged in the order of their appearance.

Mathematical operators and functions

$\lvert \cdot \rvert$	Euclidean norm
$\mathbb{E}[\cdot]$	Expectation operator (of signals)
$(\cdot)^H$	Hermitian adjoint operator
$\{\cdot\}^\top$	Transpose operator
$\partial a / \partial b$	Partial derivative of a with respect to b
∇	Del or nabla operator as vector differential operator
$e^{\{\cdot\}}$	Exponential function
$\log(\cdot)$	Natural logarithm
$\mathrm{Re}\{\cdot\}$	Real part of complex number or vector
$\mathrm{Im}\{\cdot\}$	Imaginary part of complex number or vector
$\sin(\cdot)$	Sine function
$\cos(\cdot)$	Cosine function
$\deg(\cdot)$	Polynomial degree
$\max_i \lvert \cdot \rvert$	Maximal magnitude found by iterating over i

Signals and Systems

$x(n)$	Reference signal in discrete-time domain
$P(z)$	Primary path in Z-domain

$d(n)$	Disturbance signal in discrete-time domain
$W_{\mathrm{f}}(z)$	Feedforward controller in Z-domain
$y'(n)$	Control signal to be fed to the system
$y(n)$	Control signal at the error microphone's position in discrete-time domain
$e(n)$	Residual control error in discrete-time domain
$H_{\mathrm{f}}(z)$	Feedforward control scheme's transfer function
$S(z)$	Secondary path or also *plant* in feedback control analysis
$x(t)$	Reference signal in continuous-time domain
$d(t)$	Disturbance signal in continuous-time domain
$y(t)$	Control signal at the error microphone's position in continuous-time domain
$e(t)$	Residual control error in continuous-time domain
$P(j\omega)$	Primary path's continuous frequency response
$S^{\mathrm{hyp}}(z)$	Hypothetical secondary path
$S_{\mathrm{D}}(z)$	Hypothetical secondary path's component responsible for non-causality
$S_{\overline{\mathrm{D}}}(z)$	Hypothetical secondary path's component left after extracting the delays responsible for non-causality
$W_{\mathrm{f}}^{\mathrm{hyp}}(z)$	Optimum feedforward controller in hypothetical scenario
$H_{\mathrm{f}}^{\mathrm{hyp}}(z)$	Feedforward control scheme's transfer function in hypothetical scenario
$\Phi_{ee}(z)$	Z-transform of the error signal's auto-correlation function
$D(z)$	Disturbance signal in Z-domain
$Y(z)$	Control signal at the error microphone's position in Z-domain
$\Phi_{dx}(z)$	Z-transformed cross-power spectra of the reference and disturbance signals
$\Phi_{dd}(z)$	Z-transformed cross-power spectra of the disturbance signal
$\Phi_{xx}(z)$	Z-transformed auto-power spectra of the reference signal
$C_{dx}(z)$	Magnitude-squared coherence between the reference and disturbance signals
$W_{\mathrm{f}}^{\mathrm{opt}}(z)$	Optimum feedforward controller in Z-domain
$\hat{W}_{\mathrm{f}}^{\mathrm{opt}}(z)$	Optimum feedforward controller in Z-domain for free-field excitation scenario
$x_s(n)$	Filtered-x signal
$\hat{d}(n)$	Estimated disturbance signal
$\Psi(z)$	Deviation factor between estimated and real secondary paths
$W_{\mathrm{m}}(z)$	Minimum variance controller in Z-domain
$m(n)$	Music signal to be played through the headphones
$c(n)$	Command signal used in the analysis of the minimum variance control scheme
$T(z)$	Complementary sensitivity function in Z-domain

$H_{\mathrm{m}}(z)$	Minimum variance control scheme's transfer function, also known as sensitivity function
$M(z)$	Music signal to be played through the headphones in Z-domain
$T^{\mathrm{hyp}}(z)$	Hypothetical complementary sensitivity function in Z-domain
$W^{\mathrm{hyp}}(z)$	Optimal controller given an hypothetical context in Z-domain
$H^{\mathrm{hyp}}(z)$	Hypothetical sensitivity function in Z-domain
$C_{\mathrm{m}}(z)$	Minimum variance control scheme's characteristic equation
$O(z)$	Open-loop transfer function
$\mathbf{s}_{\mathrm{i}}(n)$	Secondary path's impulse response number i of the measurement set used to derive $G_2(\Omega_k)$
$S_{\mathrm{i}}(z)$	Z-transformed secondary path number i of the measurement set used to derive $G_2(\Omega_k)$
$S_0(j\Omega_k)$	Nominal secondary path's frequency response
$S_{\mathrm{i}}(\Omega_k)$	Frequency response of the secondary path number i of the measurement set
$G_2(\Omega_k)$	Maximum multiplicative magnitude deviation over frequency of the secondary path
$O(j\Omega_k)$	Frequency response of the open-loop transfer function
$O_0(j\Omega_k)$	Frequency response of the nominal open-loop transfer function
$G_3(\Omega_k)$	Maximal amplification of $d(n)$ allowed over frequency
$G_4(\Omega_k)$	Maximal controller gain allowed over frequency
$G_1(\Omega_k)$	Spectral weighting used in the cost function
$H_{\mathrm{i}}(z)$	Internal model control scheme's transfer function, also known as sensitivity function
$W_{\mathrm{i}}(z)$	Sensitivity function or transfer function of the internal model control scheme
$\tilde{W}_{\mathrm{m}}(z)$	Equivalent minimum variance controller
$C_{\mathrm{i}}(z)$	Characteristic equation of the internal model control scheme
$O_{\mathrm{i}}(j\Omega)$	Open-loop transfer function of the internal model control scheme
$O_{\mathrm{i},0}(j\Omega)$	Nominal open-loop transfer function of the internal model control scheme
$H_{\mathrm{mi}}(z)$	Pseudo-cascaded control structure's transfer function with independent optima
$\hat{H}_{\mathrm{mi}}(z)$	Pseudo-cascaded control structure's nominal transfer function with independent optima
$\hat{H}_{\mathrm{i}}(z)$	Internal model control scheme's nominal transfer function
$C_{\mathrm{mi}}(z)$	Characteristic equation of the pseudo-cascaded system in the novel control structures
$\hat{C}_{\mathrm{mi}}(z)$	Nominal characteristic equation of the pseudo-cascaded system in the novel control structures
$O_{\mathrm{mi}}(j\Omega)$	Open-loop transfer function of the pseudo-cascaded system in the novel control structures

$H_{\text{fim}}(z)$	Novel FIM control structure's transfer function
$\hat{H}_{\text{fim}}(z)$	Novel FIM control structure's nominal transfer function
$H_{\text{fimpdo}}(z)$	Novel FIMPDO control structure's transfer function
$\hat{H}_{\text{fimpdo}}(z)$	Novel FIMPDO control structure's nominal transfer function
$H_{\text{fimdo}}(z)$	Novel FIMDO control structure's transfer function
$\hat{H}_{\text{fimdo}}(z)$	Novel FIMDO control structure's nominal transfer function
$S_{\text{f}}^{\text{fim}}(z)$	Novel FIM control structure's effective secondary path seen from the feedforward controller's perspective
$\hat{S}_{\text{f}}^{\text{fim}}(z)$	Novel FIM control structure's nominal effective secondary path seen from the feedforward controller's perspective
$S_{\text{f}}^{\text{fimpdo}}(z)$	Novel FIMPDO control structure's effective secondary path seen from the feedforward controller's perspective
$\hat{S}_{\text{f}}^{\text{fimpdo}}(z)$	Novel FIMPDO control structure's nominal effective secondary path seen from the feedforward controller's perspective
$S_{\text{f}}^{\text{fimdo}}(z)$	Novel FIMDO control structure's effective secondary path seen from the feedforward controller's perspective
$\hat{S}_{\text{f}}^{\text{fimdo}}(z)$	Novel FIMDO control structure's nominal effective secondary path seen from the feedforward controller's perspective

Variables and Parameters

n	Sample-time index in the discrete-time domain
t	Time variable
z	Complex variable of the Z-domain
ω	Frequency variable of the Fourier transform domain
Ω	Frequency variable of the discrete-time Fourier transform domain
Ω_k	Frequency variable of the discrete Fourier transform domain
D_{ps}	Delays of the secondary path in comparison to the ones in the primary path, which are responsible for the non-causality
T_s	Sampling period
f_s	Sampling frequency
L_s	Length of the secondary path's finite impulse response
L_p	Length of the primary path's finite impulse response
L_w	Length of the feedforward controller's finite impulse response
β_0	Tikhonov regularization method's parameter
μ	Gradient descent method's step-size parameter
α	Auxiliary variable used during mathematical derivations

β	Auxiliary variable used during mathematical derivations
γ	Auxiliary variable used during mathematical derivations
$\hat{\alpha}$	Auxiliary variable used during mathematical derivations
$\hat{\beta}$	Auxiliary variable used during mathematical derivations
D_s	Amount of sample-delays in the secondary path
κ	Contour in the Z-domain used in the Cauchy's argument principle
$Z_{C_\mathrm{m},\kappa}$	Number of zeros of the characteristic equation inside of the contour κ
$P_{C_\mathrm{m},\kappa}$	Number of poles of the characteristic equation inside of the contour κ
$N^{\mathrm{cw}}_{O(\kappa)}$	Number of clockwise encirclement of the Nyquist point made by the sub-contours of $O(\kappa)$
$N^{\mathrm{ccw}}_{O(\kappa)}$	Number of counter-clockwise encirclement of the Nyquist point made by the sub-contours of $O(\kappa)$
$Z_{C_\mathrm{m},\overline{c}}$	Amount of zeros outside the unit circle that the characteristic equation has
κ_c	Contour in the Z-domain considering only the unit-circle
$N^{\mathrm{cw}}_{O(\kappa)}$	Number of clockwise encirclement of the Nyquist point made by the open-loop transfer function when evaluated on the unit-circle
$N^{\mathrm{ccw}}_{O(\kappa)}$	Number of counter-clockwise encirclement of the Nyquist point made by the open-loop transfer function when evaluated on the unit-circle
Ω^{+}_{k}	Frequency variable of the discrete Fourier transform domain related to the *positive* frequencies
Δ	The subset of complex numbers that fulfills the condition $\lvert\Delta\rvert \leq 1$
$C_{\mathrm{mvc}}(\mathbf{w}_\mathrm{m})$	Minimum variance control scheme' cost function
$C'_{\mathrm{mvc}}(\mathbf{w}_\mathrm{m})$	Minimum variance control scheme' cost function calculated within the $f_\mathrm{l} - f_\mathrm{h}$ frequency range
L_m	Length of the minimum variance controller's finite impulse response
$C_{\mathrm{imc}}(\mathbf{w}_\mathrm{i})$	Internal model control scheme' cost function
$C'_{\mathrm{imc}}(\mathbf{w}_\mathrm{i})$	Internal model control scheme' cost function calculated within the $f_\mathrm{l} - f_\mathrm{h}$ frequency range
L_i	Length of the internal model controller's finite impulse response
$C_{\text{mvc-imc}}(\mathbf{w}_\mathrm{m}, \mathbf{w}_\mathrm{i})$	Cost function used for optimizing the pseudo-cascaded system of the novel control structures calculated within the $f_\mathrm{l} - f_\mathrm{h}$ frequency range

Matrices and Column Vectors

$\mathbf{d}$	First L_d samples of the disturbance signal
$\mathbf{p}$	First L_p samples of the primary path's impulse response
$\mathbf{x}$	First L_x samples of the reference signal
$\mathbf{P}$	Toeplitz matrix built with the first L_p samples of the primary path's impulse response
$\mathbf{s}$	First L_s samples of the secondary path's impulse response
$\mathbf{S}$	Toeplitz matrix built with the first L_s samples of the secondary path's impulse response
$\mathbf{w}_\mathrm{f}$	Vector of length L_w containing the feedforward controller's finite impulse response
$\mathbf{W}_\mathrm{f}$	Toeplitz matrix built with the first L_w samples of the secondary path impulse response
$\mathbf{e}$	First L_e samples of the residual error signal
$\mathbf{d}_\mathrm{zp}$	First L_d samples of the disturbance signal extended with zeroes
$\mathbf{X}$	Toeplitz matrix built with the first L_x samples of the reference signal
$\mathbf{w}_\mathrm{f}^\mathrm{opt}$	Optimal feedforward controller's finite impulse response
$\mathbf{\Phi}_{xx}$	Auto-correlation matrix of the reference signal
$\boldsymbol{\phi}_{dx}^{+}$	Vector containing the half of the cross-correlation $\phi_{dx}(\tau)$ related to the positive lags ($\tau \geq 0$)
$\mathbf{p}_{zp}$	First L_p samples of the primary path's impulse response extended with zeroes
$\mathbf{w}_\mathrm{f}(n)$	Feedforward controller's finite impulse response at sample-time n
$\nabla f_c^\mathrm{T}(\mathbf{w}_\mathrm{f}(n))$	Gradient of the cost function with respect to the controller coefficients at sample-time n
$\mathbf{x}_s$	First L_{x_s} samples of the filtered-x signal
$\mathbf{X}_s$	Toeplitz matrix built with the first L_{x_s} samples of the filtered-x signal
$\mathbf{w}_\mathrm{m}$	Vector of length L_m containing the finite impulse response of the minimum variance controller
$\mathbf{w}_\mathrm{i}$	Vector of length L_i containing the finite impulse response of the internal model controller

Abbreviations

ANC	Active noise control or active noise cancelling

FF	Feedforward control scheme
DSP	Digital signal processor
D/A	Digital-analog converter
A/D	Analog-digital converter
ZOH	Zero-order hold reconstruction method
LMS	Least mean square
dB	Decibels
MVC	Minimum variance control scheme
GM	Gain margin
PM	Phase margin
FIM	Novel control structure that combines the feedforward, minimum variance, and internal model control schemes and yields independent optimal controllers
FIMPDO	Novel control structure that combines the feedforward, minimum variance, and internal model control schemes and yields partially dependent optimal controllers
FIMDO	Novel control structure that combines the feedforward, minimum variance, and internal model control schemes and yields dependent optimal controllers
SPL	Sound pressure level

CHAPTER 1

Introduction

Active Noise Cancelling (ANC), also known as Active Noise Control, aims to reduce the sound pollution present in the environment by actively generating sound pressure waves that overlap destructively on a sweet-spot with the ones of the noise sources. Its origins can be dated back to Lueg's patent [Lueg, 1936] on the control of acoustical tonal noise inside of a duct, while its particular application to headphones can be dated to the later work of Simshauser *et al.* in [Simshauser and Hawley, 1955]. In order to achieve a perfect attenuation, the phase and the amplitude of the noise around the sweet-spot have to be matched. To estimate how sensitive the performance of such a principle is to deviations from the optimum, a hypothetical disturbance sine-wave measured at the sweet-spot

$$d(n) = A_d \cdot \sin(\Omega_0 n) \tag{1.1}$$

is used. A control signal

$$y(n) = A_y \cdot \sin(\Omega_0 n + \theta_y), \tag{1.2}$$

having the same frequency but amplitude and phase that differ from the optimum is used to cancel it. By the destructive superposition of both signals a residual error $e(n) = d(n) - y(n)$ remains after the control is applied. As a performance metric the attenuation

$$A_{\mathrm{dB}} = 10 \log_{10} \left(\frac{P_e}{P_d} \right) \mathrm{dB} \tag{1.3}$$

is defined, being P_e and P_d the average power of $e(n)$ and $d(n)$, respectively.

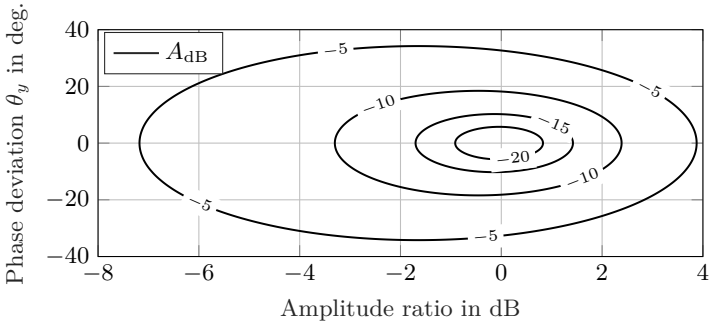

Figure 1.1.: Attenuation contours $A_{\mathrm{dB}} = 10\log_{10}\left(P_e/P_d\right)$ dB of destructively overlapping control signal $y(n) = A_y \sin(\Omega_0 n + \theta_y)$ and disturbance signal $d(n) = A_d \sin(\Omega_0 n)$. The amplitude ratio for the x-axis is calculated as $20 \cdot \log_{10}\left(A_y/A_d\right)$.

In Fig. 1.1 the contour plot of the achieved attenuation for phase deviations in the range of

$$-40^\circ < \theta_y < 40^\circ$$

and amplitude ratios between

$$-8\,\mathrm{dB} < 20 \cdot \log_{10}\left(A_y/A_d\right) < 4\,\mathrm{dB}$$

is presented. As it can be seen, all contours are concentric to the optimum, which attenuation is theoretically infinite and negative. On the one hand it can be seen that curves are symmetric with respect to the x-axis, which implies that there is no difference in the outcome if the relative phase deviation θ_y is positive or negative. On the other hand, the curves are not symmetric with respect to the y-axis. Thus, worse results are to be expected, if the control signal has a bigger amplitude than the one of the disturbance. The contours $A_{\mathrm{dB}} = -20\,\mathrm{dB}$ and $A_{\mathrm{dB}} = -15\,\mathrm{dB}$ show that for achieving a significant attenuation the amplitude and phase of the signals must not deviate more than $\pm 1\,\mathrm{dB}$ and $\pm 6^\circ$ from each other. This error margin should be maintained throughout the frequencies that comprehend the attenuation bandwidth of interest, which may contain not only periodic noise like the one of this example, but also components of stochastic nature. Different approaches can be used to achieve this, depending on the nature of the noise and the solution's context.

In the case of ANC headphones, the transducers and systems presented in Fig. 1.2 can be found. An external microphone measures a time-advanced

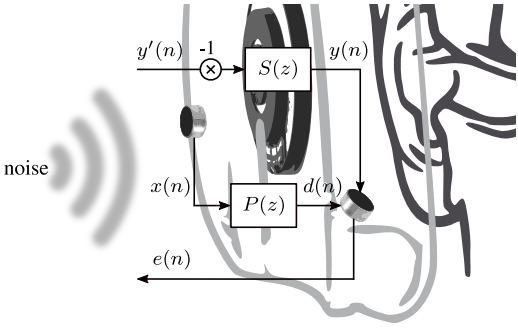

Figure 1.2.: Signals and systems around ANC headphones

reference of the incoming disturbance $x(n)$. This signal is measured again as $d(n)$, after it has entered the ear-cup and reached the so-called error microphone. Thus, $P(z)$, known as the primary path, is defined as the changes in magnitude and phase that the disturbance suffers by means of the headphones' construction materials and its angle of incidence. The control signal $y'(n)$ generated by the ANC system is phase-inverted, fed to the speaker and measured again by the error microphone as $y(n)$. Hence, the loudspeaker and the error microphone define the so-called secondary path $S(z)$, which considers the characteristics of both elements plus the acoustic path between them. At the end, the control signal $y(n)$ and the disturbance $d(n)$ overlap destructively at the error microphone's position, and the residual error $e(n)$ is generated. ANC approaches that use the residual error $e(n)$ for calculating $y'(n)$ are called feedback control schemes. On the other hand, the ones that use the time-advanced reference signal $x(n)$ for calculating $y'(n)$ are called feedforward or forward control schemes. Adaptive implementations of feedforward controllers also utilize $e(n)$ to solve the underlying optimization problem.

In this context it is assumed that the distance between the error microphone and the human ear is much smaller than the wavelength of sound to be attenuated. Therefore, the difference in magnitude and phase of the control and disturbance signals at the two positions can be considered negligible. Hence, a minimization of the residual error $e(n)$ achieved by the control scheme produces a minimization of the sound pressure reaching the human ear.

The subject of this dissertation is the combination of different control schemes into one system to improve the attenuation performance. This, without the use of extra microphones and loudspeakers. The combined control schemes impose an increment in the implementation complexity, but at the same time offer a higher design flexibility and attenuation per-

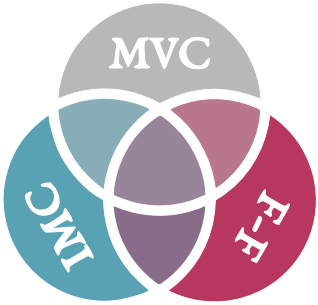

Figure 1.3.: The conceptual diagram used to graphically determine the theoretical combination possibilities of the classical control schemes.

formance. The content of this work can be conceptually visualized as the diagram presented in Fig. 1.3. In Chapter 2, Chapter 3, and Chapter 4 the feedforward (F-F), the minimum variance (MVC) and the internal model (IMC) control schemes conceptually related to the outer-most regions of the diagram are described. In these chapters, the mathematical formulations used for deriving the optimal parameters for their controllers are presented. With the help of simulations based on impulse responses measured with an ANC headphones prototype, the attenuation performance reachable with each control scheme is exemplified. In Chapter 5 the three classical control schemes are used as building blocks for their combination in pairs. The combination strategies found in the literature offer two control structures: one structure yields independent optimal solutions for the (two) controllers involved in the combination scheme; the second structure yields an optimal controller that is dependent with respect to the parameters of the other. Depending on which two schemes are considered in the combination, the content of this chapter is spread over the three triangular-shapes regions around the center in Fig. 1.3. In Chapter 6 three novel control structures are proposed, which combine simultaneously all three classical control schemes. Analogously to the combinations in pairs, the combination in triples offers three alternative structures that yield different dependency levels between their optimal controllers. This content is graphically placed at the center of the diagram in Fig. 1.3. In this chapter the achievable attenuation performance is exemplified by simulations. In Chapter 7 the ANC headphones prototype based on an FPGA-platform is equipped with real-time control algorithms. By means of a dummy-head, measurements are done under ipsilateral and contralateral stochastic excitation. The measurement results corroborate the simulations and the working principle of the proposed control schemes. In Chapter 8 the most relevant findings of this work are summarized and discussed.

CHAPTER 2

Feedforward Control

A feedforward control scheme (FF) is used in contexts where a time-advanced reference of the disturbance can be provided. As illustrated in Fig. 2.1, the reference signal $x(n)$, originated in free-field from a distant noise source, goes through the acoustic primary path $P(z)$ to arrive later at the error microphone's position as $d(n)$. Simultaneously, the same signal $x(n)$ is measured and used by the controller $W_{\mathrm{f}}(z)$ to calculate $y'(n)$. The control signal $y'(n)$ is fed to the secondary path, to destructively superpose with $d(n)$ and generate the residual control error $e(n)$. For historical reasons a subtraction has been used to conceptually emphasize that $d(n)$ and $y(n)$ overlap with opposite phases. The system's transfer function

$$H_{\mathrm{f}}(z) = \frac{E(z)}{X(z)} = P(z) - S(z) \cdot W_{\mathrm{f}}(z) \tag{2.1}$$

mathematically represents the passive and active attenuation undergone by the disturbance $x(n)$ until it reaches the error microphone. The controller $W_{\mathrm{f}}(z)$ is designed to minimize the magnitude of $H_{\mathrm{f}}(z)$ by matching the primary path's effect on $x(n)$ and compensating for the influence of the secondary path $S(z)$ on its own control signal $y'(n)$.

When this control approach is applied to headphones the elements conceptually represented in Fig. 2.1 are reordered to match the solution context, as shown in Fig. 2.2. Here the reference microphone is placed outside of the earcup and the error microphone inside of it, as close to the ear canal's entrance as possible. Because the relative position of the noise source(s) changes upon head movements, the controller $W_{\mathrm{f}}(z)$ has to be

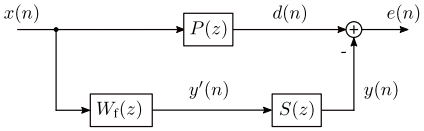

Figure 2.1.: The system diagram of a the feedforward control scheme. Represented are the feedforward controller $W_f(z)$, the primary path $P(z)$, and the secondary path $S(z)$.

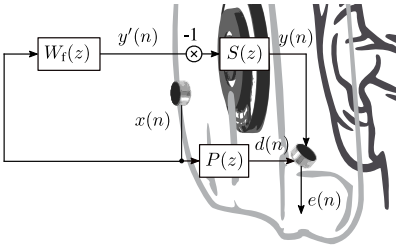

Figure 2.2.: The system diagram of a the feedforward control scheme adapted to the application on a headphones earcup. Represented are a digital feedforward controller $W_f(z)$, the primary path $P(z)$, and the secondary path $S(z)$.

continuously recalculated by a digital signal processor (DSP) and with it also the control signal $y'(n)$. Additionally, the phase inversion is introduced by digitally inverting the sign of $y'(n)$, before it is input to the secondary path $S(z)$.

The elements involved in the implementation of the controller $W_f(z)$ on a DSP platform are presented in Fig. 2.3. The upper-most part of the diagram is designated to the acoustic domain, where the acoustic signals $x(t)$, $d(t)$, $y(t)$, and $e(t)$, and the primary path $P(j\omega)$ are described in the continuous time domain. The elements of the next lower level are the microphones $M_x(j\omega)$ and $M_e(j\omega)$ and loudspeaker $L_y(j\omega)$ that provide the conversion from the acoustic domain to the electric domain and vice-versa. On the next lower level the anti-aliasing filters $F_x(j\omega)$ and $F_e(j\omega)$ and reconstruction filter $F_y(j\omega)$ required for limiting the signals' bandwidth are depicted. One level lower, the analog-digital (A/D) and digital-analog (D/A) converters together with the method used for the reconstruction of the analog signal after the D/A conversion are presented. In this specific case a zero-order hold method (ZOH) is shown, but other methods can be used here as well, e.g. first-order hold. The bottom level is the discrete time domain in which the signals of the acoustic domain are sample-wise represented as $x(n)$ and $e(n)$. Here the calculation of the control signal

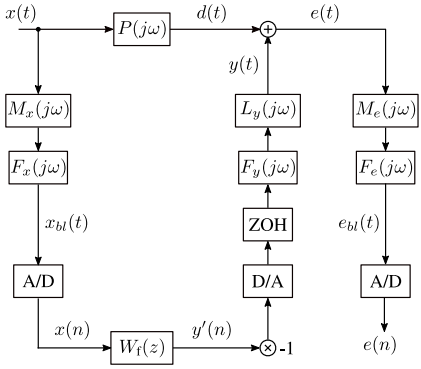

Figure 2.3.: Feedforward control scheme in its digital implementation form.

$y'(n)$ is described by the convolution between the signal $x(n)$ and the impulse response of the controller $W_f(z)$.

In the following sections the limitations of this control scheme due to the implicit causality constrain and due to loss in coherence between the measured signals are presented. These are followed by the mathematical derivation of the controller $W_f(z)$ that minimizes the residual error. Then, the iterative on-line approximation of the optimum controller by means of an adaptive filter is described. At the end, the chapter is finalized by a summary of the important facts and findings related to this control scheme.

2.1. Causality

The system's transfer function in Eq. 2.1 also defines the underlying causality constraint, i.e. for the attenuation to be total, the digital delay of the controller $W_f(z)$ plus the delay of $S(z)$ has to be smaller or equal to the acoustic delay of $P(z)$. If this is not met, then the performance of the system relies solely on the disturbance signal's characteristics. In order to quantify this effect, let the secondary path be a hypothetical system free of zeros outside the unit circle in the Z-domain, which can be divided into two components

$$S^{\mathrm{hyp}}(z) = S_{\mathrm{D}}(z) \cdot S_{\overline{\mathrm{D}}}(z), \tag{2.2}$$

with $S_{\mathrm{D}}(z) = z^{-D_{ps}}$ being the excess of D_{ps} delays of the secondary path in comparison to the ones in the primary path (which are responsible for the non-causality) and $S_{\overline{\mathrm{D}}}(z)$ being the rest of its impulse response. As the remaining delays in $S_{\overline{\mathrm{D}}}(z)$ are also contained in $P(z)$, an optimum

controller

$$W_{\mathrm{f}}^{\mathrm{hyp}}(z) = \frac{P(z)}{S_{\overline{\mathrm{D}}}(z)} \tag{2.3}$$

can be calculated without any causality or stability issues. If this optimum controller is used in Eq. 2.1, then it can be shown that the resulting system's transfer function simplifies to the one of the primary path in series connection with a feedforward comb filter with a negative gain applied to the delay line

$$H_{\mathrm{f}}^{\mathrm{hyp}}(z) = P(z)\big(1 - z^{-D_{ps}}\big). \tag{2.4}$$

So on top of the passive attenuation that the primary path introduces, the hypothetical optimal controller produces a coloration with amplification and attenuation regions, similar to the ones presented in Fig. 2.4. To be exact, this is the coloration seen at the output of the system after a period of time Δ_t greater than $D_{ps} \cdot T_s$ (being $T_s = 1/f_s$ the sampling period), as the control signal is delayed by this amount of time. Thus, for an impulsive noise excitation, the error signal $e(n)$ consists at first of an *uncontrolled* pulse, followed D_{ps}-samples after by a phase-inverted copy of it. Nevertheless, if the reference signal $x(n)$ is of stochastic but steady-state nature, then 6 dB resonances will be found at frequencies

$$f_{\mathrm{peak}} = \frac{1}{D_{ps} \cdot T_s} \cdot \left(m_{\mathrm{p}} + \frac{1}{2}\right), \tag{2.5}$$

with $m_{\mathrm{p}} \in \{0, 1, \ldots, \lfloor \frac{D_{ps}-1}{2} \rfloor\}$ and notches or attenuation regions will appear at frequencies

$$f_{\mathrm{notch}} = \frac{1}{D_{ps} \cdot T_s} \cdot m_{\mathrm{n}}, \tag{2.6}$$

with $m_{\mathrm{n}} \in \{0, 1, \ldots, \lfloor \frac{D_{ps}}{2} \rfloor\}$. In contrast, if the reference signal $x(n)$ is of periodic and steady-state nature, it is possible to achieve a perfect attenuation after $D_{ps} \cdot T_s$ seconds, provided that the relative gain and phase of $d(n)$ with respect to $x(n)$ are already known.

2.1.1. Bandwidth limitation due to non-causality scenario

In cases in which the resonances of the comb-filter effect are not tolerated, it is of importance to limit the active bandwidth of the controller $W_{\mathrm{f}}(z)$. This bandwidth can be chosen as the low-frequency region where the comb filter's frequency response remains under 0 dB. In order to find the first frequency at which the frequency response reach 0 dB, the squared magnitude of the it can be equated to one

$$|1 - z^{-D_{ps}}|^2 = 1. \tag{2.7}$$

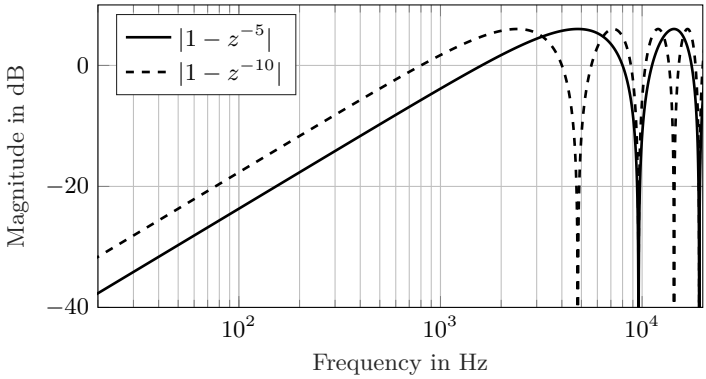

Figure 2.4.: Coloration introduced by the best achievable controller due to a non-causality equivalent to $D_{ps} = 5$ samples @ 48 kHz ($\approx 104\,\mu$s) and $D_{ps} = 10$ samples @ 48 kHz ($\approx 208\,\mu$s), respectively.

By substituting $z = e^{j\Omega}$, it can be shown

$$\left(1 - e^{j\Omega D_{ps}}\right)\left(1 - e^{-j\Omega D_{ps}}\right) = 1 \tag{2.8}$$

$$1 - e^{j\Omega D_{ps}} - e^{-j\Omega D_{ps}} + 1 = 1 \tag{2.9}$$

$$2 - \left(e^{j\Omega D_{ps}} + e^{-j\Omega D_{ps}}\right) = 1 \tag{2.10}$$

$$2 - 2 \cdot \cos(\Omega D_{ps}) = 1 \tag{2.11}$$

$$\cos(\Omega D_{ps}) = \frac{1}{2} \tag{2.12}$$

that the first intercept happens at

$$\Omega D_{ps} = \frac{\pi}{3}. \tag{2.13}$$

This can be equivalently written as

$$2 \cdot \pi \cdot \frac{f_{0\mathrm{dB}}}{f_\mathrm{s}} \cdot D_{ps} = \frac{\pi}{3}, \tag{2.14}$$

with which the frequency of the first intercept with the 0 dB level can be found

$$f_{0\mathrm{dB}} = \frac{1}{6 \cdot T_s \cdot D_{ps}}. \tag{2.15}$$

So for example, if the DSP is working at 48 kHz ($T_s \approx 20.7\,\mu$s) and the overall DSP delay is 5 samples higher than the expected acoustic delay in the primary path, then the bandwidth could be limited to 1.6 kHz, in order

to avoid any amplification.

2.1.2. Further discussion about the causality constraint

The causality constraint intuitively understood from Eq. 2.1 finds its exact form in the inequality over frequency

$$\tau_p(f) \geq \tau_{m_x}(f) + \tau_{f_x}(f) + \tau_{\text{ad}} + \tau_{\text{dsp}} + \tau_{\text{da}} + \tau_{\text{zoh}} + \tau_{f_y}(f) + \tau_{l_y}(f), \quad (2.16)$$

where the sub-indices reference the systems depicted in Fig. 2.3. Here, the group delay over frequency of the primary path $\tau_p(f)$ has to be greater or equal to the input-output delay of the DSP platform. The latter is constituted by the systems' group delay over frequency $\tau_{m_x}(f)$, $\tau_{f_x}(f)$, $\tau_{l_y}(f)$, and $\tau_{f_y}(f)$; the conversion times τ_{ad} and τ_{da}; the DSP processing time τ_{dsp}; and finally, the delay introduced by the signal reconstruction process τ_{zoh}. As can be seen, the causality constraint is not directly related to the delay in the secondary path. However, if the microphones and anti-aliasing filters for the reference and error signals are chosen to be equal ($M_e(j\omega) = M_x(j\omega)$ and $F_e(j\omega) = F_x(j\omega)$), then the causality constraint can be written as

$$\tau_p(f) \geq \tau_{\text{dsp}} + \tau_{\text{da}} + \tau_{\text{zoh}} + \tau_{f_y}(f) + \tau_{l_y}(f) + \tau_{m_e}(f) + \tau_{f_e}(f) + \tau_{\text{ad}}. \quad (2.17)$$

Thus, in this new form of the constraint the intuitive interpretation of Eq. 2.1 is correct. Now, just by knowing τ_{dsp} and measuring the impulse response of the transfer function $\hat{S}(z) = -E(z)/Y'(z)$ (see Fig. 2.3), the bandwidth in which the constraint is met can be rapidly estimated. Alternatively, the impulse response of the transfer function $E_{bl}(z)/X_{bl}(z)$ can be measured to determine the complete delay of the control system.

If the bandwidth in which Eq. 2.16 is fulfilled should be extended, then the components represented in Fig. 2.3 have to be design or chosen such that they produce the smallest delay possible. The conversion times of the A/D and D/A converters can be as small as $\tau_{ad} = \tau_{da} = 1\,\mu$s, if Successive Approximation Register (SAR) technology is utilized instead of the popular Sigma-Delta modulation. The ZOH reconstruction process introduces a delay proportional to the sample period $\tau_{zoh} = T_s/2$ [Franklin et al., 1997], because of the convolution with the rectangular function of width T_s. Some DSPs control their A/D and D/A converters with the same control signal, which implicitly imposes a processing delay $\tau_{dsp} = T_s$. Nevertheless, this is not mandatory, and decoupled control signals together with parallel processing can be used to minimize this delay down to 30-20 ns [Rivera Benois et al., 2018a] (see Sec. 3.1.1 for more details).

The group delay of the anti-aliasing and reconstruction filters can be designed to be maximal outside the frequency range of interest by increasing their order and cutoff frequencies. Alternatively, the low-pass

characteristic of the filters can be designed with a smaller order or outside the frequency range of interest, if the sampling frequency is high enough. Moreover, if the microphone and loudspeaker's frequency response is already low enough near the half of the Nyquist frequency, the order of the filters can be chosen even lower. All in all, choosing a fast A/D technology, increasing the sampling frequency, and using filters of low-order with a maximum group delay outside the critical frequency band are the main things to take into account in order to improve the frequency band where causality can be assured.

2.2. Coherence

As the control signal calculation relies on the information contained in the reference signal, only disturbances correlated with it can be attenuated. Therefore, the maximum achievable attenuation is limited by the cross-correlation between $x(n)$ and $d(n)$ [Sen and Morgan, 1996]. In order to understand how a decrease in correlation between $x(n)$ and $d(n)$ limits the achievable attenuation, the excitation by a single noise source in a free-field is replaced by a diffuse and isotropic sound field. For the analysis the error signal's auto-power spectrum is defined as the Z-transform of its auto-correlation function

$$\Phi_{ee}(z) = \mathbb{E}[|D(z) - Y(z)|^2] \tag{2.18}$$

$$= \mathbb{E}[|D(z)|^2 - D(z^{-1})Y(z) - D(z)Y(z^{-1}) + |Y(z)|^2], \tag{2.19}$$

where the expectation $\mathbb{E}[\cdot]$ implies that the Z-transforms of $D(z)$ and $Y(z)$ have been calculated based on data collected over a time span that tends to infinity [Elliott, 2001b, Section 2.4.1]. If the controller $W_\mathrm{f}(z)$ and the secondary path $S(z)$ are time-invariant systems, the control signal can be further expressed as $Y(z) = S(z)W_\mathrm{f}(z)X(z)$ and the equation takes the form

$$\begin{aligned}\Phi_{ee}(z) =& \mathbb{E}[|D(z)|^2 - D(z^{-1})S(z)W_\mathrm{f}(z)X(z) \\ &- D(z)\big(S(z^{-1})W_\mathrm{f}(z^{-1})X(z^{-1})\big) + |S(z)W_\mathrm{f}(z)X(z)|^2].\end{aligned} \tag{2.20}$$

By considering the Z-transformed cross-power spectra

$$\Phi_{dx}(z) = \mathbb{E}[D(z)X(z^{-1})] \tag{2.21}$$

and

$$\Phi_{xd}(z) = \Phi_{dx}(z^{-1}), \tag{2.22}$$

the whole expression can be expressed in terms of auto-and cross-correlation as

$$\begin{aligned}\Phi_{ee}(z) =&\Phi_{dd}(z) - S(z)W_{\mathrm{f}}(z)\Phi_{dx}(z^{-1}) \\ &- \left(S(z^{-1})W_{\mathrm{f}}(z^{-1})\right)\Phi_{dx}(z) + |S(z)W_{\mathrm{f}}(z)|^2\Phi_{xx}(z).\end{aligned} \tag{2.23}$$

Following a similar analysis in [Sen and Morgan, 1996, Section 3.1.2], if the zero-valued quantity $|\Phi_{dx}(z)|^2/\Phi_{xx}(z) - |\Phi_{dx}(z)|^2/\Phi_{xx}(z)$ is added to Eq. 2.23 and the identity $\Phi_{xx}(z) = \Phi_{xx}(z^{-1})$ is used, then Eq. 2.23 can be re-written as

$$\Phi_{ee}(z) = \left(1 - \frac{|\Phi_{dx}(z)|^2}{\Phi_{dd}(z)\Phi_{xx}(z)}\right)\Phi_{dd}(z) + \left|\frac{\Phi_{dx}(z)}{\Phi_{xx}(z)} - W_{\mathrm{f}}(z)S(z)\right|^2\Phi_{xx}(z). \tag{2.24}$$

The first term determines the minimum achievable error imposed by the magnitude-squared coherence (MSC) between $x(n)$ and $d(n)$ given by

$$C_{dx}(z) = \frac{|\Phi_{dx}(z)|^2}{\Phi_{dd}(z)\Phi_{xx}(z)}, \tag{2.25}$$

which is not subject to change by the controller $W_{\mathrm{f}}(z)$. It has been found in [Morrow, 1971], that under this diffuse and isotropic sound field excitation, Eq. 2.25 can be formulated as a frequency-dependent function of the distance between the (in this context reference and error) microphones δ_{xd} in meters as

$$C_{dx}(f, \delta_{xd}, c) = \left(\frac{sin(2\pi f\frac{\delta_{xd}}{c})}{2\pi f\frac{\delta_{xd}}{c}}\right)^2, \tag{2.26}$$

being c the speed of sound in the medium. In Fig. 2.5 the solution of Eq. 2.26 for the case $\delta_{xd} = 0.03\,\mathrm{m}$ and $c = 343\,\mathrm{m/s}$ is presented, together with the maximum achievable attenuation over frequency $\Phi_{ee}^{\min}(f)/\Phi_{dd}(f)$. It can be seen that for two microphones separated only by air, the MSC decreases by 3 dB at approx. 2.5 kHz. This produces a magnitude minima at frequencies multiple of 5.7 kHz. The consecutive peaks in between the minima decay at a rate of 20 dB per decade. As an effect of this, a maximum attenuation of -45 dB is achievable at 20 Hz. This attenuation decreases at a rate of 20 dB per decade, leading to an intersection between the two curves at approx. 2.5 kHz.

The extrapolation of this result to the case of headphones is nevertheless more complex, since the microphones are not separated only by air, but rather by the earcup. As the speed of sound is inverse-proportional to the density of the transmission medium, any solid placed in between reference and error microphone would imply a consecutive increase in the speed of sound and a shift of the first minimum of $C_{dx}(f)$ to a higher frequency.

If one comes back to the single-source free-field excitation and the mea-

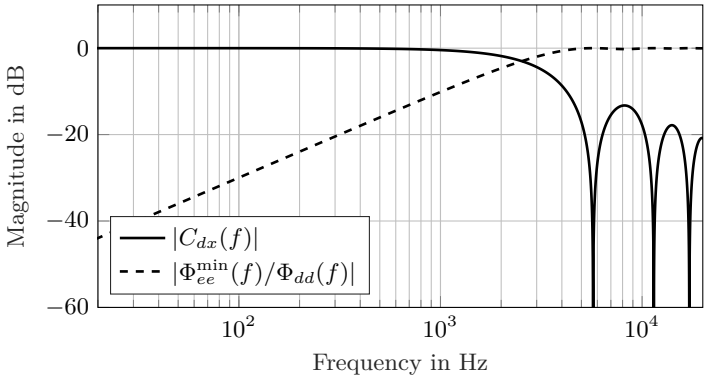

Figure 2.5.: Maximum achievable attenuation $\Phi_{ee}^{\min}(f)/\Phi_{dd}(f)$ due to the magnitude-squared coherence over frequency $C_{dx}(f)$ for a microphone distance $\delta_{xd} = 3\,\text{cm}$ separated only by air, when the system is subject to the excitation of a diffuse isotropic sound field.

surement noise in $x(n)$ is neglected, the correlation functions can be expressed as

$$\Phi_{dx}(z) = P(z)\Phi_{xx}(z) \tag{2.27}$$

and

$$\Phi_{dd}(z) = |P(z)|^2\Phi_{xx}(z). \tag{2.28}$$

Replacing these in the magnitude-squared coherence in Eq. 2.25

$$\hat{C}_{dx}(z) = \frac{|P(z)\Phi_{xx}(z)|^2}{|P(z)|^2\Phi_{xx}(z)\Phi_{xx}(z)} \Rightarrow 1, \tag{2.29}$$

simplifies to one, showing that in case of a free-field excitation the maximum achievable attenuation is not limited by coherence. The contexts in which one can find a perfect free- or diffuse-field are rare, and one is more likely to find some weighted combination of both. Nevertheless, it is important to mathematically understand both extreme cases and their implications.

2.3. The Wiener Controller

The minimization of the error signal's auto-power spectrum in Eq. 2.24 is achieved through the optimization of $W_\text{f}(z)$. For finding the mathematical expression of this optimal controller Eq. 2.24 is differentiated with respect

to $W_\mathrm{f}(z)$

$$\frac{\partial \Phi_{ee}(z)}{\partial W_\mathrm{f}(z)} = -2\left(\frac{\Phi_{dx}(z)}{\Phi_{xx}(z)} - W_\mathrm{f}(z)S(z)\right)^\mathrm{H} \Phi_{xx}(z)S(z), \tag{2.30}$$

with $(\cdot)^\mathrm{H}$ being the Hermitian operator. Then the result is equated to zero and under the constraint that $\Phi_{xx}(z)S(z) \neq 0$ the optimal controller

$$W_\mathrm{f}^\mathrm{opt}(z)S(z) = \frac{\Phi_{dx}(z)}{\Phi_{xx}(z)} \tag{2.31}$$

finds an expression which depends on the secondary path, the cross-correlation between signals and the auto-correlation of the reference. Alternatively, if a free-field excitation is considered, it can be shown by using Eq. 2.27 that Eq. 2.31 resolves to

$$\hat{W}_\mathrm{f}^\mathrm{opt}(z)S(z) = P(z). \tag{2.32}$$

These optimal solutions to the minimization of Eq. 2.24 are called unconstrained Wiener filters [Elliott, 2001b, Section 2.4.1], as they are neither limited in their causality nor in their stability. As the secondary path $S(z)$ is in acoustic applications a non-minimum-phase system, due to its delay and possible zeros outside of the unit-circle, a straightforward division of both sides of Eq. 2.32 by $S(z)$ can not directly follow. Moreover, using this expression may lead to a non-causal and/or unstable controller which can not be implemented. As a first alternative, the secondary path could be first separated

$$S(z) = S_\mathrm{mp}(z)S_{\overline{\mathrm{mp}}}(z) \tag{2.33}$$

in its minimum-phase $S_\mathrm{mp}(z)$ and non-minimum-phase $S_{\overline{\mathrm{mp}}}(z)$ components, before computing the division. This would produce a controller

$$W_\mathrm{f}^\mathrm{smp}(z) = \frac{1}{S_\mathrm{mp}(z)}\frac{\Phi_{dx}(z)}{\Phi_{xx}(z)}. \tag{2.34}$$

which incorporates only the minimum-phase components of $S(z)$. However, this does not take advantage of the fact that the causality components in $\Phi_{dx}(z)$ may dominate over the non-causal ones. This because the part of the diffuse field that would reach the error microphone before reaching the reference one is subject to the shadowing effect of the human-head. Moreover, it can be shown that by replacing $W_\mathrm{f}(z) = W_\mathrm{f}^\mathrm{smp}(z)$ and $S(z) = S_\mathrm{mp}(z)S_{\overline{\mathrm{mp}}}(z)$ in Eq. 2.24, the residual

$$\Phi_{ee}(z)\Big|_{W_\mathrm{f}^\mathrm{smp}} = \left(1 - \frac{|\Phi_{dx}(z)|^2}{\Phi_{dd}(z)\Phi_{xx}(z)}\right)\Phi_{dd}(z) + \left|\left(1 - S_{\overline{\mathrm{mp}}}(z)\right)\frac{\Phi_{dx}(z)}{\Phi_{xx}(z)}\right|^2 \Phi_{xx}(z), \tag{2.35}$$

would limit the attenuation performance by incorporating in $S_{\overline{\text{mp}}}(z)$ all delay components and zeros outside of the unit circle of $S(z)$.

2.3.1. The constrained time-domain derivation

As seen from the Z-transform analysis, by working in a transform domain is difficult to incorporate constraints to the solution that could be directly introduced in a time-domain analysis. To find an optimal solution for $W_{\text{f}}(z)$, which takes advantage of the causal components in $\Phi_{dx}(z)$ and yields a causal and stable controller with a finite-length impulse response, the notation for the analysis in time-domain is to be defined. Let the following example column vectors

$$\mathbf{d}_{L_d\times 1} = \begin{bmatrix} d_0 \\ d_1 \\ \vdots \\ d_{L_d-1} \end{bmatrix}, \mathbf{p}_{L_p\times 1} = \begin{bmatrix} p_0 \\ p_1 \\ \vdots \\ p_{L_p-1} \end{bmatrix}, \tag{2.36}$$

and

$$\mathbf{x}_{L_x\times 1} = \begin{bmatrix} x_0 \\ x_1 \\ \vdots \\ x_{L_x-1} \end{bmatrix} \tag{2.37}$$

be the first L_d, L_p, and L_x samples of the signals or system impulse responses $d(n)$, $p(n)$, and $x(n)$, respectively. Then, let $\mathbf{d}$, $\mathbf{p}$, and $\mathbf{x}$ be related by the convolution defined by the scalar product

$$\mathbf{d} = \mathbf{P}\cdot\mathbf{x}, \tag{2.38}$$

being $\mathbf{P}$ the Toeplitz matrix created by repeating $\mathbf{p}$ L_x times along the diagonal

$$\begin{bmatrix} d_0 \\ d_1 \\ \vdots \\ d_{L_d-1} \end{bmatrix} = \begin{bmatrix} p_0 & \dots & 0 \\ \vdots & \ddots & \vdots \\ p_{L_p-1} & & p_0 \\ \vdots & \ddots & \vdots \\ 0 & \dots & p_{L_p-1} \end{bmatrix} \cdot \begin{bmatrix} x_0 \\ x_1 \\ \vdots \\ x_{L_x-1} \end{bmatrix}. \tag{2.39}$$

Consequently, their lengths are related by

$$L_d = L_p + L_x - 1. \tag{2.40}$$

Making use of this notation to describe the feedforward system in Fig. 2.1 the error signal

$$\mathbf{e} = \mathbf{d}_{\mathrm{zp}} - \mathbf{S} \cdot \mathbf{W}_{\mathrm{f}} \cdot \mathbf{x}, \tag{2.41}$$

can be defined, where $\mathbf{d}_{\mathrm{zp}}$ is the vector $\mathbf{d}$ of L_d elements extended with zeroes to reach the length $L_s + L_w + L_x - 2$. Later on, it will be shown that L_d can not be chosen arbitrarily. Using Eq. 2.41, one can define the minimization's cost function as the expectation of the quadratic error

$$\mathbb{E}[\mathbf{e}^{\mathrm{T}}\mathbf{e}] = \mathbb{E}[(\mathbf{d}_{\mathrm{zp}} - \mathbf{S} \cdot \mathbf{W}_{\mathrm{f}} \cdot \mathbf{x})^{\mathrm{T}}(\mathbf{d}_{\mathrm{zp}} - \mathbf{S} \cdot \mathbf{W}_{\mathrm{f}} \cdot \mathbf{x})]. \tag{2.42}$$

By considering the involved systems as time-invariant and using the commutative property of the convolution, the expression can be rewritten as

$$\mathbb{E}[\mathbf{e}^{\mathrm{T}}\mathbf{e}] = \mathbb{E}[(\mathbf{d}_{\mathrm{zp}} - \mathbf{X} \cdot \mathbf{S} \cdot \mathbf{w}_{\mathrm{f}})^{\mathrm{T}}(\mathbf{d}_{\mathrm{zp}} - \mathbf{X} \cdot \mathbf{S} \cdot \mathbf{w}_{\mathrm{f}})]. \tag{2.43}$$

In order to find the controller's finite impulse response $\mathbf{w}_{\mathrm{f}}$ that minimizes the objective function, the gradient of Eq. 2.43 with respect to the impulse response coefficients is calculated

$$\frac{\partial \mathbb{E}[\mathbf{e}^{\mathrm{T}}\mathbf{e}]}{\partial \mathbf{w}_{\mathrm{f}}} = -2 \cdot \mathbb{E}[(\mathbf{d}_{\mathrm{zp}} - \mathbf{X} \cdot \mathbf{S} \cdot \mathbf{w}_{\mathrm{f}})^{\mathrm{T}} \cdot \mathbf{X} \cdot \mathbf{S}] \tag{2.44}$$

and equated to zero. If the transpose of both sides is taken

$$\mathbf{S}^{\mathrm{T}} \cdot \mathbb{E}[\mathbf{X}^{\mathrm{T}} \cdot \mathbf{X}] \cdot \mathbf{S} \cdot \mathbf{w}_{\mathrm{f}}^{\mathrm{opt}} = \mathbf{S}^{\mathrm{T}} \cdot \mathbb{E}[\mathbf{X}^{\mathrm{T}} \cdot \mathbf{d}_{\mathrm{zp}}], \tag{2.45}$$

the equality fulfilled by the optimal controller's impulse response $\mathbf{w}_{\mathrm{f}}^{\mathrm{opt}}$ can be formulated. In it two important quantities can be found: First, the auto-correlation matrix of the reference signal $x(n)$

$$\mathbf{\Phi}_{xx} = \mathbb{E}[\mathbf{X}^{\mathrm{T}} \cdot \mathbf{X}], \tag{2.46}$$

where the expectation $\mathbb{E}[\cdot]$ implies that the calculation has been time-averaged over a period of time that tends to infinity; and second, the half of the cross-correlation $\phi_{dx}(\tau)$ related to the positive lags ($\tau \geq 0$)

$$\boldsymbol{\phi}_{dx}^{+} = \mathbb{E}[\mathbf{X}^{\mathrm{T}} \cdot \mathbf{d}_{\mathrm{zp}}], \tag{2.47}$$

where the expectation $\mathbb{E}[\cdot]$ implies once again that the calculation has been time-averaged. In order to avoid any information loss, the length of the vector $\mathbf{d}$ has to be chosen as $L_d = L_s + L_w - 1$, with L_s and L_w being the secondary path's and controller's impulse response lengths, respectively. If L_d is chosen following this rule, the vector $\mathbf{d}_{\mathrm{zp}}$ contains exactly $L_x - 1$

zeroes, and the sliding window of the cross-correlation calculation

$$\begin{bmatrix} \phi_{dx}(0) \\ \phi_{dx}(1) \\ \vdots \\ \phi_{dx}(L_\phi - 1) \end{bmatrix} = \begin{bmatrix} x_0 & \dots & 0 \\ \vdots & \ddots & \vdots \\ x_{L_x-1} & & x_0 \\ \vdots & \ddots & \vdots \\ 0 & \dots & x_{L_x-1} \end{bmatrix}^{\mathrm{T}} \cdot \begin{bmatrix} d_0 \\ \vdots \\ d_{L_d-1} \\ 0 \\ \vdots \\ 0 \end{bmatrix} \tag{2.48}$$

finishes with the last vector element being $\phi_{dx}(L_\phi - 1) = x_0 \cdot d_{L_d-1}$. By using Eq. 2.46 and Eq. 2.47 in Eq. 2.45 the optimal solution for the controller coefficients

$$\mathbf{w}_{\mathrm{f}}^{\mathrm{opt}} = (\mathbf{S}^{\mathrm{T}} \cdot \boldsymbol{\Phi}_{xx} \cdot \mathbf{S})^{-1} \cdot \mathbf{S}^{\mathrm{T}} \cdot \boldsymbol{\phi}_{dx}^{+}, \tag{2.49}$$

can be found, provided that the matrix $(\mathbf{S}^{\mathrm{T}} \cdot \boldsymbol{\Phi}_{xx} \cdot \mathbf{S})$ is nonsingular. Alternatively, if the free-field excitation scenario is similarly analyzed, the optimum solution takes the form

$$\hat{\mathbf{w}}_{\mathrm{f}}^{\mathrm{opt}} = (\mathbf{S}^{\mathrm{T}} \cdot \boldsymbol{\Phi}_{xx} \cdot \mathbf{S})^{-1} \cdot \mathbf{S}^{\mathrm{T}} \cdot \boldsymbol{\Phi}_{xx} \cdot \mathbf{p}_{zp}, \tag{2.50}$$

where p_{zp} is the zero-padded vector of the first L_p samples of the primary path's *causal* impulse response.

As stated in [Elliott, 2001b, Section 2.5.1], for cases in which $(\mathbf{S}^{\mathrm{T}} \cdot \boldsymbol{\Phi}_{xx} \cdot \mathbf{S})$ is indeed singular, these equations can not be used for calculating the optimum controller. However, the matrix's singularity can be avoided through the use of the Tikhonov regularization method

$$\tilde{\mathbf{w}}_{\mathrm{f}}^{\mathrm{opt}} = (\mathbf{S}^{\mathrm{T}} \cdot \boldsymbol{\Phi}_{xx} \cdot \mathbf{S} + \beta_0 \cdot I)^{-1} \cdot \mathbf{S}^{\mathrm{T}} \cdot \boldsymbol{\phi}_{dx}^{+}, \tag{2.51}$$

by adding to it the identity matrix I multiplied by a small scalar β_0. It can be shown that this expression is the optimal solution of the minimization problem

$$\min_{\mathbf{w}_{\mathrm{f}}} \left(\mathbb{E}[\mathbf{e}^{\mathrm{T}}\mathbf{e}] + \beta_0 \mathbf{w}_{\mathrm{f}}^{\mathrm{T}} \mathbf{w}_{\mathrm{f}} \right), \tag{2.52}$$

where the weighted sum of squared controller coefficients is added to the cost function. If the parameter β_0 is increased, the optimum steers towards solutions with a controller with a lower gain over frequency. Thus, the same principle can be used in cases when $(\mathbf{S}^{\mathrm{T}} \cdot \boldsymbol{\Phi}_{xx} \cdot \mathbf{S})$ is not singular, in order to achieve some degree of control over the controller's gain.

Examples

The result examples presented here are a reference for the achievable performance of the feedforward scheme. They will be used later on in this

dissertation to analyze and understand the improvements achieved with the novel control structures. The examples are performance estimations based on the primary and secondary paths' impulse responses measured on a real device. Therefore, only a free-field excitation is considered here. For this, the measurement procedure and parameters described in [Rivera Benois et al., 2016] are applied to the prototype presented in [Rivera Benois et al., 2019] for the measurement of a primary path impulse response with length $L_p = 8192$. Here, the sound source is placed 1 m at the left of a dummy-head wearing the headphones prototype, while the left earcup's microphones are used for recording. Additionally, the procedure and parameters described in [Rivera Benois et al., 2019] are used for measuring a secondary path impulse response of length $L_s = 2048$. Here the controller's platform is included in the processing chain, in order to include the A/D delay τ_{ad}, processing delay τ_{dsp} and D/A delay τ_{da} in the measurement. The resulting impulse responses are presented in Fig. 2.6 using a logarithmic x-axis. The first samples of the the primary path's impulse response show a pre-ringing (they are not perfectly zero), which is produced by the limited bandwidth of the measurement speaker. Its peak magnitude is reached at the 20^{th} sample with a positive value, because the impinging sound pressure wave on the reference microphone increases the sound pressure inside of the earcup at the same time. The impulse response's tail settles to zero. The secondary path has four first samples that are close to zero. Its peak magnitude is reached at its 6^{th} sample with a negative value, because the headphone's drive and microphones are directed in the same direction. Its impulse response settles to zero at the end of its length, as well. Based on the low-magnitude of the starting samples of both impulse responses and the position of their respective peaks, a satisfactory degree of causality can be expected.

The magnitude frequency response of both impulse responses is presented in Fig. 2.7. The primary path shows a rough low-pass behavior mainly produced by the closed-back earcup's construction materials. The frequency response can be divided in three frequency regions: A first one being the pass-band with attenuation values below the 10 dB, which extends to approx. 190 Hz; A second region in the mid-frequencies that extend up to the 4 kHz, with attenuation values varying between 10 and 30 dB; And a third region in the high-frequencies, with attenuation values that vary around the 40 dB, which can be as high as 60 dB. The secondary path frequency response can be divided similarly in three region: a low-frequency region with a gain that varies around the 10 dB; a mid-frequency region with a gain that varies around the 2.5 dB; And a high-frequency region with variations imposed by the shape of the ear, as the wavelengths of frequencies higher than roughly 4.5 kHz are comparable to the size of the ear [Rivera Benois et al., 2019]. The difference in gain between both systems is caused by the amplifier used to drive the headphones's speakers,

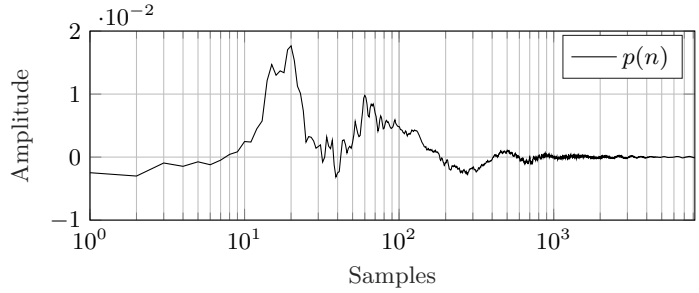

(a) *Primary path*

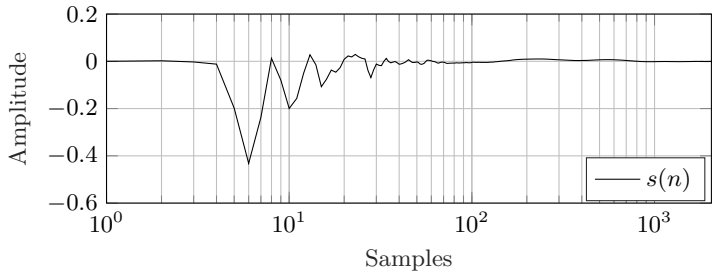

(b) *Secondary path*

Figure 2.6.: System impulse responses. Please note that the x-axis is in logarithmic scale. Parameters: $f_s = 48\,\text{kHz}$, $L_s = 2048$, $L_p = 8192$.

which is part of the controller platform, and therefore, also a sub-system inside of the secondary path. For more details about these measurements, please refer to the cited publications.

For the controller calculations, a free-field excitation scenario with a flat power spectral density is considered, which enables the use of the measured primary path impulse response and at the same time simplifies the auto-correlation matrix Φ_{xx} to the identity matrix I. The feedforward controllers are derived following Eq. 2.50 for the classical controller. Then, the system impulse responses with length 8192 of the system $h_\text{f}(n)$ are calculated by means of a sample-by-sample simulation of the system under control.

In Fig. 2.8 the impulse responses of two systems are compared: the first system $h_\text{f}(n)|L_w = 64$ is under the effect of a controller with an impulse response of *short* length $L_w < L_p$; the second system $h_\text{f}(n)|L_w = 8192$ is under the effect of a controller with an impulse response of length equal to the one of the primary path $L_w = L_p$. As a reference, the primary

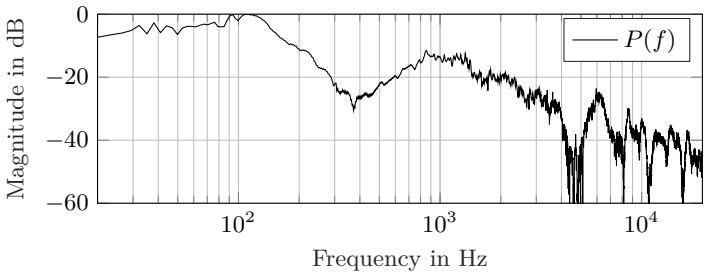

***(a)** Primary path*

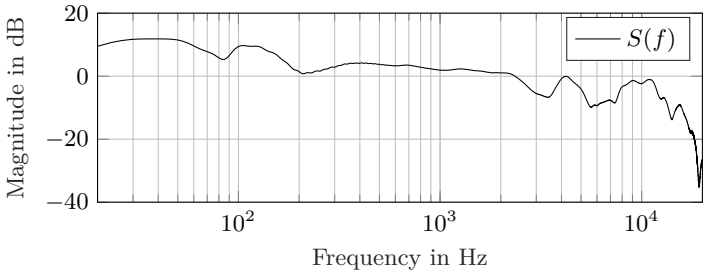

***(b)** Secondary path*

Figure 2.7.: System magnitude frequency responses. Parameters: $f_s = 48\,\text{kHz}$, $L_s = 2048$, $L_p = 8192$.

path impulse response $p(n)$ is presented as a reference of the system in the absence of control. Please note that the x-axis is in logarithmic scale. It can be seen from the first four samples of all three curves, that the four delays in the secondary path unable both controllers to achieve any change in the impulse response, because of the causality limitations. Thus, the first samples of both systems are equal to the ones of the primary path. From the 5^{th} to approx. the 40^{th} sample, both impulse responses have a similar positive transient that holds in a constant positive value. From the 40^{th} to approximately the 70^{th} sample $h_{\text{f}}(n)|L_w = 64$ shows a divergent oscillatory behavior when the impulse response approaches to the end of the controller's length. This effect moves together with different controller lengths L_w and the amount of samples delays of the secondary path (omitted here for sake of space). The tail that follows is the primary path $p(n)$ minus the response of the secondary path to the cease of control signal coming from the controller. It can be seen from $h_{\text{f}}(n)|L_w = 8192$, that if the controller is as long as the primary path, its tail slowly settles

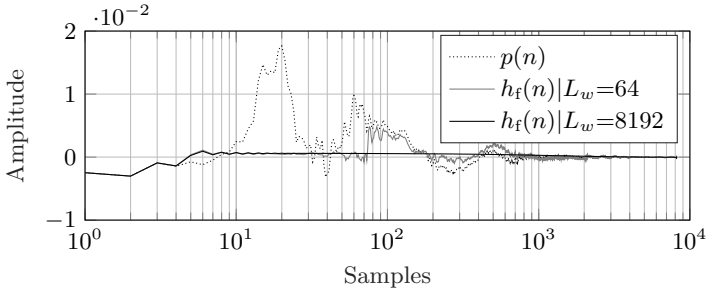

Figure 2.8.: System impulse response $h_\mathrm{f}(f)$ compared to the system subject to no control $p(n)$. Please note that the x-axis is in logarithmic scale. Parameters: $f_s = 48\,\mathrm{kHz}$, $L_s = 2048$, $L_p = 8192$, $\Phi_{xx} = I$.

to zero without oscillations.

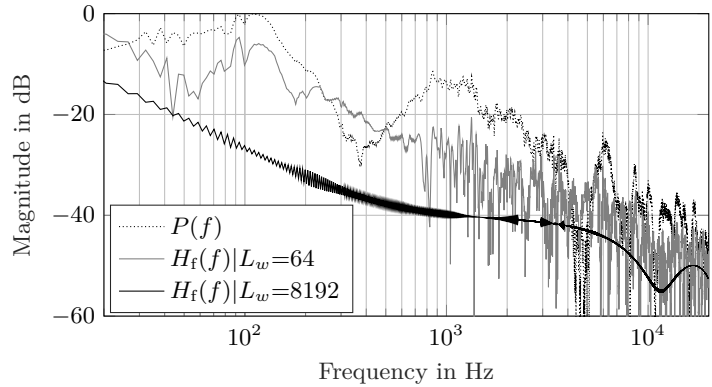

Figure 2.9.: System's frequency response $H_\mathrm{f}(f)$ compared to the system subject to no control $P(f)$. Parameters: $f_s = 48\,\mathrm{kHz}$, $L_s = 2048$, $L_p = 8192$, $\Phi_{xx} = I$.

In Fig. 2.9 the frequency response of the impulse responses in Fig. 2.8 are presented. It can be seen from comparing the primary path $P(f)$ with the frequency response of the long controller $H_\mathrm{f}(n)|L_w = 8192$, that peak attenuation values of 30 dB are possible. Although, not all frequencies are attenuated, as it is the case with the frequencies in the 5-6 kHz range. Some structures artifacts are visible but not dominant, which are originated during the matrix inversion. As the calculations are performed in single precision, because of RAM memory-usage considerations. Under the

effect of the short controller $H_\mathrm{f}(n)|L_w = 64$ the attenuation values drop significantly with a relative high variance. Nevertheless, it can be seen that in the 30-250 Hz and 0.5-4 kHz frequency ranges attenuation values of roughly 15 dB are still achievable. However, around 20 Hz and in the 250-500 Hz frequency range amplifications are produced, i.e. within the frequency range in which ANC should be effective the most.

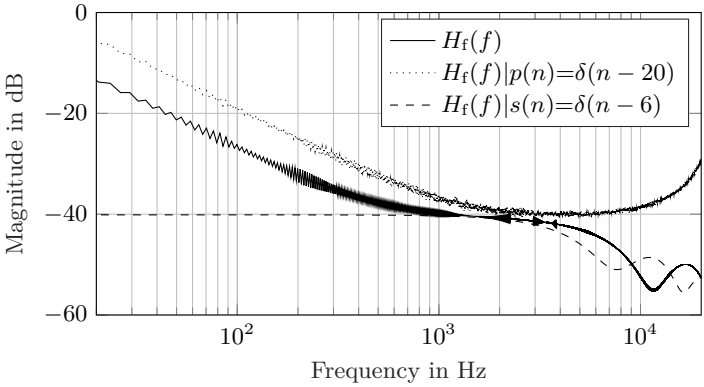

Figure 2.10.: System's frequency response $H_\mathrm{f}(f)$ compared to the hypothetical scenarios in which either the primary path is a delay of 20 samples $H_\mathrm{f}(f)|p(n)=\delta(n-20)$ or the secondary path is a delay of 6 samples $H_\mathrm{f}(f)|s(n)=\delta(n-6)$. Note: All controllers are recalculated based on their hypothetical systems. Parameters: $f_s = 48\,\mathrm{kHz}$, $L_w = 8192$, $L_s = 2048$, $L_p = 8192$, $\Phi_{xx} = I$.

In order to understand the origin of the optimal frequency response $H_\mathrm{f}(n)|L_w = 8192$, two hypothetical scenarios are evaluated and compared with it in Fig. 2.10. In the first one, the primary path impulse response is replaced by a delay placed at its original peak magnitude, e.i. at sample time $n = 20$. This enables to focus on the limits imposed by the inversion of the secondary path, as the primary path influence is limited. The Wiener controller is re-calculated and based on it, the system frequency response $H_\mathrm{f}(f)|p(n)=\delta(n-20)$ is generated based on the impulse response of a sample-by-sample simulation. The frequency response shows a limitation in the low-frequencies that decreases at a rate of 20 dB. This reaches a plateau of -40 dB at 2 kHz, which increases to -30 dB between 10 and 20 kHz. In the first second hypothetical scenario, the secondary path path impulse response is replaced by a delay placed at its original peak magnitude, e.i. at sample time $n = 6$. This enables to focus on the limits imposed by the primary path and a simplified causality limitation

produced by the idealized secondary path. The hypothetical system frequency response $H_{\mathrm{f}}(f)|s(n)=\delta(n-6)$ shows a roughly low-pass behavior with a 3.6 kHz cutoff frequency and a pass-band with gain of -40 dB. This is the frequency response of the first six samples of the primary path, which are the only that effectively become part of the system impulse response. If one compares $H_{\mathrm{f}}(n)$ with the two hypothetical scenarios, it can be seen that the limitations in the low- and mid-frequency region are originated in the inversion of the secondary path. At the same time, the frequency response in the high frequencies is originated by the first samples of the primary path, which pass uncontrolled because of the delays in the secondary path. The fact that the limitations due to the inversion of the secondary path do not increase again in the high-frequencies implies that a positive interaction for the controller occurs between the primary path and the secondary path. This could be for example pole-zero cancellations, that would simplify the naive controller solution $P(f)/S(f)$.

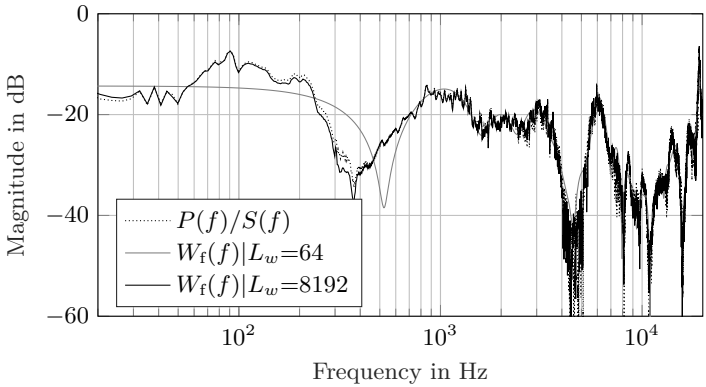

Figure 2.11.: Controller's frequency response $W_{\mathrm{f}}(f)$ for two different lengths. Parameters: $f_s = 48\,\mathrm{kHz}$, $L_s = 2048$, $L_p = 8192$, $\Phi_{xx} = I$.

The frequency response of both controllers $W_{\mathrm{f}}(f)|L_w = 64$ and $W_{\mathrm{f}}(f)|L_w = 8192$ are presented in Fig. 2.11. Together with them, the magnitude response of the naive optimum controller $P(f)/S(f)$ is presented as a reference. It can be seen that the longer controller $W_{\mathrm{f}}(f)L_w = 8192$ is over all frequencies very close to the ideal solution. Only in the low-frequencies some deviations are visible, which are produced by the limitations in the secondary path inversion. In contrast, the shorter controller $W_{\mathrm{f}}(f)|L_w = 64$ shows significant deviations, specially in the low-frequency region. The gain excess in the 250-500 Hz frequency range is the responsible for the amplifications seen before in Fig. 2.9.

All in all, it can be concluded from the examples presented in this section that even with a very long controller, the achievable attenuation reaches a limit and that in some frequency regions some amplifications can occur. The performance in the low-frequencies is dominated by the limitations in the secondary path inversion. In the high-frequencies, the delays in the secondary path together with the first samples of the primary path impulse response determine the frequency response. The controller length determines up to which sample the primary path impulse response can be suppressed. This decreases the achievable attenuation over all frequencies, as one could expect, with an important variance.

2.4. The Adaptive Controller

As seen in the previous section, in order to calculate the Wiener controller time-consuming and computationally demanding tasks have to be performed. First, the cross- and auto-correlations have to be calculated and time-averaged during a period of time. Afterwards, the matrix inversion $(\mathbf{S}^{\mathrm{T}} \cdot \mathbf{\Phi}_{xx} \cdot \mathbf{S})^{-1}$ has to be performed. At last, the optimal controller $\mathbf{w}_{\mathrm{f}}^{\mathrm{opt}}$ has to be calculated following Eq. 2.49. Unfortunately, any change in the sound field that implicates a change in the auto- or cross-correlation between the signals would require to re-calculate $\mathbf{w}_{\mathrm{f}}^{\mathrm{opt}}$. The same applies for changes in the secondary path $S(z)$. Nevertheless, the search for the optimal solution can also be performed in a continuous iterative way, such that, if the sound field changes, then the current estimation of the optimal controller automatically steers in the direction of the new optimum. Using the gradient descent method, such an adaptive iterative controller can be formulated. Using the coefficients' update equation

$$\mathbf{w}_{\mathrm{f}}(n+1) = \mathbf{w}_{\mathrm{f}}(n) - \frac{\mu}{2} \cdot \nabla f_c^{\mathrm{T}}(\mathbf{w}_{\mathrm{f}}(n)), \tag{2.53}$$

the new vector of coefficients $\mathbf{w}_{\mathrm{f}}(n+1)$ can be calculated based on the current ones $\mathbf{w}_{\mathrm{f}}(n)$, the current gradient of the quadratic error with respect to the controller coefficients $\nabla f_c^{\mathrm{T}}(\mathbf{w}_{\mathrm{f}}(n))$, and a small scalar μ called the step-size. With each iteration of this algorithm, the coefficient set moves slowly against the gradient of the cost function, in direction to the minimum.

In order to find an expression for the gradient $\nabla f_c^{\mathrm{T}}(\mathbf{w}_{\mathrm{f}}(n))$, the cost function in Eq. 2.43 is redefined by replacing the expectation operand by the equivalent mean over L_e values

$$\mathbb{E}[\mathbf{e}^{\mathrm{T}}\mathbf{e}] \approx \frac{(\mathbf{d}_{\mathrm{zp}} - \mathbf{S} \cdot \mathbf{W}_{\mathrm{f}} \cdot \mathbf{x})^{\mathrm{T}}(\mathbf{d}_{\mathrm{zp}} - \mathbf{S} \cdot \mathbf{W}_{\mathrm{f}} \cdot \mathbf{x})}{L_e}. \tag{2.54}$$

The gradient of the cost function with respect to the controller parameters

changes respectively to

$$\nabla f_c(\mathbf{w}_\mathrm{f}) = \frac{\partial \mathbb{E}[\mathbf{e}^\mathrm{T}\mathbf{e}]}{\partial \mathbf{w}_\mathrm{f}} \approx \frac{-2}{L_e} \cdot (\mathbf{d}_\mathrm{zp} - \mathbf{X} \cdot \mathbf{S} \cdot \mathbf{w}_\mathrm{f})^\mathrm{T} \cdot \mathbf{X} \cdot \mathbf{S} \tag{2.55}$$

Subsequently, Eq.2.41 is used to replace the vectors in round-parentheses by the error signal vector, and both sides of the equation are transposed

$$\nabla f_c^\mathrm{T}(\mathbf{w}_\mathrm{f}) \approx \frac{-2}{L_e} \cdot \mathbf{S}^\mathrm{T} \cdot \mathbf{X}^\mathrm{T}\mathbf{e}. \tag{2.56}$$

If a vector $\mathbf{x}_s$ of length $L_{x_s} = L_s + L_x - 1$ is defined as the *filtered-x* signal

$$\mathbf{x}_s = \mathbf{S} \cdot \mathbf{x}, \tag{2.57}$$

it can be shown that its associated Toeplitz matrix of dimensions $L_e \times L_w$ is defined by

$$\mathbf{X}_s = \mathbf{X} \cdot \mathbf{S}. \tag{2.58}$$

By using this result in Eq. 2.56, the transposed gradient takes the form

$$\nabla f_c^\mathrm{T}(\mathbf{w}_\mathrm{f}) \approx \frac{-2}{L_e} \cdot \mathbf{X}_s^\mathrm{T} \cdot \mathbf{e}, \tag{2.59}$$

which is the cross-correlation $\boldsymbol{\phi}^+_{x_s e}$ averaged over L_e values, related to the positive lags between the error signal $e(n)$ and the filtered reference $x_s(n)$. By using this equation in Eq. 2.53, the coefficients could be updated every L_e samples following

$$\mathbf{w}_\mathrm{f}(n+1) = \mathbf{w}_\mathrm{f}(n) + \frac{\mu}{L_e} \cdot \mathbf{X}_s^\mathrm{T} \cdot \mathbf{e}, \tag{2.60}$$

known as the Block Filtered-x Least Mean Square adaptation algorithm. However, this would involve updating and storing an $L_e \times L_w$ matrix. As a cheaper alternative, the instantaneous estimation (or average over one sample) of the cross-correlation

$$\nabla f_c^\mathrm{T}(\mathbf{w}_\mathrm{f}(n)) \approx -2 \cdot \mathbf{x}_s^\mathrm{T} \cdot e(n). \tag{2.61}$$

is used instead, where

$$\mathbf{x}_s^\mathrm{T} = \begin{bmatrix} x_s(n) \\ x_s(n-1) \\ \vdots \\ x_s(n-L_w+1) \end{bmatrix} \tag{2.62}$$

is the vector of last L_w samples of the filtered-x signal $x_s(n)$. By using

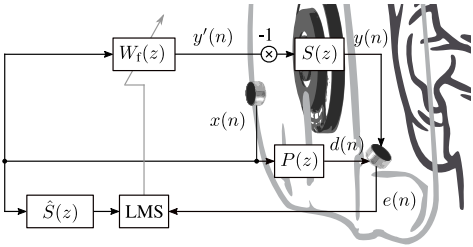

Figure 2.12.: The system diagram of the Filtered-x LMS adaptation algorithm applied to headphones.

Eq. 2.61 in Eq. 2.53, the coefficients' update equation can be formulated as

$$\mathbf{w}_\mathrm{f}(n+1) = \mathbf{w}_\mathrm{f}(n) + \mu \cdot \mathbf{x}_s^\mathrm{T} \cdot e(n), \tag{2.63}$$

which is the update equation of the well-known Filtered-x Least Mean Square (Filtered-x LMS) adaptation algorithm [Widrow et al., 1981,Burgess, 1981]. When this adaptation algorithm is used in headphones, the diagram presented in Fig. 2.12 is used. With each new sample $x(n)$ a FIFO buffer $\underline{x}$ of the length L_w is updated. Later, one control signal's output sample is generated by performing the vector multiplication

$$y'(n) = \underline{x}^\mathrm{T} \cdot \mathbf{w}_\mathrm{f}(n). \tag{2.64}$$

Subsequently, with the same sample $x(n)$ the FIFO buffer $\underline{x}_s$ of the length L_s is updated. Then one sample of the filtered-reference is generated

$$x_s(n) = \underline{x}_s^\mathrm{T} \cdot \mathbf{s}, \tag{2.65}$$

where $\mathbf{s}$ is a vector containing the first L_s samples of the measured impulse response of the secondary path $S(z)$. Afterwards, each sample of $x_s(n)$ is stored in the buffer $\mathbf{x}_s$ that is used for updating the coefficients by following Eq. 2.63.

2.4.1. Controller gain minimization

As explained at the end of Sec. 2.3, by including in the cost function the sum of squared controller coefficients weighted by the scalar parameter β_0

$$\min_{\mathbf{w}_\mathrm{f}} \mathbb{E}[\mathbf{e}^\mathrm{T}\mathbf{e}] + \beta_0 \mathbf{w}_\mathrm{f}^\mathrm{T} \mathbf{w}_\mathrm{f}, \tag{2.66}$$

the gain of the feedforward controller $\mathbf{w}_\mathrm{f}$ can also be penalize. This can be used, for example, to avoid solutions which produce control signals outside of the dynamic range of the system. With this change, the gradient of the

cost function with respect to the controller coefficients $\mathbf{w}_\mathrm{f}$ changes to

$$\nabla f_c(\mathbf{w}_\mathrm{f}) = \frac{\partial \mathbb{E}[\mathbf{e}^\mathrm{T}\mathbf{e}]}{\partial \mathbf{w}_\mathrm{f}} \approx \frac{-2}{L_e} \cdot (\mathbf{d}_\mathrm{zp} - \mathbf{X}\cdot\mathbf{S}\cdot\mathbf{w}_\mathrm{f})^\mathrm{T} \cdot \mathbf{X}\cdot\mathbf{S} + \frac{2\cdot\beta_0}{L_e}\cdot\mathbf{w}_\mathrm{f}^\mathrm{T}. \quad (2.67)$$

If this expression is transposed

$$\nabla f_c^\mathrm{T}(\mathbf{w}_\mathrm{f}) \approx \frac{-2}{L_e} \cdot \mathbf{S}^\mathrm{T}\cdot\mathbf{X}^\mathrm{T}\cdot(\mathbf{d}_\mathrm{zp} - \mathbf{X}\cdot\mathbf{S}\cdot\mathbf{w}_\mathrm{f}) + \frac{2\cdot\beta_0}{L_e}\cdot\mathbf{w}_\mathrm{f}, \quad (2.68)$$

and the vectors in the round parenthesis are replaced following Eq. 2.41 by the error signal vector

$$\nabla f_c^\mathrm{T}(\mathbf{w}_\mathrm{f}) \approx \frac{-2}{L_e} \cdot \mathbf{S}^\mathrm{T}\cdot\mathbf{X}^\mathrm{T}\cdot\mathbf{e} + \frac{2\cdot\beta_0}{L_e}\cdot\mathbf{w}_\mathrm{f}, \quad (2.69)$$

the gradient averaged over L_e samples can be found. Subsequently, the filtered-reference's Toeplitz matrix defined in Eq. 2.58 is used

$$\nabla f_c^\mathrm{T}(\mathbf{w}_\mathrm{f}) \approx \frac{-2}{L_e} \cdot \mathbf{X}_s^\mathrm{T}\cdot\mathbf{e} + \frac{2\cdot\beta_0}{L_e}\cdot\mathbf{w}_\mathrm{f}, \quad (2.70)$$

and the cheaper instantaneous estimate of the gradient is chosen instead

$$\nabla f_c^\mathrm{T}(\mathbf{w}_\mathrm{f}(n)) \approx -2\cdot\mathbf{x}_s^\mathrm{T}\cdot e(n) + 2\cdot\beta_0\cdot\mathbf{w}_\mathrm{f}. \quad (2.71)$$

This equation is used to replace the gradient in Eq. 2.53

$$\mathbf{w}_\mathrm{f}(n+1) = \mathbf{w}_\mathrm{f}(n) + \mu\cdot\mathbf{x}_s^\mathrm{T}\cdot e(n) - \mu\cdot\beta_0\cdot\mathbf{w}_\mathrm{f}(n), \quad (2.72)$$

which then formulates the coefficients update equation

$$\mathbf{w}_\mathrm{f}(n+1) = \mathbf{w}_\mathrm{f}(n)\big(1-\mu\cdot\beta_0\big) + \mu\cdot\mathbf{x}_s^\mathrm{T}\cdot e(n), \quad (2.73)$$

of the well-known leaky Filtered-x LMS algorithm [Elliott et al., 1987]. So, by means of this update equation the *Tikhonov-normalized* Wiener controller in Eq. 2.51 can be estimated in real-time.

2.4.2. The step-size

In order to yield a stable adaptation, μ has to be chosen according to

$$0 < \mu < \frac{2}{(L_\mathrm{w}+\Delta)\mathbb{E}[x_s^2]}, \quad (2.74)$$

where Δ is the delay introduced by the secondary path and $\mathbb{E}[x_s^2]$ is the expectation of the squared filtered-reference signal $x_s(n)$ (this can be replaced by the signal power P_{x_s}, if $x(n)$ is a deterministic signal) [Kuo and Morgan, 2000]. The maximum μ value in Eq. 2.74 is only a theoret-

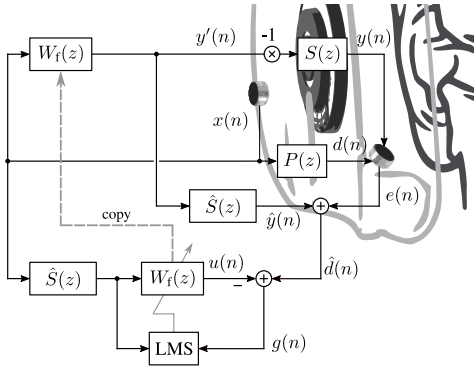

Figure 2.13.: The system diagram of the Modified Normalized Filtered-x LMS adaptation algorithm applied to headphones.

ical one, and if a fast adaptation is desired, an iterative search has to be performed with an $x(n)$ that produces a stable $\mathbb{E}[x_s^2]$. Alternatively, the search can be simplified, if a sample-by-sample estimation of $\mathbb{E}[x_s^2]$ is included in the adaptation algorithm. This can be done based on the last L_w observations of $x_s(n)$, as $\mathbb{E}[x_s^2] \approx (\mathbf{x}_s^\mathrm{T} \cdot \mathbf{x}_s)/L_\mathrm{w}$. This yields the so-called Normalized FxLMS (NFxLMS) [Sen and Morgan, 1996]. Its coefficients' update equation

$$\mathbf{w}_\mathrm{f}(n+1) = \mathbf{w}_\mathrm{f}(n) + \mu(n) \cdot \mathbf{x}_s^\mathrm{T} \cdot e(n) \tag{2.75}$$

contains a time-varying step-size $\mu(n)$ given by

$$\mu(n) = \frac{\mu_0}{\mathbf{x}_s^\mathrm{T} \cdot \mathbf{x}_s}, \tag{2.76}$$

where μ_0 is chosen as

$$0 < \mu_0 < \frac{2}{(1 + \Delta/L_\mathrm{w})}. \tag{2.77}$$

Thus, the search for the highest μ, now μ_0, can be be carried out in scenarios with changing $\mathbb{E}[x_\mathrm{s}^2]$ and the result will depend only on the delay of the secondary path Δ and the length of the controller L_w.

The modified filtered-x LMS

In practice, the search for an optimal μ_0 is rather impractical and should not be performed in the presence of a human subject, because of the risk of an unstable adaptation. A variation of the NFxLMS called the Modified

NFxLMS (MNFxLMS) [Bao et al., 1992, Bjarnason, 1992] simplifies the search for an optimum μ_0. Its system diagram is presented in Fig. 2.13. As can be seen, an estimated secondary path $\hat{S}(z)$ is used to estimate the disturbance signal $d(n)$ from the measured error signal $e(n)$. The estimated $\hat{d}(n)$ is used in combination with the filtered $x(n)$ to isolate a copy of the controller and adapt it using

$$\mathbf{w}_\mathrm{f} = \mathbf{w}_\mathrm{f} + \mu(n) \cdot \mathbf{x}_\mathrm{s} \cdot \left(\hat{d}(n) - \mathbf{x}_\mathrm{s}^\mathrm{T} \cdot \mathbf{w}_\mathrm{f}\right), \tag{2.78}$$

i.e. the LMS algorithm [Widrow et al., 1975]. By doing this, the controller coefficients are corrected using a local error estimation, independently from the delays and current state of the secondary path. This changes the theoretical boundaries for stable μ_0 to

$$0 < \mu_0 < 2. \tag{2.79}$$

Now the search is narrowed to a range of values in which only the performance of the attenuation varies, as a high μ_0 value produces a fast adaptation but a low attenuation, whereas a low μ_0 value produces a slow adaptation but a high attenuation.

2.4.3. Adaptation stability

The adaptation algorithms presented so far rely on the estimated secondary path $\hat{S}(z)$ for a correct estimation of the gradient of the cost function $\nabla f_c^\mathrm{T}(\mathbf{w}_\mathrm{f})$. As the secondary path $S(z)$ is a system that may vary between different headphones wearing situations, substantial differences between this and the estimated system $\hat{S}(z)$ may appear. These can drive the adaptation into instability or impose a severe limitation on the maximum step-size μ_0. In order to derive the constraints that have to be fulfilled to avoid the instability, the factor $\Psi(z)$ is used to describe the relation between both systems

$$\hat{S}(z) = \Psi(z) S(z). \tag{2.80}$$

The Filtered-x LMS structure in Fig. 2.12 is analyzed taking into account the update equation of the Block Filtered-x LMS

$$W_\mathrm{f}(z, n) = W_\mathrm{f}(z, n - L_e) + \mu \cdot \hat{S}(z^{-1}, n - L_e) X(z^{-1}, n - L_e) E(z, n - Le). \tag{2.81}$$

Here, non-overlapping frames of L_e samples of the signals are considered, while the L_e-samples long impulse responses of the systems are used. The z arguments are evaluated at k frequencies following the well-known sub-

stitution $z = e^{j\Omega_k}$

$$W_{\mathrm{f}}(\Omega_k, n) = W_{\mathrm{f}}(\Omega_k, n-L_e) + \mu \cdot \hat{S}^*(\Omega_k, n-L_e) X^*(\Omega_k, n-L_e) E(\Omega_k, n-Le), \tag{2.82}$$

in order to follow an analysis in the Discrete Fourier Transform domain. Because the energy content of the reference and disturbance are considered constant during the adaptation, only the controller's time dependency is taken into account

$$W_m = W_{m-1} + \mu \cdot \hat{S}^* \cdot X^* \cdot E, \tag{2.83}$$

expressed now with the time frame index m. The error signal E is replaced

$$W_m = W_{m-1} + \mu \cdot \hat{S}^* \cdot X^*(D - X \cdot W_{m-1} \cdot S), \tag{2.84}$$

to find its dependency on the *old* controller W_{m-1}. This is factorized

$$W_m = (1 - \mu \cdot \hat{S}^* \cdot X^* \cdot X \cdot S) W_{m-1} + \mu \cdot \hat{S}^* \cdot X^* \cdot D, \tag{2.85}$$

and defining

$$\alpha = 1 - \mu \cdot \hat{S}^* \cdot X^* \cdot X \cdot S \tag{2.86}$$

and

$$\beta = \mu \cdot \hat{S}^* \cdot X^* \cdot D, \tag{2.87}$$

rewritten as

$$W_m = \alpha \cdot W_{m-1} + \beta. \tag{2.88}$$

If iterative replacements of this equations are used, the dependency of W_m on its past value W_{m-M}

$$W_m = \alpha^M \cdot W_{m-M} + \beta \sum_{i=0}^{M-1} \alpha^i \tag{2.89}$$

can be found. This equation is used to express the optimum

$$W_{\mathrm{f}}^{\mathrm{opt}} = \lim_{M \to \infty} \left(\alpha^M \cdot W_{\mathrm{f}}^{\mathrm{init}} + \beta \sum_{i=0}^{M-1} \alpha^i \right) \tag{2.90}$$

in the limit $M \to \infty$, as a function of the initial coefficient set $W_{\mathrm{f}}^{\mathrm{init}}$ and the adaptation parameters found in α and β. Thus, if $1 > |\alpha|$, then the influence of the initial value decreases exponentially with every iteration, which is zero in the limit $M \to \infty$. Moreover, if the constraint $1 > |\alpha|$ is fulfilled, the geometric series is known to converge to the solution

$$W_{\mathrm{f}}^{\mathrm{opt}} = \frac{\beta}{1 - \alpha}. \tag{2.91}$$

If the definitions of α and β are used, then the optimum can be expressed as

$$W_f^{\mathrm{opt}} = \frac{\hat{S}^* \cdot X^* \cdot D}{\hat{S}^* \cdot X^* \cdot X \cdot S}. \tag{2.92}$$

By using Eq. 2.80 to substitute $\hat{S}$

$$W_f^{\mathrm{opt}} = \frac{\Psi^* \cdot S^* \cdot X^* \cdot D}{\Psi^* \cdot S^* \cdot X^* \cdot X \cdot S}, \tag{2.93}$$

it can be shown that the adaptive controller converges to the real optimum

$$W_{\mathrm{f}}^{\mathrm{opt}} = \frac{S^* \cdot X^* \cdot D}{S^* \cdot X^* \cdot X \cdot S} = (S^* \cdot \Phi_{xx} \cdot S)^{-1} S^* \cdot \Phi_{dx} \tag{2.94}$$

given that the constraint $1 > |\alpha|$ is fulfilled. To explore under which circumstances this can be ensured, this expression is expanded in the following sequence of equivalences

$$1 > |1 - \mu \cdot \Psi^* \cdot S^* \cdot X^* \cdot X \cdot S| \tag{2.95}$$

$$1 > |1 - \mu \cdot \Psi^* \cdot \Phi_{x_s x_s}| \tag{2.96}$$

$$1 > |1 - \mu \cdot \Psi^* \cdot \Phi_{x_s x_s}|^2 \tag{2.97}$$

$$1 > \mathrm{Re}\{1 - \mu \cdot \Psi^* \cdot \Phi_{x_s x_s}\}^2 + \mathrm{Im}\{1 - \mu \cdot \Psi^* \cdot \Phi_{x_s x_s}\}^2 \tag{2.98}$$

$$\begin{aligned} 1 > {} & 1 - 2\mu \cdot |\Psi| \cdot \cos(-\angle\Psi) \cdot \Phi_{x_s x_s} + (\mu \cdot |\Psi| \cdot \cos(-\angle\Psi) \cdot \Phi_{x_s x_s})^2 \\ & + (\mu \cdot |\Psi| \cdot \sin(-\angle\Psi) \cdot \Phi_{x_s x_s})^2 \end{aligned} \tag{2.99}$$

$$1 > 1 - 2\mu \cdot |\Psi| \cdot \cos(\angle\Psi) \cdot \Phi_{x_s x_s} + (\mu \cdot |\Psi| \cdot \Phi_{x_s x_s})^2 \tag{2.100}$$

$$0 > (\mu \cdot |\Psi| \cdot \Phi_{x_s x_s})^2 - 2 \cdot \cos(\angle\Psi) \cdot (\mu \cdot |\Psi| \cdot \Phi_{x_s x_s}). \tag{2.101}$$

If the last inequality is analyzed as a quadratic equation, the range of valid values is determined by its two zeroes

$$0 < \mu \cdot |\Psi| \cdot \Phi_{x_s x_s} < 2 \cdot \cos(\angle\Psi). \tag{2.102}$$

This inequality implies that to yield a stable adaptation and successful convergence to a solution, the phase difference between $S(z)$ and $\hat{S}$ has to stay within the range

$$-90^\circ < \angle\Psi < 90^\circ \tag{2.103}$$

for <u>all</u> frequencies Ω_k. Furthermore, if $|\Psi| \neq 0$ holds, then the inequality can be reformulated

$$0 < \mu \cdot \Phi_{x_s x_s} < 2 \cdot \frac{\cos(\angle\Psi)}{|\Psi|} \tag{2.104}$$

and the right-hand side plotted as contours for different Ψ as in Fig. 2.14. Here it can be seen how the maximum achievable $\mu \cdot \Phi_{x_s x_s}$ is exponentially

limited by the deviations in phase $\angle\Psi$, by dropping to zero as the phase gets near to either $90°$ or $-90°$. At the same time, the magnitude deviation is inverse proportional to $\mu \cdot \Phi_{x_s x_s}$. Thus, its highest value that is allowed decreases when $|\Psi|$ is bigger than one and it increases exponentially when it approaches zero.

If the system is excited on the entire frequency range, then $\Phi_{x_s x_s} \neq 0$ holds and the inequality can be formulated as

$$0 < \mu < \frac{2}{\Phi_{x_s x_s}} \cdot \frac{\cos(\angle\Psi)}{|\Psi|}, \tag{2.105}$$

for all frequencies Ω_k. Finally, to find one step-size μ for the Block Filtered-x LMS that fulfills this inequality over all frequencies Ω_k, the smallest value of the right-hand side should be taken

$$0 < \mu < \min\left(\frac{2}{\Phi_{x_s x_s}(\Omega_k)} \cdot \frac{\cos(\angle\Psi(\Omega_k))}{|\Psi(\Omega_k)|}\right). \tag{2.106}$$

As the effect of the deviations in the estimated secondary path can be isolated in the factor $\cos(\angle\Psi(\Omega_k))/|\Psi(\Omega_k)|$, this can be used for extending the constraint in Eq. 2.74 for the maximum step-size for the Filtered-x LMS.

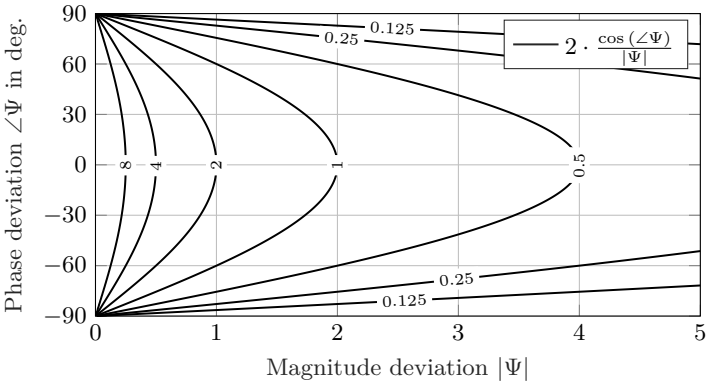

Figure 2.14.: Contour plot of the limit imposed by the magnitude and phase deviations Ψ contained in $\hat{S}(z)$ to the maximum achievable $\mu\Phi_{xx}$ for the Filtered-x LMS.

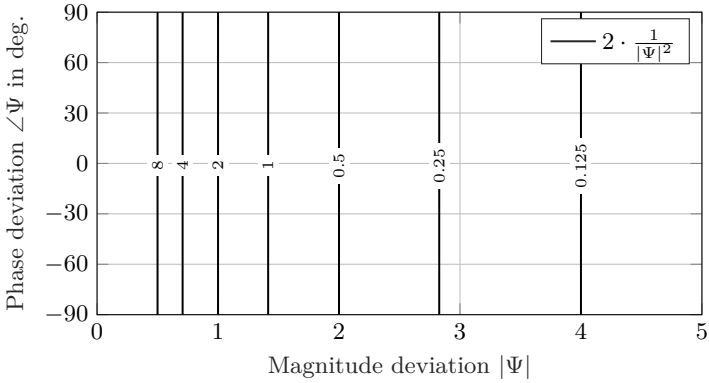

Figure 2.15.: Contour plot of the limit imposed by the magnitude deviations Ψ contained in $\hat{S}(z)$ to the maximum achievable $\mu\Phi_{xx}$ for the Modified Filtered-x LMS.

Modified filtered-x LMS adaptation stability

A similar analysis is performed with the Modified Filtered-x LMS presented in Fig. 2.13, in order to show that the system converges to the real optimum and also to derive the stability constraint of its adaptation. For that, the coefficients' update equation in Eq. 2.78 is analogously rewritten

$$W_m = W_{m-1} + \mu \cdot \hat{S}^* \cdot X^* \cdot (\hat{D}_{m-1} - X \cdot \hat{S} \cdot W_{m-1}) \tag{2.107}$$

and factorized

$$W_m = (1 - \mu \cdot \hat{S}^* \cdot X^* \cdot X \cdot \hat{S}) W_{m-1} + \mu \cdot \hat{S}^* \cdot X^* \cdot \hat{D}_{m-1}. \tag{2.108}$$

By defining the constant

$$\hat{\alpha} = 1 - \mu \cdot \hat{S}^* \cdot X^* \cdot X \cdot \hat{S} \tag{2.109}$$

and the variable

$$\hat{\beta}_{m-1} = \mu \cdot \hat{S}^* \cdot X^* \cdot \hat{D}_{m-1}, \tag{2.110}$$

the equation can be rewritten as

$$W_m = \hat{\alpha} \cdot W_{m-1} + \hat{\beta}_{m-1}. \tag{2.111}$$

If iterative replacements of this equation are performed, then the W_m can be expressed as

$$W_m = \hat{\alpha}^M \cdot W_{m-M} + \sum_{i=0}^{M-1} \hat{\alpha}^i \cdot \hat{\beta}_{m-1-i}. \tag{2.112}$$

The variable $\hat{\beta}_{m-1-i}$ is expanded

$$\begin{aligned}
\hat{\beta}_{m-1-i} &= \mu \cdot \hat{S}^* \cdot X^* \cdot \hat{D}_{m-1-i} && (2.113)\\
&= \mu \cdot \hat{S}^* \cdot X^* \big(D + X \cdot W_{m-1-i}(\hat{S} - S)\big) && (2.114)\\
&= \mu \cdot \hat{S}^* \cdot X^* \cdot D + \mu \cdot \hat{S}^* \cdot X^* \cdot X \cdot (\hat{S} - S) W_{m-1-i}, && (2.115)
\end{aligned}$$

and by defining

$$\beta = \mu \cdot \hat{S}^* \cdot X^* \cdot D \tag{2.116}$$

and

$$\gamma = \mu \cdot \hat{S}^* \cdot X^* \cdot X \cdot (\hat{S} - S), \tag{2.117}$$

it is reformulated as

$$\hat{\beta}_{m-1-i} = \beta + \gamma \cdot W_{m-1-i}. \tag{2.118}$$

Using this formulation, Eq. 2.112 can be expressed as

$$\begin{aligned}
W_m &= \hat{\alpha}^M \cdot W_{m-M} + \sum_{i=0}^{M-1} \hat{\alpha}^i (\beta + \gamma \cdot W_{m-1-i}) && (2.119)\\
&= \hat{\alpha}^M \cdot W_{m-M} + \beta \sum_{i=0}^{M-1} \hat{\alpha}^i + \gamma \sum_{i=0}^{M-1} \hat{\alpha}^i \cdot W_{m-1-i}. && (2.120)
\end{aligned}$$

This equation is used to express the optimum

$$W_{\mathrm{f}}^{\mathrm{opt}} = \lim_{M \to \infty} \left(\hat{\alpha}^M \cdot W_{\mathrm{f}}^{\mathrm{init}} + \beta \sum_{i=0}^{M-1} \hat{\alpha}^i + \gamma \sum_{i=0}^{M-1} \hat{\alpha}^i \cdot W_{m-1-i} \right) \tag{2.121}$$

in the limit $M \to \infty$, as a function of the initial coefficient set $W_{\mathrm{f}}^{\mathrm{init}}$, the adaptation parameters found in $\hat{\alpha}$ and β, and the frequency-weighted accumulation of the past values of the controller. In the limit $M \to \infty$ though, the optimum has been reached. Thus, for the limit $M \to \infty$ the sum can be also written as

$$\lim_{M \to \infty} \left(\gamma \sum_{i=0}^{M-1} \hat{\alpha}^i \cdot W_{m-1-i} \right) = \lim_{M \to \infty} \left(\gamma \sum_{i=0}^{M-1} \hat{\alpha}^i \cdot W_{\mathrm{f}}^{\mathrm{opt}} \right) \tag{2.122}$$

and with it also Eq. 2.121 as

$$W_{\mathrm{f}}^{\mathrm{opt}} = \lim_{M\to\infty}\left(\hat{\alpha}^M \cdot W_{\mathrm{f}}^{\mathrm{init}} + \beta\sum_{i=0}^{M-1}\hat{\alpha}^i + \gamma\cdot W_{\mathrm{f}}^{\mathrm{opt}}\sum_{i=0}^{M-1}\hat{\alpha}^i\right). \tag{2.123}$$

As it can be extrapolated from the analysis of the filtered-x LMS case, if the condition $1 > |\hat{\alpha}|$ is fulfilled, then the limit solves to

$$W_{\mathrm{f}}^{\mathrm{opt}} = \frac{\beta}{1-\hat{\alpha}} + W_{\mathrm{f}}^{\mathrm{opt}}\frac{\gamma}{1-\hat{\alpha}} \tag{2.124}$$

$$\rightarrow W_{\mathrm{f}}^{\mathrm{opt}} = \frac{\beta}{1-\hat{\alpha}-\gamma}. \tag{2.125}$$

By using the definitions of $\hat{\alpha}$, β, and γ in Eq. 2.109, Eq. 2.116, and Eq. 2.117, respectively, it can be shown

$$W_f^{\mathrm{opt}} = \frac{\mu\cdot\hat{S}^*\cdot X^*\cdot D}{1-1+\mu\cdot\hat{S}^*\cdot X^*\cdot X\cdot\hat{S}-\mu\cdot\hat{S}^*\cdot X^*\cdot X\cdot(\hat{S}-S)} \tag{2.126}$$

$$= \frac{\hat{S}^*\cdot X^*\cdot D}{\hat{S}^*\cdot X^*\cdot X\cdot S}. \tag{2.127}$$

that the the Modified Filtered-x LMS also converges to the real optimum. However, its convergence stability depends on the constraint

$$1 > |\hat{\alpha}|. \tag{2.128}$$

If this is expanded using Eq. 2.109

$$1 > |1-\mu\cdot\hat{S}^*\cdot X^*\cdot X\cdot\hat{S}| \tag{2.129}$$

$$1 > |1-\mu\cdot|\Psi|^2\cdot S^*\cdot X^*\cdot X\cdot S| \tag{2.130}$$

$$1 > |1-\mu\cdot|\Psi|^2\cdot\Phi_{x_sx_s}| \tag{2.131}$$

$$1 > \sqrt{\left(1-\mu\cdot|\Psi|^2\cdot\Phi_{x_sx_s}\right)^2} \tag{2.132}$$

$$1 > \left(1-\mu\cdot|\Psi|^2\cdot\Phi_{x_sx_s}\right)^2 \tag{2.133}$$

$$1 > 1-2\cdot\left(\mu\cdot|\Psi|^2\cdot\Phi_{x_sx_s}\right)+\left(\mu\cdot|\Psi|^2\cdot\Phi_{x_sx_s}\right)^2 \tag{2.134}$$

$$0 > (\mu\cdot|\Psi|^2\cdot\Phi_{x_sx_s})^2 - 2\cdot(\mu\cdot|\Psi|^2\cdot\Phi_{x_sx_s}). \tag{2.135}$$

and analyzed as a quadratic equation, the range of valid values is determined by

$$0 < \mu\cdot|\Psi|^2\cdot\Phi_{x_sx_s} < 2. \tag{2.136}$$

If $|\Psi|^2 \neq 0$ holds, then this can be written as

$$0 < \mu \cdot \Phi_{x_s x_s} < 2 \cdot \frac{1}{|\Psi|^2}. \tag{2.137}$$

Thus, the maximum μ is independent of the phase deviation $\angle\Psi$, but it is inverse proportional to the squared magnitude deviation $|\Psi|^2$, as plotted in Fig. 2.15. Finally, if $\Phi_{x_s x_s} \neq 0$, then the step-size μ for the Modified Filtered-x LMS can be chosen as

$$0 < \mu < \min\left(\frac{2}{\Phi_{x_s x_s}(\Omega_k)} \cdot \frac{1}{|\Psi(\Omega_k)|^2}\right). \tag{2.138}$$

Analog to the Filtered-x LMS, the factor $1/|\Psi(\Omega_k)|^2$ can be used in Eq. 2.79 to extend the constraint for cases in which the estimated secondary path $\hat{S}(z)$ and the real one $S(z)$ are not equal.

2.5. Summary

In the present chapter the feedforward control scheme has been presented. In Sec. 2.1 the causality limitation due to the working principle based on a time-advanced reference $x(n)$ is described. If the control chain requires more time to generate the control signal $y(n)$ than the time that it takes to the reference $x(n)$ to arrive at the error microphone in the form of $d(n)$, then the superposition will not be perfectly destructive. As result of that, the residual error $e(n)$ is shaped by the comb-filter effect presented in Fig. 2.4, with some attenuation regions an others where amplification occurs. Depending on the solution context, a possible counter-measure could be to increase the distance between reference and error microphones. This, measuring the reference signal $x(n)$ closer to the noise source. However, in Sec. 2.2 it is shown that increasing the distance between both microphones may lead to another problem: If the sound field is of isotropic and diffuse nature, then the reference signal $x(n)$ may not be correlated with $d(n)$ anymore. This loss in correlation limits the maximum attenuation as presented in Fig. 2.5. It is left to the engineer to find an optimum solution to the trade-off between both effects, based on the solution's context.

In Sec. 2.3 the derivation of the optimum feedforward controller $\mathbf{w}_\mathrm{f}^\mathrm{opt}$ is presented. Equation 2.49 provide the controller's impulse response coefficients that minimize the expectation of the quadratic error. Based on impulse responses measured from a real headphones prototype, examples are presented in Sec. 2.3.1 to evaluate the achievable results. It is concluded that even with a very long impulse response, the achievable attenuation reaches a limit and that in some frequency regions amplifications can occur. The performance in the low-frequencies is dominated by the limitations in the secondary path inversion. In the high-frequencies, the frequency re-

sponse is determined by the delays in the secondary path together with the first samples of the primary path's impulse response. If the chosen controller length is shorter than the one of the primary path, this length determines up to which sample the primary path impulse response can be suppressed. This decreases the achievable attenuation over all frequencies with an important variance.

In Sec. 2.4 adaptation algorithms are presented, which aim to approximate $\mathbf{w}_{\mathrm{f}}^{\mathrm{opt}}$ based on iterations performed in real-time, while the system is in operation. This enables the controller to find a new optimum upon changes in the energy content of the noise signal. However, when using these algorithms a trade-off between convergence speed and the achievable attenuation has to be made by choosing the adaptation step-size μ_0. The boundaries to choose this parameter rely on the correct approximation of the secondary path. Furthermore, it is shown that, if the Filtered-x LMS is used (see Fig. 2.12), a phase error bigger than $\pm 90^\circ$ can force the adaptation to instability. However, if the Modified Normalized Filtered-x LMS is used instead (see Fig. 2.13), this problem can be circumvented. Then, only the error in estimating the system's magnitude over frequency is of relevance for the stability.

In the following chapter a different control scheme is presented, which avoids the use of a time-advanced reference $x(n)$. Instead of that, it works as a feedback system, using the residual error $e(n)$ as input for calculating its control signal. This enables it to circumvent coherence problem, as its input and outputs are co-located. However, it is going to be shown that its *reactive* working principle makes it subject to new practical and mathematical considerations.

CHAPTER 3

Minimum Variance Control

Feedback systems are preferred over the feedforward ones in contexts where there is no economical way to provide a time-advanced reference to all noise sources, or for systems which have to perform upon fast moving sources. In contrast to the feedforward controller, the feedback one calculates its output based on the error signal, instead of the time-advanced reference. The Minimum Variance Control (MVC) structure, also known in the literature as classical feedback control scheme, is presented in Fig. 3.1. The controller $W_{\mathrm{m}}(z)$ is designed such that the command signal $c(n)$ is replicated at the output of the *plant* $S(z)$. Its output signal $y(n)$ is subject to the external disturbance $d(n)$, which generates an effective system output $e(n)$. A negative feedback loop is used to calculate a correction factor by subtracting $e(n)$ from $c(n)$, which is fed to the controller $W_{\mathrm{m}}(z)$.

Under ideal circumstances, the effective system's output $e(n)$ follows the

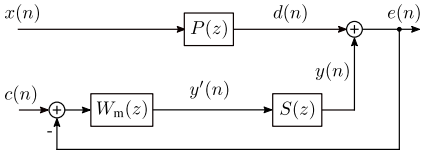

Figure 3.1.: The block diagram of the minimum variance control scheme. Represented are the feedback controller $W_{\mathrm{m}}(z)$, the primary path $P(z)$, and the secondary path $S(z)$.

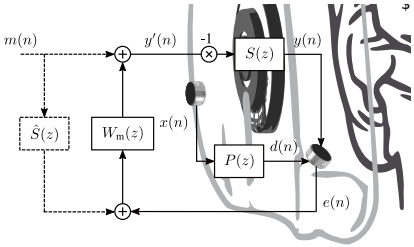

Figure 3.2.: The system diagram of a the feedback control scheme adapted to the application on a headphones earcup. Represented are a digital feedback controller $W_\mathrm{m}(z)$, the primary path $P(z)$, and the secondary path $S(z)$. Optionally, a music signal $m(n)$ can be integrated in the signal flow by using an estimated secondary path $\hat{S}(z)$, as in [Liebich et al., 2016].

command signal $c(n)$ closely, implying that the transfer function

$$T(z) = \frac{E(z)}{C(z)} = \frac{S(z) \cdot W_\mathrm{m}(z)}{1 + S(z) \cdot W_\mathrm{m}(z)}, \tag{3.1}$$

also known as *complementary sensitivity function*, is close to unity. Furthermore, the system transfer function

$$H_\mathrm{m}(z) = \frac{E(z)}{D(z)} = \frac{1}{1 + S(z) \cdot W_\mathrm{m}(z)}, \tag{3.2}$$

also called *sensitivity function*, is close to zero, thus rejecting the disturbance $d(n)$ in the effective system output $e(n)$. For achieving this, the controller $W_\mathrm{m}(z)$ is designed to maximize the denominator of $H_\mathrm{m}(z)$, while respecting certain stability and performance constraints.

When this control approach is applied to headphones the elements conceptually represented in Fig. 3.1 are reordered to match the solution context, as shown in Fig. 3.2. As can be seen, the reference microphone placed outside the earcup is not used by the controller, but is kept only for the conceptual description of the primary path. The error microphone is placed inside the earcup and its signal is used as input for the controller $W_\mathrm{m}(z)$. In this context, rather than driving the system with a control signal $c(n)$, the integration of a music signal $m(n)$ is required. For this, an estimated secondary path $\hat{S}(z)$ is used to incorporate $m(n)$ in the signal flow. This coupling generates the transfer function

$$\frac{E(z)}{M(z)} = -S(z)\frac{1 + \hat{S}(z) \cdot W_\mathrm{m}(z)}{1 + S(z) \cdot W_\mathrm{m}(z)}. \tag{3.3}$$

If $\hat{S}(z)=S(z)$ is chosen, the transfer function simplifies to $\frac{E(z)}{M(z)}=-S(z)$, and $m(n)$ reaches the error microphone uncolored by the controller $W_{\mathrm{m}}(z)$. If the headphones are well-designed, the effect of the secondary path $S(z)$ does not need further treatment.

The first application of this control scheme on a headrest was proposed by Olson and May in [Olson and May, 1953, Olson, 1961], while its application to headphones for the control of periodic signals was presented by Simhauser and Hawley [Simshauser and Hawley, 1955]. The design of a controller capable of attenuating low-frequency broadband noise was presented by Bose in [Bose, 1985]. Nowadays, the design and optimization of such systems are based on the mixed-sensitivity H_∞ method proposed by Zames in [Zames, 1981]. Successful applications of this method to the specific case of ANC headphones can be found in the literature, e. g. for analog [Bai and Lee, 1997] and digital [Liebich et al., 2016] controllers' circuitry. Here, an emphasis on robust stability and performance is made, for which an uncertainty model of the secondary path is built from a set of measurements. This model is used to establish the variability over frequency that the secondary path has on different headphones' wearing situations. This variability is then used for building worst-case mathematical constraints for the controller's optimization based on an H_∞ cost function. One drawback of this approach is that a pole-zero model of each secondary path has to be matched to the measurements first, instead of using the measured impulse responses directly. Another drawback is that the optimized controller has to have a state-space formulation.

An alternative to H_∞ was proposed by Rafaely in [Rafaely, 1997] on the optimization of an Internal Model Controller [Morari and Zafiriou, 1989] by means of an H_2/H_∞ design method. For more details about this, please refer to Section 4. The robust stability against the uncertainty in the secondary path is the same as in the H_∞ method, but a cost function based on the 2-norm is used instead. Moreover, the pole-zero system modeling is avoided by the use of measured impulse responses, and the state-space controller is substituted by a finite impulse response (FIR) filter. This formulation is adopted in this Chapter, in order to optimize the impulse response a minimum variance controller. As shown by Rafaely, if the problem can be formulated as a convex optimization task [Gill et al., 1981], a solution based on sequential quadratic programming (SQP) [Fletcher, 1987] yields a global optimum subject to the designed constraints.

3.1. Limitations due to Delays

Let us assume a hypothetical secondary path

$$S^{\mathrm{hyp}}(z) = z^{-D_s}, \tag{3.4}$$

which is composed only by a delay of D_s samples. In this scenario, the best causal controller would achieve to track the command signal with the same delay D_s [Skogestad and Postlethwaite, 2005]. At the same time this implies a complementary transfer function

$$T^{\mathrm{hyp}}(z) = z^{-D_s} \tag{3.5}$$

with the same delay of D_s samples. Equating this to the definition of the complementary sensitivity function found in Eq. 3.1

$$\frac{S^{\mathrm{hyp}}(z) \cdot W_{\mathrm{m}}^{\mathrm{hyp}}(z)}{1 + S^{\mathrm{hyp}}(z) \cdot W_{\mathrm{m}}^{\mathrm{hyp}}(z)} = z^{-D_s} \tag{3.6}$$

and replacing the hypothetical secondary path in it

$$\frac{z^{-D_s} \cdot W_{\mathrm{m}}^{\mathrm{hyp}}(z)}{1 + z^{-D_s} \cdot W_{\mathrm{m}}^{\mathrm{hyp}}(z)} = z^{-D_s}, \tag{3.7}$$

the best causal controller for this scenario can be found

$$W_{\mathrm{m}}^{\mathrm{hyp}}(z) = \frac{1}{1 - z^{-D_s}}. \tag{3.8}$$

Replacing this hypothetical controller in the sensitivity function of Eq. 3.2 yields

$$H_{\mathrm{m}}^{\mathrm{hyp}}(z) = 1 - z^{-D_s}. \tag{3.9}$$

This means that, the best achievable system transfer function is found to be the one of a feedforward comb filter, as presented in Fig. 2.4. Thus, the feedback controller behaves similarly to a feedforward system subject to an overall control delay greater than the acoustic delay of the primary path. Refer to Sec. 2.1 for more details. Thus, the feedback controller is fundamentally a reactive system subject to performance limitations imposed by the delay in the secondary path $S(z)$. Moreover, a destructive overlap of the control signal with the disturbance can only take place as long as the disturbance's statistical characteristics and frequency content do not change during the D_s samples. Thus, control of impulsive noise is not possible with this control scheme.

If the amplifications produced by the comb filter are not tolerable, the controller is limited to act within a specific bandwidth. This bandwidth can be found to be approximately

$$f_{0\mathrm{dB}} < \frac{1}{6 \cdot D_s \cdot T_s}, \tag{3.10}$$

with T_s as the sampling period, if a similar analysis as the one presented in Sec. 2.1.1 is followed [Elliott, 2008].

The sources of delays in a digital implementation of a feedback controller

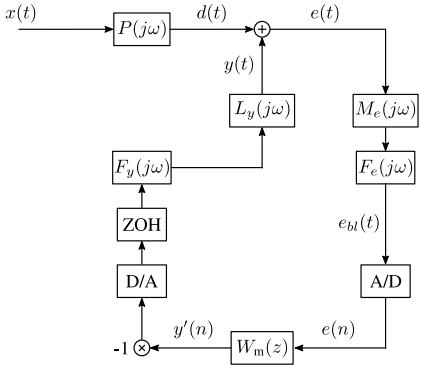

Figure 3.3.: Minimum variance control scheme in its digital implementation form.

are presented in Fig. 3.3. The upper-most part of the diagram is designated just to the acoustic domain, where the acoustic signals $x(t)$, $d(t)$, $y(t)$, and $e(t)$, and the primary path $P(j\omega)$ are described in the continuous time domain. The elements of the next lower level are the loudspeaker $L_y(j\omega)$ and the microphone $M_x(j\omega)$, which provide the conversion from the electric domain to the acoustic domain and vice-versa. On the next lower level the reconstruction filter $F_y(j\omega)$ and the anti-aliasing filter $F_e(j\omega)$, which are required for limiting the signals' bandwidth are depicted. On the level below, the analog-digital (A/D) and digital-analog (D/A) converters together with the method used for the reconstruction of the analog signal after the D/A conversion are presented. In this specific case a zero-order hold method (ZOH) is shown. The bottom level is the discrete time domain, in which calculation of the control signal $y'(n)$ is described by the convolution between the sampled error signal $e(n)$ and the impulse response of the controller $W_m(z)$. So the overall delay in the secondary path

$$\tau_s(f) = \tau_{m_e}(f) + \tau_{f_e}(f) + \tau_{\mathrm{ad}} + \tau_{\mathrm{dsp}} + \tau_{\mathrm{da}} + \tau_{\mathrm{zoh}} + \tau_{f_y}(f) + \tau_{l_y}(f) \quad (3.11)$$

can be calculated by adding the group-delay of the microphone $\tau_{m_e}(f)$, the group-delay of the anti-aliasing filter $\tau_{f_e}(f)$, the analog-digital conversion delay τ_{ad}, the processing delay τ_{dsp}, the digital-analog conversion delay τ_{da}, the zero-order hold implicit delay τ_{zoh} of $T_s/2$, the group-delay of the reconstruction filter $\tau_{f_y}(f)$, and the group-delay of the loudspeaker $\tau_{l_y}(f)$. The group-delay of the loudspeaker and the microphone have to be measured together, as it is important to include the physical distance and influence of the acoustic system between them.

As already mentioned in Sec. 2.1.2, the system can be optimized for minimum delay by increasing the sampling frequency and choosing the cut-off frequencies of the filters away from the frequency range of interest. Moreover, choosing a fast digital-analog conversion technology. i.e. SAR, can bring the conversion delays down to 1 μs. However, in order to decrease the processing delay τ_{dsp} below the sampling period T_s, the convolution has be performed in a specific order and the DAC and ADC control signals have to be decoupled. How this is done is presented in the following subsection.

3.1.1. Towards low-latency processing

The discrete-time filtering of a causal recursive filter and its input signal $x(n)$ can be written as two sums

$$y(n) = \sum_{k=0}^{K} b_k \cdot x(n-k) - \sum_{l=1}^{L} a_l \cdot y(n-l), \tag{3.12}$$

where the first one describes the interaction of its input samples with its feed-forward filter coefficients b_k, and the second one the interaction of its past outputs with its feedback coefficients a_l. For the case of a non-recursive filter, e.i. an FIR filter, the second sum disappears. Depending on the order of the filter, the computational power of the target platform, and the strategy of calculation, the time needed to calculate both sums of products for one input sample, called the processing latency, may increase beyond the sampling period or decrease below it. The first case would produce that the result of the convolution will not be ready before the new input sample comes, while the second case would produce a result before the next sample arrives. If ADC and DAC units are clocked with the same signal, i.e. coupled together, the processing latency will have an *effective* value that is a multiple of the sampling period and greater or equal to its *real* value. To get rid of this undesirable extra processing latency and reach an *effective* value equal to the *real* value, the ADC and DAC units should be decoupled.

If the sampling period is as long as or longer than the time required to calculate the convolution, then the input and output samples involved in the convolution do not change during its calculation. In that case, the first term of the left sum of products may be pulled out

$$y(n) = b_0 \cdot x(n) + \sum_{k=1}^{K} b_k \cdot x(n-k) - \sum_{l=1}^{L} a_l \cdot y(n-l) \tag{3.13}$$

to show that besides $x(n)$, all other input samples were already known before starting with the calculation. This fact is strategically used to

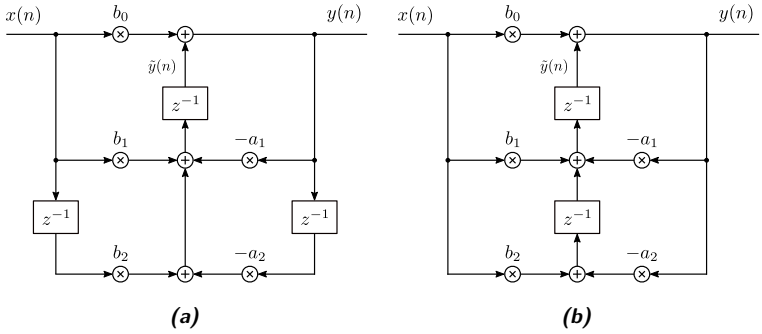

Figure 3.4.: Special cases of a 2nd order IIR filter: (a) Hybrid Form I and and (b) Transposed Direct Form II.

prepare a precalculated output for the next sample time $n+1$

$$\tilde{y}(n+1) = \sum_{k=1}^{K} b_k \cdot x(n-k+1) - \sum_{l=1}^{L} a_l \cdot y(n-l+1). \tag{3.14}$$

Then, upon the arrival of the next input sample $x(n+1)$, only one multiplication and one addition have to be performed

$$y(n+1) = b_0 \cdot x(n+1) + \tilde{y}(n+1). \tag{3.15}$$

Once these two calculations are ready, the D/A is signaled to convert the output sample. Hence, from the moment in which the A/D provides $x(n+1)$ and the respective control signal $y(n+1)$ is handed-over to the D/A, only the time required to calculate one multiplication and one addition is required.

If this simple strategy is implemented with an IIR Direct Form I subblock for the calculation of $\tilde{y}(n+1)$, then the implementation is a special case of an IIR Hybrid Form I (see Fig. 3.4a). In this case we will say that the convolution calculation is *decoupled* from the filter's memory. If the precalculation is applied iteratively, then the behavior matches the well-known IIR Transposed Direct Form II (see Fig. 3.4b).

3.2. Stability

The stability of a feedback system can be determined by analyzing its *characteristic equation*

$$C_{\mathrm{m}}(z) = 1 + S(z) \cdot W_{\mathrm{m}}(z), \tag{3.16}$$

which corresponds to the denominator of the sensitivity and complementary sensitivity functions. The locations of the zeros of this equation are the same as the positions of the poles of the sensitivity and complementary sensitivity functions. Thus, if the characteristic equation has a zero outside the unit circle, then the feedback system has an unstable pole. This is a very straightforward stability analysis, if the pole-zero descriptions of $S(z)$ and $W_{\mathrm{m}}(z)$ are available. However, in acoustics such descriptors are inconvenient, due to the high complexity, delays, and variability that the acoustic systems have [Elliott, 2008].

As an alternative, the Nyquist stability criterion [Nyquist, 1932] in the Z-domain [Franklin et al., 1997] can be applied to determine the stability of systems for which only the frequency responses and/or impulse responses are known. The analysis makes use of the Cauchy's argument principle

$$-\oint_{\kappa} \frac{C'_{\mathrm{m}}(z)}{C_{\mathrm{m}}(z)} dz = 2 \cdot \pi \cdot j \cdot (Z_{C_{\mathrm{m}},\kappa} - P_{C_{\mathrm{m}},\kappa}). \tag{3.17}$$

It states that the contour integration of the logarithmic derivative of $C_{\mathrm{m}}(z)$ is proportional to the difference between the number of zeros $Z_{C_{\mathrm{m}},\kappa}$ and poles $P_{C_{\mathrm{m}},\kappa}$ of C_{m} contained within the contour κ. Because the problematic zeros are found outside the unit circle, the contour κ presented in Fig. 3.5a is used. For comparison the contour used for an s-domain analysis is presented in Fig. 3.5b as well. As can be seen, both contours enclose without self-intersections the regions where the problematic zeros may be located. Since both contours are clockwise oriented, a minus sign is used in front of the integral in Eq. 3.17.

In general, the analysis is continued by determining the amount of unstable poles inside κ that the controller $W_{\mathrm{m}}(z)$ and the secondary path $S(z)$ have. Once this is determined, it is used to replace $P_{C_{\mathrm{m}},\kappa}$ in Eq. 3.17, because the poles of these systems are the same as the poles of the characteristic equation $C_{\mathrm{m}}(z)$. However, the control of unstable systems is outside the scope of the present work and for our analysis $P_{C_{\mathrm{m}},\kappa} = 0$ will cover all relevant cases. Thus, Eq. 3.17 is re-arranged

$$Z_{C_{\mathrm{m}},\kappa} = -\frac{1}{2 \cdot \pi \cdot j} \oint_{\kappa} \frac{C'_{\mathrm{m}}(z)}{C_{\mathrm{m}}(z)} dz \tag{3.18}$$

to find the amount of problematic zeros $Z_{C_{\mathrm{m}},\kappa}$ with help of the weighted

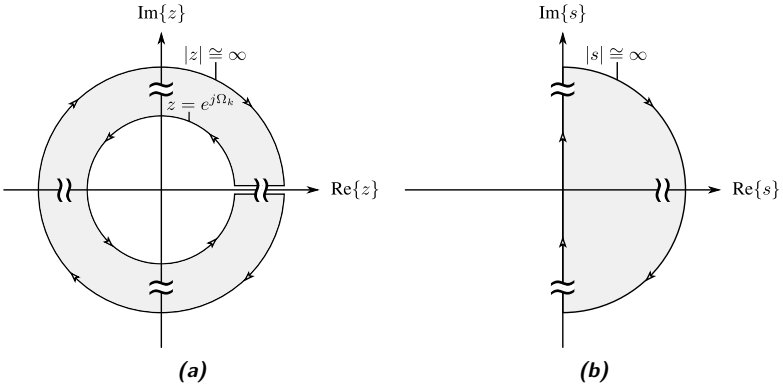

Figure 3.5.: Nyquist criterion evaluation contour: (a) for discrete time systems in the z-domain and (b) for time continuous systems in the s-domain given in [Franklin et al., 1997].

contour integral over κ. If the substitution $C_{\mathrm{m}}(z) = O(z) + 1$ is used in Eq. 3.18

$$Z_{C_{\mathrm{m}},\kappa} = -\frac{1}{2 \cdot \pi \cdot j} \oint_{\kappa} \frac{O'(z)}{O(z)+1} dz, \tag{3.19}$$

then the contour integral can be expressed in terms of the *open-loop transfer function*

$$O(z) = W_{\mathrm{m}}(z) \cdot S(z). \tag{3.20}$$

Subsequently, instead of calculating the integral over κ in z, the integral is reformulated following the contour $O(\kappa)$ in O, such that Eq. 3.19 simplifies to

$$Z_{C_{\mathrm{m}},\kappa} = -\frac{1}{2 \cdot \pi \cdot j} \oint_{O(\kappa)} \frac{1}{O+1} dO. \tag{3.21}$$

Now, instead of calculating the right-hand side of Eq. 3.21 to find $Z_{C_{\mathrm{m}},\kappa}$, the Cauchy's integral formula

$$\frac{1}{2 \cdot \pi \cdot j} \oint_{cc} \frac{g(x)}{x-a} dx = \begin{cases} g(a) & a \text{ inside } cc \\ 0 & \text{otherwise} \end{cases} \tag{3.22}$$

is used to find the solution. It states that if the point in the complex plane $x = a$ is contained in the counterclockwise-oriented contour cc without self-intersections, then the contour integral evaluates to $g(a)$, and otherwise to zero. The contour cc can be oriented in the clockwise direction (renamed

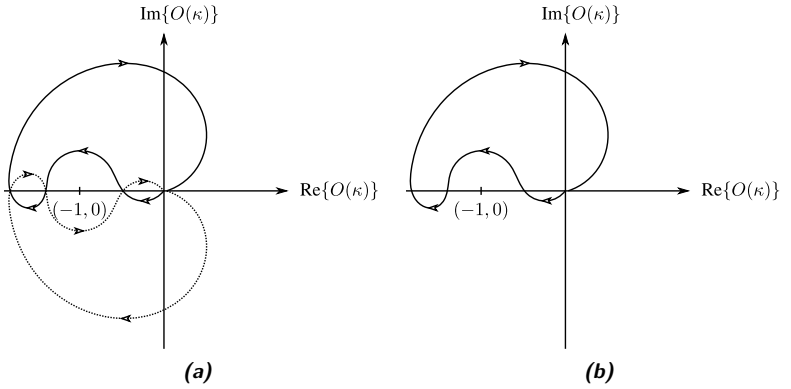

Figure 3.6.: Nyquist plot example of an stable system: (a) The open-loop transfer function $O(z)$ evaluated along the contour κ; and (b) the open-loop transfer function $O(z)$ evaluated along the upper-half of the unit circle.

as c), if a compensating change of sing is used in the integral

$$-\frac{1}{2\cdot\pi\cdot j}\oint_c \frac{g(x)}{x-a}dx = \begin{cases} g(a) & a \text{ inside } c \\ 0 & \text{otherwise} \end{cases} \tag{3.23}$$

such that it matches the orientation of $O(\kappa)$. If the function $g(x) = 1$, the Nyquist point $a = (-1, 0)$, the variable $x = O$, and the clockwise-oriented contour $c = O(\kappa)$ are chosen, then this can be used for the current analysis

$$Z_{C_{\mathrm{m}},\kappa} = -\frac{1}{2\cdot\pi\cdot j}\oint_{O(\kappa)} \frac{1}{O+1}dO = \begin{cases} 1 & (-1,0) \text{ inside } O(\kappa) \\ 0 & \text{otherwise} \end{cases} \tag{3.24}$$

to solve Eq. 3.21 by visual inspection of $O(\kappa)$.

One complication arises from the contour $O(\kappa)$, because there is no restriction that ensures that it contains no intersection with itself. So, as in the examples presented in Fig. 3.6a and in Fig. 3.7a, there can be sub-contours that encircle areas of the complex plane with different orientations. In this case, the total number of unstable roots equals

$$Z_{C_{\mathrm{m}},\kappa} = N^{\mathrm{cw}}_{O(\kappa)} - N^{\mathrm{ccw}}_{O(\kappa)}, \tag{3.25}$$

where $N^{\mathrm{cw}}_{O(\kappa)}$ is the number of clockwise encirclement of the Nyquist point made by the sub-contours of $O(\kappa)$ and $N^{\mathrm{ccw}}_{O(\kappa)}$ is the number of counter-clockwise ones.

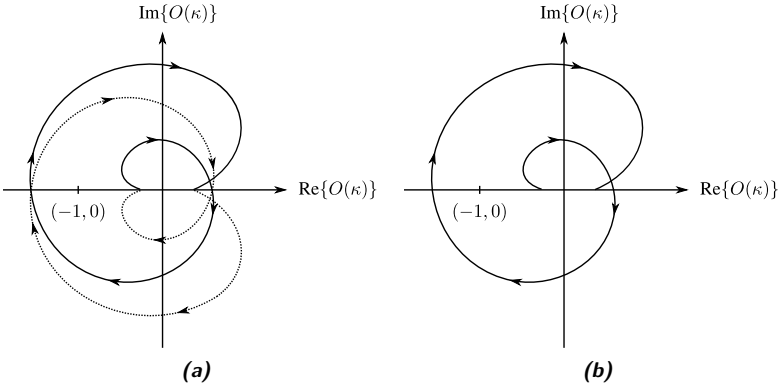

Figure 3.7.: Nyquist plot example of an unstable system: (a) The open-loop transfer function $O(z)$ evaluated along the contour κ; and (b) the open-loop transfer function $O(z)$ segment corresponding to the upper-half of the unit circle.

3.2.1. Simplification of the contour analysis

In practical applications of this analysis there are three important simplifications that are made on the contour $O(\kappa)$. First, because of the delays in the impulse response of the open-loop $O(z)$, the evaluation of $O(\kappa)$ on the more distant contour section (where $|z| \cong \infty$) results in values that are zero in the limit. Therefore, their visualization is neglected, as with a radius close to zero they can not encircle the Nyquist point in any direction. Second, the connection of the inner and outer section of the contour is chosen arbitrarily, so it can not determine the stability of the system and is therefore also excluded. And third, $O(\kappa)$ can be completely described by the evaluation of κ on the upper-half of to the unit-circle. As shown in Fig. 3.6b and Fig. 3.7b, by considering the half of the sub-contours and their orientations, the stability or instability of the feedback loop can still be visually determined. Because of the above described simplifications, the following discussion is motivated to provide proof that the simplifications can not compromise the accuracy of the analysis.

An equivalent analysis to the one already presented can be achieved using the two contour integrals

$$Z_{C_\mathrm{m},\bar{c}} = \frac{1}{2 \cdot \pi \cdot j} \left(\oint_{\kappa_\infty} \frac{C'_\mathrm{m}(z)}{C_\mathrm{m}(z)} dz - \oint_{\kappa_c} \frac{C'_\mathrm{m}(z)}{C_\mathrm{m}(z)} dz \right), \tag{3.26}$$

to calculate the amount of zeroes $Z_{C_\mathrm{m},\bar{c}}$ outside the unit circle that the

characteristic function C_m has. It should not be forgotten, that here the controller and the secondary path are stable systems, and therefore, $P_{C_\mathrm{m},\bar{c}} = 0$ holds. Here, the first contour integral is calculated over the circle $|z| \cong \infty$ to obtain the difference between the overall amount of zeroes and poles in the entire z-domain. On the other hand, the second contour integral is calculated over the unit circle $z = e^{j\Omega_k}$ and provides information about the difference between zeroes and poles inside of it.

The value of the first integral can be calculated by the following polynomial-degree analysis. If the open-loop transfer function is divided for the analysis

$$O(z) = \frac{N(z)}{D(z)} \tag{3.27}$$

in its numerator $N(z)$ and its denominator $D(z)$, it is known that for realizable systems the degree of the numerator polynomial $\deg(N)$ has to be smaller or equal to the degree of the denominator $\deg(D)$. In the case of the present application, the more restrictive case

$$\deg(N) < \deg(D) \tag{3.28}$$

has to be enforced, in order to avoid a delay-free loop condition in the feedback system. Equation 3.27 is used in Eq. 3.16 to replace the open-loop

$$C_\mathrm{m}(z) = \frac{D(z) + N(z)}{D(z)} \tag{3.29}$$

in the characteristic equation. It is known that the degree of the addition of two polynomials is lower or equal than the highest degree of the operands, i.e. $\deg(D + N) \leq \max(\deg(D), \deg(N))$. However, in cases where the polynomials are known to be of different degrees, the equality

$$\deg(D + N) = \max(\deg(D), \deg(N)) \tag{3.30}$$

holds. If Eq. 3.28 is applied, then the equality

$$\deg(D + N) = \deg(D) \tag{3.31}$$

is found. This implies that in the characteristic equation $C_\mathrm{m}(z)$ the amount of poles and zeroes are equal and, therefore, the left-hand side integral in Eq. 3.26

$$\oint_{\kappa_\infty} \frac{C'_\mathrm{m}(z)}{C_\mathrm{m}(z)} dz = 0 \tag{3.32}$$

evaluates to zero. Then Eq. 3.26 can be re-written as

$$Z_{C_\mathrm{m},\bar{c}} = -\frac{1}{2 \cdot \pi \cdot j} \oint_{\kappa_c} \frac{C'_\mathrm{m}(z)}{C_\mathrm{m}(z)} dz, \tag{3.33}$$

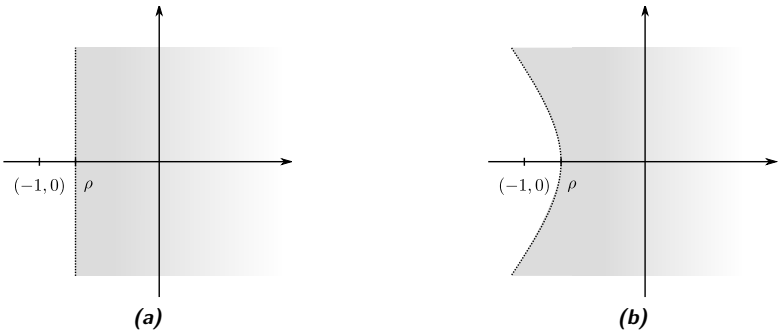

Figure 3.8.: Solution space (in gray) produced by the nominal stability constraints in the Nyquist plot of the contour $O(j\Omega_k^+) = \hat{S}(j\Omega_k^+) \cdot W_\mathrm{m}(j\Omega_k^+)$. In (a) the solution space of the constraint based on a vertical line and in (b) the solution space of the constraint based on a hyperbolic curve.

where the amount of zeroes outside the unit circle $Z_{C_\mathrm{m},\overline{c}}$ of $C_\mathrm{m}(z)$ can be determined by the contour integral along the unit circle κ_c.

Following the same procedure to derive Eq. 3.25 in the past section, it can be shown that the number of unstable roots

$$Z_{C_\mathrm{m},\overline{c}} = N^{\mathrm{cw}}_{O(\kappa_c)} - N^{\mathrm{ccw}}_{O(\kappa_c)} \tag{3.34}$$

equals to the number of clockwise encirclement of the Nyquist point made by the sub-contours of the open-loop evaluated on the unit circle $N^{\mathrm{cw}}_{O(\kappa_c)}$, minus the counter-clockwise ones $N^{\mathrm{ccw}}_{O(\kappa_c)}$.

3.2.2. Nominal stability

In order to analyze the stability of the system without having to repeatedly plot the contour produced by the controller under design, mathematical constraints based on inequalities can be used. These restrict the area of the Nyquist plot where the open-loop contour is allowed to move, so that an encirclement of the Nyquist point is not possible.

The first of these constraints is based on a vertical line

$$\left|O(j\Omega_k^+)\right| \leq \left|2 \cdot \rho + O(j\Omega_k^+)\right| \tag{3.35}$$

that crosses the x-axis on the point $(-\rho, 0)$, as shown in Fig. 3.8a. The parameter is chosen $0 < \rho < 1$, such that the Nyquist point is excluded, but maintaining the origin $(0, 0)$ inside the area. Although this constraint is simple and effective to avoid an encirclement of the Nyquist point, it is

too restrictive. As a further more relaxed alternative, the left-hand half of an hyperbola

$$|\varrho - O(j\Omega_k^+)| \leq |\varrho + O(j\Omega_k^+)| + 2 \cdot \rho, \tag{3.36}$$

with foci at $(-\varrho, 0)$ and $(\varrho, 0)$ can be used, as shown in Fig. 3.8b. Here, the parameter $0 < \rho < 1$ determines the intersect of the hyperbola with the x-axis at the point $(-\rho, 0)$. The curvature of the hyperbola is controlled by its asymptotes

$$y = \pm \frac{\sqrt{\varrho^2 - \rho^2}}{\rho} \cdot x, \tag{3.37}$$

with x and y as the standard variables for the cartesian plane. Thus, the more distant the foci, the closer the hyperbola gets to a vertical line. It is worth to explicitly mention that the constraint $\rho < \varrho$ has to be fulfilled and that it is not recommended to take a ϱ too close to ρ, as this will cause an very (horizontally) flat and thin hyperbola. Thus, when using sampled frequencies, consecutive points in the contour may jump over the forbidden area, as the phase variation may be relatively high. This could produce an encirclement of the Nyquist point, which may not be detected by evaluating the constraint.

Gain and phase margins

Given that the feedback loop has been correctly designed to be stable, a quantitative measure of its robustness towards changes on the secondary path $S(z)$ can be extracted from the Nyquist plot. As shown in Fig. 3.9, by evaluating the open-loop on the upper-half of the unit circle $O(\kappa_c^+)$, two intersections can be found. The first one is the closest to the Nyquist point that the contour does with the x-axis. The magnitude of the contour at that point is the reciprocal of the Gain Margin (GM). The GM is the increment in gain that the secondary path can have before the system becomes unstable. The second intersection is the closest intersection to the Nyquist point that the contour does with the unit circle. The angle formed between the Nyquist point and the intersection point is called the Phase Margin PM. The PM is the variation in phase that the secondary path $S(z)$ can have before the feedback system becomes unstable.

If the inequality based on the vertical line in Eq. 3.35 is used, then the achievable gain margin

$$\frac{1}{\mathrm{GM_{VL}}} \leq \rho \tag{3.38}$$

is directly constrained by the parameter ρ. Moreover, the minimum ensured phase margin

$$\mathrm{PM_{VL}} \geq \arccos(\rho) \tag{3.39}$$

is determined by the intersect of the vertical line with the unit circle. Thus,

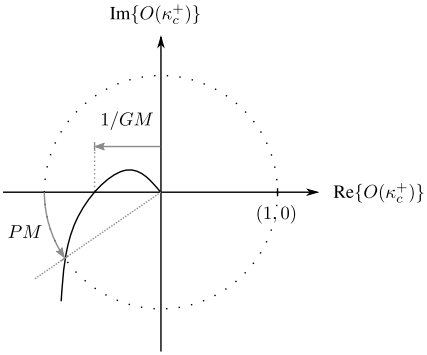

Figure 3.9.: Gain margin GM and phase margin PM determined by visual inspection of the Nyquist plot of the open-loop evaluated along the upper-half of the unit circle $O(\kappa_c^+)$.

the smaller the ρ, the bigger the phase margin. If the inequality based on the hyperbola in Eq. 3.36 is used instead, then the achievable gain margin

$$\frac{1}{\mathrm{GM_H}} \leq \rho \tag{3.40}$$

is also constrained by the parameter ρ. The phase margin in this case can be calculated by finding the intersection of the hyperbola with the unit circle. This results in a minimum phase margin given by

$$\mathrm{PM_H} \geq \arccos\left(\sqrt{\frac{\rho^2 \cdot \varrho^2 + \rho^2 - \rho^4}{\varrho^2}}\right). \tag{3.41}$$

A disadvantage of these measures of stability is that they can not be used to foresee the stability of the system upon simultaneous changes in gain and phase. For addressing these cases, robust stability constraints are going to be derived in the next section, based on an uncertainty model built on different secondary path measurements.

3.2.3. Robust stability

In the context of ANC headphones, the secondary path $S(z)$ varies from person to person, because of anatomical reasons, and may change drastically, because of varying wearing situations. In order to incorporate this variability in the controller design method, a so-called multiplicative uncertainty model [Skogestad and Postlethwaite, 2005] is built. A multiplicative uncertainty model is based on a set of I finite impulse responses of the secondary path, measured under different wearing situations and us-

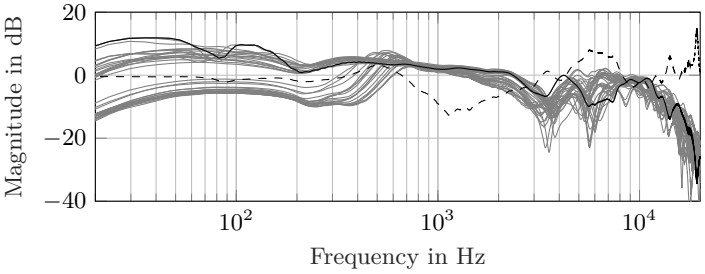

Figure 3.10.: Frequency responses of the secondary paths measured with six subjects and six wearing positions. The nominal secondary path $S_0(f)$ (——) used for the calculation of the multiplicative uncertainty $G_2(f)$ (- - -) are highlighted.

ing different human subjects. The finite impulse responses $\mathbf{s}_i(n)$ of length L_s and $i \in \{0, \cdots, I-1\}$ are Z-transformed

$$S_{\mathrm{i}}(z) = \sum_{n=0}^{L_s-1} \mathbf{s}_{\mathrm{i}}(n) z^{-n} \tag{3.42}$$

and evaluated over the unit-circle following the substitution rule $z = e^{j\Omega_k}$, with $\Omega_k = \frac{2\pi}{N}k$ and $k \in \{0, 1, \ldots, N-1\}$. The result is used to calculate the secondary path's maximum multiplicative magnitude deviation over frequency

$$G_2(\Omega_k) = \max_i \left| \frac{S_i(j\Omega_k) - S_0(j\Omega_k)}{S_0(j\Omega_k)} \right|, \tag{3.43}$$

with $S_0(j\Omega_k)$ being the nominal secondary path impulse response. This can be chosen as the impulse response $\mathbf{s}_i(n)$ that produces the $G_2(\Omega_k)$ with the smallest maximal magnitude over frequency. The maximum multiplicative magnitude deviation $G_2(\Omega_k)$ is used then to model the secondary path as

$$S(j\Omega_k) = S_0(j\Omega_k)\Big(1 + G_2(\Omega_k) \cdot \Delta(j\Omega_k)\Big), \tag{3.44}$$

being Δ the subset of complex numbers that fulfills the condition

$$|\Delta(j\Omega_k)| \leq 1, \forall \Omega_k. \tag{3.45}$$

As a result of this, the phase deviation is unbounded.

Example In Fig. 3.10 the frequency response of 36 measured secondary paths are presented in gray. The measurements were conducted following

the parameters presented in [Rivera Benois and Zölzer, 2019], with six subjects wearing the headphones in six different positions. From these six, three of them are tight-fit positions, as the ones described in [Rivera Benois and Zölzer, 2019], and the other three are lose-fit positions with 1, 2, and 3 cm distance from the earcup's cushion to the subject's heads. The nominal secondary path $S_0(f)$, presented in black, is chosen as the impulse response in the measurement set that produces the smallest multiplicative uncertainty $G_2(f)$, presented in dashed black. It can be seen, that in the low-frequencies the measurements can be grouped in two sub-sets: the first having a positive gain, due to the tight-fit scenario, and the second having a loss in gain, due to the lose-fit scenario. As a result of the decrease in gain in the low-frequencies, a resonance in the 300-700 Hz range is produced. In the 3-4 kHz and 5-6 kHz frequency ranges a high variability can be seen. After the 10 kHz all measured secondary paths show a low-pass behavior. The multiplicative uncertainty $G_2(f)$ shows in the low-frequencies a value close to unity, produced by the high-gain that $S_0(f)$ has in comparison to the rest of the secondary paths. In the 300-700 Hz range the resonances produce an increment in uncertainty. However, between 700 Hz and 2 kHz the variability between secondary paths decreases again and with it also $G_2(f)$. Nevertheless, in the the 3-4 kHz and 5-6 kHz ranges, where the gain drops with high variability, the uncertainty increases respectively. In frequencies higher than 10 kHz it can be seen that the low-pass behavior of the secondary path comes with a high variability, which also increases $G_2(f)$ to its highest value near 20 kHz. From this example it could be seen that the multiplicative uncertainty moves around the 0 dB, remaining within the ± 20 dB range.

Given the redefinition of the secondary path in Eq. 3.44, a controller can be designed to be robustly stable upon changes in the secondary path. This can be determined by evaluating the controller's Z-transformed impulse response $\mathbf{w}_\mathrm{m}(n)$ of length L_m in the frequencies of interest Ω_k, and calculating the open-loop transfer function. By substituting Eq. 3.44 in Eq. 3.20 this yields

$$O(j\Omega_k) = W_\mathrm{m}(j\Omega_k) \cdot S_0(j\Omega_k)\Big(1 + G_2(\Omega_k) \cdot \Delta(j\Omega_k)\Big). \tag{3.46}$$

By using the Nyquist stability criterion for stable plants and discrete-time controllers (which is the case with these secondary paths and controllers based on FIR filters [Franklin et al., 1997]), a Nyquist plot, like the one in Fig. 3.11, of the *nominal* open-loop transfer function

$$O_0(j\Omega_k) = W_\mathrm{m}(j\Omega_k) \cdot S_0(j\Omega_k) \tag{3.47}$$

can be drawn. By following the curve from low to high frequencies, the number of unstable poles in Eq. 3.2 can be determined by counting the

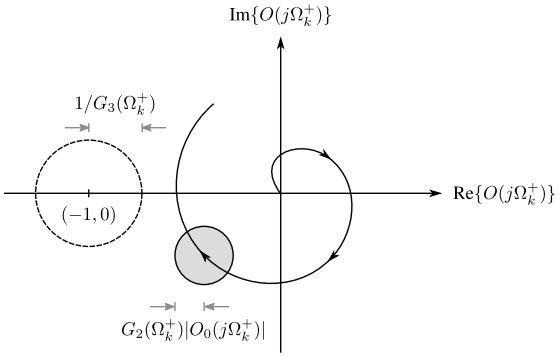

Figure 3.11.: Nyquist plot of the MVC open-loop system $O(j\Omega_k^+)$ evaluated in the *positive* frequencies $0 \leq \Omega_k < \pi$, with uncertainty $G_2(\Omega_k^+)$ and specified maximal disturbance amplification $G_3(\Omega_k^+)$.

number of clockwise encirclements that the curve does around the Nyquist point $(-1, 0)$. If no clockwise encirclements occur, then the system is *nominally* stable and the analysis can be carried out further. In a second step the discs

$$O_r(j\Omega_k) = G_2(\Omega_k) \cdot \Delta(j\Omega_k) \cdot O_0(j\Omega_k) \tag{3.48}$$

with frequency-dependent radii $G_2(\Omega_k)|O_0(j\Omega_k)|$ are added on top of the nominal open-loop curve by following the equation

$$O(j\Omega_k) = O_0(j\Omega_k) + O_r(j\Omega_k). \tag{3.49}$$

Finally, if no disc touches the Nyquist point $(-1, 0)$, then the system is *robustly* stable [Rafaely, 1997]. This graphical analysis can be expressed mathematically as the inequality

$$G_2(\Omega_k)|O_0(j\Omega_k)| < |1 + O_0(j\Omega_k)|, \tag{3.50}$$

which implies that the radius of the disc has to be smaller than the distance of the contour to the Nyquist point $(-1, 0)$. Thus, this inequality can be used as constraint during the optimization of the controller's impulse response $\mathbf{w}_\mathrm{m}$ to ensure that the optimal solution is robustly stable.

3.3. Disturbance Enhancement

In the context of acoustics, the secondary path is a non-minimum phase system, because of the inherent causality that the distance between the

loudspeaker and the microphone introduces. Moreover, this system is also stable, as it is a feedforward concatenation of stable subsystems. Because of the low-pass characteristic that each one of these subsystems has, the secondary path frequency response tends to zero in the limit $f \to \infty$. It is known that, if the secondary path of these characteristics (stable, non-minimum phase and proper) has at least two poles more than zeroes, then the *Bode sensitivity integral*

$$\int_0^\infty 20 \cdot \log_{10} |H_\mathrm{m}(j\omega)| d\omega = 0 \tag{3.51}$$

of the equivalent continuous-time sensitivity transfer function $H_\mathrm{m}(j\omega)$ equals zero. This implies that for an attenuation achieved in one frequency, an amplification of the same magnitude is produced in another frequency. Because of this, different approaches are used to identify the frequency regions that should be attenuated and which ones can be amplified. Some of these methods can make use of the psychoacoustic aspects of human hearing system to optimize the controller $W_\mathrm{m}(z)$ for human subjects [Rivera Benois and Zölzer, 2019].

In order to limit the amplification over frequency that this effect may cause, the frequency response of the sensitivity function $H_\mathrm{m}(j\Omega_k)$ can be limited by the frequency-dependent real-valued parameter $G_3(\Omega_k)$

$$|H_\mathrm{m}(j\Omega_k)| \leq G_3(\Omega_k) \tag{3.52}$$

during the optimization of the controller $W_\mathrm{m}(z)$. The constraint can be also formulated in terms of the open-loop $O(j\Omega_k)$

$$|1 + O(j\Omega_k)| \geq \frac{1}{G_3(\Omega_k)}, \tag{3.53}$$

or explicitly in terms of the controller $W_\mathrm{m}(z)$ and secondary path $S(z)$

$$|1 + S(j\Omega_k) \cdot W_\mathrm{m}(j\Omega_k)| \geq \frac{1}{G_3(\Omega_k)}. \tag{3.54}$$

In order to account for the variability of the secondary path, the multiplicative uncertainty model of Eq. 3.44 is used together with a graphical analysis of the Nyquist plot, similar to the one performed for the stability constraint. Thus, the system can be designed to have a *nominal* performance, under which no point of the nominal open-loop transfer function $O_0(j\Omega_k)$ is allowed to enter the circle drawn by $1/G_3(\Omega_k)$. This yields the already known inequality

$$|1 + O_0(j\Omega_k)| \geq \frac{1}{G_3(\Omega_k)}. \tag{3.55}$$

Furthermore, the system can be designed to have a *robust* performance, under which circumstances no elements in the discs $O_r(j\Omega_k)$ centered in their respective $O_0(j\Omega_k)$ curve points are allowed to enter the circle drawn by $1/G_3(\Omega_k)$. This graphical principle is equivalent to an increment of the circle's radius by the size of the discs, as

$$|1 + O_0(j\Omega_k)| \geq \frac{1}{G_3(\Omega_k)} + G_2(\Omega_k)|O_0(j\Omega_k)|. \tag{3.56}$$

Other constraints One consideration for the digital implementation is to limit the gain of the controller. This is done not only for security purposes, but also to avoid the amplification of the ADC's noise floor to a level that is audible. This can be done by comparing the magnitude response of the controller to that of a maximum gain curve as in the inequality

$$|W_\mathrm{m}(\Omega_k)| \leq G_4(\Omega_k), \tag{3.57}$$

where $G_4(\Omega_k)$ can be chosen as an inverted noise weighting curve or as a constant. Something similar can be done for the impulse response coefficients

$$\left|\mathbf{w}_\mathrm{m}\right| \leq g_5, \tag{3.58}$$

in order to limit their magnitude.

3.4. Controller Optimization

In this section, the design of the controller is formulated as a convex optimization problem. This guarantees that any local minimum found with SQP als yields the global one. The cost function is based on the frequency response of the weighted denominator of the system sensitivity function in Eq. 3.2

$$C^\mathrm{c}_\mathrm{m}(j\Omega_k) = G_1(j\Omega_k) \cdot \big(1 + W_\mathrm{m}(j\Omega_k) \cdot S_0(j\Omega_k)\big), \tag{3.59}$$

where $G_1(j\Omega_k)$ is the estimated disturbance signal's energy content and $S_0(j\Omega_k)$ is the nominal secondary path chosen for the multiplicative uncertainty model of $S(j\Omega_k)$. The cost function is defined as the sum over squared values of $C^\mathrm{c}_\mathrm{m}(j\Omega_k)$

$$C_\mathrm{mvc}(\mathbf{w}_\mathrm{m}) = \frac{2}{N} \sum_{k=0}^{N/2-1} \left|C^\mathrm{c}_\mathrm{m}(j\Omega_k)\right|^2. \tag{3.60}$$

This cost function builds a quadratic dependency with respect to the controller coefficients $\mathbf{w}_\mathrm{m}$ and is tightly related to the 2-norm of its DTFT counterpart. Alternatively, the sum can be calculated over a frequency

range of interest

$$C'_{\mathrm{mvc}}(\mathbf{w}_{\mathrm{m}}) = \frac{2}{k_{\mathrm{h}} - k_{\mathrm{l}} + 1} \sum_{k=k_{\mathrm{l}}}^{k_{\mathrm{h}}} \left| C^{\mathrm{c}}_{\mathrm{m}}(j\Omega_k) \right|^2, \tag{3.61}$$

starting from k_l and ending at k_h, the indices of the lowest f_{l} and highest f_{h} frequencies, respectively. The sum over a desired attenuation bandwidth of interest was suggested by Pawelczyk in [Pawełczyk, 2002], for the optimization of analogue recursive feedback controllers.

Constraints Together with the cost functions, the constraints are also re-defined to yield a convex programming problem. These changes do not alter the effect of the constraints on the optimal solution, but introduce a quadratic dependency with respect to the controller coefficients $\mathbf{w}_{\mathrm{m}}$ [Rafaely, 1997]. Additionally, the constraints are evaluated only on *positive* frequencies, in order to avoid extra computational load due to redundancies. Based on these principles, the inequalities for nominal stability in Eq. 3.35 and Eq. 3.36 take the form

$$\left| O_0(j\Omega_k^+) \right|^2 \leq \left| 2 \cdot \rho + O_0(j\Omega_k^+) \right|^2, \tag{3.62}$$

and

$$|\varrho - O_0(j\Omega_k^+)|^2 \leq |\varrho + O_0(j\Omega_k^+)|^2 + 4 \cdot \rho |\varrho + O_0(j\Omega_k^+)| + 4 \cdot \rho^2. \tag{3.63}$$

The robust stability constraint in Eq. 3.50 is re-written as

$$G_2^2(\Omega_k^+)|O_0(j\Omega_k^+)|^2 < |1 + O_0(j\Omega_k^+)|^2, \tag{3.64}$$

while the inequality for nominal performance in Eq. 3.55 and for robust performance in Eq. 3.56 are re-written as

$$|1 + O_0(j\Omega_k^+)|^2 \geq \frac{1}{G_3^2(\Omega_k^+)} \tag{3.65}$$

and

$$\frac{1}{G_3^2(\Omega_k^+)} + 2\frac{G_2(\Omega_k^+)}{G_3(\Omega_k^+)}|O_0(j\Omega_k^+)| + G_2^2(\Omega_k^+)|O_0(j\Omega_k^+)|^2 < |1 + O_0(j\Omega_k^+)|^2 \tag{3.66}$$

Additionally, the constraints for gain limiting in Eq. 3.57 and impulse response coefficients' magnitude in Eq. 3.58 are also re-written in its respective squared terms as

$$|W_{\mathrm{m}}(j\Omega_k^+)|^2 \leq G_4^2(\Omega_k^+). \tag{3.67}$$

and

$$\left|\mathbf{w}_{\mathrm{m}}\right|^2 \leq g_5^2. \tag{3.68}$$

3.4.1. Optimization results

The optimizations results presented in this section are obtained using the nonlinear programming solver `fmincon()` together with the SQP algorithm from the MATLAB 2019a optimization toolbox. The parameters `MaxIterations` and `MaxFunctionEvaluations` are set to $\max(200, L_{\mathrm{m}})$ and $200 \cdot L_{\mathrm{m}}$, respectively. All the optimization runs presented here found the optimal solution before reaching these iteration limits. The starting solution for the coefficients' optimization is set to zero. The sampling frequency $f_s = 48\,\mathrm{kHz}$ and the FFT length $N = 4096$ are chosen.

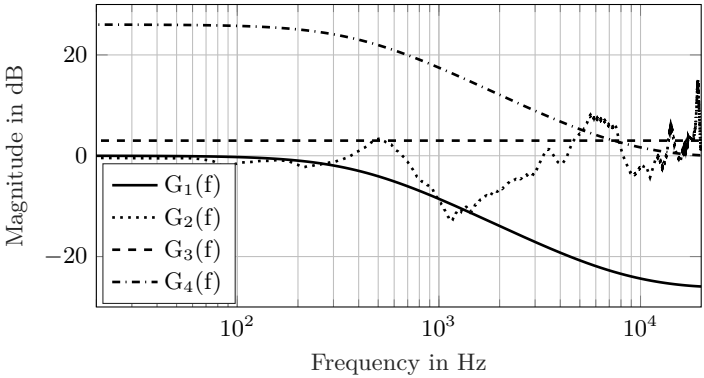

Figure 3.12.: Frequency dependent parameters used for the optimization of the MVC impulse response: The weighting function $G_1(f)$, the multiplicative uncertainty $G_2(f)$, the maximum amplification of 3 dB $G_3(f)$ and the maximum controller gain $G_4(f)$.

In Fig. 3.12 the frequency-dependent parameters used during the optimization are presented. G_1 is chosen as the frequency response of a first-order high-cut shelving filter with cut-off frequency $f_c = 8\,\mathrm{kHz}$ and $-26\,\mathrm{dB}$ in the stop-band, mimicking the passive attenuation of the primary path over frequency. The multiplicative uncertainty G_2 is calculated from the impulse response measurements of the secondary path presented in Fig. 3.10. The maximum sensitivity function's disturbance amplification G_3 is chosen as 3 dB. The maximum controller gain over frequency G_4 is chosen as G_1 scaled up, such that an amplification of 26 dB is reached in the pass-band.

The following results are presented so that the influence of variations on the constraints and the optimization parameters are understood.

Nominal stability constraints As the first step, the nominal stability constraint to be used during the rest of the optimizations is evaluated. For this, the controller's impulse response length is set to 256 coefficients. The cost function in Eq. 3.61 with lower index $k_l = 0$ and higher index $k_h = 170$ are used, which yields a weighted sum over all positive frequencies below 2 kHz. The first impulse response is subject to the hyperbolic constraint in Eq. 3.36, with foci at $(-2, 0)$ and $(2, 0)$, and intersection with the x-axis at the point $(-0.8, 0)$. According to Eq. 3.40 and Eq. 3.41 this yields a $\mathrm{GM_H} \geq 1.25$ and a $\mathrm{PM}_H \geq 33.36°$, respectively. The second impulse response is subject to the vertical line constraint in Eq. 3.35, with x-axis intersection at $(-0.8, 0)$. According to Eq. 3.38 and Eq. 3.39 this yields a $\mathrm{GM_{VL}} \geq 1.25$ and a $\mathrm{PM}_V L \geq 36.87°$, respectively.

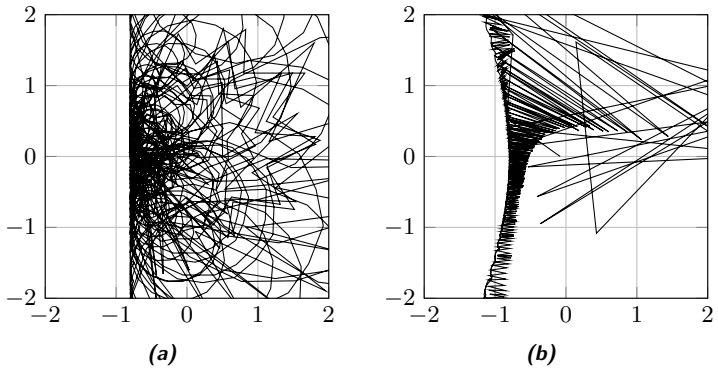

Figure 3.13.: The Nyquist plot produced by the contour $O(j\Omega_k^+) = S_0(j\Omega_k^+) \cdot W_\mathsf{m}(j\Omega_k^+)$, when subject to the (a) vertical line constraint and the (b) hyperbolic curve constraint. Both intersections are set to $(-0.8, 0)$ and the foci to $(-2, 0)$ and $(2, 0)$. Parameters: $f_s = 48\,\mathrm{kHz}$, $N = 4096$, $L_\mathsf{m} = 256$, $f_\mathsf{l} = 0\,\mathrm{Hz}$, $f_\mathsf{h} = 2\,\mathrm{kHz}$.

The obtained Nyquist plots presented in Fig. 3.13 show that the contour of the open-loop follows the boundary imposed by the constraints very closely. Thus, the hyperbolic curve offers its optimal impulse response additional freedom at the cost of a small decrement in the PM. The sensitivity functions presented in Fig. 3.14 corroborate the better results achievable with the hyperbolic curve constraint. Furthermore, not only the attenuation magnitude is higher, but also the achieved attenuation bandwidth.

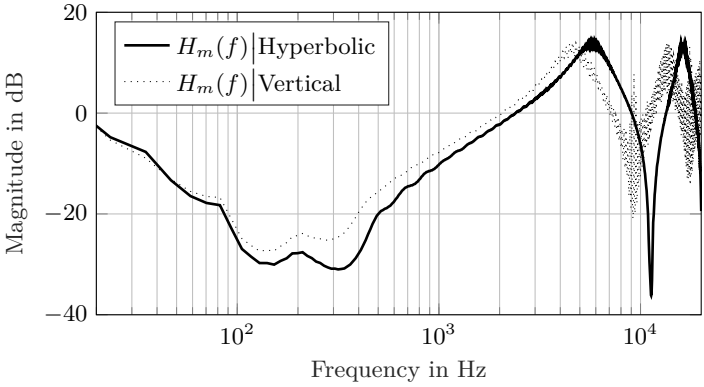

Figure 3.14.: Development of the optimal sensitivity function $H_\mathrm{m}(f)$ when it is subject to the the hyperbolic and vertical nominal stability constraints. Both intersection are set to $(-0.8, 0)$ and the foci to $(-2, 0)$ and $(2, 0)$. Parameters: $f_s = 48\,\mathrm{kHz}$, $N = 4096$, $L_\mathrm{m} = 256$, $f_\mathrm{l} = 0\,\mathrm{Hz}$, $f_\mathrm{h} = 2\,\mathrm{kHz}$.

Further design constraints As a second step, the development of the optimal controller subject to increasingly restrictive constraints is analyzed. For this, the controller impulse response length is set to $L_\mathrm{m} = 256$ and the hyperbolic nominal stability constraint is used. As seen before in Fig. 3.14, if the controller is only constrained to be nominally stable, an important attenuation can be achieved within the bandwidth defined by the cost function and G_1. However, the optimal controller not only has a high gain within the desired attenuation bandwidth, but also at very high frequencies, where it is known that the secondary path varies substantially.

In order to avoid these high gains, the controller's frequency response is limited with $G_4(f)$ from Fig. 3.12. The restrictive effect of the constraint on the controller's gain can be seen from $W_\mathrm{m}(f)\big|G_4$ in Fig. 3.15. Between 5 kHz and 20 kHz the controller reaches the maximum gain given by G_4. Limiting the gain of the controller also limits the attenuation bandwidth in its sensitivity function $H_\mathrm{m}(f)\big|G_4$ presented in Fig. 3.16. Nevertheless, this also minimizes the gain of the resonances produced by the waterbed-effect in the frequencies outside the attenuation bandwidth. An important resonance of 13 dB at approx. 4 kHz remains. In order to achieve a some control over the waterbed-effect, the nominal performance constraint together with $G_3(f)$ is used. Its effect on $H_\mathrm{m}(f)\big|G_3G_4$ can be seen in Fig. 3.16. Here, no amplification produced by the waterbed-effect

exceeds the given limit of 3 dB. A negative effect of this is that the attenuation magnitude and bandwidth decrease and that an amplification appears between 40 and 50 Hz.

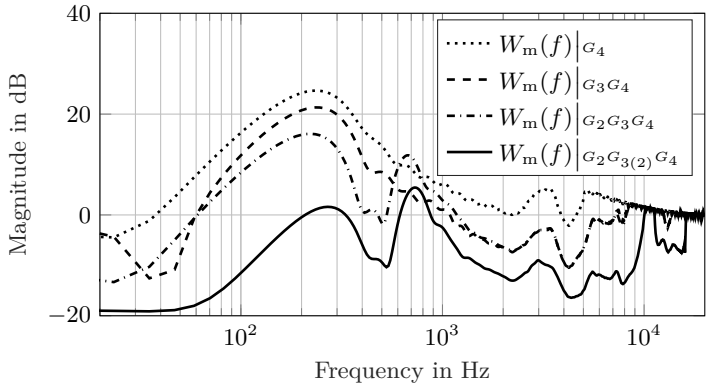

Figure 3.15.: Development of the optimal controller $W_\mathrm{m}(f)$ when constraints are enforced in increasingly restrictive order. The hyperbola intersection is set to $(-0.8, 0)$ and the foci to $(-2, 0)$ and $(2, 0)$. Parameters: $f_s = 48\,\mathrm{kHz}$, $N = 4096$, $L_\mathrm{m} = 256$, $f_\mathrm{l} = 0\,\mathrm{Hz}$, $f_\mathrm{h} = 2\,\mathrm{kHz}$.

If the robust stability constraint based on $G_2(f)$ is introduced, a change in attenuation performance can be seen in $H_\mathrm{m}(f)\big|G_2G_3G_4$ from Fig. 3.16. Thus, the increase in uncertainty that $G_2(f)$ shows between 400 and 600 Hz in Fig. 3.12 imposes a limitation in the achieved attenuation. At the same time, the smaller uncertainty between 700 and 3000 Hz allows an improvement in the achieved attenuation between 600 and 1500 Hz. If the robust performance constraint is enforced, the maximum amplification parameter $G_3(f)$ is evaluated taking in consideration the uncertainty $G_2(f)$ following the inequality in Eq. 3.56. The effect of the combined parameters is an important loss in attenuation in $H_\mathrm{m}(f)\big|G_2G_3(2)G_4$. However, the maximal amplification produced by the sensitivity function also decreases to approx. 1.5 dB. If both curves $W_\mathrm{m}(f)\big|G_2G_3G_4$ and $W_\mathrm{m}(f)\big|G_2G_3(2)G_4$ are compared in Fig. 3.15, it can be seen that the magnitude responses are very similar and that the effect of the robust performance constraint limits the gain of the controller in an almost homogeneous way throughout frequency.

Controller's impulse response length In a third step, the effect of the impulse response's length is analyzed. For these optimizations the solution is subject to the nominal and robust stability constraints, together with

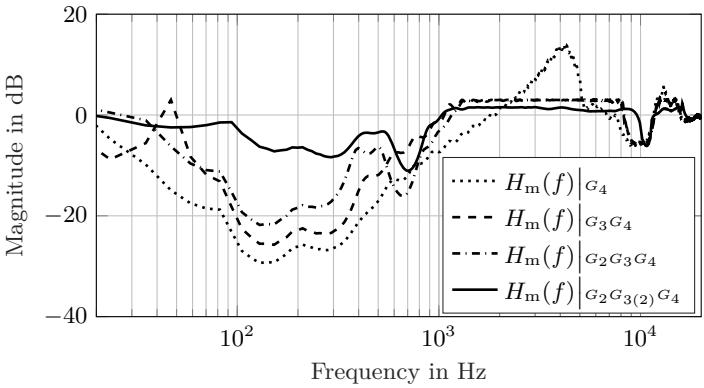

Figure 3.16.: Development of the optimal sensitivity function $H_\mathrm{m}(f)$ when constraints are enforced in increasingly restrictive order. The hyperbola intersection is set to $(-0.8, 0)$ and the foci to $(-2, 0)$ and $(2, 0)$. Parameters: $f_s = 48\,\mathrm{kHz}$, $N = 4096$, $L_\mathrm{m} = 256$, $f_\mathrm{l} = 0\,\mathrm{Hz}$, $f_\mathrm{h} = 2\,\mathrm{kHz}$.

the maximum controller gain and nominal performance constraint. Thus, equivalent to the case $H_\mathrm{m}(f)\big|G_2G_3G_4$. As can be seen from the results presented in Fig. 3.17, even with a very short impulse response of $L_\mathrm{m} = 8$, a broad attenuation bandwidth of 2 kHz can be achieved. The attenuation covers more critical bands, while its magnitude dominates over the small amplifications produced in the mid- and high-frequencies. If the impulse response is increased to $L_\mathrm{m} = 32$, the attenuation bandwidth decreases to 1.6 kHz, but the attenuation around 1 kHz is increased from 2.6 dB to 6.9 dB. With a further increase to $L_\mathrm{m} = 128$ the attenuation levels around 10 dB can be reached. At the same time this implicates an almost flat amplification of 3 dB in the frequency range between 1.4 and 8 kHz. With a length of $L_\mathrm{m} = 512$ an important attenuation between 100 and 200 Hz is produced, although with a overall smaller attenuation bandwidth and an amplification between 30 and 40 Hz. Thus, it could be seen that the longer impulse response is, the smaller the attenuation bandwidth gets in favor of a higher attenuation magnitude. In order to control this effect, $G_3(f)$ can be used to fix the minimum attenuation bandwidth to the one achievable by a shorter controller. Such that, the controller length is invested in the increment of the attenuation magnitude.

Cost function bandwidth In a fourth step, the effect of the cost function bandwidth is analyzed. For this effect, the lowest frequency is set to $f_\mathrm{l} = 0$ and the highest frequency f_h, up to which the cost function is calcu-

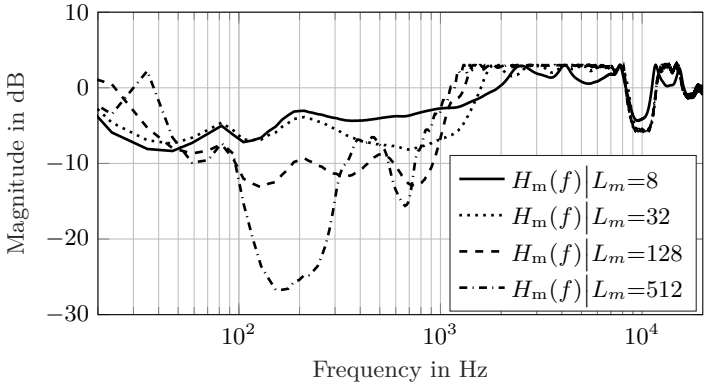

Figure 3.17.: Optimum sensitivity functions obtained with different impulse response lengths. The hyperbola intersection is set to $(-0.8, 0)$ and the foci to $(-2, 0)$ and $(2, 0)$. Parameters: $f_s = 48\,\text{kHz}$, $N = 4096$, $f_\text{l} = 0\,\text{Hz}$, $f_\text{h} = 2\,\text{kHz}$, constraints combination $G_2G_3G_4$.

lated, is incremented. For these optimizations the solution is subject to the nominal and robust stability constraints, together with the maximum controller gain and nominal performance constraint. Thus, equivalent to the case $H_\text{m}(f)\big|G_2G_3G_4$. In Fig. 3.18 the results for the four different bandwidths are presented. It can be seen that, if the bandwidth is limited to 100 Hz, then a better attenuation in the low frequencies can be achieved. However, a prominent ripple is produced outside that frequency range, with amplifications that remain below the 3 dB constraint. The same is also seen in the results for $f_\text{h} = 200$, although the effect is less dominant. This kind of behavior can be controlled, if a further constraint is used to set the maximum attenuation outside the attenuation bandwidth. If f_h is further incremented to 500 Hz, the attenuation in frequencies lower than 160 Hz decreases in favor of an improvement in the frequencies up to 850 Hz. The ripple decreases to a minimum. If the bandwidth is incremented up to 2 kHz, then neither further improvements in the attenuation of higher frequencies nor a decrement in the ripple are perceived. Further optimizations were performed with a bandwidth up to 3 kHz, but they were omitted, because no visible difference with the 2 kHz could be seen.

3.5. Summary

In this chapter the minimum variance control scheme has been presented. Its working principle allows the attenuation of a disturbance signal $d(n)$

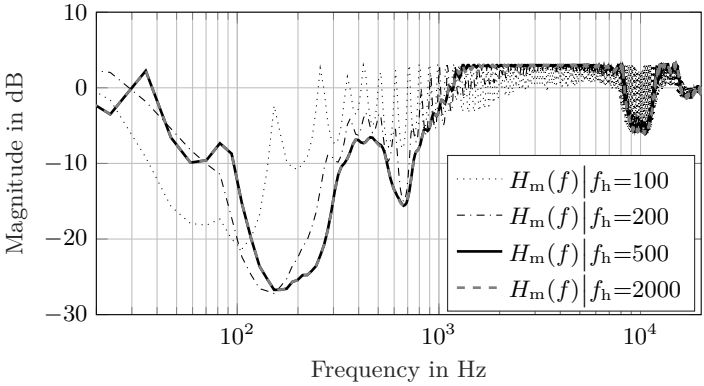

Figure 3.18.: Optimum sensitivity functions obtained with different cost function bandwidths. The hyperbola intersection is set to $(-0.8, 0)$ and the foci to $(-2, 0)$ and $(2, 0)$. Parameters: $f_s = 48\,\text{kHz}$, $N = 4096$, $L_m = 512$, $f_l = 0\,\text{Hz}$, constraints combination $G_2 G_3 G_4$.

without the need for a time-advanced reference $x(n)$, but instead by measuring the residual error $e(n)$. Because of its feedback working principle, the system is not subject to the limitation of the FF control scheme due to the loss in correlation between $x(n)$ and $d(n)$. However, because of the feedback loop built by the controller $W_m(z)$, the system is subject to stability considerations instead. For taking these into account while designing the controller, stability constraints based on the frequency responses of the controller $W_m(f)$ and the secondary path $S(f)$ have been developed in Sec. 3.2. These constraints are extended to provide stability even in contexts where the secondary path varies over time and frequency. This is achieved by measuring its uncertainty over frequency $G_2(f)$ for different headphones' wearing situations.

One of the downsides of the feedback controller is the waterbed-effect. This basically produces for any attenuation of the disturbance in one frequency region, an equivalent amplification in another frequency range. In order to gain some control over this effect, performance constraints have been developed in Sec. 3.3. These constraints limit the maximum amplification that the system may produce on $d(n)$, given by the frequency-dependent parameter $G_3(f)$. If the secondary path's uncertainty over frequency $G_2(f)$ is considered, a maximum amplification can be ensured for all measured wearing situations.

In Sec. 3.4 the optimization of the controller's finite impulse response $\mathbf{w}_m(n)$ has been formulated as a convex problem. Thus, an optimiza-

tion routine based on the SQP algorithm ensures to find the optimum controller that minimizes the given cost function, subject to the stability and performance constraints. Based on this formulation optimization runs were performed under different parameter constellations. From them it is concluded that the impulse response length does not limit the attenuation bandwidth, but instead the attenuation magnitude. The secondary path's uncertainty over frequency $G_2(f)$ shapes the attenuation magnitude within the achieved attenuation bandwidth. Thus, in frequency regions where $G_2(f)$ is high, the attenuation magnitude gets smaller. On the other hand, in frequency regions where $G_2(f)$ is low, the attenuation magnitude gets higher. If the cost function's bandwidth is limited to very low frequencies, a better attenuation magnitude inside of its frequency range can be achieved. However, a strong ripple effect is produced outside of its bandwidth. The magnitude of the ripple decreases when a higher cost function bandwidths are used. At the same time the attenuation bandwidth is increased. However, after the attenuation bandwidth reaches a maximum, further increments in the cost function bandwidth do not alter the achieved result.

CHAPTER 4

Internal Model Control

In order to partially overcome the bandwidth limitations of the Minimum Variance Controller, and extend the attenuation capabilities of the feedback control system to tonal components, the Internal Model Control (IMC) [Morari and Zafiriou, 1989] can be used. Its block diagram is presented in Fig. 4.1. The system uses an estimated secondary path $\hat{S}(z)$ to estimate $d(n)$, by compensating the influence of the control signal $y(n)$ on the residual error $e(n)$. The estimated disturbance $\hat{d}(n)$ is used as an input for the controller $W_{\mathrm{i}}(z)$ to calculate the control signal $y'(n)$. Thus, by means of the secondary path estimate $\hat{S}(z)$, clipping effects suffered by the control signal $y(n)$ can also be modeled and compensated, before the control signal is calculated [Pawełczyk, 2005].

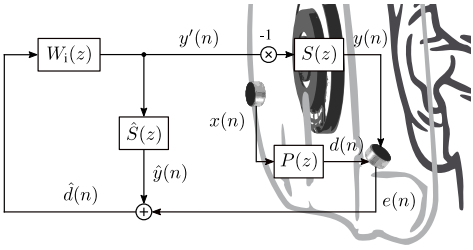

Figure 4.1.: System block diagram of the Internal Model Control scheme applied to headphones.

From the system block diagram the equations

$$E(z) = D(z) - S(z) \cdot Y'(z) \tag{4.1}$$

and

$$Y'(z) = W_{\mathrm{i}}(z)\big(\hat{S}(z) \cdot Y'(z) + E(z)\big) \tag{4.2}$$

$$\rightarrow Y'(z) = \frac{W_{\mathrm{i}}(z)}{1 - \hat{S}(z) \cdot W_{\mathrm{i}}(z)} E(z), \tag{4.3}$$

are derived. Using Eq. 4.3 to replace $Y'(z)$ in Eq. 4.1

$$E(z) = D(z) - S(z) \frac{W_{\mathrm{i}}(z)}{1 - \hat{S}(z) \cdot W_{\mathrm{i}}(z)} E(z) \tag{4.4}$$

$$\rightarrow E(z) \left(1 + S(z) \frac{W_{\mathrm{i}}(z)}{1 - \hat{S}(z) \cdot W_{\mathrm{i}}(z)} \right) = D(z) \tag{4.5}$$

$$\rightarrow E(z) \left(\frac{1 + \big(S(z) - \hat{S}(z)\big) W_{\mathrm{i}}(z)}{1 - \hat{S}(z) \cdot W_{\mathrm{i}}(z)} \right) = D(z) \tag{4.6}$$

the system's sensitivity function

$$H_{\mathrm{i}}(z) = \frac{E(z)}{D(z)} = \frac{1 - \hat{S}(z) \cdot W_{\mathrm{i}}(z)}{1 + \big(S(z) - \hat{S}(z)\big) \cdot W_{\mathrm{i}}(z)} \tag{4.7}$$

can be derived. If this equation is compared to the one of the MVC system in Eq. 3.2, it can be seen that the feedback produced by the controller $W_{\mathrm{i}}(z)$ is being reduced by the factor $S(z) - \hat{S}(z)$. Furthermore, if $\hat{S}(z) = S(z)$ holds and the equation

$$D(z) = P(z) \cdot X(z) \tag{4.8}$$

is used to include the influence of the primary path in Eq. 4.7

$$\frac{E(z)}{X(z)} = P(z)\big(1 - S(z) \cdot W_{\mathrm{i}}(z)\big), \tag{4.9}$$

then the IMC finds its feedforward equivalent system (see Fig. 4.2). So the condition $\hat{S}(z) = S(z)$ is a sufficient stability condition, given that the controller itself is stable. The controller that minimizes the transfer function

$$\hat{W}_{\mathrm{i}}^{\mathrm{opt}}(z) \approx \frac{1}{S(z)} \tag{4.10}$$

is the inverse of the secondary path, which can only be estimated because the system $S(z)$ is non-minimum phase. The immediate advantage of this approach is that the controller $W_{\mathrm{i}}(z)$ can be derived using the Wiener

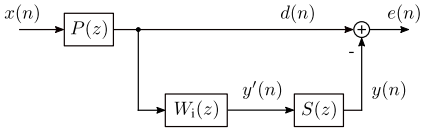

Figure 4.2.: System block diagram of the Internal Model Control feedforward equivalent system when the condition $\hat{S}(z) = S(z)$ is fulfilled.

formulations presented in the Sec. 2.3 [Elliott, 2001b]. Moreover, by doing some adaptations, the implementation of an adaptive controller using the Filtered-x LMS algorithm is also possible. However, this equivalent feedforward system is constantly under the comb filter effect depicted in Fig. 2.4. The magnitude of this effect is in this case higher, because of the absence of the primary path $P(z)$ in the direct path to compensate for the delays in the secondary path. Nevertheless, the causality limitations do not limit the system's capability to attenuate periodic noise.

In this chapter the H_2/H_∞ method proposed by Rafaely in [Rafaely, 1997] for the convex optimization of an FIR filter as IMC controller is used. As shown by Rafaely, if the problem can be formulated as a convex optimization task [Gill et al., 1981], then a solution based on SQP [Fletcher, 1987] yields a global optimum subject to the designed constraints. The stability analysis in this work is slightly different, though, because a further analysis of the inner stability of the system and the constraints' solution space is done. Moreover, as already seen in Chapter 3, the stability and disturbance enhancement constraints are derived directly in the discrete Fourier transform.

The rest of this chapter is structured as follows: In the following section, the robust stability and disturbance enhancement constraints for the case of the IMC system are derived based on the multiplicative uncertainty model described in Sec. 3.2.3. Afterwards in Sec. 4.5, the off-line optimization of this controller is formulated as a convex optimization task. Later on, in Sec. 4.6 the case of an adaptive controller based on the leaky feedback FxLMS [Elliott et al., 1987] is presented an extended in the frequency domain in order to incorporate the design constraints. Afterwards in Sec. 4.6.1 off-line optimization results are presented to understand the effects of its parameters and constraints. The chapter closes with summary of the most important facts and findings related to this control scheme.

4.1. Controller Inner Stability

As can be seen in Fig. 4.1, the IMC produces an inner positive feedback by means of the estimated secondary path $\hat{S}(z)$. This cancels the outer negative feedback of the real secondary path $S(z)$. The inner positive

feedback can be encapsulated inside an equivalent MVC controller

$$\tilde{W}_{\mathrm{m}}(z) = \frac{Y'(z)}{E(z)} = \frac{W_{\mathrm{i}}(z)}{1 - \hat{S}(z) \cdot W_{\mathrm{i}}(z)}. \tag{4.11}$$

Its stability can be ensured if the constraint

$$|\hat{S}(j\Omega_k) \cdot W_{\mathrm{i}}(j\Omega_k)| < 1 \tag{4.12}$$

is enforced [Rafaely, 1997]. However, this constraint is too restrictive, because it confines the inner open-loop contour inside a circle of radius 1 (see Fig. 4.3a), while only an encirclement of the point (1,0) should be avoided. Consider in the case of a positive feedback the point $(1, 0)$ as the equivalent Nyquist point, as the characteristic function of the feedback system is built on a subtraction. As an alternative to this, a vertical line

$$|\hat{S}(j\Omega_k) \cdot W_{\mathrm{i}}(j\Omega_k)| < |2 \cdot \rho - \hat{S}(j\Omega_k) \cdot W_{\mathrm{i}}(j\Omega_k)| \tag{4.13}$$

with the parameter $0 < \rho < 1$ can be used, to place a vertical boundary crossing the point $(\rho, 0)$, as shown in Fig. 4.3b. As a further more relaxed alternative, the left-hand half of a hyperbola

$$|\varrho + O(j\Omega_k^+)| \leq |\varrho - O(j\Omega_k^+)| + 2 \cdot \rho, \tag{4.14}$$

with foci at $(-\varrho, 0)$ and $(\varrho, 0)$ can be used, as shown in Fig. 4.3c. Here, the parameter $0 < \rho < 1$ determines the intersection of the hyperbola with the x-axis at the point $(-\rho, 0)$. It is worth to mention that it is not recommended to take values for ϱ and ρ too close to each other, because this will create a horizontally-thin hyperbola. This could enable an encirclement, which may not be detected by evaluating the constraint on sampled frequencies.

4.2. System Stability

Given the inner stability of the controller, the analysis of the overall system follows similarly to the one of the MVC presented in Sec. 3.2. Hence, the stability of the IMC system is determined by its characteristic equation

$$C_{\mathrm{i}}(z) = 1 + \big(S(z) - \hat{S}(z)\big) W_{\mathrm{i}}(z). \tag{4.15}$$

Thus, the number of unstable roots

$$Z_{C_{\mathrm{i}},\bar{c}} = N^{\mathrm{cw}}_{O_{\mathrm{i}}(j\Omega)} - N^{\mathrm{ccw}}_{O_{\mathrm{i}}(j\Omega)} \tag{4.16}$$

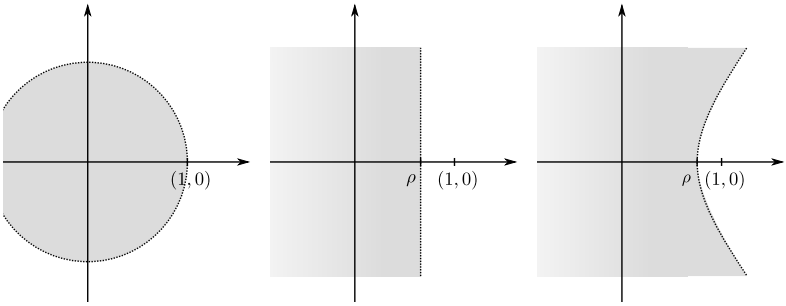

Figure 4.3.: Solution space (in gray) produced by the different controller stability constraints in the Nyquist plot of the contour $\hat{S}(j\Omega_k) \cdot W_\mathrm{i}(j\Omega_k)$.

equals the number of clockwise encirclements of the Nyquist point made by the sub-contours of the IMC open-loop

$$O_\mathrm{i}(j\Omega) = \big(S(j\Omega) - \hat{S}(j\Omega)\big)W_\mathrm{i}(j\Omega) \tag{4.17}$$

evaluated on the unit circle $N^{\mathrm{cw}}_{O_\mathrm{i}(j\Omega)}$, minus the counter-clockwise ones $N^{\mathrm{ccw}}_{O_\mathrm{i}(j\Omega)}$. So, if the equality $\hat{S}(z) = S(z)$ holds, then the radius of the contour has magnitude zero and therefore can not encircle the Nyquist point. This implies that, given a stable controller $W_\mathrm{i}(z)$, the equality

$$\hat{S}(z) = S(z). \tag{4.18}$$

is the *nominal* stability constraint of the IMC feedback system.

It is known from the previous chapters, that the secondary path of an ANC headphones application may vary substantially over time under different wearing situations. In order to account for this variability, the secondary path's multiplicative uncertainty model of Eq. 3.44 is used to replace $S(z)$ in Eq. 4.17. If $S_0(z) = \hat{S}(z)$ is chosen, then the IMC open-loop transfer function can be expressed in terms of the maximal normalized magnitude deviation $G_2(\Omega_k)$ and the unbounded phase $\Delta(j\Omega_k)$

$$O_\mathrm{i}(j\Omega) = G_2(\Omega_k) \cdot \Delta(j\Omega_k) \cdot S_0(j\Omega) \cdot W_\mathrm{i}(j\Omega). \tag{4.19}$$

Thus the contour of the open-loop generates a set of discs centered in the origin as presented in Fig. 4.4, which have frequency-dependent radii of magnitude

$$G_2(\Omega)|O_{\mathrm{i},0}(j\Omega)|, \tag{4.20}$$

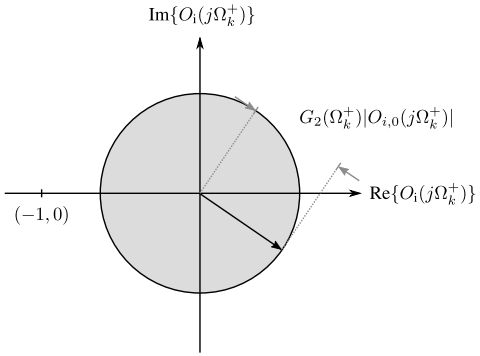

Figure 4.4.: Nyquist plot of the IMC open-loop system $O(j\Omega_k^+)$ evaluated in the *positive* frequencies $0 \leq \Omega_k < \pi$ with uncertainty $G_2(\Omega_k^+)$.

with

$$O_{\mathrm{i},0}(j\Omega) = S_0(j\Omega) \cdot W_\mathrm{i}(j\Omega). \tag{4.21}$$

Then the robust stability constraint

$$G_2(\Omega)|S_0(j\Omega) \cdot W_\mathrm{i}(j\Omega)| < 1 \tag{4.22}$$

is used to avoid that the discs encircle the Nyquist point. Alternatively, the inequality can be written as

$$|S_0(j\Omega) \cdot W_\mathrm{i}(j\Omega)| < \frac{1}{G_2(\Omega)} \tag{4.23}$$

to define a circular region of robust stable solutions.

4.3. Disturbance Enhancement

As already mentioned in Sec. 3.3, the performance achieved by a feedback system is limited by the so-called waterbed effect. This means that, an attenuation achieved in one frequency range produces an equivalent amplification in another region of the frequency domain. In order to limit this amplification side-effect, the IMC sensitivity function can be constrained during the design process of the controller $W_\mathrm{i}(z)$

$$|H_\mathrm{i}(j\Omega_k)| \leq G_3(\Omega_k) \tag{4.24}$$

to be smaller or equal to a frequency-dependent factor $G_3(\Omega_k)$. This inequality can be formulated as a *nominal* performance constraint

$$|1 - S_0(j\Omega) \cdot W_\mathrm{i}(j\Omega)| \leq G_3(\Omega_k), \tag{4.25}$$

where the estimated and the nominal secondary paths are equal to the real one $S(z)$. This defines a region of possible solutions for $W_{\mathrm{i}}(z)$ that fulfill the constraint. Graphically it can be interpreted as a circle centered at $(1,0)$ with radius $G_3(\Omega_k)$ that confines the contour $O_{\mathrm{i},0}(j\Omega)$.

In order to take the variability of the secondary path into account, the sensitivity function as defined in Eq. 4.7 is used instead

$$\left| \frac{1 - \hat{S}(j\Omega_k) \cdot W_{\mathrm{i}}(j\Omega_k)}{1 + \big(S(j\Omega_k) - \hat{S}(j\Omega_k)\big) \cdot W_{\mathrm{i}}(j\Omega_k)} \right| \leq G_3(\Omega_k), \tag{4.26}$$

together with the secondary path's multiplicative uncertainty model of Eq. 3.44 and the condition $\hat{S}(j\Omega_k) = S_0(j\Omega_k)$

$$\left| \frac{1 - S_0(j\Omega) \cdot W_{\mathrm{i}}(j\Omega)}{1 + G_2(\Omega_k) \cdot \Delta(j\Omega_k) \cdot S_0(j\Omega) \cdot W_{\mathrm{i}}(j\Omega)} \right| \leq G_3(\Omega_k). \tag{4.27}$$

If both sides are multiplied by the denominator of the inequality's left-hand side

$$\big|1 - S_0(j\Omega) \cdot W_{\mathrm{i}}(j\Omega)\big| \leq G_3(\Omega_k) \big|1 + G_2(\Omega_k) \cdot \Delta(j\Omega_k) \cdot S_0(j\Omega) \cdot W_{\mathrm{i}}(j\Omega)\big|, \tag{4.28}$$

both sides are divided by the factor $G_3(\Omega_k)$

$$\frac{1}{G_3(\Omega_k)} \big|1 - S_0(j\Omega) \cdot W_{\mathrm{i}}(j\Omega)\big| \leq \big|1 + G_2(\Omega_k) \cdot \Delta(j\Omega_k) \cdot S_0(j\Omega) \cdot W_{\mathrm{i}}(j\Omega)\big|, \tag{4.29}$$

and the worst case scenario for the right-hand side is taken

$$\frac{1}{G_3(\Omega_k)} \big|1 - S_0(j\Omega) \cdot W_{\mathrm{i}}(j\Omega)\big| \leq 1 - G_2(\Omega_k) \big|S_0(j\Omega) \cdot W_{\mathrm{i}}(j\Omega)\big|, \tag{4.30}$$

then the *robust* performance constraint

$$\frac{1}{G_3(\Omega_k)} \big|1 - S_0(j\Omega) \cdot W_{\mathrm{i}}(j\Omega)\big| + G_2(\Omega_k) \big|S_0(j\Omega) \cdot W_{\mathrm{i}}(j\Omega)\big| \leq 1 \tag{4.31}$$

can be found [Rafaely, 1997]. From this equation the nominal sensitivity function $H_{\mathrm{i},0}(j\Omega) = 1 - S_0(j\Omega) \cdot W_{\mathrm{i}}(j\Omega)$ and the nominal complementary sensitivity function $T_{\mathrm{i},0}(j\Omega) = S_0(j\Omega) \cdot W_{\mathrm{i}}(j\Omega)$ can be identified. Given the direct dependency between these two functions, a robust performance constraint parameter $G_3(\Omega_k)$ for a given $G_2(\Omega_k)$ may generate an empty solution space.

Other constraints One consideration for the digital implementation is to limit the gain of the controller. This is done not only for security purposes, but also to avoid the amplification of the ADC's noise floor to a level that

can be heard. This can be done by comparing the magnitude response of the equivalent MVC controller to the one of a maximum gain curve as in the inequality

$$\left|\tilde{W}_{\mathrm{m}}(j\Omega_k)\right| \leq G_4(\Omega_k), \tag{4.32}$$

where $G_4(\Omega_k)$ can be chosen as an inverted noise weighting curve or as a low-shelving filter frequency response. In order to use this constraint during the optimization, the frequency response of $\tilde{W}_{\mathrm{m}}(z)$ in Eq. 4.11

$$\left|\frac{W_{\mathrm{i}}(j\Omega_k)}{1-\hat{S}(j\Omega_k)\cdot W_{\mathrm{i}}(j\Omega_k)}\right| \leq G_4(\Omega_k) \tag{4.33}$$

is used. If $\tilde{W}_{\mathrm{m}}(j\Omega_k)$ is stable, then both sides can be multiplied by the denominator of the left-hand side

$$\left|W_{\mathrm{i}}(j\Omega_k)\right| \leq G_4(\Omega_k)\left|1-\hat{S}(j\Omega_k)\cdot W_{\mathrm{i}}(j\Omega_k)\right|, \tag{4.34}$$

to yield the constraint for maximum gain of the equivalent MVC controller.

4.4. The Solution Space

As seen in the previous sections, during the design of the IMC controller several constraints have to be considered. These constraints limit the set of values that the nominal open-loop $S_0(j\Omega)\cdot W_{\mathrm{i}}(j\Omega)$ is allowed to take. Thus, although the controller inner stability, the system stability and the disturbance enhancement are presented individually, their parameters have to be chosen together. Mainly because some parameter set may produce an empty solution space in the Nyquist plot, which makes the search for an optimum unfeasible.

As a first example, Fig. 4.5 is presented. Here a low secondary path multiplicative uncertainty $G_2(j\Omega_k)$ produces a circle radius bigger than unity. The first controller inner stability constraint (Eq. 4.12) is chosen, in order to prevent an encirclement of the point $(1,0)$. Additionally, the system nominal performance constraint (Eq. 4.25) is used to prevent an amplification of the disturbance. The parameter $G_3(j\Omega_k)$ is chosen in the range $0 < G_3 < 1$, which is equivalent to forcing the solution to produce attenuation throughout all frequencies, thus, negating the well-known feedback system limitation introduced by the waterbed-effect. A further problem with this parameter combination is that the solution space is restricted to the right-hand side of the Nyquist plot. Thus, the open-loop is allowed to have a maximum delay of a half of a sample. As an implication of this, the controller has to compensate for the delays of the secondary path, and with it to be partially or completely non-causal. Because of this, G_3 should be chosen according to $1 < G_3$, such that the open-loop remains unconstrained in phase and the controller is not forced to be non-causal.

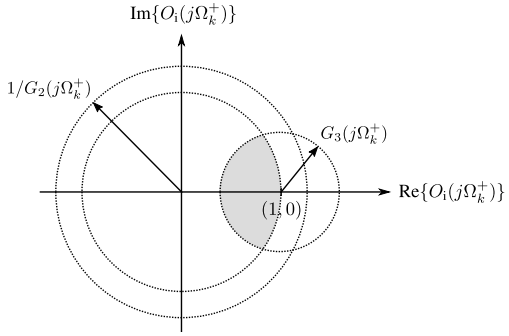

Figure 4.5.: Example of a solution space (marked in gray), when the controller inner stability constraint (Eq. 4.12), the system robust stability constraint (Eq. 4.23), and system nominal performance constraint (Eq. 4.25) are used together.

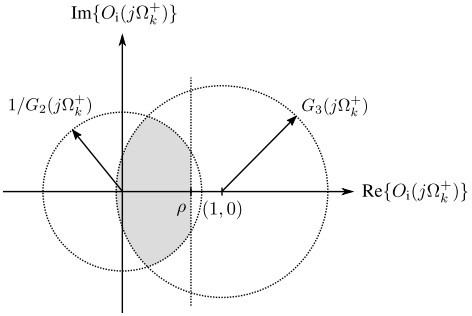

Figure 4.6.: Example of a solution space (marked in gray), when the controller inner stability constraint (Eq. 4.13), the system robust stability constraint (Eq. 4.23), and system nominal performance constraint (Eq. 4.25) are used together.

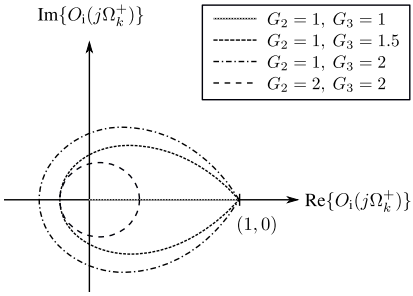

Figure 4.7.: Restriction to the solution space produced by the IMC robust performance constraint (Eq. 4.31) and the parameters G_2 and G_3. Please note that for the case $G_2 = 1, G_3 = 1$, the solution space is the segment $0 \leq \mathrm{Re}\{j\Omega_k^+\} \leq 1$ of the line $\mathrm{Im}\{j\Omega_k^+\} = 0$

As a further example, Fig. 4.6 is presented. Here the system nominal performance constraint (Eq. 4.25) is parameterized respecting the feasibility consideration for non-minimum phase secondary paths, i.e. $1 < G_3$. Thus, allowing the open-loop to have solutions with zero gain and arbitrary phase. The uncertainty in the secondary path produces a $G_2(j\Omega_k)$ with a radius smaller than 1. Therefore, imposing a maximal attenuation of $20 \cdot \log_{10}(1 - 1/G_2)\,\mathrm{dB}$. The controller inner stability constraint (Eq. 4.13) is in this case smaller than the reciprocal of $G_2(j\Omega_k)$, i.e. $\rho < 1/G_2(j\Omega_k)$. This imposes an inferior maximal attenuation of $20 \cdot \log_{10}(1 - \rho)\,\mathrm{dB}$. Although this seems to be counterproductive, it is required in order to ensure that the controller remains stable during its optimization. Choosing ρ at unity or too close to it may produce unstable controllers, if an encirclement is hidden between the discrete contour evaluation points.

Until now only the nominal performance constraint (Eq. 4.25) has been used. The incorporation of the robust performance constraint (Eq. 4.31) in the design workflow can replace the robust system stability constraint because of the following reason. The constraint can be considered as the combination of the robust stability constraint

$$G_2(\Omega_k)|S_0(j\Omega_k) \cdot W_\mathrm{i}(j\Omega_k)| < 1 \tag{4.35}$$

and nominal performance constraints, written as

$$\frac{1}{G_3(\Omega_k)}|1 - S_0(j\Omega_k) \cdot W_\mathrm{i}(j\Omega_k)| \leq 1, \tag{4.36}$$

into a single formulation

$$\frac{1}{G_3(\Omega_k)}\left|1 - S_0(j\Omega_k)\cdot W_\mathrm{i}(j\Omega_k)\right| + G_2(\Omega_k)\left|S_0(j\Omega_k)\cdot W_\mathrm{i}(j\Omega_k)\right| \leq 1. \quad (4.37)$$

Because both addends are real and strictly positive, if this constraint is met, so are the single ones. In Fig. 4.7 some examples of the robust performance constraint for different parameters G_2 and G_3 are presented. It can be seen that for $G_2 = 1$ and $G_3 = 1$ the solution lies on the x-axis and comprehends the segment $0 \leq \mathrm{Re}\{j\Omega_k^+\} \leq 1$ of the line $\mathrm{Im}\{j\Omega_k^+\} = 0$. It is also a subset of the solution space that the robust stability and nominal performance constraint would impose together, as expected. Furthermore, if the maximum amplification parameter G_3 is incremented to 1.5 or 2.0, the solution space takes the form of a water drop, incorporating the origin and the point $(1, 0)$. Thus, the controller inner stability constraint (Eq. 4.13) or (Eq. 4.14) would be required in order to limit the gain inside the inner feedback loop. If the secondary path multiplicative uncertainty is incremented to $G_2 = 2$, then the solution space decreases to a small ellipse which does not encircles the point $(1, 0)$. Thus, the incorporation of the controller inner stability constraint would not be mandatory. Hence, under certain parameter considerations the robust performance constraint can be used to ensure controller inner stability, system robust stability and robust performance.

4.5. Controller Optimization

In this section the design of the impulse response of the controller $\mathbf{w}_\mathrm{i}(n)$ is presented. The design is formulated as a convex optimization problem. This ensures that the local minima found by means of SQP corresponds to the global one. The objective function presented here is based on the weighted IMC nominal sensitivity function

$$C_\mathrm{i}^\mathrm{c}(j\Omega_k) = G_1(\Omega_k)\cdot\Big(1 - S_0(j\Omega_k)\cdot W_\mathrm{i}(j\Omega_k)\Big), \quad (4.38)$$

where $G_1(j\Omega_k)$ represents the disturbance signal's energy content over frequency. If the frequency-dependent sensitivity of the human hearing system should be taken into account, then this can be weighted with a noise weighting curve, e.g. A, C, or ITU-R 468 curve. The cost function is based on the sum over squared magnitude values of the frequency response of $C_\mathrm{i}(j\Omega_k)$. The values are generated by evaluating Eq. 4.38 around the upper-half of the unit-circle

$$C_\mathrm{imc}(\mathbf{w}_\mathrm{i}) = \frac{2}{N}\sum_{k=0}^{N/2-1}\left|C_\mathrm{i}^\mathrm{c}(j\Omega_k)\right|^2. \quad (4.39)$$

This cost function builds a quadratic dependency with respect to the controller coefficients $\mathbf{w}_\mathrm{m}$ and is tightly related with the 2-norm of its DTFT counterpart. Alternatively, the sum can be calculated within an attenuation bandwidth of interest

$$C'_{\mathrm{imc}}(\mathbf{w}_\mathrm{i}) = \frac{2}{k_\mathrm{h} - k_\mathrm{l} + 1} \sum_{k=k_\mathrm{l}}^{k_\mathrm{h}} \left| C_\mathrm{i}^\mathrm{c}(j\Omega_k) \right|^2, \tag{4.40}$$

as suggested by Pawelczyk in [Pawełczyk, 2002]. Here k_l is the FFT frequency index related to the lowest frequency of interest f_l and k_h is the one related to the highest frequency of interest f_h.

Constraints In order to yield a convex problem, not only the cost functions have to produce a quadratic dependency with respect to the parameters, but also the constraints. Because in this context a constraint enforced on the *positive* frequencies is automatically fulfilled on the *negative* frequencies, their evaluation is limited to the former ones. For this purpose, the controller inner stability constraints can be re-written as

$$|\hat{S}(j\Omega_k^+)W_\mathrm{i}(j\Omega_k^+)|^2 < 1, \tag{4.41}$$

$$|\hat{S}(j\Omega_k^+)W_\mathrm{i}(j\Omega_k^+)|^2 < |2 \cdot \rho - \hat{S}(j\Omega_k^+)W_\mathrm{i}(j\Omega_k^+)|^2, \tag{4.42}$$

and

$$|\varrho + \hat{S}W_\mathrm{i}|^2 < |\varrho - \hat{S}W_\mathrm{i})|^2 + 4\rho|\varrho - \hat{S}W_\mathrm{i}| + 4\rho^2. \tag{4.43}$$

The robust stability constraint is re-written as

$$G_2^2(\Omega_k^+)|S_0(j\Omega_k^+)W_\mathrm{i}(j\Omega_k^+)|^2 < 1, \tag{4.44}$$

the nominal performance constraint as

$$|1 - S_0(j\Omega_k^+)W_\mathrm{i}(j\Omega_k^+)|^2 \leq G_3^2(\Omega_k^+), \tag{4.45}$$

and, omitting the dependency on Ω_k^+, the robust performance constraint as

$$\frac{1}{G_3^2}\left|1 - S_0 \cdot W_\mathrm{i}\right|^2 + 2\frac{G_2}{G_3}\left|1 - S_0 \cdot W_\mathrm{i}\right|\left|S_0 \cdot W_\mathrm{i}\right| + G_2^2\left|S_0 \cdot W_\mathrm{i}\right|^2 \leq 1. \tag{4.46}$$

Finally, the equivalent MVC maximum gain constraint is formulated as

$$\left|W_\mathrm{i}(j\Omega_k^+)\right|^2 \leq G_4^2(j\Omega_k^+)\left|1 - \hat{S}(j\Omega_k^+) \cdot W_\mathrm{i}(j\Omega_k^+)\right|^2. \tag{4.47}$$

4.6. The Adaptive Controller

As noticed by Rafaely in [Rafaely, 1997], if an equivalent leaky Filtered-x LMS algorithm [Elliott et al., 1987] is derived for the IMC structure, then the sensitivity function in Eq. 4.7 and the condition $\hat{S}(z) \neq S(z)$ would yield a non-convex problem. So, under any change on the secondary path $S(z)$ the adaptive controller would not reach the optimum and it could diverge into an unstable state. Therefore, the adaptive controller is derived based on the IMC nominal sensitivity function, as also proposed for the off-line controller optimization in Sec. 4.5. Thus, the gradient of the cost function with respect to the IMC controller coefficients $\mathbf{w}_\mathrm{i}$

$$\nabla f_c(\mathbf{w}_\mathrm{i}) = \frac{\partial \mathbb{E}[\mathbf{e}^\mathrm{T}\mathbf{e}]}{\partial \mathbf{w}_\mathrm{i}} \approx \frac{-2}{L_e} \cdot (\mathbf{d}_\mathrm{zp} - \mathbf{D}\cdot\mathbf{S}\cdot\mathbf{w}_\mathrm{i})^\mathrm{T} \cdot \mathbf{D}\cdot\mathbf{S} + \frac{2\cdot\beta_0}{L_e}\cdot\mathbf{w}_\mathrm{i}^\mathrm{T}. \quad (4.48)$$

is expressed based on its equivalent feedforward system. If this expression is transposed

$$\nabla f_c^\mathrm{T}(\mathbf{w}_\mathrm{i}) \approx \frac{-2}{L_e} \cdot \mathbf{S}^\mathrm{T} \cdot \mathbf{D}^\mathrm{T} \cdot (\mathbf{d}_\mathrm{zp} - \mathbf{D}\cdot\mathbf{S}\cdot\mathbf{w}_\mathrm{i}) + \frac{2\cdot\beta_0}{L_e}\cdot\mathbf{w}_\mathrm{i}, \quad (4.49)$$

and the vectors in the round parenthesis are replaced by the one of the estimated feedforward error signal

$$\nabla f_c^\mathrm{T}(\mathbf{w}_\mathrm{i}) \approx \frac{-2}{L_e} \cdot \mathbf{S}^\mathrm{T} \cdot \mathbf{D}^\mathrm{T} \cdot \mathbf{e}_\mathrm{f} + \frac{2\cdot\beta_0}{L_e}\cdot\mathbf{w}_\mathrm{f}, \quad (4.50)$$

the gradient averaged over L_e samples can be found. Subsequently, the filtered-*disturbance*'s Toeplitz matrix equivalently defined as in Eq. 2.58 is used

$$\nabla f_c^\mathrm{T}(\mathbf{w}_\mathrm{i}) \approx \frac{-2}{L_e} \cdot \mathbf{D}_s^\mathrm{T} \cdot \mathbf{e}_\mathrm{f} + \frac{2\cdot\beta_0}{L_e}\cdot\mathbf{w}_\mathrm{i}. \quad (4.51)$$

and the cheaper instantaneous estimate of the gradient is chosen instead

$$\nabla f_c^\mathrm{T}(\mathbf{w}_\mathrm{i}(n)) \approx -2\cdot\mathbf{d}_s^\mathrm{T}\cdot e_\mathrm{f}(n) + 2\cdot\beta_0\cdot\mathbf{w}_\mathrm{i}. \quad (4.52)$$

This equation is used to replace the gradient in Eq. 2.53

$$\mathbf{w}_\mathrm{i}(n+1) = \mathbf{w}_\mathrm{i}(n) + \mu\cdot\mathbf{d}_s^\mathrm{T}\cdot e_\mathrm{f}(n) - \mu\cdot\beta_0\cdot\mathbf{w}_\mathrm{i}(n), \quad (4.53)$$

which then formulates the coefficients update equation

$$\mathbf{w}_\mathrm{i}(n+1) = \mathbf{w}_\mathrm{i}(n)\big(1-\mu\cdot\beta_0\big) + \mu\cdot\mathbf{d}_s^\mathrm{T}\cdot e_\mathrm{f}(n). \quad (4.54)$$

In order to implement the adaptive filter, the system diagram proposed by Rafaely and depicted in Fig. 4.8 is used. Similarly to the Modified Normalized Filtered-x LMS algorithm (see Sec. 2.4.2) the system is divided in two sections: the upper section takes care of the calculation of the con-

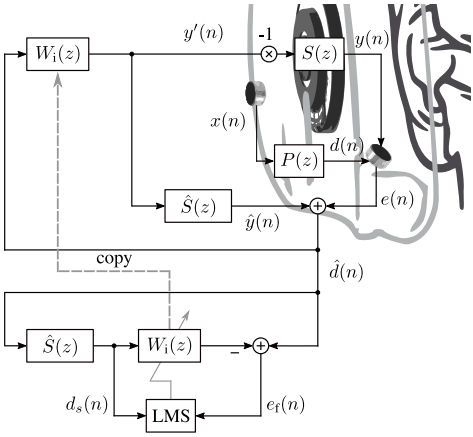

Figure 4.8.: The system diagram of the Modified Normalized Filtered-d LMS adaptation algorithm applied to headphones [Rafaely, 1997].

trol signal; and the lower section adapts an isolated copy of the controller coefficients using the LMS algorithm. An advantage of this is that the controller converges faster, because the control signal calculated with its current coefficients $d_s(n) * \mathbf{w}_{\mathrm{i}}(n)$ does not go through the secondary path (and through its delay) before generating the error $e_{\mathrm{f}}(n)$. Therefore, this instant error is directly correlated with the current coefficient set and not with the past ones.

Robust Stability As proposed by Rafaely, the robust stability constraint in Eq. 4.22 can be incorporated in the coefficients' update equation

$$\mathbf{w}_{\mathrm{i}} = \mathrm{DFT}^{-1}\left\{W_{\mathrm{i}}(k) - \beta_0|S_0(k)G_2(k)|W_{\mathrm{i}}(k) + \mu S_0^*(k)D^*(k)E(k)\right\}_+ \tag{4.55}$$

of a frequency-domain Filtered-x LMS [Shynk, 1992] algorithm, with $\mathrm{DFT}^{-1}\{\cdot\}_+$ as the causal part of the inverse Discrete Fourier Transform (DFT). By doing so, a frequency selective leakage factor can be introduced. In this work, however, this adaptive approach is only described for completeness and will not be evaluated afterwards.

4.6.1. Optimization results

The optimizations results presented in this section are obtained using the nonlinear programming solver `fmincon()` together with the SQP algorithm from the MATLAB 2019a optimization toolbox. The parameters

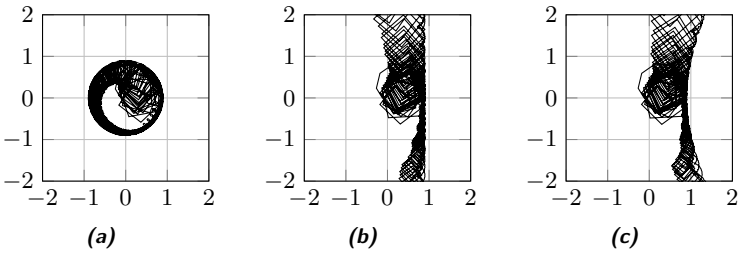

Figure 4.9.: The Nyquist plot produced by the contour $O(j\Omega_k^+) = S_0(j\Omega_k^+) \cdot W_i(j\Omega_k^+)$, when subject to (a) the circular constraint, (b) the vertical line constraint and (c) the hyperbolic curve constraint. The circle radius is set to 0.9, the vertical line intersection is set to $(0.9, 0)$, and the hyperbola's intersection is set to $(0.9, 0)$ and the foci to $(-2, 0)$ and $(2, 0)$. Parameters: $f_s = 48\,\text{kHz}$, $N = 8192$, $L_i = 128$, $f_l = 0\,\text{Hz}$, $f_h = 3\,\text{kHz}$.

`MaxIterations` and `MaxFunctionEvaluations` are set to $\max(400, L_i)$ and $400 \cdot L_i$, respectively. Nevertheless, all the optimization runs found the optimal solution before reaching these iteration limits. The starting solution for the coefficients optimization is set to zero. The sampling frequency $f_s = 48\,\text{kHz}$ and the FFT length $N = 8192$ are chosen. In Fig. 3.12 the frequency-dependent parameters used during the optimization are presented, which are the same ones utilized during the optimization of the MVC controller.

Nominal stability constraints As a first step, the three nominal stability constraints are compared, in order to choose which one should be used for the rest of the optimizations. For this, the impulse response length is set to $L_i = 128$, and the cost function is calculated with $f_l = 0$ and $f_h = 3\,\text{kHz}$. In order to make the results comparable, the circular constraint has a radius of 0.9, the vertical constraint has intersects the x-axis at $(0.9, 0)$, and the hyperbolic constraint has its intersection with the x-axis at $(0.9, 0)$ and its foci at $(-2, 0)$ and $(2, 0)$. These parameters also help to set a security gap between the contour and the Nyquist point.

In Fig. 4.9 the three Nyquist plots of the contours generated by the constraints are presented. As can be seen, they effectively avoid the encirclement of the Nyquist point. However, they offer very different solution spaces. As can be seen from the non-smooth contours, the security gaps are indeed required to avoid encirclements hidden between consecutive evaluation points. Moreover, for the hyperbolic constraint a bigger security gap may be required to avoid evaluation points connecting over the curvature of

the constraint. In Fig. 4.10 the sensitivity functions generated by the same controllers is presented. For frequencies below 350 Hz the constraints do not show significant differences. However, for higher frequencies it is clear that the circular constraint not only limits the highest reachable attenuation, but also its bandwidth. Nevertheless, the limitation also maintains the disturbance enhancement generated at 6 and 16.2 kHz under certain boundaries. Near the same frequencies the other two constraints show important amplifications. From the three constraints, the one based on the vertical line offers the best trade-off between the required security gap size and the achievable attenuation performance.

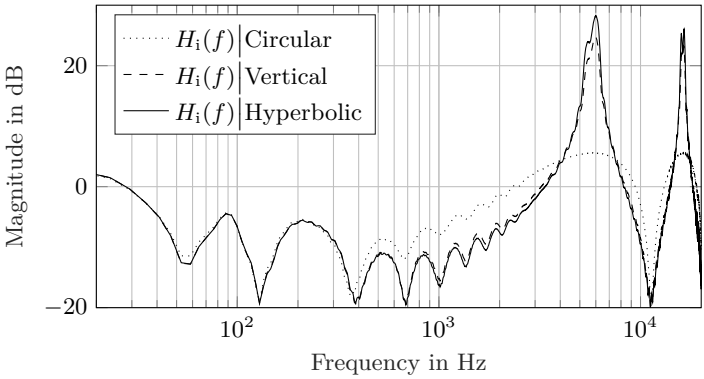

Figure 4.10.: Development of the optimal sensitivity function $H_\mathrm{m}(f)$ when using different nominal stability constraints. The circle radius is set to 0.9, the vertical line intersection is set to $(0.9, 0)$, and the hyperbola's intersection is set to $(0.9, 0)$ and the foci to $(-2, 0)$ and $(2, 0)$. Parameters: $f_\mathrm{s} = 48\,\mathrm{kHz}$, $N = 8192$, $L_\mathrm{i} = 128$, $f_\mathrm{l} = 0\,\mathrm{Hz}$, $f_\mathrm{h} = 3\,\mathrm{kHz}$.

Further design constraints As a second step, the development of the optimal sensitivity function is evaluated under increasingly restrictive constraints. For this, the controller's impulse response length is set to $L_\mathrm{i} = 128$, the vertical boundary constraint with intersection at $(0.9, 0)$ is used, and the cost function is accumulated over the lower $f_\mathrm{l} = 0\,\mathrm{Hz}$ and higher $f_\mathrm{h} = 3\,\mathrm{kHz}$ frequencies. In Fig. 4.11 and Fig. 4.12 the results are presented. It can be seen from $W_\mathrm{i}(f)\big|G_4$ that the gain limitation on the equivalent MVC controller does not imply a restriction on the IMC controller's gain. This is because of the more complex dependency between both given by Eq. 4.11. Nevertheless, the attenuation and amplification produced in its sensitivity function $H_\mathrm{i}(f)\big|G_4$ between 10 and 20 kHz are much less present. As an effective measure against the remaining amplification peak at 6 kHz

in the sensitivity function, the disturbance enhancement constraint parameterized with $G_3(f)$ from Fig. 3.12 is used. It can be seen that the sensitivity function $H_\mathrm{i}(f)\big|G_3G_4$ produces no amplification higher that the given 3 dB. As a positive side-effect of this, the controller $W_\mathrm{i}(f)\big|G_3G_4$ produces gains not higher than 4 dB. However, the constraint produces a loss in attenuation starting from 340 Hz onward, throughout a transition band which ends in the plateau of 3 dB between 3 and 8 kHz.

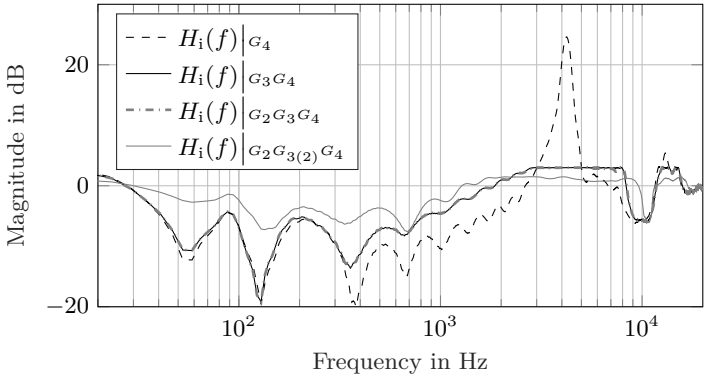

Figure 4.11.: Development of the optimal sensitivity function $H_\mathrm{i}(f)$ when constraints are enforced in increasingly restrictive order. The vertical boundary intersection is set to $(0.9, 0)$. Parameters: $f_s = 48\,\mathrm{kHz}$, $N = 8192$, $L_\mathrm{i} = 128$, $f_\mathrm{l} = 0\,\mathrm{Hz}$, $f_\mathrm{h} = 3\,\mathrm{kHz}$.

The robust stability constraint built on the multiplicative uncertainty over frequency $G_2(f)$ is used to ensure that the system remains stable upon variations in the secondary path $S(f)$. If the optimization is additionally subject to this constraint, then very few changes can be seen from comparing its sensitivity function $H_\mathrm{i}(f)\big|G_2G_3G_4$ with the one of the previous case $H_\mathrm{i}(f)\big|G_3G_4$. The same is the case when comparing its controller $W_\mathrm{i}(f)\big|G_2G_3G_4$ with the previous one $W_\mathrm{i}(f)\big|G_3G_4$. The small but still visible differences concentrate in the range 5.5-8.5 kHz, where $G_2(f)$ presents a increment in uncertainty. Therefore, the restriction imposed by the robust stability constraint is comparable to the one generated by the other two restrictions before. Moreover, this could offer a less computationally expensive alternative for either off-line or on-line optimizations. However, if robust performance is required, then it can be seen from $W_\mathrm{i}(f)\big|G_2G_{3(2)}G_4$ that the controller changes substantially. This produces losses in attenuation magnitude and bandwidth in its related sensitivity function $H_\mathrm{i}(f)\big|G_2G_{3(2)}G_4$. Nevertheless, this also comes with a lower dis-

turbance enhancement, which approximately decreases to 1.5 dB.

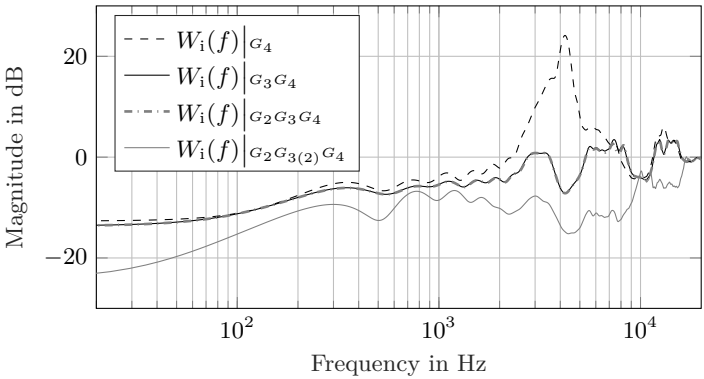

Figure 4.12.: Development of the optimal controller $W_\mathrm{i}(f)$, when constraints are enforced in increasingly restrictive order. The vertical boundary intersection is set to $(0.9, 0)$. Parameters: $f_s = 48\,\mathrm{kHz}$, $N = 8192$, $L_\mathrm{i} = 128$, $f_\mathrm{l} = 0\,\mathrm{Hz}$, $f_\mathrm{h} = 3\,\mathrm{kHz}$.

Controller's impulse response length As a third step, the effect of the impulse response length L_i is evaluated. For this, the cost function is calculated over the frequency range resulting from $f_\mathrm{l} = 0\,\mathrm{Hz}$ and $f_\mathrm{h} = 3\,\mathrm{kHz}$. The optimization is subject to the constraint combination $G_2G_3G_4$, i.e. the vertical nominal stability constraint, the maximum equivalent MVC controller gain $G_4(f)$, the nominal performance limit $G_3(f)$ and the robust stability constraint based on $G_2(f)$ are used. The results are presented in Fig. 4.13. With an impulse response of $L_\mathrm{i} = 4$ the same attenuation bandwidth can be achieved as with longer impulse responses, and this combined with a moderate disturbance enhancement. However, the attenuation magnitude is significantly lower for frequencies higher than 100 Hz. With an impulse response of $L_\mathrm{i} = 16$ the attenuation magnitude achieved in frequencies higher than 600 Hz is comparable to the ones achieved with longer impulse responses. With $L_\mathrm{i} = 64$ the attenuation magnitude in the range 100 and 600 Hz improves significantly. With $L_\mathrm{i} = 256$ it can be seen that the increment in impulse response length decreases the ripple effect in the attenuation and transition band of the sensitivity function, which magnitude is higher in the lower-frequencies. If the sensitivity function $H_\mathrm{i}(f)\big|L_\mathrm{i} = 256$ is compared to the curve of $|1 - z^{-5}|$ in Fig. 2.4, one can see that for frequencies higher than 300 Hz the attenuation and amplification regions of both curves resemble very much. Thus, it is to be expected

that the longer the impulse response L_i is, the closer the system gets to the comb-filter imposed by the delays in the secondary path.

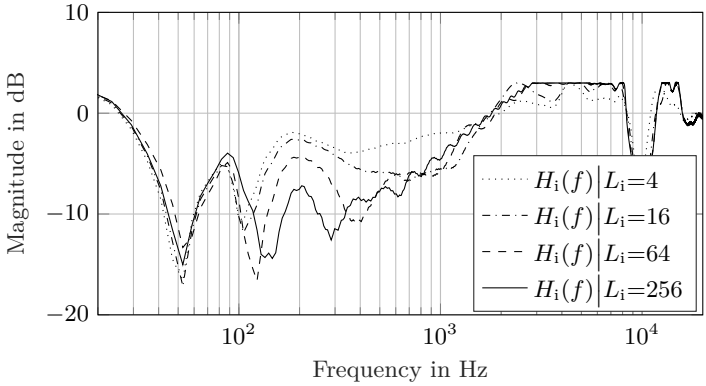

Figure 4.13.: Optimum sensitivity functions obtained with different impulse response lengths L_i. The optimization is subject to the constraint combination $G_2G_3G_4$. The vertical boundary intersection is set to $(0.9, 0)$. Parameters: $f_\mathrm{s} = 48\,\mathrm{kHz}$, $N = 8192$, $f_\mathrm{l} = 0\,\mathrm{Hz}$, $f_\mathrm{h} = 3\,\mathrm{kHz}$.

Cost function's bandwidth As a fourth step, the effect of the cost function's bandwidth is evaluated. For this purpose, the cost function's lowest frequency is set to $f_\mathrm{l} = 0$ and the highest one f_h is incremented, in order to generate four different cost function bandwidths. The optimization is subject to the constraint combination $G_2G_3G_4$, with a vertical boundary intersection set to $(0.9, 0)$, and with an impulse response length of $L_\mathrm{i} = 256$. The results are presented in Fig. 4.14. It can be seen that for $f_\mathrm{h} = 200\,\mathrm{Hz}$ an attenuation bandwidth of 300 Hz is achieved. Its magnitude is not over all frequencies better than other settings in the same bandwidth. Hence, by just decreasing f_h the limitation given by the controller length L_i can not be completely circumvented. Moreover, a ripple effect in the pass-band is very prominent, producing important variations of up to 10 dB between 4 and 5 kHz. With $f_\mathrm{h} = 500\,\mathrm{Hz}$ the attenuation bandwidth increases to 1.2 kHz and the ripple effect decreases significantly. Moreover, the attenuation within the range of frequencies above 200 Hz and below 1 kHz is better than with any other setting. With $f_\mathrm{h} = 2000\,\mathrm{Hz}$ the attenuation between 200 Hz and 1 kHz decreases in favor of the attenuation bandwidth, which increases up to 2 kHz. At 2 kHz a jump up to the 3 dB pass-band is seen. Thus, around these f_h values, a trade-off between attenuation magnitude and attenuation bandwidth can be observed. With $f_\mathrm{h} = 3000\,\mathrm{kHz}$

neither the attenuation magnitude nor the attenuation bandwidth change. Instead, the transition band is extended up to 3 kHz. Thus, the maximum amplification is not reached at 2 kHz, but rather at 3 kHz. A further increment of the cost function bandwidth to 4 kHz did not produce any improvements and is therefore excluded. Hence, from the results it can be said that by changing f_h the transition band can be shortened or extended. A short transition band produces a strong ripple in the pass-band, while a long transition band can reduce the bandwidth in which the disturbance is amplified.

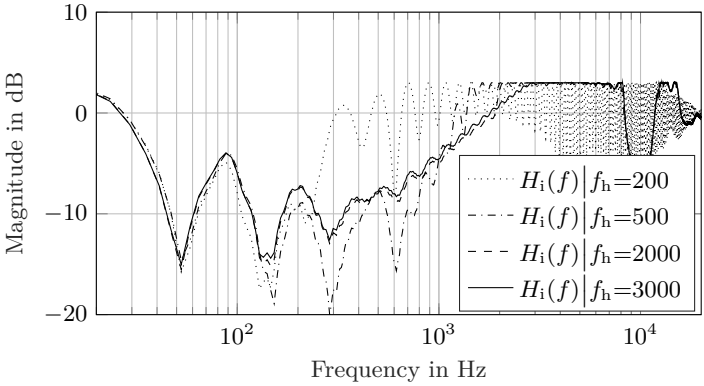

Figure 4.14.: Optimum sensitivity functions obtained with different cost function bandwidths. The optimization is subject to the constraint combination $G_2 G_3 G_4$. The vertical boundary intersection is set to $(0.9, 0)$. Parameters: $f_s = 48\,\mathrm{kHz}$, $N = 8192$, $f_\mathrm{l} = 0\,\mathrm{Hz}$, $L_\mathrm{i} = 256$.

4.7. Summary

In the present chapter the internal model control scheme has been presented. Its feedback working principle based on an estimated secondary path allows it to be analyzed as a feedforward equivalent system. Based on this, the limitations imposed by the secondary path's delays are estimated. As result of this analysis, the minimum residual error $e(n)$ is found to be shaped by the comb-filter effect presented in Fig. 2.4.

In Sec. 4.1 the considerations regarding the stability of the *digital* feedback loop built by $W_i(z)$ and the estimated secondary path $\hat{S}(z)$ inside the IMC scheme are described. Thus, this inner loop works similarly to an MVC controller built on a positive feedback loop. Based on these considerations, less restrictive inner stability constraints than the ones found in

the literature, based on vertical and hyperbolic boundaries, are described.

In Sec. 4.2 and Sec. 4.3 the stability and disturbance enhancement constraints are respectively presented. For the former, the secondary path's uncertainty over frequency $G_2(f)$ is used as parameter; while for the latter, the frequency-dependent maximum amplification parameter $G_3(f)$ is used. In Sec. 4.4 the dependencies of the solution space with respect to the constraints is graphically described. Based on these, practical considerations when choosing the parameters $G_2(f)$ and $G_3(f)$ are discussed, in order to ensure a feasible optimization of the controller $W_i(z)$.

In Sec. 4.6 the search of an optimum controller impulse response $\mathbf{w}_\mathrm{i}$ is formulated as a convex optimization problem subject to design constraints. From the optimization results it is concluded that by choosing the less restrictive controller's inner stability constraints, the solution space can be extended before other constraints are enforced during the optimization. If the maximum controller gain constraint G_4 and the nominal performance constraint G_3 are already enforced, then the robust stability constraint G_2 introduces almost no change in the optimum. If the controller length L_i is incremented, the attenuation and amplification regions in the sensitivity function $H_\mathrm{i}(f)$ get closer to the one of a comb-filter imposed by the secondary path's delays. By varying the cost function's bandwidth the transition band can be extended, but only up to the one imposed by the comb-filter effect. Moreover, changes in the cost function's bandwidth can be used to slightly improve the results in the attenuation band.

CHAPTER 5

Hybrid and Pseudo-Cascaded Control Structures

The control structures presented in this section aim to combine the attenuation capabilities of two classical control structures into a single system. The increase in complexity is compensated by the design-flexibility and higher attenuation levels they can achieve together. These combinations are based on two combination strategies: The first one is the so-called hybrid system principle, in which a feedforward and a feedback algorithm are combined to generate a single improved control system; the second one is the pseudo-cascading principle, in which two feedback systems use an internal estimation of the residual error in order to emulate a cascaded control system. In both combination strategies the combination has two alternatives, i.e. one that produces independent optimal solutions for its controllers or one that creates a dependency between them. Their system transfer functions and the changes they introduce in the effective primary and secondary paths are utilized to understand these behaviors. Their derivations are presented in detail in Appendix A.

5.1. Minimum Variance Control combined with Internal Model Control

The MVC-IMC pseudo-cascaded combination proposed in [Schumacher et al., 2011] for a digital IMC and analog MVC implementation, got simplified later on in [Rivera Benois et al., 2017] by a fully digital implementation of it. The resulting system diagram is presented in Fig. 5.1a. In the bottom part the IMC structure can be seen. The estimated signal $\hat{e}_{\mathrm{m}}(n)$ is

an estimation of the residual error left by the MVC. Thus, the MVC works as first control stage, while the IMC as the second one. Both controllers, $W_{\mathrm{i}}(z)$ and $W_{\mathrm{m}}(z)$, are connected in parallel for generating individual control signals, which are summed up and sing-inverted before they are fed to the secondary path. The system's transfer function

$$H_{\mathrm{mi}}(z) = \frac{E(z)}{D(z)} = \frac{1 - \hat{S}(z)W_{\mathrm{i}}(z)}{1 + S(z)W_{\mathrm{m}}(z) + \big(S(z) - \hat{S}(z)\big)W_{\mathrm{i}}(z)} \tag{5.1}$$

presents the numerator of Eq. 4.7 and a denominator that is almost an additive combination of the ones of Eq. 3.2 and Eq. 4.7. If $\hat{S}(z) = S(z)$ holds, then the denominator reduces to the one in Eq. 3.2, and both controllers can be designed independently. However, no stability and performance analysis can be found in the literature regarding what happens if this condition is not met. Thus, a more reliable design method for these controllers still has to be developed. The effective secondary path seen by the IMC controller

$$\hat{S}_{\mathrm{i}}^{\mathrm{mi}}(z) = -\frac{E(z)}{Y_{\mathrm{i}}'(z)} = S(z)\frac{1 + \hat{S}(z)W_{\mathrm{m}}(z)}{1 + S(z)W_{\mathrm{m}}(z)} \tag{5.2}$$

can be calculated by considering $d(n) = 0$, $y_{\mathrm{i}}'(n)$ as the input to the system, and $e(n)$ as its output. As can be seen, the effective secondary path shows an asymptotic behavior between $S(z)$ and $\hat{S}(z)$ regarding the magnitude of $W_{\mathrm{m}}(z)$. Thus, it approximates $\hat{S}(z)$ in frequencies where $|W_{\mathrm{m}}(z)| \gg 1$, and on the other hand $S(z)$, when $|W_{\mathrm{m}}(z)| \ll 1$. By doing so, the magnitude of $W_{\mathrm{m}}(z)$ may partially help the adaptation algorithm to overcome mismatches between $S(z)$ and $\hat{S}(z)$.

5.1.1. Alternative structure with dependent internal model control optimum

An alternative IMC-MVC combination can be found earlier in the literature [Tay and Moore, 1991, Elliott, 2001a, Pawełczyk, 2003, Song et al., 2005]. Its block diagram is presented in Fig. 5.1b. Here the MVC uses directly the error signal $e(n)$ to calculate $y_{\mathrm{m}}'(n)$, which alters the effective secondary path seen from the IMC perspective

$$S_{\mathrm{i}}^{\mathrm{mido}}(z) = -\frac{E(z)}{Y_{\mathrm{i}}'(z)} = \frac{S(z)}{1 + S(z)W_{\mathrm{m}}(z)}. \tag{5.3}$$

This change is considered beneficial for the IMC, because under certain conditions $\frac{S(z)}{1+S(z)W_{\mathrm{m}}(z)}$ is easier to control and model than $S(z)$ [Elliott, 2001a]. Furthermore, if $\hat{S}_{\mathrm{i}}(z) = \frac{\hat{S}(z)}{1+\hat{S}(z)W_{\mathrm{m}}(z)}$ is chosen, then the system's

transfer function (omitting the argument z) yields

$$H_{\text{mido}} = \frac{1 + \hat{S} \cdot W_{\text{m}} - \hat{S} \cdot W_{\text{i}}}{1 + (S + \hat{S}) \cdot W_{\text{m}} + S \cdot \hat{S} \cdot W_{\text{m}}^2 + (S - \hat{S}) \cdot W_{\text{i}}}. \tag{5.4}$$

The denominator can be interpreted as the approximation of a squared binomial with a residual. The residual can be zero, under which circumstances $\hat{S}(z) = S(z)$ holds and the system's transfer function simplifies to

$$\hat{H}_{\text{mido}}(z) = \frac{1 - \frac{S(z)}{1+S(z)W_{\text{m}}(z)} W_{\text{i}}(z)}{1 + S(z)W_{\text{m}}(z)}. \tag{5.5}$$

As can be seen by comparing with Eq. 5.1, the change in the effective secondary path alters mainly the influence of $W_{\text{i}}(z)$. This influence of the MVC over the control effort of the IMC is what is understood as the dependent internal model control optimum. However, a stability and performance analysis has to be carried out, in order to design controllers for this specific structure, as in many applications $\hat{S}(z)$ deviates significantly from $S(z)$.

5.2. Minimum Variance Control combined with Feedforward Control

In solutions where the electronics of an adaptive feedforward control are available, an MVC controller can improve the attenuation performance, without significantly incrementing the implementation effort. The block diagram presented in Fig. 5.2a depicts the MVC-FF combination suggested in [Bai and Lin, 1997, Carme, 1999, Rafaely and Jones, 2002, Håkansson et al., 2002, Streeter et al., 2004]. The MVC and FF controllers ($W_{\text{m}}(z)$ and $W_{\text{f}}(z)$, respectively) work independent from each other. The reference signal $x(n)$ and error signal $e(n)$ are used to calculate the control signals $y'_{\text{f}}(n)$ and $y'_{\text{m}}(n)$ in parallel. The addition of both signals $y'(n)$ is sign-inverted and then fed to the secondary path. The system's transfer function

$$H_{\text{fm}}(z) = \frac{E(z)}{X(z)} = \frac{P(z) - S(z)W_{\text{f}}(z)}{1 + S(z)W_{\text{m}}(z)} \tag{5.6}$$

reflects a combined passive and active attenuation effect, where the controllers work independent from each other. Thus, a multiplicative combination of Eq. 2.1 and Eq. 3.2 can be seen. Due to the MVC control loop, the effective secondary path

$$S_{\text{f}}^{\text{fm}}(z) = -\frac{E(z)}{Y'_{\text{f}}(z)} = \frac{S(z)}{1 + S(z)W_{\text{m}}(z)} \tag{5.7}$$

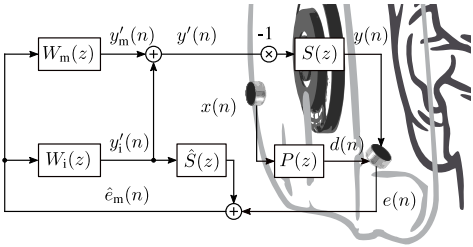

(a) *MVC-IMC combination with independent optima*

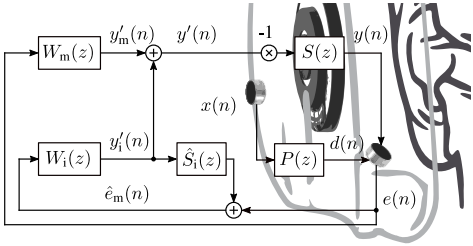

(b) *MVC-IMC combination with dependent optima*

Figure 5.1.: Hybrid control structures involving the combination of the MVC with the IMC approaches: (a) the structure with independent IMC optimal controller, and (b) the structure with dependent IMC optimal controller.

seen between the feedforward control signal $y'_\mathrm{f}(n)$ and the error signal $e(n)$ changes to the same expression found in Eq. 5.3. Thus, this structure may profit from an effective secondary path that is easier to control and model.

5.2.1. Alternative structure with dependent feedforward optimum

An alternative to the previous structure is found in the literature later on in [Foudhaili, 2008, Rivera Benois et al., 2018b]. In Fig. 5.2b the block diagram of the structure is presented. An approximation of the secondary path $\hat{S}(z)$ is used to make an estimation of $y'_\mathrm{f}(n)$ at the error microphone's position $\hat{y}_\mathrm{f}(n)$. This estimation is used to negate the effect of the FF controller on the error signal $e(n)$, before this is used by the MVC to calculate $y'_\mathrm{m}(n)$. By doing so, the effective secondary path seen from the FF perspective

$$S_\mathrm{f}^\mathrm{fmdo}(z) = -\frac{E(z)}{Y'_\mathrm{f}(z)} = S(z)\frac{1+\hat{S}(z)W_\mathrm{m}(z)}{1+S(z)W_\mathrm{m}(z)} \tag{5.8}$$

changes to the one already seen in Eq. 5.2, and produces a change in the system's transfer function

$$H_{\mathrm{fmdo}}(z) = \frac{P(z)}{1 + S(z)W_{\mathrm{m}}(z)} - S(z)W_{\mathrm{f}}(z)\frac{1 + \hat{S}(z)W_{\mathrm{m}}(z)}{1 + S(z)W_{\mathrm{m}}(z)}. \tag{5.9}$$

The change can be interpreted as a change in the effective primary path $P(z)$ by the transfer function of the MVC. Furthermore, if the optimal solution of $W_{\mathrm{f}}(z)$

$$W_{\mathrm{f}}^{\mathrm{opt}}(z) = \frac{P(z)}{S(z)} \cdot \frac{1}{1 + \hat{S}(z)W_{\mathrm{m}}(z)}, \tag{5.10}$$

is derived from $H_{\mathrm{fmdo}}(z)$, then a decrease in the FF control effort can be found in regions where the MVC is effective. Thus, the new FF optimum may target a frequency region where the MVC attenuation is not dominant. This effect is the cause for the dependent feedforward optimum.

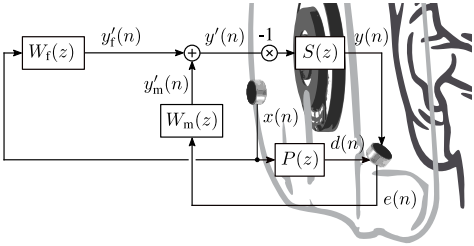

(a) *MVC-FF combination with independent optima*

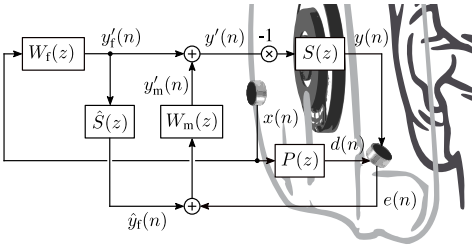

(b) *MVC-FF combination with dependent optima*

Figure 5.2.: Hybrid control structures involving the combination of the MVC with the FF approaches: (a) the structure with independent FF optimal controller, and (b) the structure with dependent FF optimal controller.

5.3. Internal Model Control combined with Feedforward Control

The IMC-FF combination [Kong et al., 1998,Hansen, 2001,Wu et al., 2015, Rivera Benois et al., 2017] offers the possibility to design both feedforward and feedback controllers based on Wiener filter formulations or on similar adaptation algorithms. In Fig. 5.3a an illustration of its block diagram is presented. On top, the FF controller $W_\mathrm{f}(z)$ is fed with the reference signal $x(n)$, and its output $y'_\mathrm{f}(n)$ is added to the control signal $y'_\mathrm{i}(n)$ generated by the IMC controller $W_\mathrm{i}(z)$. The result of the sum $y'(n)$ is fed to the secondary path $S(z)$. In parallel, $y'_\mathrm{i}(n)$ is convolved with a model of the secondary path $\hat{S}(z)$. The result of the convolution is used afterwards to negate the influence of the IMC in the error signal $e(n)$. By doing so, an estimate of the error left by the FF $\hat{e}_\mathrm{f}(n)$ is calculated. This estimate is used as input for $W_\mathrm{i}(z)$. Then the system's transfer function

$$H_\mathrm{fi}(z) = \frac{E(z)}{X(z)} = \frac{\big(P(z) - S(z)W_\mathrm{f}(z)\big) \cdot \big(1 - \hat{S}(z)W_\mathrm{i}(z)\big)}{1 + \big(S(z) - \hat{S}(z)\big)W_\mathrm{i}(z)} \tag{5.11}$$

yields the multiplicative combination of Eq. 2.1 and Eq. 4.7. So $W_\mathrm{f}(z)$ and $W_\mathrm{i}(z)$ can be designed independently. Nevertheless, for an adaptive implementation of $W_\mathrm{f}(z)$, the effective secondary path seen from its perspective

$$S_\mathrm{f}^\mathrm{fi}(z) = -\frac{E(z)}{Y'_\mathrm{f}(z)} = S(z)\frac{1 - \hat{S}(z)W_\mathrm{i}(z)}{1 + \big(S(z) - \hat{S}(z)\big)W_\mathrm{i}(z)} \tag{5.12}$$

has to be considered. As can be seen, now the effective secondary path has to be continuously monitored upon changes of $W_\mathrm{i}(z)$ and mismatches between $S(z)$ and $\hat{S}(z)$.

5.3.1. Alternative structure with dependent feedforward optimum

An alternative to the previous IMC-FF combination [Sen and Morgan, 1996, Johansson et al., 1997, Tseng et al., 1998, Chong et al., 2005, Wang et al., 2012] partially circumvents the monitoring of $\hat{S}_\mathrm{f}^\mathrm{lms}(z)$, based on a small change. The block diagram in Fig. 5.3b illustrates it. By adding first $y'_\mathrm{f}(n)$ and $y'_\mathrm{i}(n)$ and using the resulting $y'(n)$ for the convolution with $\hat{S}(z)$ in the IMC, the effective secondary path of FF changes to

$$S_\mathrm{f}^\mathrm{fido}(z) = -\frac{E(z)}{Y'_\mathrm{f}(z)} = \frac{S(z)}{1 + \big(S(z) - \hat{S}(z)\big)W_\mathrm{i}(z)}. \tag{5.13}$$

As a direct effect of this change, the effective secondary path is almost independent of $W_\mathrm{i}(z)$ and only the mismatch between $S(z)$ and $\hat{S}(z)$ has to be monitored. The change also alters the system's transfer function

$$H_\mathrm{fido}(z) = \frac{P(z) \cdot \big(1 - \hat{S}(z)W_\mathrm{i}(z)\big) - S(z)W_\mathrm{f}(z)}{1 + \big(S(z) - \hat{S}(z)\big)W_\mathrm{i}(z)}, \tag{5.14}$$

which now shows a dependency between the $W_\mathrm{f}(z)$ and $W_\mathrm{i}(z)$. If $H_\mathrm{fido}(z) = 0$ is set, the optimal solution for $W_\mathrm{f}(z)$

$$W_\mathrm{f}^\mathrm{opt}(z) = \frac{P(z)}{S(z)} \cdot \big(1 - \hat{S}(z)W_\mathrm{i}(z)\big) \tag{5.15}$$

can be derived. By comparing Eq. 5.15 with Eq. 2.32, one can see that the control performance achieved by the feedback controller $W_\mathrm{i}(z)$ changes the effective primary path, and with it the control effort of $W_\mathrm{f}(z)$. This influence may steer the FF optimum in the same way it was seen in Sec. 5.2.1.

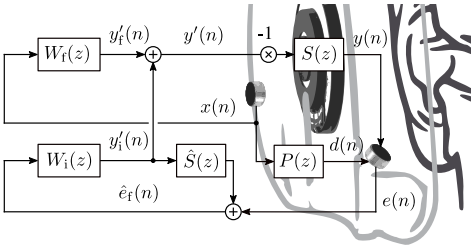

(a) *IMC-FF combination with independent optima*

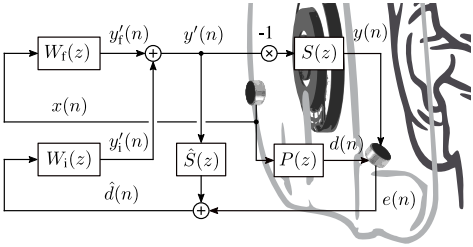

(b) *IMC-FF combination with dependent optima*

Figure 5.3.: Hybrid control structures involving the combination of the IMC with the FF approaches: (a) the structure with independent FF optimal controller, and (b) the structure with dependent FF optimal controller.

5.4. Summary

In this chapter an overview of the six possible combinations of the classical control structures for active noise control is presented. With MVC-IMC combinations one can have a system which performance is more robust to moving noise sources. Nevertheless, the stability analysis regarding deviations of the estimated secondary path from the real one is still to be developed. With IMC-FF combinations one could profit from two adaptive controllers working together. However, this requires a continuous monitoring of the effective secondary path, so that the adaptation of the FF controller remains stable. Finally, with MVC-FF combinations the stability and performance considerations rely on the analysis of the MVC only. Moreover, the MVC-FF combination with FF dependent optimum may steer the FF to find an optimal solution in frequency regions where this feedback approach is not effective anymore.

CHAPTER 6

Novel Control Structures

In the previous chapter it has been shown how the three classical active noise control structures can be combined in pairs into hybrid or pseudo-cascaded control systems. The increase in implementation complexity is compensated by the design-flexibility and higher attenuation levels they can achieve together. Although the advantages of these combinations are already well documented, more combination strategies are still not found in the literature. In the present chapter the combination of all three control structures into one system is described. The systems are based on two combination strategies. The first one is the so-called hybrid system principle, in which a feedforward and a feedback algorithm are combined to generate a single improved control system. The second one is the pseudo-cascading principle, in which feedback systems make a beforehand estimation of the residual error and use this information to calculate an improved control signal. The combination of all three control schemes offers at the same time three alternatives, which allow the design of the controllers in different dependency levels. A low dependency level allows the re-use of already existent ANC know-how, while a high dependency level offers the collective optimization of all controllers. All in all, the systems' flexibility and attenuation performance is improved with no need for extra microphones or loudspeakers.

In the following section, the pseudo-cascaded MVC-IMC feedback system proposed by Schumacher in [Schumacher et al., 2011] in its fully digital implementation [Rivera Benois et al., 2017] is used as the basis for the upcoming combination alternatives. Based on the analysis, stability and performance constraints are derived for the correct design and optimiza-

tion of its components. Afterwards, the block diagrams of the novel control structures are presented. This is directly followed by a transfer function derivation, which is going to be the base for establishing the dependency level that the system offers. Finally, optimal solutions for the feedforward controllers are derived and gradient estimations are calculated for its use on an adaptive control strategy.

6.1. Feedback Controller Inner Stability

The stability analysis presented here considers only the feedback components of the control structures that are presented in the following sections. Hence, the analysis applies also to the MVC-IMC combination with independent optima presented in Fig. 5.1a. Similarly to the case of the IMC, the stability analysis of the new control structure starts by first establishing the controller's inner stability. For this, the transfer function of its equivalent MVC controller $\tilde{W}(z)$ has to be derived. Considering an inactive disturbance ($x(n) = 0$ and $d(n) = 0$) and an open-loop analysis (no equation relating the error signal $e(n)$ as a function of the control signal $y(n)$) the equations

$$Y'(z) = Y'_{\mathrm{m}}(z) + Y'_{\mathrm{i}}(z), \tag{6.1}$$

$$Y'_{\mathrm{m}}(z) = W_{\mathrm{m}}(z)\big(\hat{Y}_{\mathrm{i}}(z) + E(z)\big), \tag{6.2}$$

$$Y'_{\mathrm{i}}(z) = W_{\mathrm{i}}(z)\big(\hat{Y}_{\mathrm{i}}(z) + E(z)\big), \tag{6.3}$$

and

$$\hat{Y}_{\mathrm{i}}(z) = \hat{S}(z)Y'_{\mathrm{i}}(z) \tag{6.4}$$

are derived. By using Eq. 6.4 to replace $\hat{Y}_{\mathrm{i}}(z)$ in Eq. 6.3

$$Y'_{\mathrm{i}}(z) = W_{\mathrm{i}}(z)\big(\hat{S}(z)Y'_{\mathrm{i}}(z) + E(z)\big) \tag{6.5}$$

$$\rightarrow Y'_{\mathrm{i}}(z) = \frac{W_{\mathrm{i}}(z)}{1 - \hat{S}(z)W_{\mathrm{i}}(z)}E(z) \tag{6.6}$$

the IMC control signal $Y'_{\mathrm{i}}(z)$ can be expressed as a function of the error signal $E(z)$. If this equation is used together with Eq. 6.4 to replace $\hat{Y}_{\mathrm{i}}(z)$ in Eq. 6.2

$$Y'_{\mathrm{m}}(z) = W_{\mathrm{m}}(z)\left(\frac{\hat{S}(z)W_{\mathrm{i}}(z)}{1 - \hat{S}(z)W_{\mathrm{i}}(z)}E(z) + E(z)\right) \tag{6.7}$$

$$\rightarrow Y'_{\mathrm{m}}(z) = \frac{W_{\mathrm{m}}(z)}{1 - \hat{S}(z)W_{\mathrm{i}}(z)}E(z), \tag{6.8}$$

then the same can be done for the MVC control signal $Y'_{\mathrm{m}}(z)$. Using this equation together with Eq. 6.6 to replace the MVC and IMC control signals in Eq. 6.1

$$Y'(z) = \frac{W_{\mathrm{m}}(z)}{1 - \hat{S}(z)W_{\mathrm{i}}(z)}E(z) + \frac{W_{\mathrm{i}}(z)}{1 - \hat{S}(z)W_{\mathrm{i}}(z)}E(z) \tag{6.9}$$

$$= \left(\frac{W_{\mathrm{m}}(z) + W_{\mathrm{i}}(z)}{1 - \hat{S}(z)W_{\mathrm{i}}(z)}\right)E(z) \tag{6.10}$$

the equivalent MVC controller transfer function

$$\tilde{W}_{\mathrm{m}}(z) = \frac{Y'(z)}{E(z)} = \frac{W_{\mathrm{m}}(z) + W_{\mathrm{i}}(z)}{1 - \hat{S}(z) \cdot W_{\mathrm{i}}(z)} \tag{6.11}$$

can be derived. As can be seen, the denominator of the equation is the same as the one found for the IMC controller in Eq. 4.11. Hence, the controller's inner stability of the present structure can be ensured by using an internally-stable IMC controller. For this, the same principles presented in Sec. 4.1 can be used.

6.2. Feedback System Stability

The stability of the feedback system in its closed-loop operation can be determined by the analysis of the system's transfer function in Eq. 5.1. Its denominator

$$C_{\mathrm{mi}}(z) = 1 + S(z)W_{\mathrm{m}}(z) + \big(S(z) - \hat{S}(z)\big)W_{\mathrm{i}}(z) \tag{6.12}$$

forms the characteristic equation. This is analyzed for its nominal form

$$\hat{C}_{\mathrm{mi}}(z) = 1 + S_0(z)W_{\mathrm{m}}(z), \tag{6.13}$$

under which the nominal secondary path $S_0(z) = S(z)$ and the estimated secondary path $\hat{S}(z) = S(z)$ are equal to the real one. If this characteristic equation is compared to the one of the MVC controller case in Eq. 3.16, it can be seen that they are equal. Therefore, the system's nominal stability constraint can be fulfilled by using a nominally stable MVC controller. For details about the MVC nominal stability refer to Sec. 3.2.

Given that the system is nominally stable, its robust stability can be analyzed. For it, the multiplicative uncertainty model of the secondary path in Eq. 3.44 is used. Replacing $S(z)$ with Eq. 3.44 in Eq. 6.12, the characteristic equation

$$C_{\mathrm{mi}} = 1 + S_0 \cdot W_{\mathrm{m}} + S_0 \cdot G_2 \cdot \Delta \cdot \big(W_{\mathrm{m}} + W_{\mathrm{i}}\big) \tag{6.14}$$

can be formulated. The argument $j\Omega_k$ is omitted in this and in further equations. Thus, the number of unstable roots

$$Z_{C_{\mathrm{mi}},\bar{c}} = N^{\mathrm{cw}}_{O_{\mathrm{mi}}} - N^{\mathrm{ccw}}_{O_{\mathrm{mi}}} \tag{6.15}$$

equals the number of clockwise encirclement of the Nyquist point made by the sub-contours of the open-loop

$$O_{\mathrm{mi}} = S_0 \cdot W_{\mathrm{m}} + S_0 \cdot G_2 \cdot \Delta \cdot \left(W_{\mathrm{m}} + W_{\mathrm{i}}\right) \tag{6.16}$$

evaluated on the unit circle $N^{\mathrm{cw}}_{O_{\mathrm{mi}}(j\Omega_k)}$, minus the counter-clockwise ones $N^{\mathrm{ccw}}_{O_{\mathrm{mi}}(j\Omega_k)}$. Under this consideration, the robust stability of the system can be ensured by imposing the constraint

$$\left|1 + S_0 \cdot W_{\mathrm{m}}\right| > G_2 \cdot \left|S_0 \cdot \left(W_{\mathrm{m}} + W_{\mathrm{i}}\right)\right|. \tag{6.17}$$

Its left-hand side corresponds to the distance from the nominal contour to the point $(-1, 0)$ and the right-hand side corresponds to the discs' radii weighted by the multiplicative uncertainty $G_2(\Omega_k)$. If $W_{\mathrm{m}}(j\Omega_k)$ is set to zero, then this robust stability constraint simplifies to the one of the IMC controller in Eq. 4.23. If on the other hand $W_{\mathrm{i}}(j\Omega_k)$ is set to zero, then this robust stability constraint simplifies to the one of the MVC controller in Eq. 3.50. Hence, for this constraint to be fulfilled it is necessary, but it is not sufficient, that both the MVC and the IMC controller are robust stable.

6.3. Feedback System Disturbance Enhancement

As part of the design of the combined controller, the disturbance amplification that the waterbed-effect is allowed to produce has to be controlled. As it has been stated before, since this is a feedback controller analysis, the feedforward part of the combined controller is not considered here. Hence, for the analysis the frequency response of the MVC-IMC combination with independent controllers from Eq. 5.1 is used

$$\left|\frac{1 - \hat{S} \cdot W_{\mathrm{i}}}{1 + S \cdot W_{\mathrm{m}} + \left(S - \hat{S}\right) W_{\mathrm{i}}}\right| \leq G_3, \tag{6.18}$$

instead of the one of the whole $H_{\mathrm{fim}}(j\Omega_k)$. In a first nominal analysis, where $S(j\Omega_k) = S_0(j\Omega_k)$ and $\hat{S}(j\Omega_k) = S_0(j\Omega_k)$ hold, this inequality takes the form

$$\left|\frac{1 - S_0 \cdot W_{\mathrm{i}}}{1 + S_0 \cdot W_{\mathrm{m}}}\right| \leq G_3. \tag{6.19}$$

Here, the nominal transfer functions of both subsystems can be seen. Given that the system is nominally stable, both sides of the inequality are mul-

tiplied by the denominator of the left-hand side

$$\left|1 - S_0 \cdot W_\mathrm{i}\right| \leq G_3 \left|1 + S_0 \cdot W_\mathrm{m}\right| \tag{6.20}$$

so that the nominal performance constraint can be found. If $W_\mathrm{m}(j\Omega_k)$ is set to zero, then this nominal performance constraint simplifies to the one of the IMC controller in Eq. 4.25. If on the other hand $W_\mathrm{i}(j\Omega_k)$ is set to zero, then this nominal performance constraint simplifies to the one of the MVC controller in Eq. 3.54. Hence, for this constraint to be fulfilled it is necessary but not sufficient, that both the MVC and the IMC controller meet the amplification limit $G_3(\Omega_k)$ under nominal conditions.

In order to establish a constraint for the robust analysis, the multiplicative uncertainty model of the secondary path in Eq. 3.44 is used in Eq. 6.18 and the estimated secondary path $\hat{S}(j\Omega_k)$ is set to the nominal one $S_0(j\Omega)$

$$\left| \frac{1 - S_0 \cdot W_\mathrm{i}}{1 + S_0 \cdot W_\mathrm{m} + S_0 \cdot G_2 \cdot \Delta \cdot \left(W_\mathrm{m} + W_\mathrm{i}\right)} \right| \leq G_3. \tag{6.21}$$

Both sides of the equation are divided by $G_3(\Omega_k)$ and, provided that the system is robustly stable, multiplied by the denominator of the left-hand side

$$\frac{1}{G_3}\left|1 - S_0 \cdot W_\mathrm{i}\right| \leq \left|1 + S_0 \cdot W_\mathrm{m} + S_0 \cdot G_2 \cdot \Delta \cdot \left(W_\mathrm{m} + W_\mathrm{i}\right)\right|. \tag{6.22}$$

Then, the most restrictive case

$$\frac{1}{G_3}\left|1 - S_0 \cdot W_\mathrm{i}\right| \leq \left|1 + S_0 \cdot W_\mathrm{m}\right| - G_2 \cdot \left|S_0 \cdot \left(W_\mathrm{m} + W_\mathrm{i}\right)\right| \tag{6.23}$$

is taken in order to find the robust performance constraint of the controller. Once again it is found that, if $W_\mathrm{i}(j\Omega_k)$ is set to zero, then the constraint simplifies to the one of the MVC controller in Eq. 3.56. Equivalently, if $W_\mathrm{m}(j\Omega_k)$ is set to zero, then the constraint simplifies to the one of the IMC controller in Eq. 4.31. Hence, for this constraint to be fulfilled it is necessary but not sufficient, that both the MVC and the IMC controller meet their individual robust performance constraints.

Other constraints One consideration for the digital implementation is to limit the gain of the controller. This is done not only for security purposes, but also to avoid the amplification of the ADC's noise floor to a level that is audible. This can be done by comparing the magnitude response of the equivalent MVC controller $\tilde{W}_\mathrm{m}(j\Omega_k)$ to the one of a maximum gain curve

$$\left|\tilde{W}_\mathrm{m}\right| \leq G_4, \tag{6.24}$$

where $G_4(\Omega_k)$ can be chosen as an inverted noise weighting curve or as a constant value. In order to use this constraint during the optimization of the system's parameters, Eq. 6.11 is used to replace $\tilde{W}_\mathrm{m}(j\Omega_k)$

$$\left|\frac{W_\mathrm{m}+W_\mathrm{i}}{1-\hat{S}\cdot W_\mathrm{i}}\right| \leq G_4. \tag{6.25}$$

If the IMC controller is internally stable, then both sides can be multiplied by the denominator of the left-hand side

$$\left|W_\mathrm{m}+W_\mathrm{i}\right| \leq G_4\left|1-\hat{S}\cdot W_\mathrm{i}\right|, \tag{6.26}$$

to yield the constraint for maximum gain of the equivalent MVC controller.

6.4. Feedback Controller Optimization

In this section the design of the impulse responses $\mathbf{w}_\mathrm{m}(n)$ and $\mathbf{w}_\mathrm{i}(n)$ is formulated as a cost function minimization subject to the constraints described above. The cost function is based on the magnitude frequency response of the *nominal* system

$$\left|\hat{H}_\mathrm{mi}\right| = \left|\frac{1-S_0\cdot W_\mathrm{i}}{1+S_0\cdot W_\mathrm{m}}\right|, \tag{6.27}$$

from which the natural logarithm is calculated

$$\log\left|\hat{H}_\mathrm{mi}\right| = \log\left|1-S_0\cdot W_\mathrm{i}\right| - \log\left|1+S_0\cdot W_\mathrm{m}\right|. \tag{6.28}$$

A calculation of dB-values is also possible here, although it has no influence on the results obtained. Subsequently, the discrete frequencies are weighted by means of $G_1(\Omega_k)$ and accumulated between the frequencies of interest

$$C_\mathrm{mvc\text{-}imc}(\mathbf{w}_\mathrm{m},\mathbf{w}_\mathrm{i}) = \frac{2}{k_\mathrm{h}-k_\mathrm{l}+1}\sum_{k=k_\mathrm{l}}^{k_\mathrm{h}} G_1(\Omega_k)\log\left|\hat{H}_\mathrm{mi}(j\Omega_k)\right|. \tag{6.29}$$

Here, k_l and k_h are the FFT frequency indices related to the lowest frequency f_l and highest frequency f_h of interest, respectively. In this way both controllers can be optimized simultaneously. However, there is no guarantee that a local optimum will yield the global one, because the calculation of the logarithm in the cost function breaks the quadratic dependency with respect to the parameters.

Constraints In order to help the optimization algorithm achieve its goal, the constraints have to be formulated such that they build a squared de-

pendency with respect to the optimization parameters. As it is already explained in the above sections, the inner controller stability depends solely on the IMC's inner stability (see Sec. 4.5). Furthermore, the feedback system's nominal stability depends on the MVC's nominal stability (see Sec. 3.4).

The system's robust stability constraint in Eq. 6.17 is re-written as

$$\left|1 + S_0 \cdot W_\mathrm{m}\right|^2 > G_2^2 \cdot \left|S_0 \cdot \left(W_\mathrm{m} + W_\mathrm{i}\right)\right|^2. \tag{6.30}$$

The nominal performance constraint in Eq. 6.20 is re-formulated as

$$\left|1 - S_0 \cdot W_\mathrm{i}\right|^2 \leq G_3^2 \left|1 + S_0 \cdot W_\mathrm{m}\right|^2, \tag{6.31}$$

and the robust performance constraint in Eq. 6.23 as

$$\begin{aligned} &\frac{1}{G_3^2}\left|1 - S_0 \cdot W_\mathrm{i}\right|^2 \leq \left|1 + S_0 \cdot W_\mathrm{m}\right|^2 \\ &-2 \cdot G_2 \left|S_0 \cdot \left(W_\mathrm{m} + W_\mathrm{i}\right)\right| \left|1 + S_0 \cdot W_\mathrm{m}\right| + G_2^2 \left|S_0 \cdot \left(W_\mathrm{m} + W_\mathrm{i}\right)\right|^2. \end{aligned} \tag{6.32}$$

The maximum equivalent MVC gain constraint from Eq. 6.26 is written as

$$\left|W_\mathrm{m} + W_\mathrm{i}\right|^2 \leq G_4^2 \left|1 - \hat{S} \cdot W_\mathrm{i}\right|^2. \tag{6.33}$$

Similarly as with the optimizations of the single controller impulse responses, $\mathbf{w}_\mathrm{i}$ and $\mathbf{w}_\mathrm{m}$, these constraints are evaluated only on the positive frequencies of interest.

6.4.1. Optimization results

The optimization results presented in this section were obtained using the nonlinear programming solver `fmincon()` together with the SQP algorithm from the MATLAB 2019a optimization toolbox. The parameters `MaxIterations` and `MaxFunctionEvaluations` were set to $\max(400, L_\mathrm{m} + L_\mathrm{i})$ and $400 \cdot (L_\mathrm{m} + L_\mathrm{i})$, respectively. Although, all the optimizations found the optimal solution before reaching these iteration limits. The starting solution for the coefficients' optimization is set to zero. The sampling frequency $f_s = 48\,\mathrm{kHz}$ and the FFT length $N = 8192$ were chosen. In Fig. 3.12 the frequency-dependent parameters used during the optimization are presented, which are the same ones utilized during the optimization of the MVC and IMC controllers. The MVC's nominal stability constraint based on the hyperbolic boundary intersects the x-axis at the point $(-0.8, 0)$ and has its foci at $(-2, 0)$ and $(2, 0)$. The IMC's inner stability constraint based on the vertical boundary intersects the x-axis at the point $(0.9, 0)$. These constraints are already known to the reader from the past chapters and therefore, are not further analyzed here.

Design constraints The effect of the constraints over the optimal solution is presented in Fig. 6.1 following an increasingly restrictive order. For this, a constant cost function bandwidth ($f_\mathrm{l} = 0\,\mathrm{Hz}$ and $f_\mathrm{h} = 3\,\mathrm{kHz}$), and a constant controller impulse response length ($L_m = 64$ and $L_i = 64$) are used. It can be seen from $H_\mathrm{mi}(f)\big|G_4$ that when the system is subject to the equivalent MVC controller's maximum gain limit $G_4(\Omega)$ an attenuation bandwidth of 1.7 kHz with attenuation levels between 20 dB and 40 dB can be achieved. However, an amplification region between 1.7 kHz and 5 kHz with a peak value of 23 dB is produced, too. If the disturbance enhancement constraint based on $G_3(\Omega)$ is imposed on the system's sensitivity function $H_\mathrm{mi}(f)$, then this amplification region falls under the threshold of 3 dB. However, it is seen in $H_\mathrm{mi}(f)\big|G_3G_4$ that, because of the waterbed-effect, the attenuation bandwidth decreases from 1.7 kHz to 900 Hz and that the the achieved attenuation drops by 7-20 dB. If the robust stability constraint based on the secondary path multiplicative uncertainty $G_2(\Omega)$ is enforced, then less attenuation is achieved between 128 and 714 Hz, most probably because of the increase in uncertainty that $G_2(\Omega)$ has between 300 and 700 Hz. Nevertheless, the attenuation is improved outside this frequency range, which extends the attenuation bandwidth to 1.2 kHz. At last, if the robust performance constraint is imposed, then it can be seen from $H_\mathrm{mi}(f)\big|G_2G_{3(2)}G_4$, that an important magnitude in attenuation is lost together with a decrease in attenuation bandwidth from 1.2 kHz to 1 kHz. Nevertheless, the amplification in the mid- and high-frequencies decreases to levels around the 1.5 dB.

Combination of sensitivity functions The multiplicative effect that the connection strategy of this pseudo-cascaded control structure has over the sensitivity function of its sub-structures is investigated. For this purpose, the curve $H_\mathrm{mi}(f)\big|G_2G_3G_4$ from Fig. 6.1 is presented together with the sensitivity functions of its MVC and IMC sub-control structures in Fig. 6.2. Here, the combination of the sensitivity functions $H_\mathrm{m}(f)$ and $H_\mathrm{i}(f)$ can be analyzed in three frequency ranges: first, the low-frequency range from approx. 30 to 400 Hz, where both sub-structures' attenuation is combined to achieved a higher one in $H_\mathrm{mi}(f)$; then, a mid-frequency range starting approx. at 400 Hz and ending at 1.2 kHz, where the MVC shows a dominant attenuation performance, which is then shaped by the IMC's influence; finally, a high-frequency range starting at 1.2 kHz and continuing thereof, in which both sensitivity functions oscillate opposite to each other around a level of 1.5 dB, from which the achieved collective amplification of 3 dB is reached.

Controllers' impulse response length The effect of the controllers' impulse response length is investigated. For this purpose, the system is

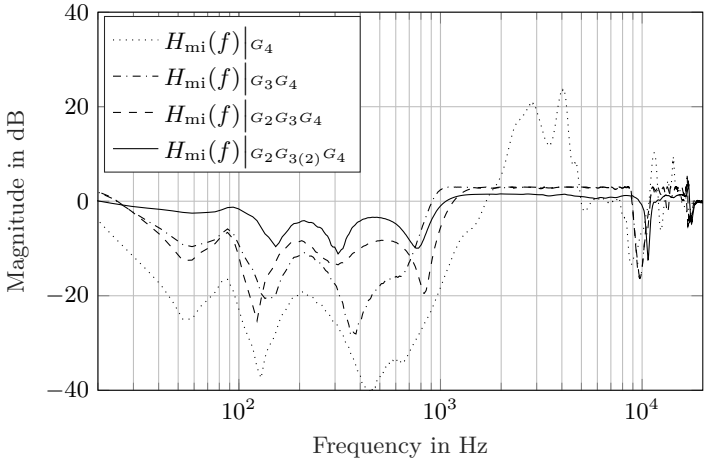

Figure 6.1.: Development of the optimal sensitivity function $H_{\mathrm{mi}}(f)$ when constraints are enforced in increasingly restrictive order. The IMC vertical boundary intersection is set to $(0.9, 0)$ and the MVC hyperbolic boundary intersection to $(-0.8, 0)$ and foci to $(-2, 0)$ and $(2, 0)$. Parameters: $f_s = 48\,\mathrm{kHz}$, $N = 8192$, $L_{m,i} = 64$, $f_{\mathrm{l}} = 0\,\mathrm{Hz}$, $f_{\mathrm{h}} = 3\,\mathrm{kHz}$.

subject to the maximum gain, robust stability and nominal performance constraints, and only the length of the controllers is varied. The results achieved are presented in Fig. 6.3. From $H_{\mathrm{mi}}(f)\big|L_{\mathrm{m,i}}{=}4$ it can be seen that with lengths as short as 4 coefficients each, an attenuation of around 10 dB can be achieved for frequencies below 200 Hz, with an attenuation bandwidth of up to approx. 1.9 kHz. This is achieved with a disturbance enhancement that is inferior to the one of higher order controllers. If the length of the controllers is incremented to 16 coefficients, then an improvement in attenuation magnitude is seen between 100 Hz and 1.2 kHz. This enables the controller to reach 15 dB of attenuation at 700 Hz. The improvement comes with a loss in the attenuation bandwidth from 1.9 kHz to 1.3 kHz. If the length of the controllers is incremented to 64 coefficients, then the attenuation bandwidth decreases to approx. 1.2 kHz and the attenuation reached below 60 Hz decreases as well. In exchange the attenuation of around 10 dB is extended from 40 Hz up to 1 kHz, reaching peak values of approx. 25 dB. The disturbance enhancement produces a relatively flat plateau starting at 1.4 kHz and ending at 8.6 kHz.

Pseudo-cascaded compared to single optimized systems In order to establish in which extent the pseudo-cascaded system may offer an advan-

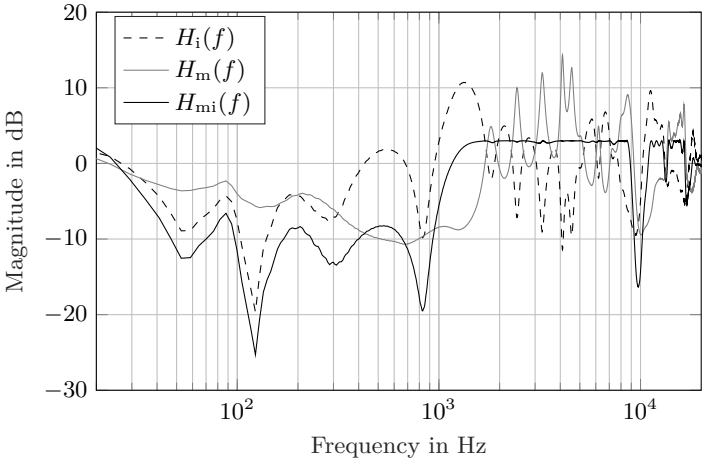

Figure 6.2.: Development of the optimal sensitivity function $H_{\mathrm{mi}}(f)$ as a combination of the sensitivity functions of its MVC and IMC controllers. The optimization is subject to the constraint combination $G_2 G_3 G_4$. The IMC vertical boundary intersection is set to $(0.9, 0)$ and the MVC hyperbolic boundary intersection to $(-0.8, 0)$ and foci to $(-2, 0)$ and $(2, 0)$. Parameters: $f_s = 48\,\mathrm{kHz}$, $N = 8192$, $L_{m,i} = 64$, $f_{\mathrm{l}} = 0\,\mathrm{Hz}$, $f_{\mathrm{h}} = 3\,\mathrm{kHz}$.

tage over the MVC and the IMC formulations, the three systems are compared using equivalent controller lengths. This means that, if the pseudo-cascaded system uses two controllers with 4 coefficients each, then the MVC and the IMC counterparts will use a controller of 8 coefficients. Of course, this comparison is only fair when comparing the pseudo-cascaded system with the IMC, because both make use of an estimated secondary path. Nevertheless, an optimum MVC controller serves as a reference of an efficient solution. As a first set of solutions for comparison, Fig. 6.4 is presented. The pseudo-cascaded system uses two controllers with 4 coefficients each, whereas the IMC and the MVC a controller of length 8 each. Here it can be seen that the important differences between the three approaches are concentrated in the frequencies below 200 Hz, whereas beyond this frequency, all three behave very similarly. Below 200 Hz the MVC produces an attenuation that shows an increment towards the low-frequencies, which allows it to achieve a higher attenuation at frequencies below 26 Hz. The IMC and the pseudo-cascaded solutions follow a very similar behavior, producing strong attenuation at 50 Hz and 100 Hz. The pseudo-cascaded system shows a constant higher attenuation of 2-3 dB when compared to the IMC.

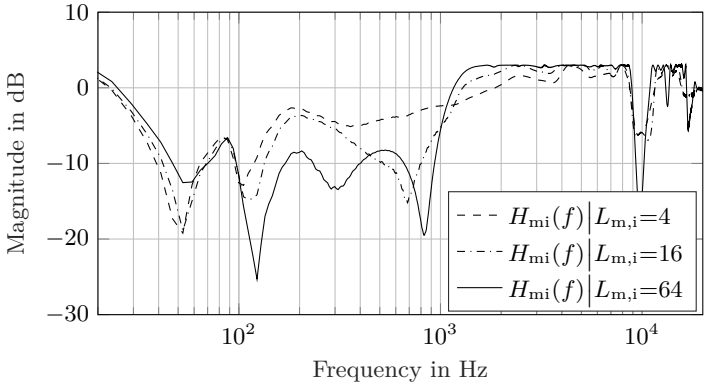

Figure 6.3.: Optimum sensitivity functions obtained with different impulse response lengths L_i and L_m. The optimization is subject to the constraint combination $G_2G_3G_4$. The IMC vertical boundary intersection is set to $(0.9, 0)$ and the MVC hyperbolic boundary intersection to $(-0.8, 0)$ and foci to $(-2, 0)$ and $(2, 0)$. Parameters: $f_\mathrm{s} = 48\,\mathrm{kHz}$, $N = 8192$, $f_\mathrm{l} = 0\,\mathrm{Hz}$, $f_\mathrm{h} = 3\,\mathrm{kHz}$.

As a second set of solutions for comparison, Fig. 6.5 is presented. For the optimizations, the length of the impulse responses has been increased by a factor 16. In the graph it can be seen, that in the low-frequencies a stop-band is being produced, followed by a transition band around the 1 kHz, which finishes in a 3 dB pass-band that extends up to 8.6 kHz. In the stop-band all three approaches show a ripple effect, with peaks and notches located at (almost) the same frequencies. The deepest notches are produced by the IMC and pseudo-cascaded systems, of which the latter shows the highest attenuation magnitude. Only between 300 and 400 Hz there is an inversion, due to the IMC transition band. The MVC shows a similar behavior to the pseudo-cascaded system, but an incapability to produce attenuation levels higher than 15 dB. This is probably because the pseudo-cascaded system still has a comparative advantage because of its recursive nature through the use of the secondary path.

6.5. Novel Control Structure with Low Dependency Level

In this section a feedforward controller $W_\mathrm{f}(z)$ is combined with the pseudo-cascaded feedback controller analyzed in the previous sections into the FF-IMC-MVC structure, from now on called FIM. The goal of this structure is to combine the nominal transfer functions of its sub-structures in a multiplicative way, i.e. $\hat{H}_\mathrm{fim}(z) = \hat{H}_\mathrm{f}(z) \cdot \hat{H}_\mathrm{i}(z) \cdot H_\mathrm{m}(z)$. To achieve this, the

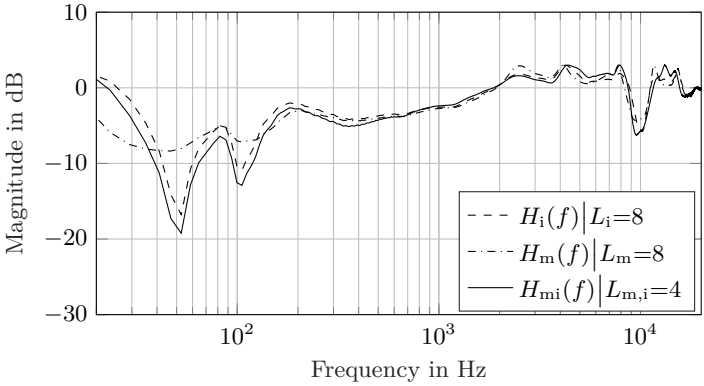

Figure 6.4.: Comparison of the optimal sensitivity function of the pseudo-cascaded system $H_{\mathrm{mi}}(f)$ with the optimal sensitivity functions of an MVC and an IMC controllers having the same combined impulse response lengths. The optimization is subject to the constraint combination $G_2G_3G_4$. The IMC vertical boundary intersection is set to $(0.9, 0)$ and the MVC hyperbolic boundary intersection to $(-0.8, 0)$ and foci to $(-2, 0)$ and $(2, 0)$. Parameters: $f_s = 48\,\mathrm{kHz}$, $N = 8192$, $f_{\mathrm{l}} = 0\,\mathrm{Hz}$, $f_{\mathrm{h}} = 3\,\mathrm{kHz}$.

structure presented in Fig. 6.6 is proposed. As can be seen, the pseudo-cascaded feedback system is based on the MVC-IMC combination with independent optima from Fig. 5.1a. Moreover, if the MVC-IMC subsystem is conceptually encapsulated into a single block, it can be seen from Fig. 5.2a that the feedforward and feedback systems are combined following the MVC-FF combination strategy with independent optima. Hence, it is expected that the controllers are independent from each other. To corroborate this hypothesis, a transfer function analysis has to be performed. From Fig. 6.6, the equations

$$E(z) = D(z) - Y(z) \tag{6.34}$$

$$D(z) = P(z)X(z) \tag{6.35}$$

$$Y(z) = S(z)\big(Y_{\mathrm{f}}'(z) + Y_{\mathrm{i}}'(z) + Y_{\mathrm{m}}'(z)\big) \tag{6.36}$$

$$Y_{\mathrm{f}}'(z) = W_{\mathrm{f}}(z)X(z) \tag{6.37}$$

$$Y_{\mathrm{m}}'(z) = W_{\mathrm{m}}(z)\big(\hat{S}(z)Y_{\mathrm{i}}'(z) + E(z)\big) \tag{6.38}$$

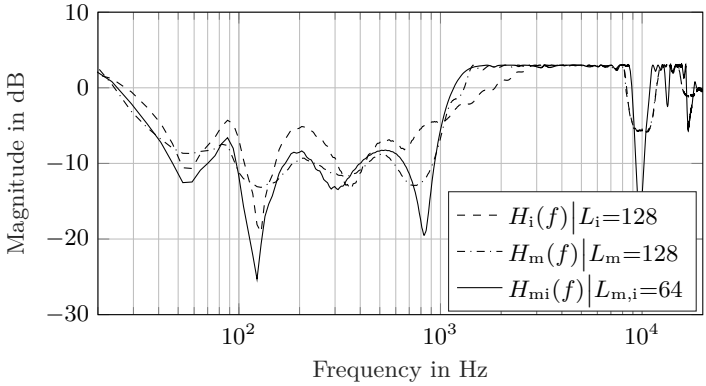

Figure 6.5.: Comparison of the optimal sensitivity function of the pseudo-cascaded system $H_\mathrm{mi}(f)$ with the optimal sensitivity functions of an MVC and an IMC controllers having the same combined impulse response lengths. The optimization is subject to the constraint combination $G_2G_3G_4$. The IMC vertical boundary intersection is set to $(0.9, 0)$ and the MVC hyperbolic boundary intersection to $(-0.8, 0)$ and foci to $(-2, 0)$ and $(2, 0)$. Parameters: $f_\mathrm{s} = 48\,\mathrm{kHz}$, $N = 8192$, $f_\mathrm{l} = 0\,\mathrm{Hz}$, $f_\mathrm{h} = 3\,\mathrm{kHz}$.

and

$$Y_\mathrm{i}'(z) = W_\mathrm{i}(z)\big(\hat{S}(z)Y_\mathrm{i}'(z) + E(z)\big) \tag{6.39}$$

$$\rightarrow Y_\mathrm{i}'(z) = \frac{W_\mathrm{i}(z)}{1 - \hat{S}(z)W_\mathrm{i}(z)}E(z) \tag{6.40}$$

are derived. Using Eq. 6.40 to replace Y_i' in Eq. 6.38

$$Y_\mathrm{m}'(z) = W_\mathrm{m}(z)\left(\frac{\hat{S}(z)W_\mathrm{i}(z)}{1 - \hat{S}(z)W_\mathrm{i}(z)}E(z) + E(z)\right), \tag{6.41}$$

the MVC control signal

$$Y_\mathrm{m}'(z) = \frac{W_\mathrm{m}(z)}{1 - \hat{S}(z)W_\mathrm{i}(z)}E(z) \tag{6.42}$$

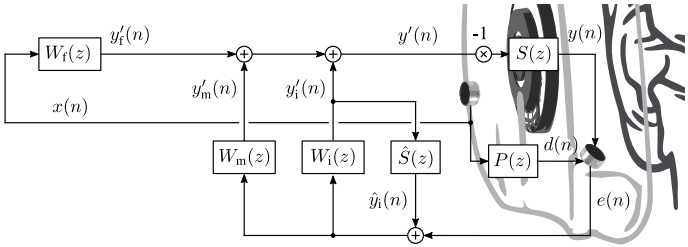

Figure 6.6.: Novel hybrid control structure with independent optima.

can be formulated as a function of the error signal $E(z)$. Using Eq. 6.37, Eq. 6.40, and Eq. 6.42 to replace the individual control signals in Eq. 6.36

$$Y(z) = S(z)\left(W_\mathrm{f}(z)X(z) + \frac{W_\mathrm{i}(z)}{1-\hat{S}(z)W_\mathrm{i}(z)}E(z) + \frac{W_\mathrm{m}(z)}{1-\hat{S}(z)W_\mathrm{i}(z)}E(z)\right), \tag{6.43}$$

the system's control signal

$$Y(z) = S(z)\left(W_\mathrm{f}(z)X(z) + \frac{W_\mathrm{i}(z)+W_\mathrm{m}(z)}{1-\hat{S}(z)W_\mathrm{i}(z)}E(z)\right) \tag{6.44}$$

can be formulated as a function of the reference signal $X(z)$ and the residual error $E(z)$. By using Eq. 6.44 and Eq. 6.35 in Eq. 6.34

$$E = P\cdot X - S\left(W_\mathrm{f}\cdot X + \frac{W_\mathrm{i}+W_\mathrm{m}}{1-\hat{S}\cdot W_\mathrm{i}}E\right) \tag{6.45}$$

$$\rightarrow E = \left(P - S\cdot W_\mathrm{f}\right)X - S\left(\frac{W_\mathrm{i}+W_\mathrm{m}}{1-\hat{S}\cdot W_\mathrm{i}}\right)E \tag{6.46}$$

$$\rightarrow \left(P - S\cdot W_\mathrm{f}\right)X = E\left(\frac{1-\hat{S}\cdot W_\mathrm{i}+S\cdot W_\mathrm{i}+S\cdot W_\mathrm{m}}{1-\hat{S}\cdot W_\mathrm{i}}\right) \tag{6.47}$$

$$\rightarrow \left(P - S\cdot W_\mathrm{f}\right)X = E\left(\frac{1+\left(S-\hat{S}\right)W_\mathrm{i}+S\cdot W_\mathrm{m}}{1-\hat{S}\cdot W_\mathrm{i}}\right) \tag{6.48}$$

the system's transfer function can be derived

$$H_\mathrm{fim}(z) = \frac{E(z)}{X(z)} = \frac{\left(1-\hat{S}(z)W_\mathrm{i}(z)\right)\left(P(z)-S(z)W_\mathrm{f}(z)\right)}{1+S(z)W_\mathrm{m}(z)+\left(S(z)-\hat{S}(z)\right)W_\mathrm{i}(z)}. \tag{6.49}$$

It can be seen by comparing this equation with the transfer functions of the MVC-IMC combination in Eq. 5.1 and of the FF system in Eq. 2.1, that this structure yields the multiplicative combination of the transfer

functions of all control schemes. In cases in which $\hat{S}(z) = S(z)$ holds, the transfer function simplifies to its nominal form

$$\hat{H}_{\mathrm{fim}}(z) = \frac{1 - S(z)W_{\mathrm{i}}(z)}{1 + S(z)W_{\mathrm{m}}(z)}\big(P(z) - S(z)W_{\mathrm{f}}(z)\big). \tag{6.50}$$

From the nominal transfer function one can see that in a context in which the secondary path is perfectly known, each one of the controllers can be designed independently. For example, the feedforward controller can be derived based only on the primary and secondary path, thus, minimizing only its own transfer function. The next section investigates to which extent the independent optimization of the feedforward controller is possible.

6.5.1. The optimal feedforward controller

Given that the feedback components of the system have been designed, the optimal feedforward controller can be calculated. Its derivation is based on the nominal transfer function of the system in Eq. 6.50, in which it is assumed that the estimated and nominal secondary paths are equal to the real one. The transfer function is used to express the error signal

$$E(z) = \frac{1 - S(z)W_{\mathrm{i}}(z)}{1 + S(z)W_{\mathrm{m}}(z)}\big(P(z)X(z) - S(z)W_{\mathrm{f}}(z)X(z)\big) \tag{6.51}$$

as a function of the reference signal $X(z)$ and the controllers $W_{\mathrm{i}}(z)$, $W_{\mathrm{m}}(z)$, and $W_{\mathrm{f}}(z)$. The equality $D(z) = P(z)X(z)$ is used

$$E(z) = \frac{1 - S(z)W_{\mathrm{i}}(z)}{1 + S(z)W_{\mathrm{m}}(z)}\big(D(z) - S(z)W_{\mathrm{f}}(z)X(z)\big), \tag{6.52}$$

in order to include the disturbance signal $D(z)$ in the stochastic excitation analysis later on. It can be seen from Eq. 6.52 that the feedback subsystems produce the same coloration in the disturbance signal $D(z)$ as in the control signal coming from the feedforward controller $W_{\mathrm{f}}(z)$. The nominal transfer function of the IMC controller (re-written from Eq. 4.7)

$$\hat{H}_{\mathrm{i}}(z) = 1 - S(z)W_{\mathrm{i}}(z) \tag{6.53}$$

and the transfer function of the MVC controller (re-written from Eq. 3.2)

$$H_{\mathrm{m}}(z) = \frac{1}{1 - S(z)W_{\mathrm{m}}(z)} \tag{6.54}$$

are used to replace their contributions in Eq. 6.52

$$E(z) = \hat{H}_{\mathrm{i}}(z)H_{\mathrm{m}}(z)\big(D(z) - S(z)W_{\mathrm{f}}(z)X(z)\big). \tag{6.55}$$

Now, as already discussed in Sec. 2.3, the search for an optimum controller in the Z-domain may yield a controller $W_\mathrm{f}(z)$ that is non-causal or non-stable, or both. Therefore, in order to find the finite impulse response of the causal feedforward controller $\mathbf{w}_\mathrm{f}$ the notation and considerations presented in Sec. 2.3.1 are used. As a first step, the equation is re-written

$$\mathbf{e} = \mathbf{H}_\mathrm{i} \cdot \mathbf{H}_\mathrm{m} \cdot \mathbf{d}_\mathrm{zp} - \mathbf{H}_\mathrm{i} \cdot \mathbf{H}_\mathrm{m} \cdot \mathbf{S} \cdot \mathbf{W}_\mathrm{f} \cdot \mathbf{x}, \tag{6.56}$$

in its equivalent vector-matrix form based on the signals' vectors and systems' impulse responses and Toeplitz matrices. Considering linearity and time invariance, this is rearranged as

$$\mathbf{e} = \mathbf{D}_\mathrm{zp} \cdot \mathbf{H}_\mathrm{i} \cdot \mathbf{h}_\mathrm{m} - \mathbf{X} \cdot \mathbf{H}_\mathrm{i} \cdot \mathbf{H}_\mathrm{m} \cdot \mathbf{S} \cdot \mathbf{w}_\mathrm{f}. \tag{6.57}$$

Using this equation, the optimization's cost function is defined as the expectation of the quadratic error $\mathbb{E}[\mathbf{e}^\mathrm{T}\mathbf{e}]$. In order to find the controller's finite impulse response $\mathbf{w}_\mathrm{f}$ that minimizes this cost function, its gradient with respect to the impulse response coefficients is calculated

$$\frac{\partial \mathbb{E}[\mathbf{e}^\mathrm{T}\mathbf{e}]}{\partial \mathbf{w}_\mathrm{f}} = -2 \cdot \mathbb{E}[(\mathbf{D}_\mathrm{zp} \cdot \mathbf{H}_\mathrm{i} \cdot \mathbf{h}_\mathrm{m} - \mathbf{X} \cdot \mathbf{H}_\mathrm{i} \cdot \mathbf{H}_\mathrm{m} \cdot \mathbf{S} \cdot \mathbf{w}_\mathrm{f})^\mathrm{T} \mathbf{X} \cdot \mathbf{H}_\mathrm{i} \cdot \mathbf{H}_\mathrm{m} \cdot \mathbf{S}] \tag{6.58}$$

and equated to zero. If the transpose of both sides is taken

$$\mathbf{S}^\mathrm{T} \cdot \mathbf{H}_\mathrm{m}^\mathrm{T} \cdot \mathbf{H}_\mathrm{i}^\mathrm{T} \cdot \mathbb{E}\left[\mathbf{X}^\mathrm{T} \cdot \mathbf{X}\right] \cdot \mathbf{H}_\mathrm{i} \cdot \mathbf{H}_\mathrm{m} \cdot \mathbf{S} \cdot \mathbf{w}_\mathrm{f}^\mathrm{opt} = \mathbf{S}^\mathrm{T} \cdot \mathbf{H}_\mathrm{m}^\mathrm{T} \cdot \mathbf{H}_\mathrm{i}^\mathrm{T} \cdot \mathbb{E}\left[\mathbf{X}^\mathrm{T} \cdot \mathbf{D}_\mathrm{zp}\right] \cdot \mathbf{H}_\mathrm{i} \cdot \mathbf{h}_\mathrm{m} \tag{6.59}$$

the equality fulfilled by the optimal controller's finite impulse response $\mathbf{w}_\mathrm{f}^\mathrm{opt}$ can be formulated. Based on Eq. 2.46 and Eq. 2.47

$$\mathbf{S}^\mathrm{T} \cdot \mathbf{H}_\mathrm{m}^\mathrm{T} \cdot \mathbf{H}_\mathrm{i}^\mathrm{T} \cdot \mathbf{\Phi}_{xx} \cdot \mathbf{H}_\mathrm{i} \cdot \mathbf{H}_\mathrm{m} \cdot \mathbf{S} \cdot \mathbf{w}_\mathrm{f}^\mathrm{opt} = \mathbf{S}^\mathrm{T} \cdot \mathbf{H}_\mathrm{m}^\mathrm{T} \cdot \mathbf{H}_\mathrm{i}^\mathrm{T} \cdot \mathbf{\Phi}_{dx} \cdot \mathbf{H}_\mathrm{i} \cdot \mathbf{h}_\mathrm{m} \tag{6.60}$$

the cross-correlation $\mathbf{\Phi}_{dx}$ and auto-correlation $\mathbf{\Phi}_{xx}$ functions are used to replace $\mathbb{E}\left[\mathbf{X}^\mathrm{T} \cdot \mathbf{X}\right]$ and $\mathbb{E}\left[\mathbf{X}^\mathrm{T} \cdot \mathbf{D}_\mathrm{zp}\right]$, respectively. Additionally, the auto-correlation of the reference signal $\mathbf{x}$ filtered by the transfer functions of the MVC controller $H_\mathrm{m}(z)$ and of the IMC controller $\hat{H}_\mathrm{i}(z)$ is defined as

$$\mathbf{\Phi}_{xx}^\mathrm{im} = \mathbf{H}_\mathrm{m}^\mathrm{T} \cdot \mathbf{H}_\mathrm{i}^\mathrm{T} \cdot \mathbf{\Phi}_{xx} \cdot \mathbf{H}_\mathrm{i} \cdot \mathbf{H}_\mathrm{m} \tag{6.61}$$

and the cross-correlation in an equivalent form

$$\boldsymbol{\phi}_{dx}^\mathrm{im} = \mathbf{H}_\mathrm{m}^\mathrm{T} \cdot \mathbf{H}_\mathrm{i}^\mathrm{T} \cdot \mathbf{\Phi}_{dx} \cdot \mathbf{H}_\mathrm{i} \cdot \mathbf{h}_\mathrm{m}. \tag{6.62}$$

Subsequently, these are used in the equation to yield

$$\mathbf{S}^\mathrm{T} \cdot \mathbf{\Phi}_{xx}^\mathrm{im} \cdot \mathbf{S} \cdot \mathbf{w}_\mathrm{f}^\mathrm{opt} = \mathbf{S}^\mathrm{T} \cdot \boldsymbol{\phi}_{dx}^\mathrm{im}. \tag{6.63}$$

Provided that the matrix $\mathbf{S}^{\mathrm{T}} \cdot \mathbf{\Phi}_{xx}^{\mathrm{im}} \cdot \mathbf{S}$ is not singular, the optimal solution for the finite impulse response of the feedforward controller

$$\mathbf{w}_{\mathrm{f}}^{\mathrm{opt}} = \left(\mathbf{S}^{\mathrm{T}} \cdot \mathbf{\Phi}_{xx}^{\mathrm{im}} \cdot \mathbf{S}\right)^{-1} \cdot \mathbf{S}^{\mathrm{T}} \cdot \boldsymbol{\phi}_{dx}^{\mathrm{im}} \tag{6.64}$$

can be found. As can be seen, the result is very similar to the one found in Eq. 2.49. The difference is that the feedback controllers' influence on the optimum feedforward controller is focused on the spectral weighting of the reference and disturbance signal. Although this is relevant for the calculation, other more dominant influences on the feedforward optimum are going to be seen with other combination strategies afterwards. Alternatively, if the free-field excitation scenario is similarly analyzed, the optimum solution takes the form

$$\hat{\mathbf{w}}_{\mathrm{f}}^{\mathrm{opt}} = \left(\mathbf{S}^{\mathrm{T}} \cdot \mathbf{\Phi}_{xx}^{\mathrm{im}} \cdot \mathbf{S}\right)^{-1} \cdot \mathbf{S}^{\mathrm{T}} \cdot \mathbf{\Phi}_{xx}^{\mathrm{im}} \cdot \mathbf{p}_{\mathrm{zp}}. \tag{6.65}$$

Here, the spectral-weighting imposed over Φ_{xx}^{im} by the feedback controllers can be ignored, if only the information about the primary and secondary path is known by the time of the calculation.

Optimization results

In this subsection the advantages of the FIM structure in comparison to the classical feedforward scheme are evaluated. For this purpose, a free-field excitation scenario with a flat power spectral density is considered. This enables the use of a measured primary path impulse response (in this case of length $L_p = 8192$) and at the same time simplifies the auto-correlation matrix Φ_{xx} to the identity matrix I. The nominal secondary path impulse response of length $L_s = 2048$ from the optimization of the pseudo-cascaded system is further used. Using the secondary path and the parameters of the pseudo-cascaded system, its impulse response is calculated for a length of $L_{h_{\mathrm{mi}}} = 2048$. The feedforward controllers are derived following Eq. 2.50 for the classical controller and Eq. 6.65 for the controller of the novel structure. Then, the impulse responses with length 8192 of both systems $h_{\mathrm{f}}(n)$ and $h_{\mathrm{fim}}(n)$ are calculated by means of a sample-by-sample simulation of the system under control. The resulting impulse responses are used for the evaluation.

In Fig. 6.7 the impulse responses of the primary path $p(n)$ (equivalent to the system under no control), the feedforward system $h_{\mathrm{f}}(n)$, and the FIM system $h_{\mathrm{fim}}(n)$ are presented. In Fig. 6.7a the results achieved with a controller length L_w equal to the primary path impulse response length L_p are presented. Please note that the x-axis is in logarithmic scale. It can be seen from the first four samples, that the delay of the secondary path does not allow the two controllers to achieve any control, because of the causality limitations. Therefore, the first samples of both systems are

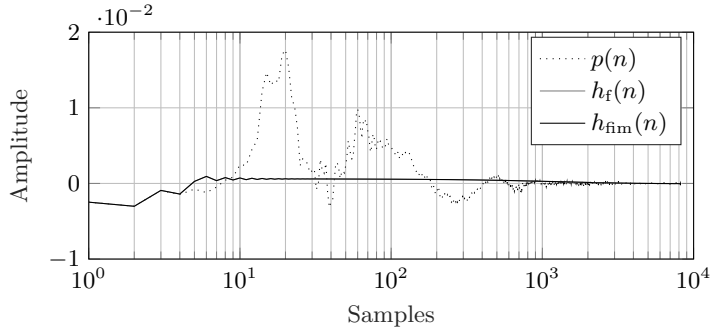

(a) $L_w = 8192$

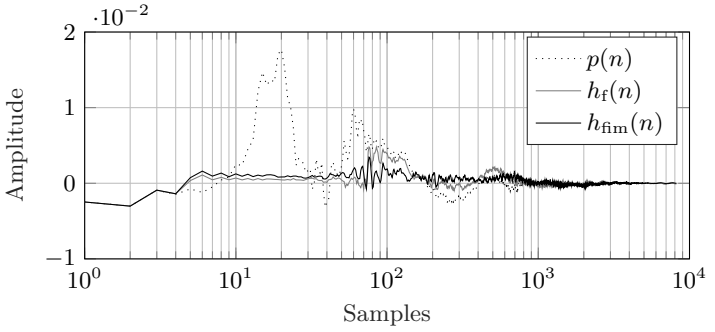

(b) $L_w = 64$

Figure 6.7.: System impulse response $h_{\mathrm{fim}}(f)$ compared to the system subject to no control $p(n)$ and subject to the classical feedforward controller $h_{\mathrm{f}}(f)$. Please note that the x-axis is in logarithmic scale. Parameters: $f_s = 48\,\mathrm{kHz}$, $L_{h_{\mathrm{i}}} = 2048$, $L_{h_{\mathrm{m}}} = 2048$, $L_{h_{\mathrm{mi}}} = 2048$, $L_s = 2048$, $L_p = 8192$, $\Phi_{xx} = I$.

equal to the ones of the primary path. It can be implied that the changes produced by the pseudo-cascaded system on the secondary path do not influence the causality limitations (at least in a visible way). From the fifth sample onward the impulse responses remain positive and equal. In both cases the impulse response decays to zero. Thus, the optimal impulse response of the FIM system is very similar to the one of the FF system.

In Fig. 6.7b the results achieved with a controller length shorter than the one of the primary path impulse response are presented. One can see that from the fifth up to approx. the 40^{th} sample, both impulse responses have a similar transient as the one seen in Fig. 6.7a, with $h_{\mathrm{fim}}(n)$ producing a slightly higher amplitude than $h_{\mathrm{f}}(n)$. From the 40^{th} to approximately

the 70^{th} sample both controllers show a divergent oscillatory behavior. However, one can see that the pseudo-cascaded system's influence in the FIM system is beneficial, because $h_{\text{fim}}(n)$ reaches lower amplitudes than $h_{\text{f}}(n)$ and a relatively steady constant value until it decays to zero. Hence, its impulse response approximates the impulse responses related to the longer controllers in Fig. 6.7a.

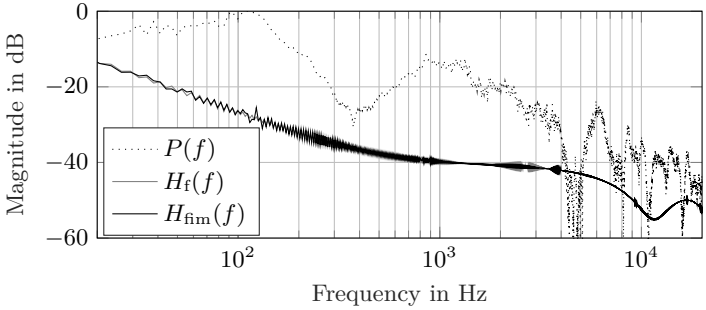

(a) $L_w = 8192$

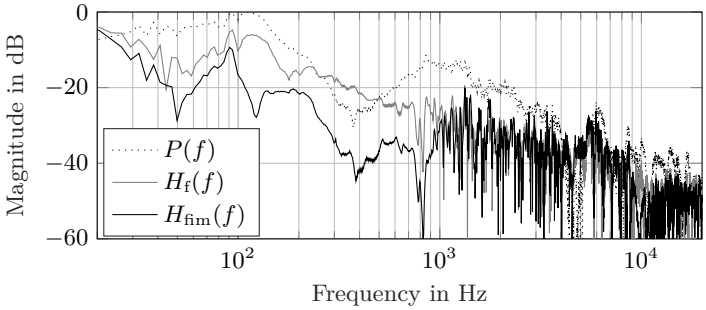

(b) $L_w = 64$

Figure 6.8.: System frequency response $H_{\text{fim}}(f)$ compared to the system subject to no control $P(f)$ and subject to the classical feedforward controller $H_{\text{f}}(f)$. Parameters: $f_s = 48\,\text{kHz}$, $L_w = 64$, $L_{h_{\text{i}}} = 2048$, $L_{h_{\text{m}}} = 2048$, $L_{h_{\text{mi}}} = 2048$, $L_s = 2048$, $L_p = 8192$, $\Phi_{xx} = I$.

In Fig. 6.8 the frequency responses of the impulse responses in Fig. 6.7 are presented. In Fig. 6.8a the results achieved with a controller length L_w equal to the primary path impulse response length L_p are presented. One can see that the frequency response achieved with both control approaches is almost identical. Hence, in this free-field excitation scenario with optimum controller length, the pseudo-cascaded system does not introduce any

advantage for the FIM in comparison to the classical feedforward system. However, if the controller length is shorter than the one of the primary path, as the case presented in Fig. 6.8b, substantial advantages can be seen. For all frequencies below 1 kHz one can see that $H_{\mathrm{fim}}(f)$ shows up to 20 dB higher attenuation than $H_{\mathrm{f}}(f)$. Furthermore, $H_{\mathrm{fim}}(f)$ shows at some frequencies (50, 400 and 800 Hz) an attenuation even higher than the one achievable with the optimum controller length. An attenuation can be achieved even in the frequency range between 250 and 500 Hz, where $H_{\mathrm{f}}(f)$ shows a peak amplification of almost 10 dB. If the improvements and the attenuation bandwidth are compared to the frequency response of the pseudo-cascaded system $H_{\mathrm{mi}}(f)$ in Fig. 6.5, it can be seen that the pseudo-cascaded system can be accounted for the additional achieved attenuation. Furthermore, $H_{\mathrm{mi}}(f)$ introduces another visible improvement in the attenuation performance in the frequency range around 10 kHz.

The frequency responses of the feedforward controllers $W_{\mathrm{f}}(f)$ and $W_{\mathrm{fim}}(f)$ are presented in Fig. 6.9. Additionally, the magnitude response of the naive optimum controller $P(f)/S(f)$ is presented as reference for an ideal controller. In Fig. 6.9a the results achieved with a controller impulse response length L_w equal to the primary path length L_p are presented. It can be seen that the feedforward controller $W_{\mathrm{f}}(f)$ is very close to the ideal controller over the entirely frequency range. In contrast, the FIM controller $W_{\mathrm{fim}}(f)$ shows deviations in the low-frequencies up to 1 kHz. Nevertheless, it is known from the results presented in Fig. 6.8a, that both systems achieve the same attenuation performance. This frequency range coincides with the attenuation bandwidth of the pseudo-cascaded system. Therefore, the deviations must be compensated by the pseudo-cascaded system.

The results achieved with a controller length L_w shorter than the one of the primary path L_p are presented in Fig. 6.9b. One can see that for frequencies higher than 1 kHz both controllers $W_{\mathrm{f}}(f)$ and $W_{\mathrm{fim}}(f)$ show a similar magnitude response. However, in the low frequencies it can be seen that $W_{\mathrm{f}}(f)$ prioritizes the frequencies below 250 Hz over the range between 250 and 700 Hz. As a result, in the same range its system frequency response $H_{\mathrm{f}}(f)$ (see Fig. 6.8b) shows an amplification with a magnitude equal to the deviation from the ideal controller. In contrast, the FIM controller shows a lower magnitude in the frequencies below 300 Hz, but a better approximation in the range between 300 and 700 Hz. The better result in this frequency range, combined with the attenuation that the pseudo-cascaded system produces helps the FIM achieve a better result in Fig. 6.8b. So basically $W_{\mathrm{fim}}(f)$ relies on the pseudo-cascaded system for the frequencies below 300 Hz and makes use of this to achieve a better result at higher frequencies.

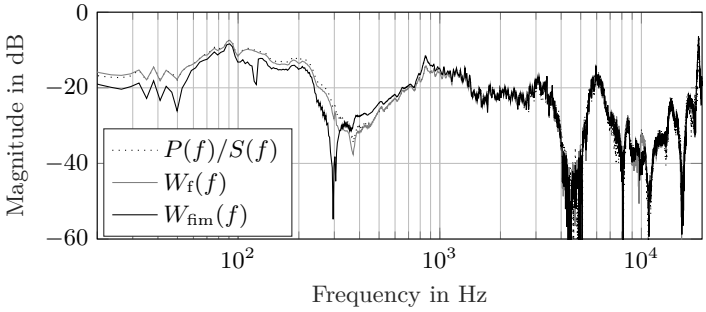

(a) $L_w = 8192$

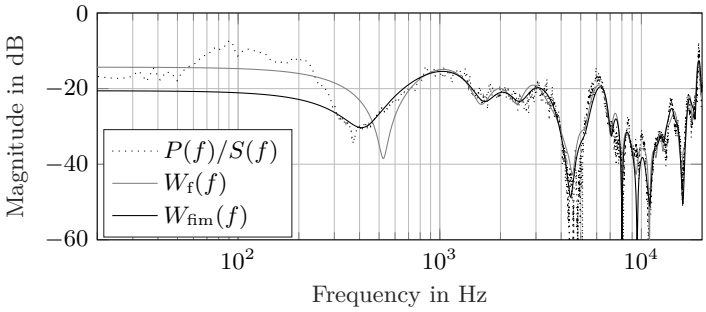

(b) $L_w = 64$

Figure 6.9.: Controller frequency response $W_{\mathrm{fim}}(f)$ compared to the one of the classical feedforward controller $W_{\mathrm{f}}(f)$. Parameters: $f_s = 48\,\mathrm{kHz}$, $L_{h_{\mathrm{i}}} = 2048$, $L_{h_{\mathrm{m}}} = 2048$, $L_{h_{\mathrm{mi}}} = 2048$, $L_s = 2048$, $L_p = 8192$, $\Phi_{xx} = I$.

The equivalent filtered-x LMS

As shown in Sec. 2.4, an adaptive controller based on the steepest descent method can be formulated. For the coefficients' update equation

$$\mathbf{w}_{\mathrm{f}}(n+1) = \mathbf{w}_{\mathrm{f}}(n) - \frac{\mu}{2} \cdot \nabla f_c^{\mathrm{T}}(\mathbf{w}_{\mathrm{f}}(n)), \tag{6.66}$$

the transposed gradient of the cost function has to be calculated. For this purpose the gradient in Eq. 6.58 is approximated by

$$\nabla f_c(\mathbf{w}_{\mathrm{f}}) = \frac{\partial \mathbb{E}[\mathbf{e}^{\mathrm{T}}\mathbf{e}]}{\partial \mathbf{w}_{\mathrm{f}}} \approx -\frac{2}{L_e}(\mathbf{D}_{\mathrm{zp}} \cdot \mathbf{H}_{\mathrm{i}} \cdot \mathbf{h}_{\mathrm{m}} - \mathbf{X} \cdot \mathbf{H}_{\mathrm{i}} \cdot \mathbf{H}_{\mathrm{m}} \cdot \mathbf{S} \cdot \mathbf{w}_{\mathrm{f}})^{\mathrm{T}} \cdot \mathbf{X} \cdot \mathbf{H}_{\mathrm{i}} \cdot \mathbf{H}_{\mathrm{m}} \cdot \mathbf{S}, \tag{6.67}$$

the mean over L_e samples. The vector within parenthesis is replaced by the one of the error signal

$$\nabla f_c(\mathbf{w}_\mathrm{f}) = \frac{\partial \mathbb{E}[\mathbf{e}^\mathrm{T}\mathbf{e}]}{\partial \mathbf{w}_\mathrm{f}} \approx -\frac{2}{L_e}\mathbf{e}^\mathrm{T} \cdot \mathbf{X} \cdot \mathbf{H}_\mathrm{i} \cdot \mathbf{H}_\mathrm{m} \cdot \mathbf{S} \tag{6.68}$$

and then both sides of the equation are transposed

$$\nabla f_c^\mathrm{T}(\mathbf{w}_\mathrm{f}) \approx -\frac{2}{L_e}\mathbf{S}^\mathrm{T} \cdot \mathbf{H}_\mathrm{m}^\mathrm{T} \cdot \mathbf{H}_\mathrm{i}^\mathrm{T} \cdot \mathbf{X}^\mathrm{T} \cdot \mathbf{e}. \tag{6.69}$$

Equivalently to the definition of the filtered-x signal, a filtered reference over the secondary path, the IMC transfer function and the MVC transfer function is defined as

$$\mathbf{x}_\mathrm{ims} = \mathbf{X} \cdot \mathbf{H}_\mathrm{i} \cdot \mathbf{H}_\mathrm{m} \cdot \mathbf{s}. \tag{6.70}$$

Simultaneously, the associated Toeplitz matrix is defined by

$$\mathbf{X}_\mathrm{ims} = \mathbf{X} \cdot \mathbf{H}_\mathrm{i} \cdot \mathbf{H}_\mathrm{m} \cdot \mathbf{S}. \tag{6.71}$$

Using this in Eq. 6.69 the transposed gradient

$$\nabla f_c^\mathrm{T}(\mathbf{w}_\mathrm{f}) \approx -\frac{2}{L_e}\mathbf{X}_\mathrm{ims}^\mathrm{T} \cdot \mathbf{e} \tag{6.72}$$

takes the form of the cross-correlation averaged over L_e values, relative to the positive lags between the new filtered-reference signal, $x_\mathrm{ims}(n)$, and the error signal, $e(n)$. As a less computationally expensive alternative, the average over one sample

$$\nabla f_c^\mathrm{T}(\mathbf{w}_\mathrm{f}(n)) \approx -2 \cdot \mathbf{x}_\mathrm{ims}^\mathrm{T} \cdot e(n) \tag{6.73}$$

with the L_w samples long vector $\mathbf{x}_\mathrm{ims}^\mathrm{T}$ is chosen. This is used to formulate the coefficients' update equation

$$\mathbf{w}_\mathrm{f}(n+1) = \mathbf{w}_\mathrm{f}(n) + \mu \cdot \mathbf{x}_\mathrm{ims}^\mathrm{T} \cdot e(n) \tag{6.74}$$

of the adaptive feedforward controller based on the Filtered-x LMS algorithm (see Fig. 2.12).

The equivalent modified normalized filtered-x LMS

As discussed in Sec. 2.4, the use of the Modified Normalized Filtered-x LMS algorithm simplifies the search for the step-size parameter μ and shows a more reliable adaptation stability. In order to be able to use this algorithm, though, the effective secondary path seen from the perspective of the feedforward controller has to be calculated. For this purpose, the reference and disturbance signals in Fig. 6.6 are set to zero $x(n)$=$d(n)$=0,

and the feedforward control signal $y_{\mathrm{f}}'(n)$ is considered the input and the residual error $e(n)$ the output of the system. Thus, the equations

$$E(z) = -S(z)\big(Y_{\mathrm{f}}'(z) + Y_{\mathrm{i}}'(z) + Y_{\mathrm{m}}'(z)\big), \tag{6.75}$$

$$Y_{\mathrm{m}}'(z) = W_{\mathrm{m}}(z)\big(\hat{S}(z)Y_{\mathrm{i}}'(z) + E(z)\big) \tag{6.76}$$

and

$$Y_{\mathrm{i}}'(z) = W_{\mathrm{i}}(z)\big(\hat{S}(z)Y_{\mathrm{i}}'(z) + E(z)\big) \tag{6.77}$$

$$= \frac{W_{\mathrm{i}}(z)}{1 - \hat{S}(z)W_{\mathrm{i}}(z)}E(z) \tag{6.78}$$

are derived. If Eq. 6.78 is used to replace $Y_{\mathrm{i}}'(z)$ in Eq. 6.76

$$Y_{\mathrm{m}}'(z) = W_{\mathrm{m}}(z)\left(\frac{\hat{S}(z)W_{\mathrm{i}}(z)}{1 - \hat{S}(z)W_{\mathrm{i}}(z)}E(z) + E(z)\right) \tag{6.79}$$

$$= \frac{W_{\mathrm{m}}(z)}{1 - \hat{S}(z)W_{\mathrm{i}}(z)}E(z), \tag{6.80}$$

then $Y_{\mathrm{m}}'(z)$ can be expressed as a function of $E(z)$. This can be used together with Eq. 6.78 in Eq. 6.75

$$E = -S\left(Y_{\mathrm{f}}' + \frac{W_{\mathrm{i}}}{1 - \hat{S}\cdot W_{\mathrm{i}}}E + \frac{W_{\mathrm{m}}}{1 - \hat{S}\cdot W_{\mathrm{i}}}E\right) \tag{6.81}$$

$$= -S\cdot Y_{\mathrm{f}}' - S\cdot\frac{W_{\mathrm{i}} + W_{\mathrm{m}}}{1 - \hat{S}\cdot W_{\mathrm{i}}}E \tag{6.82}$$

$$\rightarrow E\left(1 + S\cdot\frac{W_{\mathrm{i}} + W_{\mathrm{m}}}{1 - \hat{S}\cdot W_{\mathrm{i}}}\right) = -S\cdot Y_{\mathrm{f}}' \tag{6.83}$$

$$\rightarrow E\frac{1 + S\cdot W_{\mathrm{m}} + (S - \hat{S})W_{\mathrm{i}}}{1 - \hat{S}\cdot W_{\mathrm{i}}} = -S\cdot Y_{\mathrm{f}}' \tag{6.84}$$

to derive the FF effective secondary path

$$S_{\mathrm{f}}^{\mathrm{fim}}(z) = -\frac{E}{Y_{\mathrm{f}}'} = S(z)\frac{1 - \hat{S}(z)\cdot W_{\mathrm{i}}(z)}{1 + S(z)\cdot W_{\mathrm{m}}(z) + \big(S(z) - \hat{S}(z)\big)W_{\mathrm{i}}(z)}. \tag{6.85}$$

Thus, the secondary path is changed by the transfer function of the pseudo-cascaded system in a multiplicative way. If $\hat{S}(z) = S(z)$ holds, then the *nominal* effective secondary path

$$\hat{S}_{\mathrm{f}}^{\mathrm{fim}}(z) = S(z)\frac{1 - S(z)W_{\mathrm{i}}(z)}{1 + S(z)W_{\mathrm{m}}(z)} \tag{6.86}$$

can be found. This result is the one used for replacing the two $\hat{S}(z)$ in Fig. 2.13 used to derive the signals used during the controller adaptation. It should be noted, that the estimated secondary path inside the pseudo-cascaded system (see Fig. 6.6) remains unchanged by this effect.

Adaptation stability As discussed in Sec. 2.4.3, the stability of the adaptation algorithm can be assured by choosing a "small enough" step-size μ for its coefficients' update equation. In the case of the Filtered-x LMS its maximal value is limited, among other parameters, by the magnitude and phase error in the estimation of the secondary path used to filter the reference signal. In the case of the Modified Filtered-x LMS it has been calculated that only the magnitude mismatch introduces a limitation.

In the case of the present hybrid combination, the pseudo-cascaded system has shown in Eq. 6.72 to influence the gradient of the adaptation algorithm as well. Thus, where in the pure feedforward control structure the gradient is partially calculated by filtering the reference signal with the estimated secondary path $\hat{S}(z)$, now the same signal has to be filtered by the nominal transfer functions of the MVC and IMC controllers' control loops $H_\mathrm{m}(z)$ and $\hat{H}_\mathrm{i}(z)$, respectively. This influence can also be seen in Eq. 6.85, where the effective secondary path seen from the perspective of the feedforward controller is presented. Because the real effective secondary path $S_\mathrm{f}^\mathrm{fim}(z)$ is not at disposition (it can only be estimated), the nominal effective secondary path $\hat{S}_\mathrm{f}^\mathrm{fim}(z)$ in Eq. 6.86 is used instead during the adaptation. The relative deviation between these two

$$\hat{S}_\mathrm{f}^\mathrm{fim}(z) = \Psi_\mathrm{f}^\mathrm{fim}(z) S_\mathrm{f}^\mathrm{fim}(z) \tag{6.87}$$

is used to estimate the maximum step-size μ for the coefficients' update equation. If this is used to solve the relative deviation

$$\Psi_\mathrm{f}^\mathrm{fim}(z) = \frac{\hat{S}_\mathrm{f}^\mathrm{fim}(z)}{S_\mathrm{f}^\mathrm{fim}(z)}, \tag{6.88}$$

and Eq. 6.85 and Eq. 6.86 are used to replace the secondary paths

$$\Psi_\mathrm{f}^\mathrm{fim}(z) = \frac{\hat{S}(z)\big(1 - \hat{S}(z)W_\mathrm{i}(z)\big)}{1 + \hat{S}(z)W_\mathrm{m}(z)} \cdot \frac{1 + S(z)\cdot W_\mathrm{m}(z) + \big(S(z) - \hat{S}(z)\big)W_\mathrm{i}(z)}{S(z)\big(1 - \hat{S}(z)\cdot W_\mathrm{i}(z)\big)} \tag{6.89}$$

$$= \frac{\hat{S}(z)}{S(z)} \cdot \frac{1 + S(z)\cdot W_\mathrm{m}(z) + \big(S(z) - \hat{S}(z)\big)W_\mathrm{i}(z)}{1 + \hat{S}(z)W_\mathrm{m}(z)}, \tag{6.90}$$

an expression for the deviation can be found. The relative deviation $\hat{S}(z) = \Psi(z)S(z)$ between the estimated and the real secondary path (rewritten from Eq. 2.80) is used to replace the estimated secondary path in

the equation

$$\Psi_{\mathrm{f}}^{\mathrm{fim}}(z) = \Psi(z)\left(\frac{1 + S(z)W_{\mathrm{m}}(z)}{1 + \Psi(z)S(z)W_{\mathrm{m}}(z)} + \frac{\big(1 - \Psi(z)\big)S(z)W_{\mathrm{i}}(z)}{1 + \Psi(z)S(z)W_{\mathrm{m}}(z)}\right). \quad (6.91)$$

As a result, it can be seen that the deviation $\Psi(z)$, originally used for the simple case of a feedforward adaptive controller, is weighted over frequency by the feedback controllers $W_{\mathrm{m}}(z)$ and $W_{\mathrm{i}}(z)$. The left-hand addend shows an asymptotic behavior between unity, for the cases in which the condition $S(z)W_{\mathrm{m}}(z) \ll 1$ is fulfilled ; and $1/\Psi(z)$, when the relation $S(z)W_{\mathrm{m}}(z) \gg 1$ is fulfilled. Thus, it would probably generate a smaller deviation than in the case of a feedforward adaptive controller. The right-hand addend is of small magnitude, because of the nominal MVC transfer function attenuating effect and the product $S(z)W_{\mathrm{i}}(z)$, which is known to lie between zero and one when the IMC controller is optimized to minimize its nominal transfer function. Thus, it also would generate a deviation smaller than the one of a feedforward adaptive controller. However, the phase deviation of the combined effect can not be estimated by such simple means, and it is possible that in the case of the combined controllers the phase deviation is increased. Hence, it is recommended to use the Modified Filtered-x LMS algorithm instead of the Filtered-x LMS algorithm, to cope with this limitation.

6.6. Novel Control Structure with Medium Dependency Level

In this section the feedforward controller $W_{\mathrm{f}}(z)$ is combined with the pseudo-cascaded MVC-IMC system to produce a partial dependency between the controllers. The approach taken is to move the MVC transfer function inside the FF transfer function, i.e.

$$\hat{H}_{\mathrm{FIMPDO}}(z) = \hat{H}_{\mathrm{i}}(z) \cdot \hat{H}_{\mathrm{f}}\left(H_{\mathrm{m}}(z), z\right).$$

To achieve this, the structure presented in Fig. 6.10, named FIMPDO, is proposed. By comparing it with the previous structure in Fig. 6.6, it can be seen that an estimated secondary path $\hat{S}(z)$ is used to negate the influence of the feedforward control signal $\hat{y}_{\mathrm{f}}(n)$ on the input of the MVC controller $W_{\mathrm{m}}(z)$. The same connection strategy is used in the MVC-FF combination dependent optima Fig. 5.2b. Hence, it is expected that this will produce the desired effect in the optimum solution of $W_{\mathrm{f}}(z)$. In order to corroborate this hypothesis, a transfer function analysis has to be carried out.

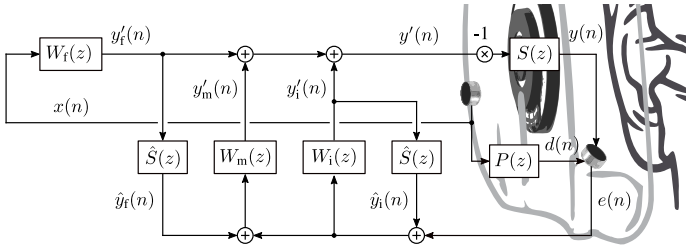

Figure 6.10.: Novel hybrid control structure with partially dependent optima.

From Fig. 6.10, the equations

$$E(z) = D(z) + Y(z) \tag{6.92}$$
$$D(z) = P(z)X(z) \tag{6.93}$$
$$Y(z) = -S(z)\big(Y'_\mathrm{f}(z) + Y'_\mathrm{i}(z) + Y'_\mathrm{m}(z)\big) \tag{6.94}$$
$$Y'_\mathrm{f}(z) = W_\mathrm{f}(z)X(z) \tag{6.95}$$
$$Y'_\mathrm{m}(z) = W_\mathrm{m}(z)\big(\hat{S}(z)Y'_\mathrm{f}(z) + \hat{S}(z)Y'_\mathrm{i}(z) + E(z)\big) \tag{6.96}$$

and

$$Y'_\mathrm{i}(z) = W_\mathrm{i}(z)\big(\hat{S}(z)Y'_\mathrm{i}(z) + E(z)\big) \tag{6.97}$$
$$= \frac{W_\mathrm{i}(z)}{1 - \hat{S}(z)W_\mathrm{i}(z)}E(z) \tag{6.98}$$

are derived. Using Eq. 6.98 and Eq. 6.95 to replace $Y'_\mathrm{i}(z)$ and $Y'_\mathrm{f}(z)$ in Eq. 6.96

$$Y'_\mathrm{m}(z) = W_\mathrm{m}(z)\left(\hat{S}(z)W_\mathrm{f}(z)X(z) + \hat{S}(z)\frac{W_\mathrm{i}(z)}{1 - \hat{S}(z)W_\mathrm{i}(z)}E(z) + E(z)\right) \tag{6.99}$$
$$= W_\mathrm{m}(z)\left(\hat{S}(z)W_\mathrm{f}(z)X(z) + \frac{1}{1 - \hat{S}(z)W_\mathrm{i}(z)}E(z)\right) \tag{6.100}$$

the MVC control signal

$$Y'_\mathrm{m}(z) = W_\mathrm{m}(z)\hat{S}(z)W_\mathrm{f}(z)X(z) + \frac{W_\mathrm{m}(z)}{1 - \hat{S}(z)W_\mathrm{i}(z)}E(z) \tag{6.101}$$

can be expressed as a function of $E(z)$ and $X(z)$. Now, if Eq. 6.95, Eq. 6.98,

and Eq. 6.101 are used to replace the control signals in Eq. 6.94

$$Y = -S\left(W_\mathrm{f}\cdot X + \frac{W_\mathrm{i}}{1-\hat{S}\cdot W_\mathrm{i}}E + W_\mathrm{m}\cdot\hat{S}\cdot W_\mathrm{f}\cdot X + \frac{W_\mathrm{m}}{1-\hat{S}\cdot W_\mathrm{i}}E\right) \tag{6.102}$$

$$= -S\left(\big(W_\mathrm{f} + W_\mathrm{m}\cdot\hat{S}\cdot W_\mathrm{f}\big)X + \frac{W_\mathrm{i}+W_\mathrm{m}}{1-\hat{S}\cdot W_\mathrm{i}}E\right), \tag{6.103}$$

then the control signal

$$Y = -\big(S\cdot W_\mathrm{f} + S\cdot W_\mathrm{m}\cdot\hat{S}\cdot W_\mathrm{f}\big)X - \frac{S\cdot W_\mathrm{i}+S\cdot W_\mathrm{m}}{1-\hat{S}\cdot W_\mathrm{i}}E \tag{6.104}$$

can be formulated as a function of $E(z)$ and $X(z)$. Using Eq. 6.93 and Eq. 6.104 in Eq. 6.92

$$E = P\cdot X - \big(S\cdot W_\mathrm{f} + S\cdot W_\mathrm{m}\cdot\hat{S}\cdot W_\mathrm{f}\big)X - \frac{S\cdot W_\mathrm{i}+S\cdot W_\mathrm{m}}{1-\hat{S}\cdot W_\mathrm{i}}E \tag{6.105}$$

$$\rightarrow E\left(1+\frac{S\cdot W_\mathrm{i}+S\cdot W_\mathrm{m}}{1-\hat{S}\cdot W_\mathrm{i}}\right) = \big(P - S\cdot W_\mathrm{f} - S\cdot W_\mathrm{m}\cdot\hat{S}\cdot W_\mathrm{f}\big)X \tag{6.106}$$

$$\rightarrow E\left(\frac{1+S\cdot W_\mathrm{m}+(S-\hat{S})W_\mathrm{i}}{1-\hat{S}\cdot W_\mathrm{i}}\right) = \big(P - S\cdot W_\mathrm{f}(1+\hat{S}\cdot W_\mathrm{m})\big)X, \tag{6.107}$$

the system's transfer function can be derived

$$H_\mathrm{fimpdo}(z) = \frac{E(z)}{X(z)} = \big(1-\hat{S}(z)W_\mathrm{i}(z)\big)\frac{P(z) - S(z)W_\mathrm{f}(z)\big(1+\hat{S}(z)W_\mathrm{m}(z)\big)}{1+S(z)W_\mathrm{m}(z)+\big(S(z)-\hat{S}(z)\big)W_\mathrm{i}(z)}. \tag{6.108}$$

As can be seen by comparing it to the transfer function of the previous system, both share the same characteristic function in the denominator and the feedback system is the same. Hence, the stability and performance constraint presented in the previous section apply in this case as well. In cases in which $\hat{S}(z) = S(z)$ holds, the transfer function simplifies to its nominal form

$$\hat{H}_\mathrm{fimpdo}(z) = \big(1-S(z)W_\mathrm{i}(z)\big)\left(\frac{P(z)}{1+S(z)W_\mathrm{m}(z)} - S(z)W_\mathrm{f}(z)\right). \tag{6.109}$$

It can be seen that the primary path's passive attenuation capability is combined with the active attenuation produced by the transfer function of the MVC control. This produces the expected change in the optimal solution of the FF controller, as it now depends on the MVC controller $W_\mathrm{m}(z)$ as well. It is expected that the control effort of the feedforward controller is lower in the frequency region where the MVC control loop is

active.

6.6.1. The optimal feedforward controller

Given that the feedback components of the system have been designed, the optimal feedforward controller can be calculated. Its derivation is based on the nominal transfer function of the system in Eq. 6.109, in which it is assumed that the estimated and nominal secondary paths are equal to the real one. The transfer function is used to express the error signal

$$E(z) = \big(1 - S(z)W_{\mathrm{i}}(z)\big)\left(\frac{P(z)X(z)}{1 + S(z)W_{\mathrm{m}}(z)} - S(z)W_{\mathrm{f}}(z)X(z)\right) \quad (6.110)$$

as a function of the reference signal $X(z)$ and the controllers $W_{\mathrm{i}}(z)$, $W_{\mathrm{m}}(z)$, and $W_{\mathrm{f}}(z)$. The equality $D(z) = P(z)X(z)$ is used

$$E(z) = \big(1 - S(z)W_{\mathrm{i}}(z)\big)\left(\frac{D(z)}{1 + S(z)W_{\mathrm{m}}(z)} - S(z)W_{\mathrm{f}}(z)X(z)\right), \quad (6.111)$$

in order to include the disturbance signal $D(z)$ in the stochastic excitation analysis later on. It can be seen from Eq. 6.111 that MVC controller $W_{\mathrm{m}}(z)$ attenuates the disturbance signal $D(z)$, while the IMC controller $W_{\mathrm{i}}(z)$ introduces a coloration in the residual error. The nominal transfer function of the IMC controller (re-written from Eq. 4.7)

$$\hat{H}_{\mathrm{i}}(z) = 1 - S(z)W_{\mathrm{i}}(z) \quad (6.112)$$

and the transfer function of the MVC controller (re-written from Eq. 3.2)

$$H_{\mathrm{m}}(z) = \frac{1}{1 - S(z)W_{\mathrm{m}}(z)} \quad (6.113)$$

are used to replace their contributions in Eq. 6.111

$$E(z) = \hat{H}_{\mathrm{i}}(z)\big(H_{\mathrm{m}}(z)D(z) - S(z)W_{\mathrm{f}}(z)X(z)\big). \quad (6.114)$$

Now, as already discussed in Sec. 2.3, the search for an optimum controller in the Z-domain may yield a controller $W_{\mathrm{f}}(z)$ that is non-causal or non-stable, or both. Therefore, in order to find the finite impulse response of the causal feedforward controller $\mathbf{w}_{\mathrm{f}}$ the notation and considerations presented in Sec. 2.3.1 are used. As a first step, the equation is re-written

$$\mathbf{e} = \mathbf{H}_{\mathrm{i}} \cdot \mathbf{H}_{\mathrm{m}} \cdot \mathbf{d}_{\mathrm{zp}} - \mathbf{H}_{\mathrm{i}} \cdot \mathbf{S} \cdot \mathbf{W}_{\mathrm{f}} \cdot \mathbf{x}, \quad (6.115)$$

in its equivalent vector-matrix form based on the signals' vectors and systems' impulse responses and Toeplitz matrices. Considering linearity and

time invariance, this is rearranged as

$$\mathbf{e} = \mathbf{D}_{\mathrm{zp}} \cdot \mathbf{H}_{\mathrm{i}} \cdot \mathbf{h}_{\mathrm{m}} - \mathbf{X} \cdot \mathbf{H}_{\mathrm{i}} \cdot \mathbf{S} \cdot \mathbf{w}_{\mathrm{f}}. \tag{6.116}$$

Using this equation, the cost function is defined as the expectation of the quadratic error $\mathbb{E}[\mathbf{e}^{\mathrm{T}}\mathbf{e}]$. In order to find the controller's finite impulse response $\mathbf{w}_{\mathrm{f}}$ that minimizes the cost function, its gradient with respect to the impulse response coefficients is calculated

$$\frac{\partial \mathbb{E}[\mathbf{e}^{\mathrm{T}}\mathbf{e}]}{\partial \mathbf{w}_{\mathrm{f}}} = -2 \cdot \mathbb{E}[(\mathbf{D}_{\mathrm{zp}} \cdot \mathbf{H}_{\mathrm{i}} \cdot \mathbf{h}_{\mathrm{m}} - \mathbf{X} \cdot \mathbf{H}_{\mathrm{i}} \cdot \mathbf{S} \cdot \mathbf{w}_{\mathrm{f}})^{\mathrm{T}} \mathbf{X} \cdot \mathbf{H}_{\mathrm{i}} \cdot \mathbf{S}] \tag{6.117}$$

and equated to zero. If the transpose of both sides is taken

$$\mathbf{S}^{\mathrm{T}} \cdot \mathbf{H}_{\mathrm{i}}^{\mathrm{T}} \cdot \mathbb{E}\left[\mathbf{X}^{\mathrm{T}} \cdot \mathbf{X}\right] \cdot \mathbf{H}_{\mathrm{i}} \cdot \mathbf{S} \cdot \mathbf{w}_{\mathrm{f}}^{\mathrm{opt}} = \mathbf{S}^{\mathrm{T}} \cdot \mathbf{H}_{\mathrm{i}}^{\mathrm{T}} \cdot \mathbb{E}\left[\mathbf{X}^{\mathrm{T}} \cdot \mathbf{D}_{\mathrm{zp}}\right] \cdot \mathbf{H}_{\mathrm{i}} \cdot \mathbf{h}_{\mathrm{m}} \tag{6.118}$$

the equality fulfilled by the optimal controller's finite impulse response $\mathbf{w}_{\mathrm{f}}^{\mathrm{opt}}$ can be formulated. Based on Eq. 2.46 and Eq. 2.47

$$\mathbf{S}^{\mathrm{T}} \cdot \mathbf{H}_{\mathrm{i}}^{\mathrm{T}} \cdot \mathbf{\Phi}_{xx} \cdot \mathbf{H}_{\mathrm{i}} \cdot \mathbf{S} \cdot \mathbf{w}_{\mathrm{f}}^{\mathrm{opt}} = \mathbf{S}^{\mathrm{T}} \cdot \mathbf{H}_{\mathrm{i}}^{\mathrm{T}} \cdot \mathbf{\Phi}_{dx} \cdot \mathbf{H}_{\mathrm{i}} \cdot \mathbf{h}_{\mathrm{m}} \tag{6.119}$$

the cross-correlation $\mathbf{\Phi}_{dx}$ and auto-correlation $\mathbf{\Phi}_{xx}$ functions are used to replace $\mathbb{E}\left[\mathbf{X}^{\mathrm{T}} \cdot \mathbf{X}\right]$ and $\mathbb{E}\left[\mathbf{X}^{\mathrm{T}} \cdot \mathbf{D}_{\mathrm{zp}}\right]$, respectively. Additionally, the auto-correlation of the reference signal $\mathbf{x}$ filtered by the transfer functions of the IMC controller $H_{\mathrm{i}}(z)$ is defined as

$$\mathbf{\Phi}_{xx}^{\mathrm{i}} = \mathbf{H}_{\mathrm{i}}^{\mathrm{T}} \cdot \mathbf{\Phi}_{xx} \cdot \mathbf{H}_{\mathrm{i}} \tag{6.120}$$

and the cross-correlation in an equivalent form

$$\mathbf{\Phi}_{dx}^{\mathrm{i}} = \mathbf{H}_{\mathrm{i}}^{\mathrm{T}} \cdot \mathbf{\Phi}_{dx} \cdot \mathbf{H}_{\mathrm{i}}. \tag{6.121}$$

Subsequently, these are used in the equation

$$\mathbf{S}^{\mathrm{T}} \cdot \mathbf{\Phi}_{xx}^{\mathrm{i}} \cdot \mathbf{S} \cdot \mathbf{w}_{\mathrm{f}}^{\mathrm{opt}} = \mathbf{S}^{\mathrm{T}} \cdot \mathbf{\Phi}_{dx}^{\mathrm{i}} \cdot \mathbf{h}_{\mathrm{m}} \tag{6.122}$$

Provided that the matrix $\mathbf{S}^{\mathrm{T}} \cdot \mathbf{\Phi}_{xx}^{\mathrm{i}} \cdot \mathbf{S}$ is not singular, the optimal solution for the finite impulse response of the feedforward controller

$$\mathbf{w}_{\mathrm{f}}^{\mathrm{opt}} = \left(\mathbf{S}^{\mathrm{T}} \cdot \mathbf{\Phi}_{xx}^{\mathrm{i}} \cdot \mathbf{S}\right)^{-1} \cdot \mathbf{S}^{\mathrm{T}} \cdot \mathbf{\Phi}_{dx}^{\mathrm{i}} \cdot \mathbf{h}_{\mathrm{m}} \tag{6.123}$$

can be found. As can be seen, the result is very similar to the one found in Eq. 2.49. The difference is that the auto- and cross-correlation functions are weighted by the IMC transfer function and more importantly, that the result is filtered by the impulse response of the MVC feedback loop $\mathbf{h}_{\mathrm{m}}$. This is what is understood as the partial dependency of the feedforward controller with respect to the MVC controller's parameters. Alternatively, if the free-field excitation scenario is similarly analyzed, the

optimum solution takes the form

$$\hat{\mathbf{w}}_{\mathrm{f}}^{\mathrm{opt}} = \left(\mathbf{S}^{\mathrm{T}} \cdot \mathbf{\Phi}_{xx}^{\mathrm{i}} \cdot \mathbf{S}\right)^{-1} \cdot \mathbf{S}^{\mathrm{T}} \cdot \mathbf{\Phi}_{xx}^{\mathrm{i}} \cdot \mathbf{H}_{\mathrm{m}} \cdot \mathbf{p}_{\mathrm{zp}}. \tag{6.124}$$

One can see that the primary path's impulse response $\mathbf{p}_{\mathrm{zp}}$ is convolved with the one of the MVC transfer function $\mathbf{h}_{\mathrm{m}}$, thus, reaffirming the direct dependency of the result with respect to the MVC controller's parameters.

Optimization results

In this subsection the advantages of the FIMPDO structure in comparison to the classical feedforward scheme (FF) are evaluated. For this purpose, the same simulation procedure and parameters described in Sec. 6.5.1 are used. For deriving the feedforward controller of the novel structure Eq. 6.124 is used. Then, the impulse responses with length 8192 of both systems $h_{\mathrm{f}}(n)$ and $h_{\mathrm{fimpdo}}(n)$ are calculated by means of a sample-by-sample simulation of the system under control. The resulting impulse responses are used for the evaluation.

In Fig. 6.11 the impulse responses of the primary path $p(n)$ (equivalent to the system under no control), the feedforward system $h_{\mathrm{f}}(n)$, and the FIMPDO system $h_{\mathrm{fimpdo}}(n)$ are presented. In Fig. 6.11a the results achieved with a controller length L_w equal to the primary path impulse response length L_p are presented. It is clear that no differences between both impulse responses can be seen. Hence, it can be implied that with the FIMPDO no changes are produced on the secondary path's influence on the causality limitations. Thus, the same results seen from the FIM structure in Fig. 6.7a are achieved.

In Fig. 6.11b the results achieved with a controller length shorter than the one of the primary path impulse response are presented. One can see that from the fifth up to approx. the 40^{th} sample both impulse responses have a very different behavior. While $h_{\mathrm{f}}(n)$ remains constant and positive, similar to the one seen in Fig. 6.11a, $h_{\mathrm{fimpdo}}(n)$ oscillates between positive and negative values. Near the 70^{th} sample both impulse responses show the transients produced by the controller's finite impulse response length L_w. The transient produced by $h_{\mathrm{fimpdo}}(n)$ is comparable to the one from $h_{\mathrm{f}}(n)$ in amplitude, so in the high frequencies the pseudo-cascaded system seems to not be effective. Nevertheless, after the 200^{th} sample the tail of $h_{\mathrm{fimpdo}}(n)$ shows a behavior closer to the one seen in the longer controllers in Fig. 6.11a. Therefore, some improvement in the low-frequency region is still to be expected.

In Fig. 6.12 the frequency responses of the impulse responses in Fig. 6.11 are presented. In Fig. 6.12a the results achieved with a controller length L_w equal to the primary path impulse response length L_p are presented. One can see that the frequency response achieved with both control ap-

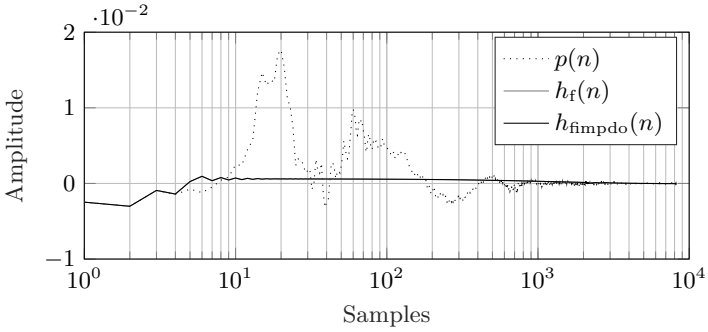

(a) $L_w = 8192$

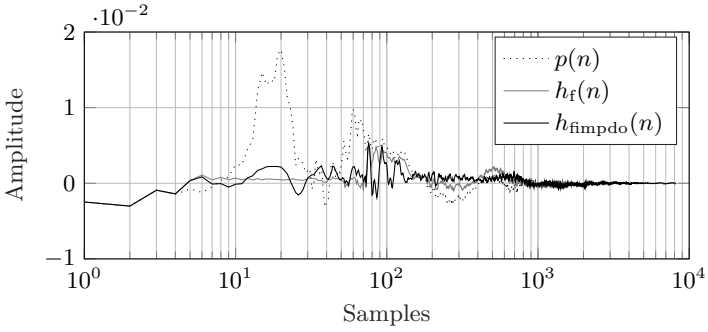

(b) $L_w = 64$

Figure 6.11.: System impulse response $h_{\text{fimpdo}}(f)$ compared to the system subject to no control $p(n)$ and subject to the classical feedforward controller $h_{\text{f}}(f)$. Please note that the x-axis is in logarithmic scale. Parameters: $f_s = 48\,\text{kHz}$, $L_{h_{\text{i}}} = 2048$, $L_{h_{\text{m}}} = 2048$, $L_{h_{\text{mi}}} = 2048$, $L_s = 2048$, $L_p = 8192$, $\Phi_{xx} = I$.

proaches is comparable, although some differences between 90 and 200 Hz can be seen. Therefore, in this free-field excitation scenario with optimum controller length, the pseudo-cascaded system does not introduce any important advantage for the FIMPDO in comparison to the classical FF system. However, if the controller length is shorter than the one of the primary path, as the case presented in Fig. 6.12b, substantial differences can be seen. On the one hand, for all frequencies between 45 Hz and 1 kHz one can see that $H_{\text{fimpdo}}(f)$ shows significant attenuation improvements when compared to $H_{\text{f}}(f)$. Furthermore, $H_{\text{fimpdo}}(f)$ shows at some frequencies (50, 450 and 850 Hz) an attenuation even higher than

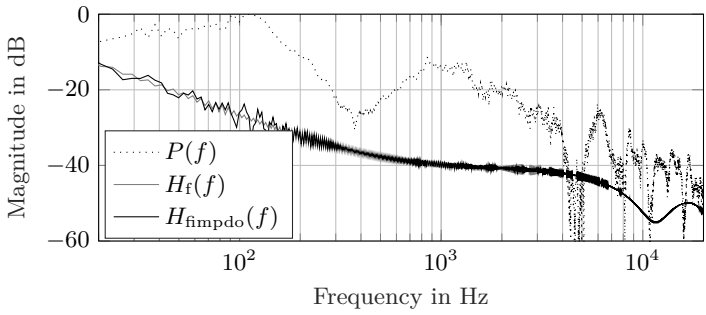

(a) $L_w = 8192$

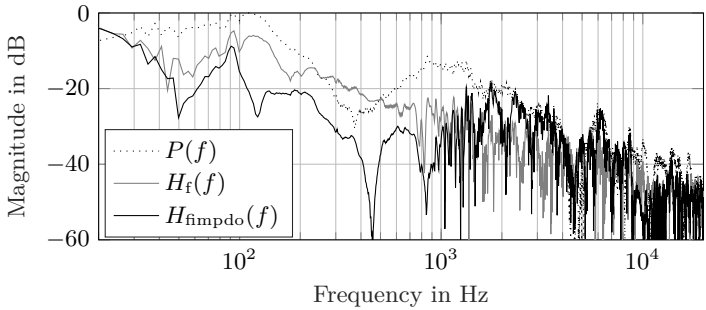

(b) $L_w = 64$

Figure 6.12.: System frequency response $H_{\mathrm{fimpdo}}(f)$ compared to the system subject to no control $P(f)$ and subject to the classical feedforward controller $H_{\mathrm{f}}(f)$. Parameters: $f_s = 48\,\mathrm{kHz}$, $L_{h_{\mathrm{i}}} = 2048$, $L_{h_{\mathrm{m}}} = 2048$, $L_{h_{\mathrm{mi}}} = 2048$, $L_s = 2048$, $L_p = 8192$, $\Phi_{xx} = I$.

the one achievable with the optimum controller length. However, a loss in attenuation between 1.8 and 3.5 kHz and around 6 kHz is also produced. It can be stated, that the hybrid combination strategy used in FIMPDO introduces attenuation improvements in the low-frequencies, but also worse attenuation performance in other frequency regions.

The frequency responses of both controllers $W_{\mathrm{f}}(f)$ and $W_{\mathrm{fimpdo}}(f)$ are presented in Fig. 6.13. Additionally, the magnitude response of the naive optimum controller $P(f)/S(f)$ is presented as reference for an ideal solution. In Fig. 6.13a the results achieved with a controller impulse response length L_w equal to the primary path length L_p are presented. It can be seen that $W_{\mathrm{f}}(f)$ is very close to the ideal controller over the entire frequency range. In contrast, $W_{\mathrm{fimpdo}}(f)$ shows substantial deviations from

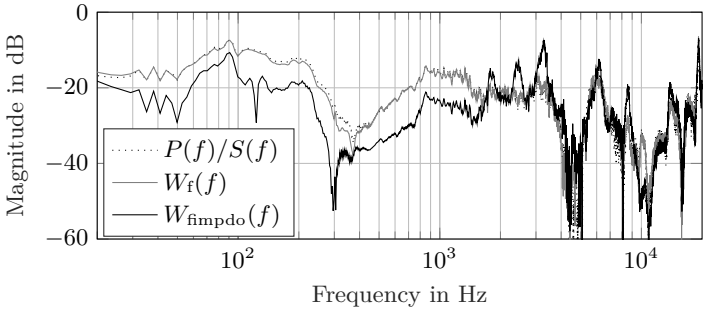

(a) $L_w = 8192$

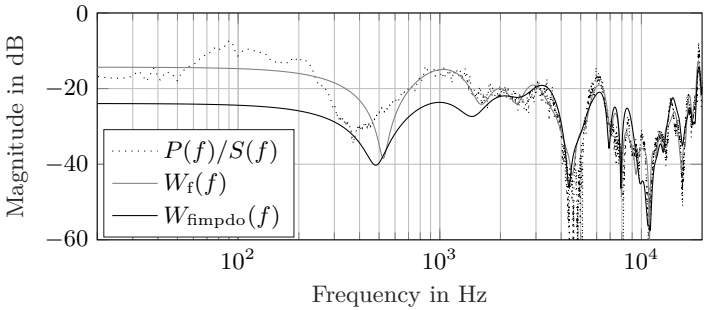

(b) $L_w = 64$

Figure 6.13.: Controller frequency response $W_{\mathrm{fimpdo}}(f)$ compared to the one of the classical feedforward controller $W_{\mathrm{f}}(f)$. Parameters: $f_s = 48\,\mathrm{kHz}$, $L_{h_{\mathrm{i}}} = 2048$, $L_{h_{\mathrm{m}}} = 2048$, $L_{h_{\mathrm{mi}}} = 2048$, $L_s = 2048$, $L_p = 8192$, $\Phi_{xx} = I$.

$P(f)/S(f)$, which are very similar to the frequency response of the MVC feedback system in Fig. 6.2. This can be explained by the direct influence that the MVC sub-system has on the feedforward controller solution, when it is calculated using Eq. 6.124. Nevertheless, it is known from the system frequency response presented in Fig. 6.12a, that both systems $H_{\mathrm{f}}(f)$ and $H_{\mathrm{fimpdo}}(f)$ achieve a comparable performance. Therefore, the deviations from the optimum are compensated by the IMC controller, which enables the complete system to achieve the same optimum performance. The results achieved with a controller length L_w shorter than the one of the primary path L_p are presented in Fig. 6.13b. One can see that for frequencies higher than 2 kHz both controllers $W_{\mathrm{f}}(f)$ and $W_{\mathrm{fimpdo}}(f)$ follow the ideal controller with some small deviations produced by the comparative lower filter-order they have. For frequencies below 2 kHz the classical

feedforward controller $W_{\mathrm{f}}(f)$ follows the ideal solution's frequency response closer than $W_{\mathrm{fimpdo}}(f)$. In this frequency range $W_{\mathrm{fimpdo}}(f)$ has roughly 10 dB less gain than $W_{\mathrm{f}}(f)$, so its effect is minimum. This means, that to achieve the attenuation presented in Fig. 6.12b, the FIMPDO relies on its pseudo-cascaded system. Although the performance in the low-frequencies is indeed better than the classical FF system, the attenuation performance achieved in the mid-frequencies is worse than with the FIM system.

The equivalent filtered-x LMS

In this section the equivalent filtered-x LMS algorithm for the FIMPDO structure is formulated. This algorithm can be used for approximating in an iterative way the Wiener controller solution evaluated in the past section. For the coefficients' update equation the transposed gradient of the cost function has to be calculated. For this purpose the gradient in Eq. 6.117 is approximated by the mean over L_e samples

$$\nabla f_c(\mathbf{w}_{\mathrm{f}}) = \frac{\partial \mathbb{E}[\mathbf{e}^{\mathrm{T}}\mathbf{e}]}{\partial \mathbf{w}_{\mathrm{f}}} \approx -\frac{2}{L_e}(\mathbf{D}_{\mathrm{zp}}\cdot\mathbf{H}_{\mathrm{i}}\cdot\mathbf{h}_{\mathrm{m}} - \mathbf{X}\cdot\mathbf{H}_{\mathrm{i}}\cdot\mathbf{S}\cdot\mathbf{w}_{\mathrm{f}})^{\mathrm{T}}\mathbf{X}\cdot\mathbf{H}_{\mathrm{i}}\cdot\mathbf{S} \quad (6.125)$$

The vector within parenthesis is replaced by the one of the error signal

$$\nabla f_c(\mathbf{w}_{\mathrm{f}}) = \frac{\partial \mathbb{E}[\mathbf{e}^{\mathrm{T}}\mathbf{e}]}{\partial \mathbf{w}_{\mathrm{f}}} \approx -\frac{2}{L_e}\mathbf{e}^{\mathrm{T}}\cdot\mathbf{X}\cdot\mathbf{H}_{\mathrm{i}}\cdot\mathbf{S} \quad (6.126)$$

and then both sides of the equation are transposed

$$\nabla f_c^{\mathrm{T}}(\mathbf{w}_{\mathrm{f}}) \approx -\frac{2}{L_e}\mathbf{S}^{\mathrm{T}}\cdot\mathbf{H}_{\mathrm{i}}^{\mathrm{T}}\cdot\mathbf{X}^{\mathrm{T}}\cdot\mathbf{e}. \quad (6.127)$$

Equivalently to the definition of the filtered-x signal, a reference signal filtered by the secondary path and the IMC transfer function is defined as

$$\mathbf{x}_{\mathrm{is}} = \mathbf{X}\cdot\mathbf{H}_{\mathrm{i}}\cdot\mathbf{s}. \quad (6.128)$$

Simultaneously, the associated Toeplitz matrix is defined by

$$\mathbf{X}_{\mathrm{is}} = \mathbf{X}\cdot\mathbf{H}_{\mathrm{i}}\cdot\mathbf{S}. \quad (6.129)$$

Using this in Eq. 6.127 the transposed gradient

$$\nabla f_c^{\mathrm{T}}(\mathbf{w}_{\mathrm{f}}) \approx -\frac{2}{L_e}\mathbf{X}_{\mathrm{is}}^{\mathrm{T}}\cdot\mathbf{e} \quad (6.130)$$

takes the form of the cross-correlation averaged over L_e values, relative to the positive lags between the new filtered-reference signal, $x_{\mathrm{is}}(n)$, and the error signal, $e(n)$. As a less computationally expensive alternative, the

average over one sample

$$\nabla f_c^{\mathrm{T}}(\mathbf{w}_{\mathrm{f}}(n)) \approx -2 \cdot \mathbf{x}_{\mathrm{is}}^{\mathrm{T}} \cdot e(n) \tag{6.131}$$

with the L_w samples long vector $\mathbf{x}_{\mathrm{is}}^{\mathrm{T}}$ is chosen. This is used to formulate the coefficients' update equation

$$\mathbf{w}_{\mathrm{f}}(n+1) = \mathbf{w}_{\mathrm{f}}(n) + \mu \cdot \mathbf{x}_{\mathrm{is}}^{\mathrm{T}} \cdot e(n) \tag{6.132}$$

of the adaptive feedforward controller based on the Filtered-x LMS algorithm (see Fig. 2.12).

The equivalent modified normalized filtered-x LMS

As already discussed before, the use of the Modified Normalized Filtered-x LMS algorithm simplifies the search for the step-size parameter μ and shows a more reliable adaptation stability. In order to be able to use this algorithm with the FIMPDO structure, the effective secondary path seen from the perspective of the feedforward controller has to be calculated. For this purpose, the reference and disturbance signals in Fig. 6.10 are set to zero $x(n)$=$d(n)$=0, and the feedforward control signal $y_{\mathrm{f}}'(n)$ is considered the input and the residual error $e(n)$ the output of the system. Thus, the equations

$$E(z) = -S\big(Y_{\mathrm{f}}'(z) + Y_{\mathrm{i}}'(z) + Y_{\mathrm{m}}'(z)\big) \tag{6.133}$$

$$Y_{\mathrm{m}}'(z) = W_{\mathrm{m}}(z)\big(\hat{S}(z)Y_{\mathrm{f}}'(z) + \hat{S}(z)Y_{\mathrm{i}}'(z) + E(z)\big) \tag{6.134}$$

and

$$Y_{\mathrm{i}}'(z) = W_{\mathrm{i}}(z)\big(\hat{S}(z)Y_{\mathrm{i}}'(z) + E(z)\big) \tag{6.135}$$

$$= \frac{W_{\mathrm{i}}(z)}{1 - \hat{S}(z)W_{\mathrm{i}}(z)}E(z) \tag{6.136}$$

are derived. If Eq. 6.136 is used to replace Y_{i}' in Eq. 6.134

$$Y_{\mathrm{m}}'(z) = W_{\mathrm{m}}(z)\left(\hat{S}(z)Y_{\mathrm{f}}'(z) + \frac{\hat{S}(z)W_{\mathrm{i}}(z)}{1 - \hat{S}(z)W_{\mathrm{i}}(z)}E(z) + E(z)\right) \tag{6.137}$$

$$= W_{\mathrm{m}}(z)\hat{S}(z)Y_{\mathrm{f}}'(z) + \frac{W_{\mathrm{m}}(z)}{1 - \hat{S}(z)W_{\mathrm{i}}(z)}E(z), \tag{6.138}$$

then $Y'_{\mathrm{m}}(z)$ can be expressed as a function of $E(z)$. This can be used together with Eq. 6.136 in Eq. 6.133

$$E = -S\left(Y'_{\mathrm{f}} + W_{\mathrm{m}} \cdot \hat{S} \cdot Y'_{\mathrm{f}} + \frac{W_{\mathrm{i}}}{1 - \hat{S} \cdot W_{\mathrm{i}}} E + \frac{W_{\mathrm{m}}}{1 - \hat{S} \cdot W_{\mathrm{i}}} E\right) \tag{6.139}$$

$$= -S \cdot Y'_{\mathrm{f}}(1 + W_{\mathrm{m}} \cdot \hat{S}) - S \cdot \frac{W_{\mathrm{i}} + W_{\mathrm{m}}}{1 - \hat{S} \cdot W_{\mathrm{i}}} E \tag{6.140}$$

$$\rightarrow E\left(1 + S \cdot \frac{W_{\mathrm{i}} + W_{\mathrm{m}}}{1 - \hat{S} \cdot W_{\mathrm{i}}}\right) = -S \cdot Y'_{\mathrm{f}}(1 + W_{\mathrm{m}} \cdot \hat{S}) \tag{6.141}$$

$$\rightarrow E \frac{1 + S \cdot W_{\mathrm{m}} + (S - \hat{S}) W_{\mathrm{i}}}{1 - \hat{S} \cdot W_{\mathrm{i}}} = -S \cdot Y'_{\mathrm{f}}(1 + W_{\mathrm{m}} \cdot \hat{S}) \tag{6.142}$$

to derive the FF effective secondary path

$$S_{\mathrm{f}}^{\mathrm{fimpdo}}(z) = -\frac{E}{Y'_{\mathrm{f}}} = S(z) \frac{\big(1 + \hat{S}(z) \cdot W_{\mathrm{m}}(z)\big) \cdot \big(1 - \hat{S}(z) \cdot W_{\mathrm{i}}(z)\big)}{1 + S(z) \cdot W_{\mathrm{m}}(z) + \big(S(z) - \hat{S}(z)\big) W_{\mathrm{i}}(z)}. \tag{6.143}$$

Thus, the secondary path is changed by the transfer function of the IMC system in a multiplicative way. If $\hat{S}(z) = S(z)$ holds, then the nominal effective secondary path

$$\hat{S}_{\mathrm{f}}^{\mathrm{fimpdo}}(z) = S(z)\big(1 - S(z) W_{\mathrm{i}}(z)\big) \tag{6.144}$$

can be found. This result is the one used to replace the two $\hat{S}(z)$ depicted in Fig. 2.13. It should be noted, that the estimated secondary path inside the pseudo-cascaded system (see Fig. 6.10) remains unchanged by this effect.

Adaptation stability In the case of the FIMPDO structure, the feedback systems influence the gradient of the adaptation algorithm as well. Thus, where in the pure feedforward control structure the gradient is partially calculated by filtering the reference signal with the estimated secondary path $\hat{S}(z)$, now the same signal has to be filtered by the estimated transfer functions of the IMC system $\hat{H}_{\mathrm{i}}(z)$. This influence can also be seen in the effective secondary path seen from the perspective of the feedforward controller (see Eq. 6.143). Because the *real* effective secondary path is not at disposition, the *estimated* nominal effective secondary path $\hat{S}_{\mathrm{f}}^{\mathrm{fimpdo}}(z)$ in Eq. 6.144 is used for the adaptation. The relative deviation between these two

$$\hat{S}_{\mathrm{f}}^{\mathrm{fimpdo}}(z) = \Psi_{\mathrm{f}}^{\mathrm{fimpdo}}(z) S_{\mathrm{f}}^{\mathrm{fimpdo}}(z) \tag{6.145}$$

is used to estimate the maximum step-size μ for the coefficients' update equation. If the equation is used to solve the relative deviation

$$\Psi_{\mathrm{f}}^{\mathrm{fimpdo}}(z) = \frac{\hat{S}_{\mathrm{f}}^{\mathrm{fimpdo}}(z)}{S_{\mathrm{f}}^{\mathrm{fimpdo}}(z)}, \tag{6.146}$$

and Eq. 6.143 and Eq. 6.144 are used to replace the secondary paths

$$\Psi_{\mathrm{f}}^{\mathrm{fimpdo}}(z) = \hat{S}(z)\big(1 - \hat{S}(z)W_{\mathrm{i}}(z)\big)\frac{1 + S(z)W_{\mathrm{m}}(z) + \big(S(z) - \hat{S}(z)\big)W_{\mathrm{i}}(z)}{S(z)\big(1 + \hat{S}(z)W_{\mathrm{m}}(z)\big)\big(1 - \hat{S}(z)W_{\mathrm{i}}(z)\big)} \tag{6.147}$$

$$= \frac{\hat{S}(z)}{S(z)}\frac{1 + S(z)W_{\mathrm{m}}(z) + \big(S(z) - \hat{S}(z)\big)W_{\mathrm{i}}(z)}{1 + \hat{S}(z)W_{\mathrm{m}}(z)} \tag{6.148}$$

an expression for the relative deviation can be found. The relative deviation $\hat{S}(z) = \Psi(z)S(z)$ between the estimated and the real secondary path is used to replace the estimated secondary path in the equation

$$\Psi_{\mathrm{f}}^{\mathrm{fimpdo}}(z) = \Psi(z)\left(\frac{1 + S(z)W_{\mathrm{m}}(z)}{1 + \Psi(z)S(z)W_{\mathrm{m}}(z)} + \frac{\big(1 - \Psi(z)\big)S(z)W_{\mathrm{i}}(z)}{1 + \Psi(z)S(z)W_{\mathrm{m}}(z)}\right). \tag{6.149}$$

As result, it is found that the FIMPDO and the FIM have the same relative deviation. Hence, for the FIMPDO it is also recommended to use the Modified Filtered-x LMS algorithm instead of the Filtered-x LMS algorithm.

6.7. Novel Control Structure with High Dependency Level

In this section, the idea of introducing dependencies between the controllers is further investigated. The approach taken is to move the IMC and MVC transfer functions inside the FF transfer function, i.e.

$$\hat{H}_{\mathrm{FIMDO}}(z) = \hat{H}_{\mathrm{f}}\left(\hat{H}_{\mathrm{i}}(z), H_{\mathrm{m}}(z), z\right).$$

In order to achieve this, the connection strategy presented in Fig. 6.14, called FIMDO, is proposed. If only the feedback controller is analyzed, it can be seen that its connections comprehend the ones of the MVC-IMC combination with independent optima from Fig. 5.1a. Therefore, no dependency between the MVC and IMC controllers is to be expected. If the MVC controller $W_{\mathrm{m}}(z)$ is removed, the connection between the feedforward controller $W_{\mathrm{f}}(z)$ and the IMC controller $W_{\mathrm{i}}(z)$ follows the one presented in Fig. 5.3b. Hence, a dependency between the two controllers is expected. Furthermore, if the IMC controller $W_{\mathrm{i}}(z)$ is removed, then the resulting structure yields the one in Fig. 5.2b of the MVC-FF with de-

pendent optima. Thus, the feedforward controller's optimum is expected to also have a dependency with respect to the MVC controller $W_{\mathrm{m}}(z)$. In order to corroborate these hypotheses, a transfer function analysis is conducted. From Fig. 6.14, the equations

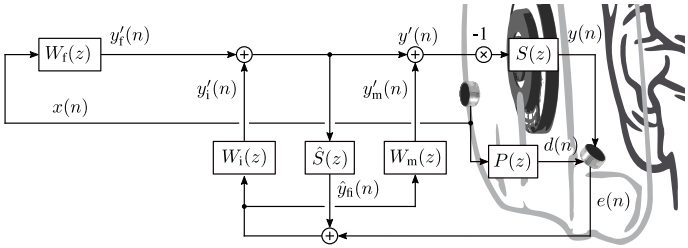

Figure 6.14.: Novel hybrid control structure with dependent optima.

$$E(z) = D(z) + Y(z) \tag{6.150}$$
$$D(z) = P(z)X(z) \tag{6.151}$$
$$Y(z) = -S(z)\big(Y'_{\mathrm{f}}(z) + Y'_{\mathrm{i}}(z) + Y'_{\mathrm{m}}(z)\big) \tag{6.152}$$
$$Y'_{\mathrm{f}}(z) = W_{\mathrm{f}}(z)X(z) \tag{6.153}$$
$$Y'_{\mathrm{m}}(z) = W_{\mathrm{m}}(z)\big(\hat{S}(z)Y'_{\mathrm{f}}(z) + \hat{S}(z)Y'_{\mathrm{i}}(z) + E(z)\big) \tag{6.154}$$

and

$$Y'_{\mathrm{i}}(z) = W_{\mathrm{i}}(z)\big(\hat{S}(z)Y'_{\mathrm{f}}(z) + \hat{S}(z)Y'_{\mathrm{i}}(z) + E(z)\big) \tag{6.155}$$
$$= \frac{W_{\mathrm{i}}(z)\big(\hat{S}(z)Y'_{\mathrm{f}}(z) + E(z)\big)}{1 - \hat{S}(z)W_{\mathrm{i}}(z)} \tag{6.156}$$

are derived. If Eq. 6.153 is used to replace the control signal $Y'_{\mathrm{f}}(z)$ in Eq. 6.156

$$Y'_{\mathrm{i}}(z) = \frac{W_{\mathrm{i}}(z)\big(\hat{S}(z)W_{\mathrm{f}}(z)X(z) + E(z)\big)}{1 - \hat{S}(z)W_{\mathrm{i}}(z)}, \tag{6.157}$$

then $Y_{\mathrm{i}}'(z)$ can be expressed as a function of the signals $X(z)$ and $E(z)$. Using this equation plus Eq. 6.153 in Eq. 6.154

$$Y_{\mathrm{m}}' = W_{\mathrm{m}}\left(\hat{S}\cdot W_{\mathrm{f}}\cdot X + \frac{\hat{S}\cdot W_{\mathrm{i}}\cdot\hat{S}\cdot W_{\mathrm{f}}}{1-\hat{S}\cdot W_{\mathrm{i}}}X + \frac{\hat{S}\cdot W_{\mathrm{i}}}{1-\hat{S}\cdot W_{\mathrm{i}}}E + E\right) \tag{6.158}$$

$$= W_{\mathrm{m}}\left(\frac{(1-\hat{S}\cdot W_{\mathrm{i}})\hat{S}\cdot W_{\mathrm{f}} + \hat{S}\cdot W_{\mathrm{i}}\cdot\hat{S}\cdot W_{\mathrm{f}}}{1-\hat{S}\cdot W_{\mathrm{i}}}X + \frac{\hat{S}\cdot W_{\mathrm{i}}}{1-\hat{S}\cdot W_{\mathrm{i}}}E + E\right) \tag{6.159}$$

$$= W_{\mathrm{m}}\left(\frac{\hat{S}\cdot W_{\mathrm{f}}}{1-\hat{S}\cdot W_{\mathrm{i}}}X + \frac{\hat{S}\cdot W_{\mathrm{i}}+1-\hat{S}\cdot W_{\mathrm{i}}}{1-\hat{S}\cdot W_{\mathrm{i}}}E\right) \tag{6.160}$$

$$= \frac{W_{\mathrm{m}}(\hat{S}\cdot W_{\mathrm{f}}\cdot X + E)}{1-\hat{S}\cdot W_{\mathrm{i}}}, \tag{6.161}$$

the same can be done for the case of Y_{m}'. Using Eq. 6.153, Eq. 6.157, and Eq. 6.161 to replace the control signals in Eq. 6.152

$$Y = -S\frac{(1-\hat{S}\cdot W_{\mathrm{i}})W_{\mathrm{f}}\cdot X + W_{\mathrm{i}}(\hat{S}\cdot W_{\mathrm{f}}\cdot X + E) + W_{\mathrm{m}}(\hat{S}\cdot W_{\mathrm{f}}\cdot X + E)}{1-\hat{S}\cdot W_{\mathrm{i}}} \tag{6.162}$$

$$= -S\frac{W_{\mathrm{f}}\cdot X + W_{\mathrm{i}}\cdot E + W_{\mathrm{m}}\cdot\hat{S}\cdot W_{\mathrm{f}}\cdot X + W_{\mathrm{m}}\cdot E}{1-\hat{S}\cdot W_{\mathrm{i}}} \tag{6.163}$$

$$= -\frac{S\cdot W_{\mathrm{f}} + S\cdot W_{\mathrm{m}}\cdot\hat{S}\cdot W_{\mathrm{f}}}{1-\hat{S}\cdot W_{\mathrm{i}}}X - \frac{S\cdot W_{\mathrm{i}} + S\cdot W_{\mathrm{m}}}{1-\hat{S}\cdot W_{\mathrm{i}}}E, \tag{6.164}$$

the combined control signal Y can be expressed as a function of X and E. Finally, this equation is used together with Eq. 6.151 in Eq. 6.150

$$E = P\cdot X - \frac{S\cdot W_{\mathrm{f}} + S\cdot W_{\mathrm{m}}\cdot\hat{S}\cdot W_{\mathrm{f}}}{1-\hat{S}\cdot W_{\mathrm{i}}}X - \frac{S\cdot W_{\mathrm{i}} + S\cdot W_{\mathrm{m}}}{1-\hat{S}\cdot W_{\mathrm{i}}}E \tag{6.165}$$

$$E = P\cdot X - \frac{S\cdot W_{\mathrm{f}}(1+\hat{S}\cdot W_{\mathrm{m}})}{1-\hat{S}\cdot W_{\mathrm{i}}}X - \frac{S\cdot W_{\mathrm{i}} + S\cdot W_{\mathrm{m}}}{1-\hat{S}\cdot W_{\mathrm{i}}}E \tag{6.166}$$

$$\rightarrow\frac{E}{X}\big(1+S\cdot W_{\mathrm{m}} + (S-\hat{S})W_{\mathrm{i}}\big) = \big(P(1-\hat{S}\cdot W_{\mathrm{i}}) - S\cdot W_{\mathrm{f}}(1+\hat{S}\cdot W_{\mathrm{m}})\big) \tag{6.167}$$

to derive the system's transfer function

$$H_{\mathrm{fimdo}}(z) = \frac{E(z)}{X(z)} = \frac{P(z)\big(1-\hat{S}(z)W_{\mathrm{i}}(z)\big) - S(z)W_{\mathrm{f}}(z)\big(1+\hat{S}(z)W_{\mathrm{m}}(z)\big)}{1+S(z)W_{\mathrm{m}}(z) + \big(S(z)-\hat{S}(z)\big)W_{\mathrm{i}}(z)}. \tag{6.168}$$

As can be seen by comparing it to the transfer function of the previous system, both share the same characteristic function in the denominator and the feedback system is the same. Hence, the stability and performance constraint presented in the previous section apply in this case as well. In cases in which $\hat{S}(z) = S(z)$ holds, the transfer function simplifies to its nominal form

$$\hat{H}_{\mathrm{fimdo}}(z) = P(z)\frac{1 - S(z)W_{\mathrm{i}}(z)}{1 + S(z)W_{\mathrm{m}}(z)} - S(z)W_{\mathrm{f}}(z). \tag{6.169}$$

It can be seen that both feedback stages are combined and a pre-attenuation of the disturbance signal is performed by them. Equivalently, it can be said that both feedback control schemes change the effective primary path. In a frequency response analysis this means that the residual error contains all frequencies that can not be attenuated by the feedback schemes. Thus, with this structure the FF optimum solution basically aims to compensate for the limitations of its feedback counterparts.

6.7.1. The optimal feedforward controller

Given that the feedback components of the system have been designed, the optimal feedforward controller can be calculated. Its derivation is based on the nominal transfer function of the system $\hat{H}_{\mathrm{fimdo}}(z)$, in which it is assumed that the estimated and nominal secondary paths are equal to the real one. The transfer function is used to express the error signal

$$E(z) = P(z)X(z)\frac{1 - S(z)W_{\mathrm{i}}(z)}{1 + S(z)W_{\mathrm{m}}(z)} - S(z)W_{\mathrm{f}}(z)X(z) \tag{6.170}$$

as a function of the reference signal $X(z)$ and the controllers $W_{\mathrm{i}}(z)$, $W_{\mathrm{m}}(z)$, and $W_{\mathrm{f}}(z)$. The equality $D(z) = P(z)X(z)$ is used

$$E(z) = D(z)\frac{1 - S(z)W_{\mathrm{i}}(z)}{1 + S(z)W_{\mathrm{m}}(z)} - S(z)W_{\mathrm{f}}(z)X(z), \tag{6.171}$$

in order to include the disturbance signal $D(z)$ in the stochastic excitation analysis later on. It can be seen from Eq. 6.171 that not only the MVC controller $W_{\mathrm{m}}(z)$ attenuates the disturbance signal $D(z)$, but also the IMC controller $W_{\mathrm{i}}(z)$. The nominal transfer function of the IMC controller (re-written from Eq. 4.7)

$$\hat{H}_{\mathrm{i}}(z) = 1 - S(z)W_{\mathrm{i}}(z) \tag{6.172}$$

and the transfer function of the MVC controller (re-written from Eq. 3.2)

$$H_{\mathrm{m}}(z) = \frac{1}{1 - S(z)W_{\mathrm{m}}(z)} \tag{6.173}$$

are used to replace their contributions in Eq. 6.111

$$E(z) = \hat{H}_{\mathrm{i}}(z) H_{\mathrm{m}}(z) D(z) - S(z) W_{\mathrm{f}}(z) X(z). \tag{6.174}$$

Now, as already discussed in Sec. 2.3, the search for an optimum controller in the Z-domain may yield a controller $W_{\mathrm{f}}(z)$ that is non-causal or non-stable, or both. Therefore, in order to find the finite impulse response of the causal feedforward controller $\mathbf{w}_{\mathrm{f}}$ the notation and considerations presented in Sec. 2.3.1 are used. As a first step, the equation is re-written

$$\mathbf{e} = \mathbf{H}_{\mathrm{i}} \cdot \mathbf{H}_{\mathrm{m}} \cdot \mathbf{d}_{\mathrm{zp}} - \mathbf{S} \cdot \mathbf{W}_{\mathrm{f}} \cdot \mathbf{x}, \tag{6.175}$$

in its equivalent vector-matrix form based on the signals' vectors and systems' impulse responses and Toeplitz matrices. Considering linearity and time invariance, this is rearranged as

$$\mathbf{e} = \mathbf{D}_{\mathrm{zp}} \cdot \mathbf{H}_{\mathrm{i}} \cdot \mathbf{h}_{\mathrm{m}} - \mathbf{X} \cdot \mathbf{S} \cdot \mathbf{w}_{\mathrm{f}}. \tag{6.176}$$

Using this equation, the cost function is defined as the expectation of the quadratic error $\mathbb{E}[\mathbf{e}^{\mathrm{T}}\mathbf{e}]$. In order to find the controller's finite impulse response $\mathbf{w}_{\mathrm{f}}$ that minimizes the cost function, its gradient with respect to the impulse response coefficients is calculated

$$\frac{\partial \mathbb{E}[\mathbf{e}^{\mathrm{T}}\mathbf{e}]}{\partial \mathbf{w}_{\mathrm{f}}} = -2 \cdot \mathbb{E}[(\mathbf{D}_{\mathrm{zp}} \cdot \mathbf{H}_{\mathrm{i}} \cdot \mathbf{h}_{\mathrm{m}} - \mathbf{X} \cdot \mathbf{S} \cdot \mathbf{w}_{\mathrm{f}})^{\mathrm{T}} \mathbf{X} \cdot \mathbf{S}] \tag{6.177}$$

and equated to zero. If the transpose of both sides is taken

$$\mathbf{S}^{\mathrm{T}} \cdot \mathbb{E}\left[\mathbf{X}^{\mathrm{T}} \cdot \mathbf{X}\right] \cdot \mathbf{S} \cdot \mathbf{w}_{\mathrm{f}}^{\mathrm{opt}} = \mathbf{S}^{\mathrm{T}} \cdot \mathbb{E}\left[\mathbf{X}^{\mathrm{T}} \cdot \mathbf{D}_{\mathrm{zp}}\right] \cdot \mathbf{H}_{\mathrm{i}} \cdot \mathbf{h}_{\mathrm{m}} \tag{6.178}$$

the equality fulfilled by the optimal controller's finite impulse response $\mathbf{w}_{\mathrm{f}}^{\mathrm{opt}}$ can be formulated. Using Eq. 2.46 and Eq. 2.47 the cross-correlation $\mathbb{E}\left[\mathbf{X}^{\mathrm{T}} \cdot \mathbf{D}_{\mathrm{zp}}\right]$ and auto-correlation $\mathbb{E}\left[\mathbf{X}^{\mathrm{T}} \cdot \mathbf{X}\right]$ functions are replaced

$$\mathbf{S}^{\mathrm{T}} \cdot \boldsymbol{\Phi}_{xx} \cdot \mathbf{S} \cdot \mathbf{w}_{\mathrm{f}}^{\mathrm{opt}} = \mathbf{S}^{\mathrm{T}} \cdot \boldsymbol{\Phi}_{dx} \cdot \mathbf{H}_{\mathrm{i}} \cdot \mathbf{h}_{\mathrm{m}}. \tag{6.179}$$

Provided that the matrix $\mathbf{S}^{\mathrm{T}} \cdot \boldsymbol{\Phi}_{xx} \cdot \mathbf{S}$ is not singular, the optimal solution for the finite impulse response of the feedforward controller

$$\mathbf{w}_{\mathrm{f}}^{\mathrm{opt}} = \left(\mathbf{S}^{\mathrm{T}} \cdot \boldsymbol{\Phi}_{xx} \cdot \mathbf{S}\right)^{-1} \cdot \mathbf{S}^{\mathrm{T}} \cdot \boldsymbol{\Phi}_{dx} \cdot \mathbf{H}_{\mathrm{i}} \cdot \mathbf{h}_{\mathrm{m}}. \tag{6.180}$$

can be found. As can be seen, the result is very similar to the one found in Eq. 2.49. As a matter of fact, it corresponds to the optimal feedforward controller when used alone, which is convolved by the impulse response of the MVC and IMC systems. This is what is understood as the dependency of the feedforward controller with respect to both feedback controllers. Alternatively, if the free-field excitation scenario is similarly analyzed, the

optimum solution takes the form

$$\hat{\mathbf{w}}_{\mathrm{f}}^{\mathrm{opt}} = \left(\mathbf{S}^{\mathrm{T}} \cdot \mathbf{\Phi}_{xx} \cdot \mathbf{S}\right)^{-1} \cdot \mathbf{S}^{\mathrm{T}} \cdot \mathbf{\Phi}_{xx} \cdot \mathbf{H}_{\mathrm{i}} \cdot \mathbf{H}_{\mathrm{m}} \cdot \mathbf{p}_{\mathrm{zp}}. \tag{6.181}$$

One can see that the primary path's impulse response $\mathbf{p}_{\mathrm{zp}}$ is convolved with the one of the MVC and IMC transfer functions. Thus, reaffirming the direct dependency of the result with respect to the feedback controllers.

Optimization results

In this subsection the advantages of the FIMDO structure in comparison to the classical feedforward scheme are evaluated. For this purpose, the same simulation procedure and parameters described in Sec. 6.5.1 are used. The feedforward controllers are derived following Eq. 2.50 for the classical controller and Eq. 6.181 for the controller of the novel structure. Afterwards, the impulse responses with length 8192 of both systems $h_{\mathrm{f}}(n)$ and $h_{\mathrm{fimdo}}(n)$ are calculated by means of a sample-by-sample simulation of the system under control. The resulting impulse responses are used for the evaluation.

In Fig. 6.15 the impulse responses of the primary path $p(n)$, the feedforward system $h_{\mathrm{f}}(n)$, and the FIMDO system $h_{\mathrm{fimdo}}(n)$ are presented. In Fig. 6.15a the results achieved with a controller length L_w equal to the primary path impulse response length L_p are presented. It is clear, that also with this novel control structure no differences can be seen when the system is compared to one that is under the control of an optimally-long feedforward controller. Hence, no improvement due to relaxations of the limitations imposed by the secondary path can be seen.

In Fig. 6.15b the results achieved with a controller length shorter than the one of the primary path impulse response are presented. One can see that from the fifth up to approx. the 40^{th} sample, both impulse responses have a similar transient, which are also similar to ones seen in Fig. 6.7a. However, $h_{\mathrm{fimdo}}(n)$ produces a slightly higher amplitude than $h_{\mathrm{f}}(n)$. Therefore, it is expected that in the frequencies near $f = 0\,\mathrm{Hz}$ the FIMDO structure achieves worse results as the FF scheme. From the 40^{th} to approximately the 70^{th} sample both controllers show a divergent oscillatory behavior. Until the 100^{th} sample, both impulse responses reach a similar amplitude. Nevertheless, after the 100^{th} sample, it can be seen that the pseudo-cascaded system favorably changes the response of the FIMDO system. Thus, several similarities can be seen by comparing the impulse response of FIMDO system and the equivalent one of the FIM system in Fig. 6.7b. The differences concentrate in the transient between the 70^{th} and 100^{th} samples, where the impulse response of the FIM system reaches smaller amplitudes than the one of the FIMDO. Hence, comparable but inferior results can be expected from FIMDO, when they are compared to

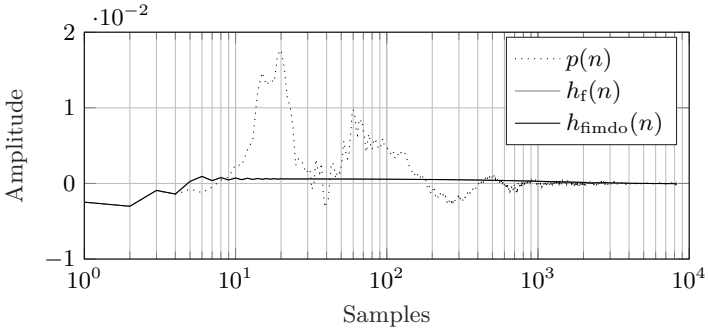

(a) $L_w = 8192$

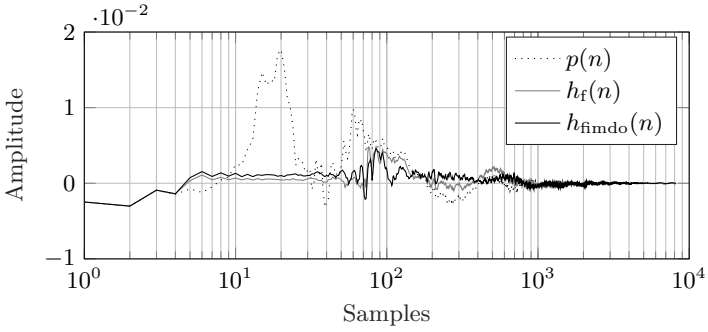

(b) $L_w = 64$

Figure 6.15.: System impulse response $h_{\text{fimdo}}(f)$ compared to the system subject to no control $p(n)$ and subject to the classical feedforward controller $h_{\text{f}}(f)$. Please note that the x-axis is in logarithmic scale. Parameters: $f_s = 48\,\text{kHz}$, $L_{h_{\text{i}}} = 2048$, $L_{h_{\text{m}}} = 2048$, $L_{h_{\text{mi}}} = 2048$, $L_s = 2048$, $L_p = 8192$, $\Phi_{xx} = I$.

the ones achievable with FIM.

In Fig. 6.16 the frequency responses of the impulse responses in Fig. 6.15 are presented. In Fig. 6.16a the results achieved with a controller length L_w equal to the primary path impulse response length L_p are presented. One can see that the frequency response achieved with both control approaches is very similar. However, if the controller length is shorter than the one of the primary path, as the case presented in Fig. 6.16b, substantial advantages can be seen. For all frequencies below 700 Hz one can see that $H_{\text{fimdo}}(f)$ shows up to 20 dB more attenuation than $H_{\text{f}}(f)$. Furthermore, $H_{\text{fimdo}}(f)$ shows at 450 Hz an attenuation even higher than the one achievable with the optimum controller length. Attenuation can be achieved

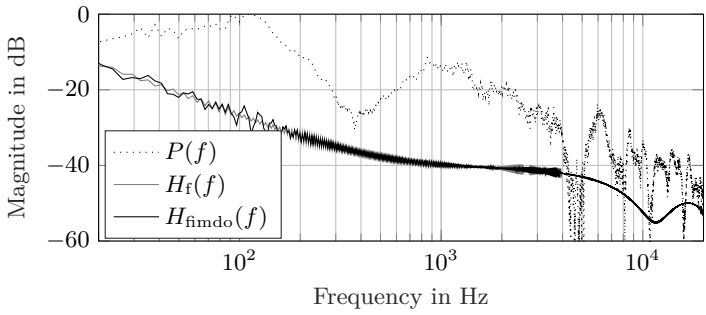

(a) $L_w = 8192$

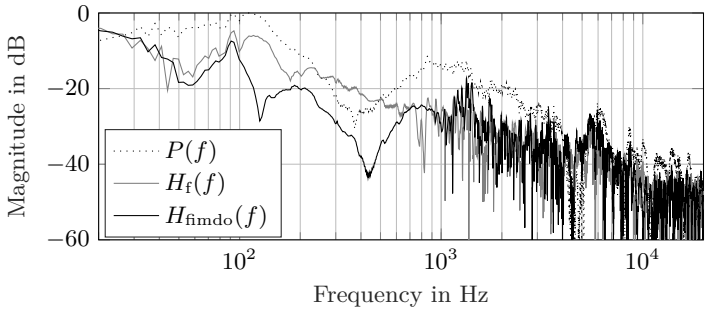

(b) $L_w = 64$

Figure 6.16.: System frequency response $H_{\mathrm{fimdo}}(f)$ compared to the system subject to no control $P(f)$ and subject to the classical feedforward controller $H_{\mathrm{f}}(f)$. Parameters: $f_s = 48\,\mathrm{kHz}$, $L_{h_{\mathrm{i}}} = 2048$, $L_{h_{\mathrm{m}}} = 2048$, $L_{h_{\mathrm{mi}}} = 2048$, $L_s = 2048$, $L_p = 8192$, $\Phi_{xx} = I$.

even in the frequency range between 250 and 500 Hz, where $H_{\mathrm{f}}(f)$ shows a peak amplification of almost 10 dB. If the improvements and its bandwidth are compared with the frequency response of the pseudo-cascaded system $H_{\mathrm{mi}}(f)$ in Fig. 6.5, it can be seen that the influence of the pseudo-cascaded system can not be directly be accounted for the extra attenuation. This is because the feedforward controller is able to find a new optimum subject to the influences of the IMC and MVC controllers. In order to know in which extend the new optimum differs from the one of the FF system, the controller's frequency response has to be analyzed.

The frequency responses of the feedforward controllers $W_{\mathrm{f}}(f)$ and $W_{\mathrm{fimdo}}(f)$ are presented in Fig. 6.17. Together with them, the magnitude response of the naive optimum controller $P(f)/S(f)$ is presented as reference for

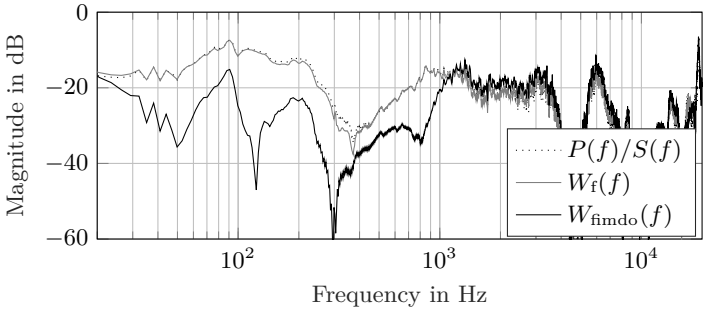

(a) $L_w = 8192$

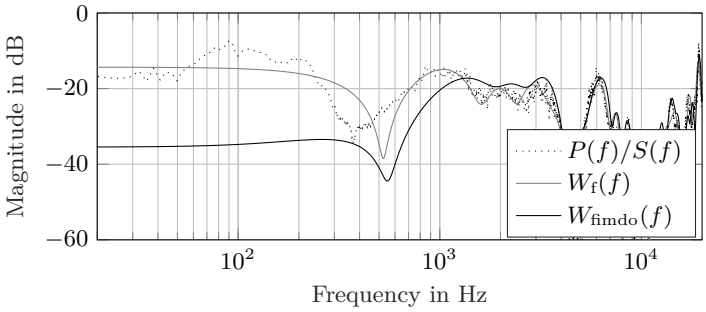

(b) $L_w = 64$

Figure 6.17.: Controller frequency response $W_{\mathrm{fimdo}}(f)$ compared to the one of the classical feedforward $W_{\mathrm{f}}(f)$. Parameters: $f_s = 48\,\mathrm{kHz}$, $L_{h_{\mathrm{i}}} = 2048$, $L_{h_{\mathrm{m}}} = 2048$, $L_{h_{\mathrm{mi}}} = 2048$, $L_s = 2048$, $L_p = 8192$, $\Phi_{xx} = I$.

an ideal controller. In Fig. 6.17a the results achieved with a controller impulse response length L_w equal to the primary path length L_p are presented. It can be seen that the feedforward controller $W_{\mathrm{f}}(f)$ is over all frequencies very close to the ideal controller. In contrast, the FIMDO controller $W_{\mathrm{fimdo}}(f)$ shows less gain in the low-frequencies up to 1 kHz and beyond this frequency, a small but homogeneous increase in gain can be seen. This deviation in gain coincides with the frequency response of the pseudo-cascaded system in Fig. 6.5. Nevertheless, it is known from the results presented in Fig. 6.16a, that both systems achieve the same attenuation performance. Therefore, the influence of the pseudo-cascaded system does not impose any limitation for the FF system to achieve the optimum.

The results achieved with a controller length L_w shorter than the one of the primary path L_p are presented in Fig. 6.17b. One can see that for fre-

quencies higher than 1 kHz $W_{\text{fimdo}}(f)$ shows a frequency response slightly higher than the one of $W_{\text{f}}(f)$. In contrast, in the low frequencies $W_{\text{fimdo}}(f)$ shows a magnitude that is 20 dB smaller than the one of $W_{\text{f}}(f)$. The better results shown in Fig. 6.16b are, therefore, achieved by the pseudo-cascaded system and are not subject to deterioration because of limitations suffered by the FF system.

The equivalent filtered-x LMS

In this section the coefficients' update equation for iteratively approximating the FIMDO feedforward optimal controller is derived. For this purpose the gradient in Eq. 6.177 is approximated by the mean over L_e samples

$$\nabla f_c(\mathbf{w}_{\text{f}}) = \frac{\partial \mathbb{E}[\mathbf{e}^{\text{T}}\mathbf{e}]}{\partial \mathbf{w}_{\text{f}}} \approx -\frac{2}{L_e}(\mathbf{D}_{\text{zp}} \cdot \mathbf{H}_{\text{i}} \cdot \mathbf{h}_{\text{m}} - \mathbf{X} \cdot \mathbf{S} \cdot \mathbf{w}_{\text{f}})^{\text{T}}\mathbf{X} \cdot \mathbf{S}. \quad (6.182)$$

The vector within parenthesis is replaced by the one of the error signal

$$\nabla f_c(\mathbf{w}_{\text{f}}) = \frac{\partial \mathbb{E}[\mathbf{e}^{\text{T}}\mathbf{e}]}{\partial \mathbf{w}_{\text{f}}} \approx -\frac{2}{L_e}\mathbf{e}^{\text{T}} \cdot \mathbf{X} \cdot \mathbf{S} \quad (6.183)$$

and then both sides of the equation are transposed

$$\nabla f_c^{\text{T}}(\mathbf{w}_{\text{f}}) \approx -\frac{2}{L_e}\mathbf{S}^{\text{T}} \cdot \mathbf{X}^{\text{T}} \cdot \mathbf{e}. \quad (6.184)$$

At this point is clear that the IMC and MVC systems do not influence the estimated gradient. Moreover, just like with the classical Filtered-x LMS algorithm, the reference signal is filtered only by the secondary path

$$\mathbf{x}_{\text{s}} = \mathbf{X} \cdot \mathbf{s}. \quad (6.185)$$

Therefore, the coefficients' update equation needed for approximating the feedforward controller of the FIMDO structure is the same as in the classical Filtered-x LMS algorithm

$$\mathbf{w}_{\text{f}}(n+1) = \mathbf{w}_{\text{f}}(n) + \mu \cdot \mathbf{x}_{\text{s}}^{\text{T}} \cdot e(n) \quad (6.186)$$

Moreover, if the FIMDO structure is implemented with such an adaptive feedforward controller $W_{\text{f}}(z)$, time-dependent feedback controllers can be used, without additional changes in the adaptation algorithm.

The equivalent modified normalized filtered-x LMS

As discussed in Sec. 2.4, the use of the Modified Normalized Filtered-x LMS algorithm simplifies the search for the step-size parameter μ and shows a more reliable adaptation stability. In order to be able to use this algorithm, though, the effective secondary path seen from the perspective

of the feedforward controller has to be calculated. For this purpose, the reference and disturbance signals in Fig. 6.14 are set to zero $x(n)$=$d(n)$=0, and the feedforward control signal $y_\mathrm{f}'(n)$ is considered the input and the residual error $e(n)$ the output of the system. Thus, the equations

$$E(z) = -S(z)\big(Y_\mathrm{f}'(z) + Y_\mathrm{i}'(z) + Y_\mathrm{m}'(z)\big), \tag{6.187}$$

$$Y_\mathrm{m}'(z) = W_\mathrm{m}(z)\big(\hat{S}(z)Y_\mathrm{f}'(z) + \hat{S}(z)Y_\mathrm{i}'(z) + E(z)\big), \tag{6.188}$$

and

$$Y_\mathrm{i}'(z) = W_\mathrm{i}(z)\big(\hat{S}(z)Y_\mathrm{f}'(z) + \hat{S}(z)Y_\mathrm{i}'(z) + E(z)\big) \tag{6.189}$$

$$= \frac{W_\mathrm{i}(z)\big(\hat{S}(z)Y_\mathrm{f}'(z) + E(z)\big)}{1 - \hat{S}(z)W_\mathrm{i}(z)} \tag{6.190}$$

are derived. If Eq. 6.190 is used to replace $Y_\mathrm{i}'(z)$ in Eq. 6.188

$$Y_\mathrm{m}' = W_\mathrm{m}\left(\hat{S}\cdot Y_\mathrm{f}' + \frac{\hat{S}\cdot W_\mathrm{i}(\hat{S}\cdot Y_\mathrm{f}' + E)}{1 - \hat{S}\cdot W_\mathrm{i}} + E\right) \tag{6.191}$$

$$= W_\mathrm{m}\left(\hat{S}\cdot Y_\mathrm{f}' + \frac{\hat{S}\cdot W_\mathrm{i}\cdot\hat{S}}{1 - \hat{S}\cdot W_\mathrm{i}}Y_\mathrm{f}' + \frac{\hat{S}\cdot W_\mathrm{i}}{1 - \hat{S}\cdot W_\mathrm{i}}E + E\right) \tag{6.192}$$

$$= \frac{\hat{S}\cdot W_\mathrm{m}}{1 - \hat{S}\cdot W_\mathrm{i}}Y_\mathrm{f}' + \frac{W_\mathrm{m}}{1 - \hat{S}\cdot W_\mathrm{i}}E \tag{6.193}$$

$$= \frac{W_\mathrm{m}(\hat{S}\cdot Y_\mathrm{f}' + E)}{1 - \hat{S}\cdot W_\mathrm{i}}, \tag{6.194}$$

then Y_m' can be expressed as a function of E. This can be used together with Eq. 6.190 in Eq. 6.187

$$E = -S\left(Y_\mathrm{f}' + \frac{W_\mathrm{m}(\hat{S}\cdot Y_\mathrm{f}' + E)}{1 - \hat{S}\cdot W_\mathrm{i}} + \frac{W_\mathrm{i}(\hat{S}\cdot Y_\mathrm{f}' + E)}{1 - \hat{S}\cdot W_\mathrm{i}}\right) \tag{6.195}$$

$$= -S\cdot Y_\mathrm{f}' - S\cdot\frac{\hat{S}(W_\mathrm{m} + W_\mathrm{i})}{1 - \hat{S}\cdot W_\mathrm{i}}Y_\mathrm{f}' - S\cdot\frac{W_\mathrm{m} + W_\mathrm{i}}{1 - \hat{S}\cdot W_\mathrm{i}}E \tag{6.196}$$

$$\rightarrow E\left(1 + S\frac{W_\mathrm{m} + W_\mathrm{i}}{1 - \hat{S}\cdot W_\mathrm{i}}\right) = -S\left(1 + \hat{S}\frac{W_\mathrm{m} + W_\mathrm{i}}{1 - \hat{S}\cdot W_\mathrm{i}}\right)Y_\mathrm{f}' \tag{6.197}$$

$$\rightarrow E\frac{1 + S\cdot W_\mathrm{m} + (S - \hat{S})W_\mathrm{i}}{1 - \hat{S}\cdot W_\mathrm{i}} = -S\cdot\frac{1 + \hat{S}\cdot W_\mathrm{m}}{1 - \hat{S}\cdot W_\mathrm{i}}\cdot Y_\mathrm{f}' \tag{6.198}$$

to derive the FF effective secondary path

$$S_{\mathrm{f}}^{\mathrm{fimdo}}(z) = -\frac{E}{Y_{\mathrm{f}}'} = S(z)\frac{1+\hat{S}(z)\cdot W_{\mathrm{m}}(z)}{1+S(z)\cdot W_{\mathrm{m}}(z)+\big(S(z)-\hat{S}(z)\big)W_{\mathrm{i}}(z)}. \tag{6.199}$$

It can be seen that the influence of the IMC controller $W_{\mathrm{i}}(z)$ is weighted by the difference between estimated and real secondary paths $\big(S(z)-\hat{S}(z)\big)$. It is also seen that on top of this, the influence of the MVC controller $W_{\mathrm{m}}(z)$ is govern by the quotient $\big(1+\hat{S}(z)\cdot W_{\mathrm{m}}(z)\big)/\big(1+S(z)\cdot W_{\mathrm{m}}(z)\big)$. So under certain circumstances their effect is minimum. Moreover, if $\hat{S}(z) = S(z)$ holds, then this yields the *nominal* effective secondary path

$$\hat{S}_{\mathrm{f}}^{\mathrm{fimdo}}(z) = S(z). \tag{6.200}$$

Therefore, for implementing the MNFxLMS algorithm, no changes are required for deriving the signals in Fig. 2.13.

Adaptation stability In the case of the FIMDO structure, the pseudo-cascaded feedback system does not influence the gradient of the adaptation algorithm under *nominal* conditions. Hence, the filtered-reference is calculated by means of the estimated secondary path $\hat{S}(z)$ from Eq. 6.200. However, the *real* secondary path from Eq. 6.199 shows a more complex dependency with respect to the feedback controllers. In order to account for any differences that the nominal and real secondary paths may have, the relative deviation

$$\hat{S}_{\mathrm{f}}^{\mathrm{fimdo}}(z) = \Psi_{\mathrm{f}}^{\mathrm{fimdo}}(z)S_{\mathrm{f}}^{\mathrm{fimdo}}(z) \tag{6.201}$$

between these two is calculated. If the equation is used to solve the relative deviation

$$\Psi_{\mathrm{f}}^{\mathrm{fimdo}}(z) = \frac{\hat{S}_{\mathrm{f}}^{\mathrm{fimdo}}(z)}{S_{\mathrm{f}}^{\mathrm{fimdo}}(z)}, \tag{6.202}$$

and Eq. 6.199 and Eq. 6.200 are used to replace the secondary paths

$$\Psi_{\mathrm{f}}^{\mathrm{fimdo}}(z) = \hat{S}(z)\frac{1+S(z)W_{\mathrm{m}}(z)+(S(z)-\hat{S}(z)W_{\mathrm{i}}(z)}{S(z)\big(1+\hat{S}(z)W_{\mathrm{m}}(z)\big)} \tag{6.203}$$

$$= \frac{\hat{S}(z)}{S(z)}\frac{1+S(z)W_{\mathrm{m}}(z)+(S(z)-\hat{S}(z)W_{\mathrm{i}}(z)}{1+\hat{S}(z)W_{\mathrm{m}}(z)} \tag{6.204}$$

an expression for the relative deviation can be found. The relative deviation $\hat{S}(z) = \Psi(z)S(z)$ between the estimated and the real secondary path

is used to replace the estimated secondary path in the equation

$$\Psi_{\mathrm{f}}^{\mathrm{fimdo}}(z) = \Psi(z)\left(\frac{1 + S(z)W_{\mathrm{m}}(z)}{1 + \Psi(z)S(z)W_{\mathrm{m}}(z)} + \frac{\big(1 - \Psi(z)\big)S(z)W_{\mathrm{i}}(z)}{1 + \Psi(z)S(z)W_{\mathrm{m}}(z)}\right). \tag{6.205}$$

As result, it can be seen that the deviation $\Psi(z)$, originally used for the simple case of a feedforward adaptive controller, is weighted over frequency by the feedback controllers $W_{\mathrm{m}}(z)$ and $W_{\mathrm{i}}(z)$. The same result has been seen for the first two novel control structures. Hence, in this case it is also recommended to use the Modified Filtered-x LMS algorithm instead of the Filtered-x LMS algorithm for iteratively finding the optimal feedforward controller.

6.8. Pseudo-Cascaded Controller Integration for Adaptive Feedforward Control

A feedforward controller's dependency on the primary path $P(z)$ makes it susceptible to performance loss upon moving noise sources. In order to cope with this issue an iterative search for a optimum impulse response $\mathbf{w}_{\mathrm{f}}$ can be implemented by means of adaptive filters. Between the adaptation algorithms analyzed in the present work, the Modified Normalized Filtered-x LMS (MNFxLMS) offers the possibility to ensure adaptation stability, provided that the maximum magnitude deviation between the estimated secondary path $\hat{S}(z)$ and the real one $S(z)$ can be estimated. Each novel control structure has shown to change the effective secondary path seen from its feedforward controller's perspective in a unique way. These changes also alter the way in which the MNFxLMS calculates the signals required for adapting the feedforward controller $W_{\mathrm{f}}(z)$. However, although the effective secondary path is indeed different, the relative deviation between estimated and real secondary path is the same. This means that the step-size μ_0 that yields a stable adaptation can be chosen equal for all three novel structures. Moreover, despite the differences between the effective secondary paths, their similarities are enough to enable their implementation in one macro-system, whose parameters can be set to yield either one of these novel control structures. The block diagram of such a macro-system is presented in Fig. 6.18. On the top, the three controllers $W_{\mathrm{f}}(z)$, $W_{\mathrm{m}}(z)$, and $W_{\mathrm{i}}(z)$ and estimated secondary path $\hat{S}(z)$ are connected in a way similar to the system presented in Fig. 6.6. On the level below, an estimated secondary path is used together with two switches to incorporate the feedforward controller signal at the right position in the pseudo-cascaded system. If both switches are off, the system yields the FIM structure presented in Fig. 6.6. If only the left-hand side switch is turned on, the connection yields the FIMPDO structure pre-

sented in Fig. 6.10. If only the right-hand side switch is turned on, the system is equivalent to the FIMDO structure presented in Fig. 6.14. In series connection with the estimated secondary path a switch with three connections is found. Depending on its position the secondary path is combined either with the nominal transfer function of the IMC system $\hat{H}_{\mathrm{i}}(z)$, for the FIMPDO structure, or with the nominal transfer function of the pseudo-cascaded system $\hat{H}_{\mathrm{mi}}(z)$, for the FIM structure. In the case of the FIMDO structure, it is known that the effective secondary path is not subject to changes due to the elements in the feedback controller. The output of the switch is used together with the residual error $e(n)$ to estimate the disturbance signal $\hat{d}(n)$ required for the system adaptation (see Fig. 2.13). One level below, the same series connection is used to provide the filtered reference to the LMS algorithm. The adaptive controller coefficients in this level are copied to the feedforward controller, in order to calculate the feedforward control signal $y'_{\mathrm{f}}(n)$.

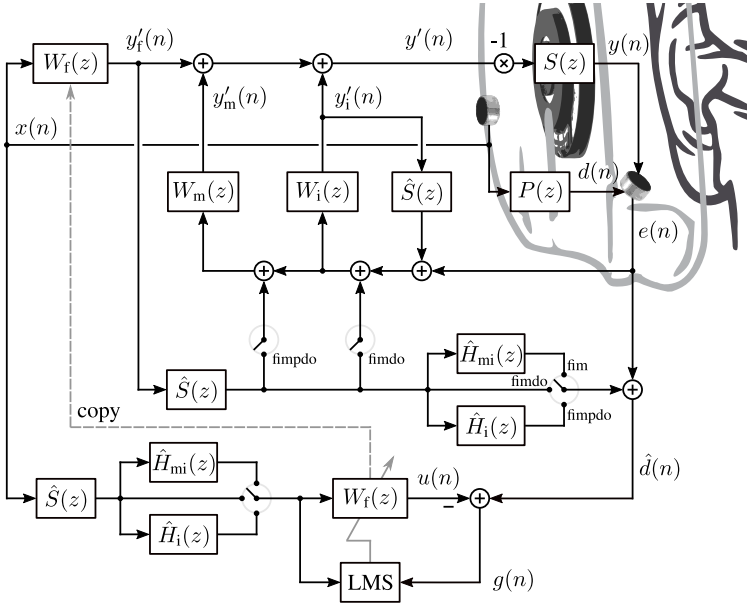

Figure 6.18.: All three novel hybrid control structures implemented in a single system using a Modified Normalized Filtered-x LMS algorithm for the adaptation of the feedforward controller.

As seen in the optimization results of all three structures, the FIMPDO structure offers the worst attenuation performance and is, therefore, not as

attractive as the other two alternatives. If its implementation is omitted, then some simplifications in the macro-controller can be done. The simplified block diagram is presented in Fig. 6.19. On the top one can see that the calculation of the control signals remains relatively unaltered. One level below one can see that, since the FIMPDO switch is not present anymore, there is no more need for keeping the estimated secondary path and the influences of the pseudo-cascaded separated. Instead of switching between outputs, now the impulse responses of the effective secondary paths are exchanged. Note that $\hat{S}_{\mathrm{f}}^{\mathrm{fimdo}}(z) = \hat{S}(z)$ and $\hat{S}_{\mathrm{f}}^{\mathrm{fim}}(z) = \hat{S}(z)\hat{H}_{\mathrm{mi}}(z)$. In case that the controller should yield the FIMDO structure, a switch is at disposition to incorporate the filtered feedforward control signal to the pseudo-cascaded system. Here, the signal is connected *outside* the pseudo-cascaded controller and not just before being used by the IMC controller $W_{\mathrm{i}}(z)$. In the lowest level, the same principle of replacing the effective secondary path with either $\hat{S}_{\mathrm{f}}^{\mathrm{fimdo}}(z)$ or $\hat{S}_{\mathrm{f}}^{\mathrm{fim}}(z)$ is followed.

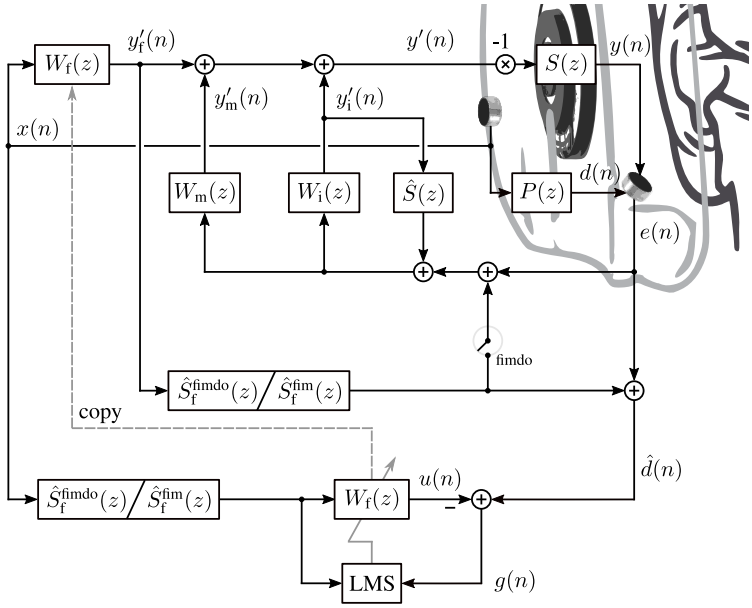

Figure 6.19.: FIM and FIMDO hybrid control structures implemented in a single system using a Modified Normalized Filtered-x LMS adaptation algorithm for the feedforward controller.

Once the feedback controllers are optimized, there is the opportunity to simplify the implementation by calculating the equivalent MVC controller

$\tilde{W}_{\mathrm{m}}(z)$. This gives the opportunity to avoid design decisions related to the fixed-point implementation of recursive systems, like for example the signals' bit-width required to achieve a minimum deviation from the original frequency response. As a result, the impulse response of an otherwise infinite response system is limited to a finite length. However, by optimizing the *shorter* impulse responses of $W_{\mathrm{i}}(z)$ and $W_{\mathrm{m}}(z)$, a far longer optimum finite impulse response can be estimated. Following this idea, the block diagram presented in Fig. 6.20 is proposed. Here, the pseudo-cascaded system and the optimum solutions for its parameters are used to calculate a finite impulse response, which is loaded in a single equivalent MVC controller $\tilde{W}_{\mathrm{m}}(z)$. The output of this system is equivalent to the addition of the outputs $y'_{\mathrm{m}}(n)$ and $y'_{\mathrm{i}}(n)$ of the MVC controller and IMC controller, respectively. Hence, before the system is turned on, an estimated secondary path $\hat{S}(z)$ and its related multiplicative uncertainty over frequency $G_2(f)$ are used together with other parameters to optimize the feedback controllers' impulse responses $\mathbf{w}_{\mathrm{i}}(z)$ and $\mathbf{w}_{\mathrm{m}}(z)$. Subsequently, these are used to estimate $\hat{H}_{\mathrm{mi}}(z)$ and with it also the effective secondary paths $\hat{S}_{\mathrm{f}}^{\mathrm{fim}}(z)$ and $\hat{S}_{\mathrm{f}}^{\mathrm{fimdo}}(z)$. In parallel to this, the equivalent MVC controller $\tilde{W}_{\mathrm{m}}(z)$ is calculated. Once the system is turned on, all parameters for the control of the macro-controller are at disposition and the adaptation of $\mathbf{w}_{\mathrm{f}}(z)$ can be started. By setting the parameters of this system correctly, all ANC structures described in this work, except for the FIMPDO structure can be implemented.

6.9. Summary

In the present chapter three novel control structures are presented. These combine all three classical control structures, namely FF, MVC, and IMC schemes, into one system. The combination of all three schemes results from the use of the hybrid combination strategy and the pseudo-cascaded combination principle. In the former a feedforward and a feedback system are combined in order to calculate a control signal exploiting the information contained in the reference signal $x(n)$ and residual error $e(n)$. In the pseudo-cascaded combination principle an estimation of the residual error produced by one feedback controller is performed to improve the control signal before this is played through the headphones.

In order to optimize the impulse response of the pseudo-cascaded system, the stability and performance principles presented in Chapter 3 and Chapter 4 are extended to the application of this more complex system. Based on the constraints derived from these principles, the co-optimization of the impulse response of both controllers $\mathbf{w}_{\mathrm{i}}$ and $\mathbf{w}_{\mathrm{m}}$ is formulated as an optimization with a non-convex cost function subject to convex constraints. Based on the optimization results it is found that the pseudo-cascaded sys-

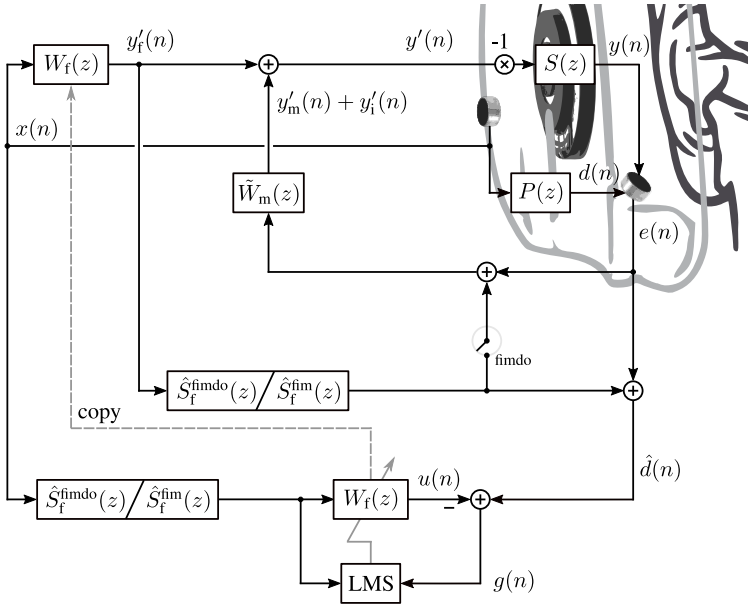

Figure 6.20.: FIM and FIMDO hybrid control structures implemented in a single system using the equivalent MVC controller $\tilde{W}_\mathrm{m}(z)$ and a Modified Normalized Filtered-x LMS adaptation algorithm for the feedforward controller.

tem produces a higher attenuation magnitude in the low frequencies than the IMC and MVC controllers. The better results come with a higher computational cost during the optimization, because of the more constraints that are required for this optimization. Nevertheless, because the pseudo-cascaded system is of recursive nature, its optimization yields an optimal infinite impulse response.

Based on three connection strategies a feedforward controller is combined to form a hybrid system with the optimized pseudo-cascaded controller. For each novel control structure an optimal Wiener controller is derived to determine the impulse response of the feedforward controller $\mathbf{w}_\mathrm{f}$. It is found that this optimum solution is different for each one of the connection strategies. To be more specific, the Wiener controller of the FIM structure can be calculated without knowing the pseudo-cascaded controller parameters exactly. This, because in its equation

$$\mathbf{w}_\mathrm{f}^\mathrm{fim} = \left(\mathbf{S}^\mathrm{T} \cdot \mathbf{\Phi}_{xx}^\mathrm{im} \cdot \mathbf{S}\right)^{-1} \cdot \mathbf{S}^\mathrm{T} \cdot \boldsymbol{\phi}_{dx}^\mathrm{im}, \tag{6.206}$$

the effect of the pseudo-cascaded system is only the one of a spectrum-weighting of the auto- and cross-correlation functions. The Wiener controller of the FIMPDO structure

$$\mathbf{w}_{\mathrm{f}}^{\mathrm{fimpdo}} = \left(\mathbf{S}^{\mathrm{T}} \cdot \mathbf{\Phi}_{xx}^{\mathrm{i}} \cdot \mathbf{S}\right)^{-1} \cdot \mathbf{S}^{\mathrm{T}} \cdot \mathbf{\Phi}_{dx}^{\mathrm{i}} \cdot \mathbf{h}_{\mathrm{m}} \tag{6.207}$$

shows an explicit dependency on to the parameters of IMC controller, as it is convolved with the IMC system's impulse response. The Wiener controller of the FIMDO structure

$$\mathbf{w}_{\mathrm{f}}^{\mathrm{fimdo}} = \left(\mathbf{S}^{\mathrm{T}} \cdot \mathbf{\Phi}_{xx} \cdot \mathbf{S}\right)^{-1} \cdot \mathbf{S}^{\mathrm{T}} \cdot \mathbf{\Phi}_{dx} \cdot \mathbf{H}_{\mathrm{i}} \cdot \mathbf{h}_{\mathrm{m}}. \tag{6.208}$$

shows an even greater dependency on the pseudo-cascaded controller. However, if these systems are implemented as adaptive controllers, these dependencies towards the pseudo-cascaded system change. Hence, although for the derivation of the FIM Wiener controller no explicit information regarding $W_{\mathrm{i}}(z)$ and $W_{\mathrm{m}}(z)$ is required, through the FIM effective secondary path

$$\hat{S}_{\mathrm{f}}^{\mathrm{fim}}(z) = S(z)\frac{1 - S(z)W_{\mathrm{i}}(z)}{1 + S(z)W_{\mathrm{m}}(z)} \tag{6.209}$$

a new dependency is found in the effective secondary path. Without this information an estimation of the cost function gradient with respect to the controller parameters is not feasible. In the case of the FIMPDO the Wiener controller requires information about the MVC controller $W_{\mathrm{m}}(z)$, but the effective secondary path

$$\hat{S}_{\mathrm{f}}^{\mathrm{fimpdo}}(z) = S(z)\left(1 - S(z)W_{\mathrm{i}}(z)\right) \tag{6.210}$$

depends only on the IMC controller's $W_{\mathrm{i}}(z)$ parameters. In the case of the FIMDO, its adaptive implementation requires an effective secondary path

$$\hat{S}_{\mathrm{f}}^{\mathrm{fimdo}}(z) = S(z), \tag{6.211}$$

which only depends on the real one. Therefore, FIMDO shows an important advantage in comparison with the other two structures, when it is implemented as an adaptive controller.

CHAPTER 7

Measurements

The overview of the experimental setup is presented in Fig. 7.1. A Neumann KU100 dummy-head is placed inside a room designed for audio-listening with dimensions 4.80 m x 4.20 m x 2.0 m. At a 1 m distance left and right from the dummy-head two Genelec 8030B speakers are placed. The speakers are connected to an RME Fireface UCX audio interface, which is used to generate the excitation signals and to record by means of the dummy-head at a sampling rate of 48 kHz. The ANC headphones prototype from [Rivera Benois et al., 2019] based on a Beyerdynamic DT 770 PRO headset customized with inner and outer electret microphones on its earcups is utilized as system under test. From this, only the earcup covering the dummy-head's right ear and the error microphone in the center position will be considered. Microphone preamplifiers with a gain of 20 dB are used to better match the expected dynamic range of the microphones' signal with the ± 10 V input range of the dSpace FPGA-based real-time platform. Additional to that, a PreSonus HP4 headphones amplifier is used to connect the two-channel output of the dSpace platform to the headphones. The excitation used is a uniformly distributed white noise signal, amplitude modulated with a modulation frequency of 70 Hz and a modulation degree of 50%, in order to generate some degree of roughness. The intensity of the signal measured at the right earcup, when played from the ipsilateral loudspeaker is 88.7 $\mathrm{dB_{SPL}}$. During the measurements the excitation signal is played either from the ipsilateral loudspeaker or from the contralateral one.

The macro-controller based on the Modified Normalized Filtered-x LMS presented in Fig. 6.20 is implemented on the FPGA-side of the dSpace

Figure 7.1.: Overview of the experimental setup used for the evaluation.

platform. The processor-side of the platform enables the communication with the FPGA-side by means of registers and buffers. Through this mechanism the adaptation, the effective secondary paths' impulse responses, the switch, and the feedback controller impulse response can be changed, without the need of a new FPGA hardware descriptor. The macro-controller works at a sampling rate of $f_s = 48\,\mathrm{kHz}$, with an internal clock of $f_{\mathrm{clk}} = 100\,\mathrm{MHz}$. The measured delay of the platform between A/D and D/A converters is $\tau_{ad} + \tau_{dsp} + \tau_{da} \approx 2.03\,\mu\mathrm{s}$. An adaptive feedforward controller $W_{\mathrm{f}}(z)$ of length $L_w = 512$ is used, which is adapted using estimated effective secondary paths $\hat{S}_{\mathrm{f}}^{fim}(z)$ and $\hat{S}_{\mathrm{f}}^{fimdo}(z)$ of lengths $L_s = 2048$. The equivalent MVC controller $\tilde{W}_{\mathrm{m}}(z)$ has an impulse response length of $L_{\tilde{w}_m}$=1024.

A measurement of the secondary path $S(z)$ is performed off-line. Through this measurement the nominal secondary path is estimated. Subsequently, the impulse responses of an MVC, an IMC, and a pseudo-cascaded controller with respective lengths $L_{\mathrm{m}} = 128$, $L_{\mathrm{i}} = 128$, and $L_{\mathrm{i,m}} = 64$ are optimized subject to the constraint combination $G_2G_3G_4$ (G_2: robust stability, G_3: nominal performance, G_4: max. equiv. MVC gain). The obtained controller parameters are used to calculate the equivalent MVC controller, which impulse response is loaded and used for the measurements. In the case of the MVC controller its impulse response is zero-padded. Additionally to this, the controller parameters and nominal secondary path are used to calculate the impulse responses of length $L_s = 2048$ of the effective secondary paths $\hat{S}_{\mathrm{f}}^{fim}(z)$ and $\hat{S}_{\mathrm{f}}^{fimdo}(z)$. For this, the impulse response of the pseudo-cascaded system $h_{\mathrm{mi}}(n)$ is calculated for a length $L_{h_{\mathrm{mi}}} = 4096$. Then the impulse response of the effective FIM secondary path is calculated by the convolution $\hat{s}_{\mathrm{f}}^{fim}(n) = \hat{s}(n) * h_{\mathrm{mi}}(n)$ and cut to the length $L_s = 2048$. As already mentioned, for the case of the FIMDO system $\hat{s}_{\mathrm{f}}^{\mathrm{fimdo}}(n) = \hat{s}(n)$ holds. Afterwards, a first run is performed with the FF, FIM, and FIMDO systems in order to find a μ_0 that yields the best overall steady-state result. The resulting μ_0=$5 \cdot 10^{-5}$ is used.

7.1. Effects of finite impulse responses

The recursive control of the pseudo-cascaded system has an infinite impulse response by nature. By calculating a *finite* impulse response of the equivalent MVC controller an implicit approximation of the controller is made. This approximation may be sufficiently accurate depending on the length of this impulse response. In order to estimate the deviation from the expected behavior, the performance of the system is simulated using two lengths, i.e. the one used for the measurements and another one that is considered too long for practical purposes. The results are presented in Fig. 7.2. The magnitudes over frequency of the two systems show a very similar performance. Only at 100 Hz and near 150 Hz deviations of around 3 dB can be seen. Hence, the impulse response length $L_{\tilde{w}_\mathrm{m}} = 1024$ is considered as appropriate to approximate the pseudo-cascaded system.

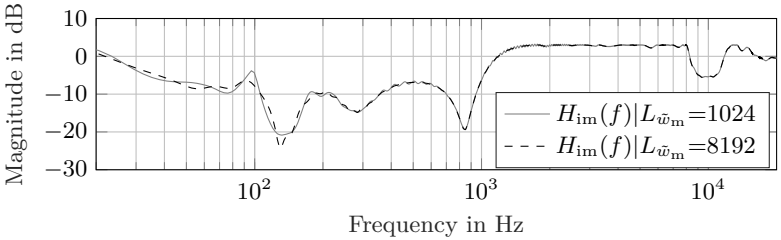

Figure 7.2.: Deviation in the transfer function $H_\mathrm{mi}(f)$ produced when the impulse response of the equivalent MVC controller is shortened to $L_{\tilde{w}_\mathrm{m}} = 1024$. Derivation parameters: $f_s = 48\,\mathrm{kHz}$, $L_s = 2048$, $L_{i,m} = 64$.

The effective secondary path's impulse response has to be stored in RAM-memory (together with the rest of the impulse responses of the macro controller) and put at disposition in real-time for the FPGA. Due to the platform's memory limitations, a length for the effective secondary paths of $L_s = 2048$ is planned. Although the length $L_s = 2048$ has been used before with satisfactory results for storing the estimated secondary path $\hat{S}(z)$ (see for example [Rivera Benois et al., 2019]), it is not clear whether the FIM effective secondary path $\hat{S}_\mathrm{f}^\mathrm{fim}(z)$ requires a longer impulse response. In order to estimate the deviations from its *correct* frequency response, an estimation of the FIM effective secondary path is done. For this, the impulse response's length of the equivalent MVC controller $L_{\tilde{w}_\mathrm{m}} = 1024$ and of the estimated secondary path $L_s = 2048$ are taken into account. With both impulse responses a finite FIM system's impulse response of length $L_{h_\mathrm{mi}} = 4096$ is calculated. Then this is used with the estimated secondary path to calculate a first FIM effective sec-

ondary path of length $L_{h_{\mathrm{mi}}} + L_s - 1 = 6143$. The frequency response of this *full-length* effective secondary path and the *short* one are presented in Fig. 7.3. In Fig. 7.3a their magnitude over frequency curves are presented together with the difference between the two $\Delta_{\mathrm{mag}}(f)$. It can be seen that through the shortened impulse response the deviations go higher than 1 dB in the frequencies below 900 Hz. These go as high as 6 dB in the 100-200 Hz frequency range. In Fig. 7.3b the phase over frequency of both impulse responses are presented, together with the difference between the two $\Delta_{\mathrm{phase}}(f)$ scaled-up by a factor 10. It can be seen that, through the shortened impulse response deviations higher than 10° in the frequencies below 300 Hz are to be found. These go higher than 30° in the 100-200 Hz frequency range. Due to the combined effect of the magnitude and phase deviation, it is assumed that the FIM system will not reach the performance expected from the simulations in Fig. 6.8.

7.2. Systems under Ipsilateral Excitation

In these measurements the excitation signal is played from the ipsilateral loudspeaker, this means, from the loudspeaker positioned at the same side as the headphones' right earcup. While the ANC system is turned off, a 30 s recording by means of the dummy-head's right ear is done. The signal's magnitude over frequency $R_{\mathrm{OFF}}(f)$ is calculated and used as reference. Afterwards, the MVC controller parameters are set, and another 30 s recording is done by means of the dummy-head's right ear. The signal's magnitude over frequency $R_{\mathrm{MVC}}(f)$ is calculated and used for the evaluation. This procedure is repeated to obtain the respective magnitudes over frequency $R_{\mathrm{IMC}}(f)$ and $R_{\mathrm{IM}}(f)$. The results are presented in Fig. 7.4. A second measurement set is done including the adaptive feedforward controller. For this, the feedforward controller adapts for 3 minutes under an ipsilateral excitation and the feedback controller's influence (not the case for the FF system). After this, the adaptation is stopped and a 30 s recording is done by means of the dummy head. The three respective magnitudes over frequency $R_{\mathrm{FF}}(f)$, $R_{\mathrm{FIM}}(f)$, and $R_{\mathrm{FIMDO}}(f)$ are presented in Fig. 7.5.

In Fig. 7.4a, it can be seen from $R_{\mathrm{MVC}}(f)$ that the MVC produces an attenuation bandwidth that extends from 20 Hz to approx. 1.1 kHz. The attenuation magnitude is roughly 10 dB within this frequency range, with the respective decrement when reaching the low and high limits of it. Starting at 1.3 kHz and ending at 3.7 kHz a disturbance enhancement bandwidth is produced, with a relatively constant amplification of 5 dB. Around 10 kHz no attenuation is seen, which instead is replaced by an amplification of 10 dB at 11.3 kHz. This is probably introduced by variations in the secondary path produced between the day it was measured and the day of

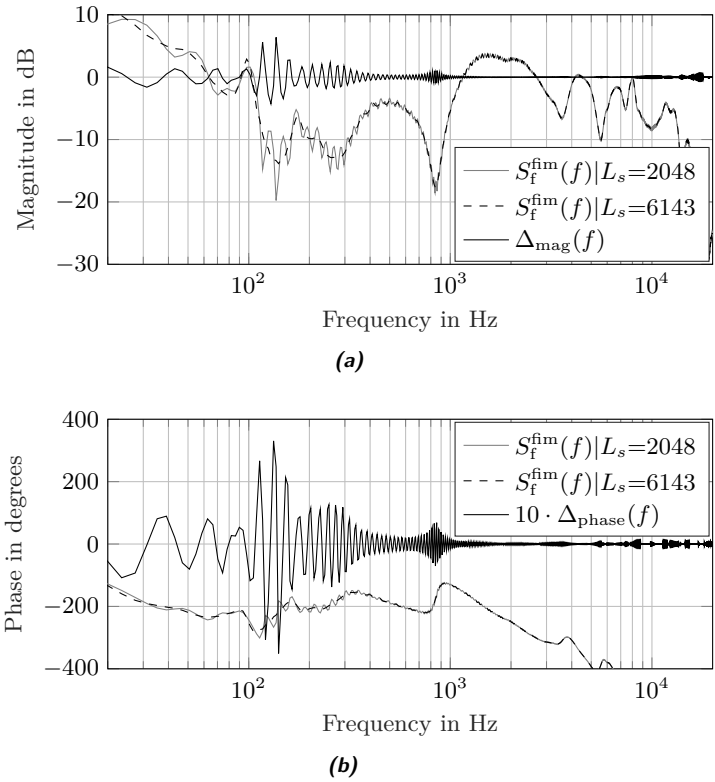

Figure 7.3.: Error in (a) magnitude and (b) phase produced when the impulse response of the FIM Effective secondary path is shortened to 2048. Derivation parameters: $f_s = 48\,\mathrm{kHz}$, $L_{\tilde{w}_m} = 1024$, $L_s = 2048$, $L_{h_{\mathrm{mi}}} = 4096$, $L_{i,m} = 64$.

the recordings.

In Fig. 7.4b, it can be seen from $R_{\mathrm{IMC}}(f)$ that the IMC produces a bigger attenuation bandwidth that extends from 35 Hz to approx. 1.5 kHz. However, the attenuation magnitude is, in comparison to $R_{\mathrm{MVC}}(f)$, inferior, although at some frequencies it also reaches 10 dB. Starting at 1.5 kHz and ending at 5.1 kHz a disturbance enhancement bandwidth is produced, with an amplification that only at its peak reaches 5 dB. Comparing the $R_{\mathrm{MVC}}(f)$ and the $R_{\mathrm{IMC}}(f)$ in the frequency range 1-3 kHz, the lower amplification of the later shows an advantage over the former, as the intensity of the resulting residual error is lower and more flat over frequency.

Around 10 kHz no attenuation is seen, which instead is replaced by the amplification of 10 dB at 11.3 kHz.

In Fig. 7.4c, it can be seen from $R_{\mathrm{IM}}(f)$ that the pseudo-cascaded system produces an attenuation bandwidth very similar to the one seen from $R_{\mathrm{MVC}}(f)$. This extends from 20 Hz to approx. 1.1 kHz. The attenuation magnitude is roughly 10 dB within this frequency range, with the respective decrement when reaching the low and high limits of it. Considering the simulation results presented in Fig. 6.5, the improvements in the 40-80 Hz, 100-150 Hz and 700-900 Hz frequency ranges can be corroborated, although in a smaller magnitude. The disturbance enhancement bandwidth starting at 1.3 kHz and ending at 3.7 kHz is almost identical to the one of the $R_{\mathrm{MVC}}(f)$, corroborating once again the simulation results.

In Fig. 7.5a, it can be seen from $R_{\mathrm{FF}}(f)$ that the FF produces an attenuation bandwidth that reaches approx. 3 kHz and extends to frequencies below 20 Hz. The attenuation magnitude varies strongly within this bandwidth, with values as high as 20 dB. Further bandwidths of attenuation are produced in the 4-5 kHz and 6-7 kHz frequency ranges. There, the attenuation magnitude reaches values as high as 10 dB. Because of the non-smooth energy distribution over frequency that $R_{\mathrm{FF}}(f)$ has, it can be said that the controller's impulse response length is still shorter than the one of the real primary path.

In Fig. 7.5b, it can be seen from $R_{\mathrm{FIM}}(f)$ that the FIM produces an attenuation bandwidth that starts approx. at 55 Hz and extends up to 1.4 kHz. The attenuation magnitude varies strongly within this bandwidth, with values as high as 20 dB. In comparison to $R_{\mathrm{FF}}(f)$ a decrease in attenuation bandwidth is clear, with some improvement around 150 Hz and in the band 300-1000 Hz. Beyond 1.4 kHz the performance seems to suffer from the amplification effect of the pseudo-cascaded system. Nevertheless, between 6-8 kHz an improvement is seen when compared to $R_{\mathrm{FF}}(f)$, with a magnitude attenuation that can reach 15 dB. The amplification at 11.3 kHz seen in the feedback systems shows the further side-effect of the pseudo-cascaded system. The absence of further improvements in attenuation in the frequencies below 55 Hz and in general in the frequencies below 1 kHz can be attributed to deviations in the effective secondary path produced by the limited impulse response length.

In Fig. 7.5c, it can be seen from $R_{\mathrm{FIMDO}}(f)$ that the FIMDO produces an attenuation bandwidth that reaches approx. 1.4 kHz and extends to frequencies below 20 Hz. Within this frequency range, its performance is overall better than the one seen from $R_{\mathrm{FIM}}(f)$. This, because of its further attenuation of the low-frequencies, which intensity makes them more relevant. When compared to the FF, the FIMDO's performance is comparable. However, it is known from the simulation results presented in Fig. 6.17, that the performance in the low-frequencies is achieved mainly by the pseudo-cascaded system. Hence, the performance in the low-frequencies

are not subject to deterioration due to changes in the direction of arrival of the disturbance. Beyond 1.4 kHz the performance of FIMDO is similar to the one of FIM, because its effective secondary path suffers less from the limited impulse response side-effects. Moreover, an improvement in the range of 6-8 kHz can be seen, with attenuation magnitudes up to 20 dB.

7.3. Systems under Contralateral Excitation

In this second set of measurements the excitation signal is played from the contralateral loudspeaker. This is done in order to evaluate to which extent the feedback systems can achieve the same attenuation performance as in an ipsilateral excitation context. At the same time, the impact of such a disadvantageous excitation is also evaluated for the feedforward systems. Here, the pseudo-cascaded system is evaluated as a possible solution for improving the overall system performance, thanks to its feedback working principle.

In Fig. 7.6a, it can be seen from $R_{\mathrm{MVC}}(f)$ that the MVC produces an attenuation bandwidth that extends from 25 Hz to approx. 1.1 kHz, hence, approximately the same bandwidth achieved with an ipsilateral excitation. The attenuation magnitude is roughly 10 dB within this frequency range, with the respective decrement when reaching the low and high limits of it, therefore, corroborating the fact that feedback systems are resilient against loss of causality and changes of direction of arrival. Beyond 1.3 kHz some degree of amplification can be seen, although it is not clear enough to know the magnitude of the amplification. However, the resonance at 11.3 kHz present in the other measurements can also be seen in this one.

In Fig. 7.6b, it can be seen from $R_{\mathrm{IMC}}(f)$ that the IMC produces a broader attenuation bandwidth that extends from 35 Hz to approx. 1.4 kHz. The attenuation magnitude is in comparison to $R_{\mathrm{MVC}}(f)$ inferior, although at some frequencies it also reaches 10 dB. Outside the attenuation bandwidth, $R_{\mathrm{IMC}}(f)$ shows the same behavior as $R_{\mathrm{MVC}}(f)$. However, in the 150-200 Hz frequency range the amplification magnitude of $R_{\mathrm{IMC}}(f)$ is about 5 dB lower than $R_{\mathrm{MVC}}(f)$.

In Fig. 7.6c, it can be seen from $R_{\mathrm{IM}}(f)$ that the pseudo-cascaded system produces an attenuation bandwidth very similar to the one seen from $R_{\mathrm{MVC}}(f)$. This extends from 25 Hz to approx. 1.1 kHz. The attenuation magnitude is roughly 10 dB within this frequency range, with the respective decrement when reaching the low and high limits of it. Considering the simulation results presented in Fig. 6.5, the improvements in the 40-80 Hz, 100-150 Hz and 700-900 Hz frequency ranges can be corroborated, although in a much smaller magnitude. The amplification produced in frequencies higher than 1.1 kHz is identical to the one of $R_{\mathrm{MVC}}(f)$.

In all sub-figures presented in Fig. 7.7 it can be seen that upon a con-

tralateral excitation a feedforward scheme achieves a limited performance. Furthermore, the achieved attenuation does not go beyond the 450 Hz, partially because the power density spectrum decreases faster over frequency than in Fig. 7.5. The effect of the pseudo-cascaded system is much less important than in Fig. 7.6c. Therefore, it can be said that the disadvantage is due to a malfunctioning of the FF system, which creates a residual noise that is more dominant than the pseudo-cascaded system. Nevertheless, it can be seen that the pseudo-cascaded system influences the feedforward controller in two different ways. Hence, it is seen from $R_{\mathrm{FIM}}(f)$ that the frequencies around 100 Hz are attenuated with a higher magnitude, while the frequencies below 57 Hz are amplified. On the other hand $R_{\mathrm{FIMDO}}(f)$ shows a similar performance as $R_{\mathrm{FF}}(f)$, but with higher attenuation levels around 20 Hz and at the frequencies where the minima of $R_{\mathrm{FF}}(f)$ are located. So, although the FIMDO does not achieve the same performance as before, its attenuation of the very low-frequencies remains intact. A better performance of the FIM system can be expected, if the limitations related to the effective secondary path impulse response length can be solved.

7.4. Summary

In this chapter measurements done with an ANC headphones prototype by means of a dummy-head are presented. The controller is programmed such that two of the novel control structures, namely FIM and FIMDO, can be directly compared under the same hardware limitations, excitation context and within a relatively short time span. In order to understand their performance, the classical FF, MVC, and IMC control schemes together with the pseudo-cascaded feedback system (MVC-IMC with independent optima) are included. Under ipsilateral excitation the FIMDO system shows to effectively improve the performance when compared to the classical FF. The FIM shows at some frequencies a better performance than FIMDO, but the problems faced during its adaptation prevent it from achieving the superior results seen in the simulations. This problem is foreseen before the measurements, because the impulse response of its effective secondary path requires a longer amount of samples in order to avoid deviations in its frequency response. Under contralateral excitation the improvement expected from the pseudo-cascaded system within the FIM and FIMDO structure is not successfully achieved. Nevertheless, because of the performance that the pseudo-cascaded system achieves when evaluated alone, a limitation coming from its working principle or implementation could be discarded. Instead, it is understood that the feedforward system problem when excited from the contralateral side appears to dominate over the whole system, introducing a residual noise that can not be compensated by the feedback controllers.

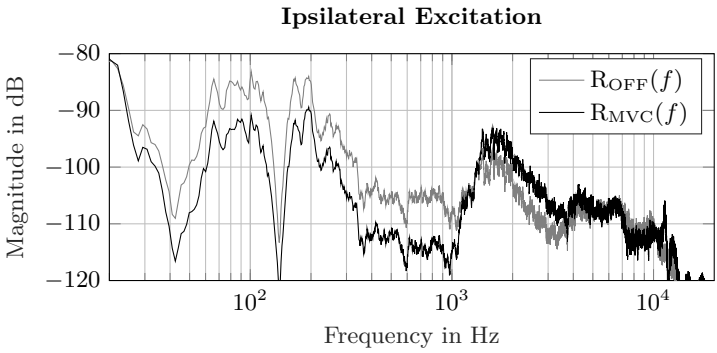

(a) *Minimum Variance Control*

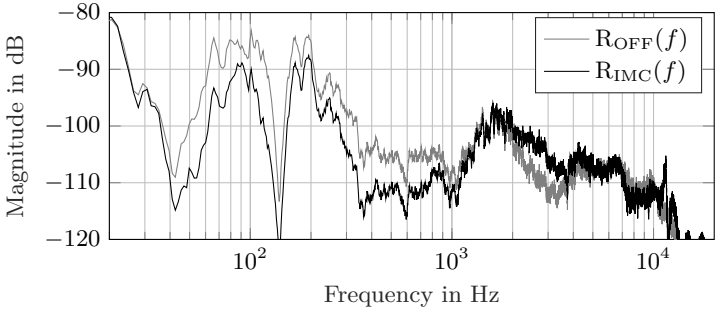

(b) *Internal Model Control*

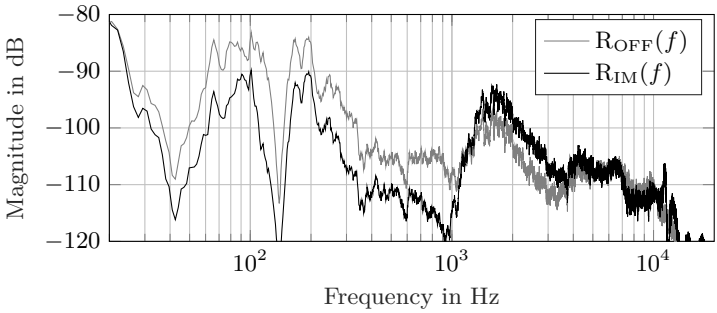

(c) *Pseudo-cascaded Internal Model and Minimum Variance Control*

Figure 7.4.: Measurements done under ipsilateral excitation at the dummy-head's right ear with feedback ANC algorithms. Macro-controller parameters: $f_s = 48\,\text{kHz}$, $L_{\tilde{w}m} = 1024$. Internal parameters: $L_m = 128$, $L_i = 128$, $L_s = 2048$, $L_{i,m} = 64$.

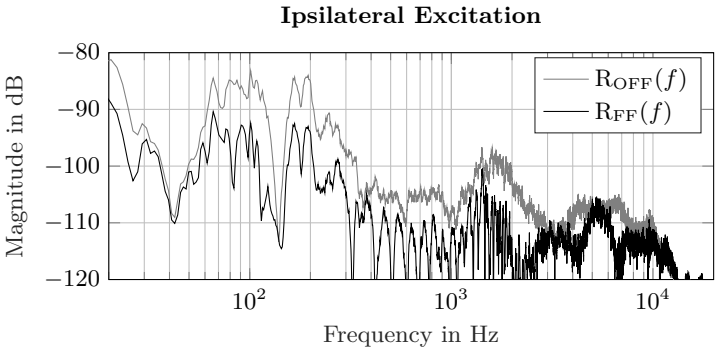

(a) *Feedforward Control*

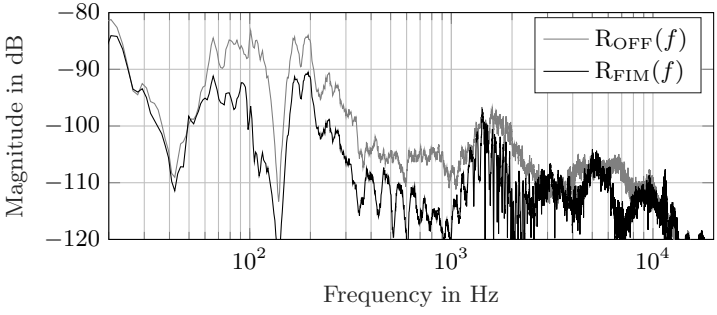

(b) *Novel FIM Control*

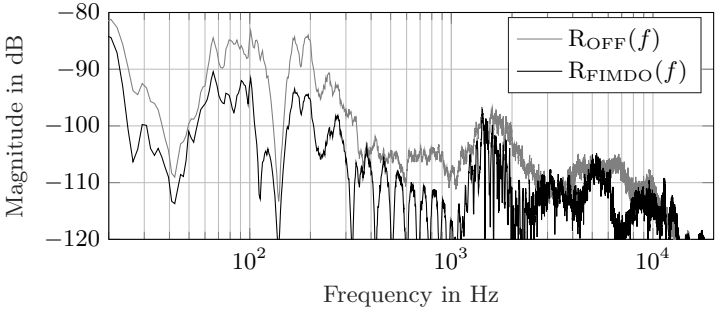

(c) *Novel FIMDO Control*

Figure 7.5.: Measurements done under ipsilateral excitation at the dummy-head's right ear with feedforward and hybrid ANC algorithms. Macro-controller parameters: $f_s = 48\,\text{kHz}$, $L_{wf} = 512$, $L_{sf} = 2048$, $L_{\tilde{w}m} = 1024$. Internal pseudo-cascaded controller parameters: $L_{i,m} = 64$, $L_s = 2048$.

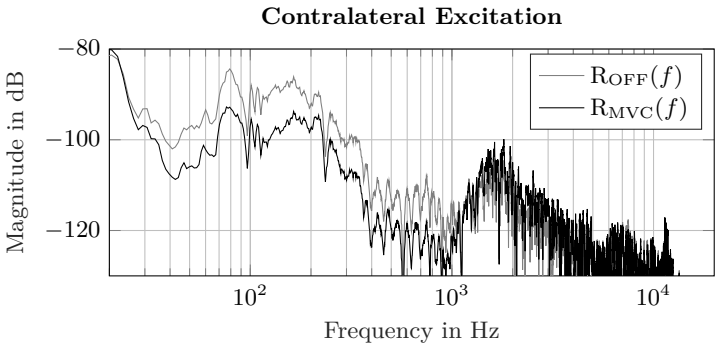

(a) *Minimum Variance Control*

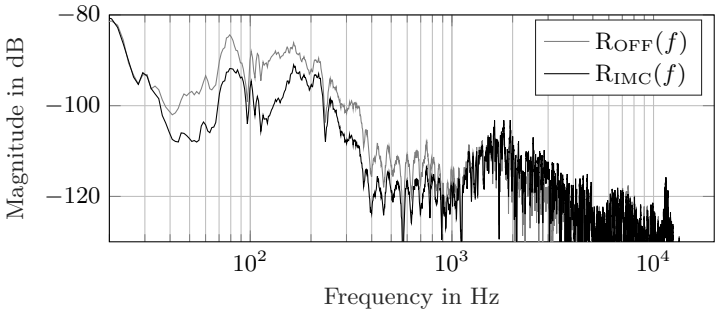

(b) *Internal Model Control*

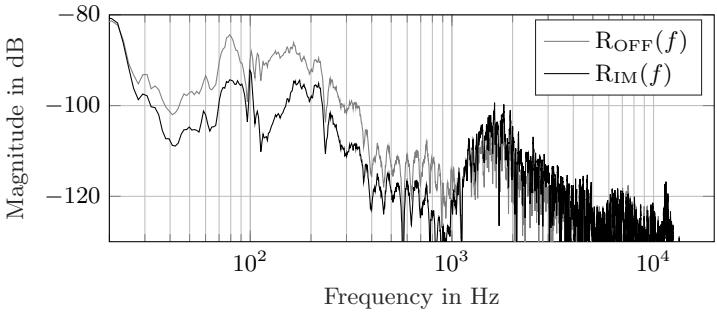

(c) *Pseudo-cascaded Internal Model and Minimum Variance Control*

Figure 7.6.: Measurements done under contralateral excitation at the dummy-head's right ear with feedback and pseudo-cascaded ANC algorithms. Macro-controller parameters: $f_s = 48\,\text{kHz}$, $L_{\tilde{w}m} = 1024$. Internal parameters: $L_m = 128$, $L_i = 128$, $L_s = 2048$, $L_{i,m} = 64$.

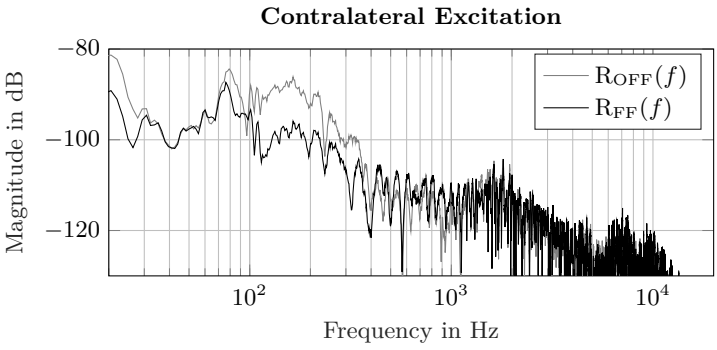

***(a)** Feedforward Control*

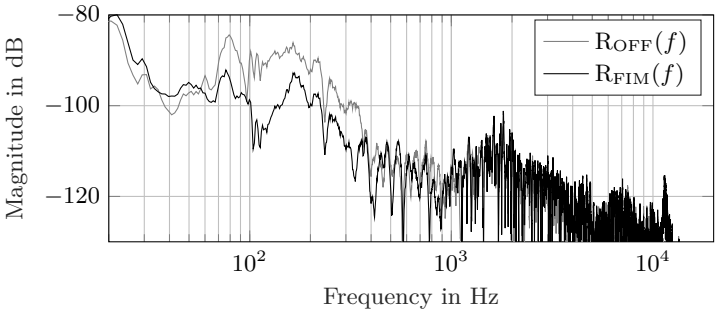

***(b)** Novel FIM Control*

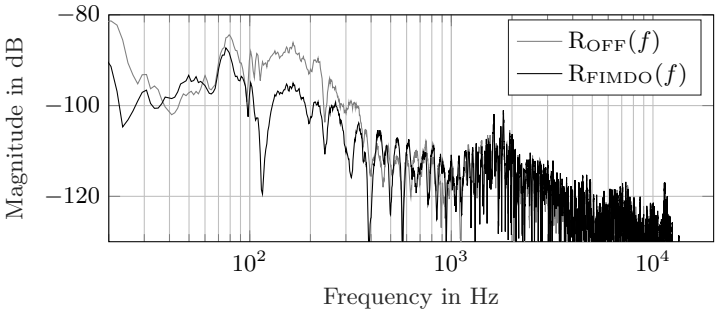

***(c)** Novel FIMDO Control*

Figure 7.7.: Measurements done under contralateral excitation at the dummy-head's right ear with feedforward and hybrid ANC algorithms. Macro-controller parameters: $f_s = 48\,\text{kHz}$, $L_{wf} = 512$, $L_{sf} = 2048$, $L_{\tilde{w}m} = 1024$. Internal pseudo-cascaded controller parameters: $L_{i,m} = 64$, $L_s = 2048$.

CHAPTER 8

Conclusions

In this work the classical control schemes, namely the FF, MVC, and IMC are presented. Their working principles are described and methods for deriving their optimal controllers are explained. Thus, in Chapter 2 the Wiener controller is presented as the optimal solution for the impulse response of $W_{\mathrm{f}}(z)$. An iterative approximation of it based on the Modified Normalized Filtered-x LMS algorithm is found to have the less restrictive adaptation stability constraints. In Chapter 3 and Chapter 4 the optimization of the impulse responses of $W_{\mathrm{m}}(z)$ and $W_{\mathrm{i}}(z)$ are formulated as convex optimization problems subject to stability, performance, and controller gain constraints. The achievable results with each control scheme and its respective optimal controller are exemplified by simulations of an ANC headphones prototype subject to an ipsilateral free-field excitation.

In Chapter 5 control structures used to combine two different control schemes are studied. Their working principles are based on the hybrid and pseudo-cascaded combination strategies. In the former a feedforward and a feedback system are combined together, in order to exploit the information contained in the reference $x(n)$ and residual error $e(n)$ signals. In the pseudo-cascaded combination strategy two feedback controllers are connected together by means of an internal estimation of the error produced by one controller. The information contained in this estimated error is used by the second controller to calculate a control signal that further minimizes the *real* residual error $e(n)$. Each combination of two control schemes (MVC-IMC, MVC-FF and IMC-FF) has one control structure that yields independent optimal controllers and a second one that introduces a dependency of one controller with respect to the parameters of the

other.

In Chapter 6 the hybrid and pseudo-cascaded combination strategies are used together to combine all three control schemes into one system. The connection variants seen in Chapter 5 that introduce dependencies of the FF controller with respect to the MVC and IMC controllers are used to produce three alternative control structures. The first variant, the FIM, yields an optimal $W_{\mathrm{f}}(z)$ that is independent of $W_{\mathrm{m}}(z)$ and $W_{\mathrm{i}}(z)$. The second variant, the FIMPDO, yields an optimal $W_{\mathrm{f}}(z)$ that is dependent with respect to $W_{\mathrm{m}}(z)$ but not with respect to $W_{\mathrm{i}}(z)$. The third variant, FIMDO, yields an optimal $W_{\mathrm{f}}(z)$ that is dependent with respect to $W_{\mathrm{m}}(z)$ and $W_{\mathrm{i}}(z)$. Simultaneously, on all variants the optimal $W_{\mathrm{m}}(z)$ and $W_{\mathrm{i}}(z)$ controllers are independent from each other. Because of this fact, the feedback controllers are co-optimized first and, based on their parameters, the optimal FF controller is calculated later.

In order to optimize the impulse responses of $W_{\mathrm{m}}(z)$ and $W_{\mathrm{i}}(z)$, the stability, performance, and gain constraints derived in Chapter 3 and Chapter 4 are extended for the application of these to the pseudo-cascaded system. The new constraints are used together with an MVC-IMC combined cost function to find the optimal parameters for the controllers. Subsequently, the calculation of the respective optimal FF controller $W_{\mathrm{f}}(z)$ follows three different Wiener controller formulations, depending on the target controller structure. Together with them, three alternative formulations of the Modified Normalized Filtered-x LMS adaptation algorithm are derived, in order to find the respective optimal controller based on the adaptive filter implementation of $W_{\mathrm{f}}(z)$.

The three Wiener controllers are evaluated by means of simulations of an ANC headphones prototype subject to an ipsilateral free-field excitation. From the results it is concluded that, if the impulse response of the FF controller $w_{\mathrm{f}}(n)$ is as long as the one of the primary path $p(n)$, the performance of the novel control structure is the same as the one of a FF control scheme. Thus, limited only by the first samples of $p(n)$, the delays in the secondary path and the inversion of it. However, if the impulse response of the FF controller is shorter than the one of the primary path, then the MVC-IMC pseudo-cascaded system effectively extends its impulse response, such that it approximates the one of a longer FF controller. This is seen in the frequency domain as an improved attenuation in the low frequencies. The best results are achieved with FIM, followed by FIMDO. FIMPDO is discarded as an attractive solution because of its inferior results.

In Chapter 7, measurements are performed with an ANC headphones prototype implementing the Modified Normalized Filtered-x LMS algorithm in its two new variants, regarding the changes required by FIM and FIMDO. During the measurements not only an ipsilateral excitation is considered, but also a contralateral one. Moreover, the room condi-

tions are the ones of a normal room for audio listening, such that a natural sound-field (this means neither a pure free-field nor a diffuse-filed, but rather a combination of both) is produced. It is found that if the impulse response of the estimated secondary path is too short, the estimation error hinders the adaptation algorithm from reaching the optimal FF controller's impulse response. Thus, under this circumstances the performance of FIMDO is better than the one of FIM, because its effective secondary path requires a shorter impulse response length to be stored. Under a contralateral excitation both control structures showed to be subject to the dominant side-effect of the FF control scheme. Hence, they are not capable of taking advantage of their pseudo-cascaded structure (IMC-MVC), because of the additive noise that the FF controller introduces. Nevertheless, when the IMC-MVC pseudo-cascaded structure is evaluated alone, its performance shows to be resilient to the contralateral excitation.

8.1. Further Research

Based on the outcome of this work and observations done during its presentation, suggestions for further research are made. These are grouped under three topics. The first topic is the use of IIR filters as controllers. The optimization results on all chapters of this work showed a performance dependency with respect to the controller length. Hence, if the FIR structure is replaced by an IIR one, comparable or better results are to be expected. One problem arises from the fact that, in order to ensure a unique global optimum, the cost function has to have a convex dependency with respect to the controller parameters. Therefore, an adequate parameterisation should be found that fulfills this constraint. Moreover, new stability constraints have to be derived for this matter, in order to ensure that the controller itself and the overall system remains stable between consecutive optimization steps.

The second topic is the use of IIR filters for approximating the effective secondary paths used by the Modified Normalized Filtered-x LMS in Fig. 6.20. It is shown by the measured results that the attenuation performance of the adaptive controller depends considerably on the accuracy of the estimation of these systems. Hence, by using IIR filters infinite impulse responses can be achieved with relatively lower memory requirements.

The third topic considers possible solutions for the problems presented by the FF system under contralateral excitation. For instance, extending the Filtered-x LMS as suggested by Foudhaili in [Foudhaili, 2008, Section 3.1.3]. The proposed algorithm considers a multiple-input single-output Filtered-x LMS algorithm. This integrates two reference signals, $x_{\mathrm{R}}(n)$ and $x_{\mathrm{L}}(n)$, and the error signal of the corresponding earcup $e_{\mathrm{R/L}}(n)$. The errors on the right and left earcups find their respective expressions

in

$$E_{\mathrm{R}}(z) = D_{\mathrm{R}}(z) - S_{\mathrm{R}}(z)\big(W_{\mathrm{f,RR}}(z)X_{\mathrm{R}}(z) + W_{\mathrm{f,LR}}(z)X_{\mathrm{L}}(z)\big) \tag{8.1}$$

and

$$E_{\mathrm{L}}(z) = D_{\mathrm{L}}(z) - S_{\mathrm{L}}(z)\big(W_{\mathrm{f,RL}}(z)X_{\mathrm{R}}(z) + W_{\mathrm{f,LL}}(z)X_{\mathrm{L}}(z)\big). \tag{8.2}$$

One disadvantage arises from the fact that each reference is used as an input for an independent controller. Hence, the system has twice the memory and computational requirements of a classical Filtered-x LMS. Nevertheless, as described by the author, the algorithm shows important improvements in scenarios with contralateral excitation. However, it is expected that the loss in MSC between the left and right sides might severely limit the achievable attenuation bandwidth, as explained in Sec. 2.2.

APPENDIX **A**

Hybrid and Pseudo-Cascaded Control Structures

In the present appendix the derivation of the transfer functions and important effective secondary paths are described in detail. Due to the length of some mathematical expressions, the dependency with respect to z is omitted. However, all the derivations are performed in the Z-domain, hence, no confusion should result from the omission. All three combinations MVC-IMC, MVC-FF, and IMC-FF are divided in two sections each. One of them regarding the combination with independent optima, and another one regarding the combination with dependent optimum.

A.1. MVC-IMC Combination with Independent Optima

Here the derivations for the system presented in Sec. 5.1 are described.

A.1.1. System's Transfer Function

From the Fig. 5.1a the equations

$$Y = -S(Y_{\mathrm{i}}' + Y_{\mathrm{m}}'), \tag{A.1}$$

$$Y_{\mathrm{i}}' = W_{\mathrm{i}} \cdot E_{\mathrm{m}}, \tag{A.2}$$

$$Y_{\mathrm{m}}' = W_{\mathrm{m}} \cdot E_{\mathrm{m}}, \tag{A.3}$$

$$E_{\mathrm{m}} = E + \hat{S} \cdot \mathrm{Y_i},' \tag{A.4}$$

and

$$E = D + Y \tag{A.5}$$

are derived. Using Eq. A.2 in Eq. A.4

$$E_{\mathrm{m}} = \frac{E}{1 - \hat{S} \cdot W_{\mathrm{i}}} \tag{A.6}$$

Using Eq. A.2, Eq. A.3, and Eq. A.6 in Eq. A.1

$$Y = -S\left(\frac{W_{\mathrm{i}}}{1 - \hat{S} \cdot W_{\mathrm{i}}} + \frac{W_{\mathrm{m}}}{1 - \hat{S} \cdot W_{\mathrm{i}}}\right)E \tag{A.7}$$

$$= -S\left(\frac{W_{\mathrm{i}} + W_{\mathrm{m}}}{1 - \hat{S} \cdot W_{\mathrm{i}}}\right)E \tag{A.8}$$

Using Eq. A.8 in Eq. A.5

$$E = D - S\left(\frac{W_{\mathrm{i}} + W_{\mathrm{m}}}{1 - \hat{S} \cdot W_{\mathrm{i}}}\right)E \tag{A.9}$$

$$\rightarrow D = E\left(1 + S\frac{W_{\mathrm{i}} + W_{\mathrm{m}}}{1 - \hat{S} \cdot W_{\mathrm{i}}}\right) \tag{A.10}$$

$$\rightarrow D = E\left(\frac{1 - \hat{S} \cdot W_{\mathrm{i}} + S \cdot W_{\mathrm{i}} + S \cdot W_{\mathrm{m}}}{1 - \hat{S} \cdot W_{\mathrm{i}}}\right) \tag{A.11}$$

$$\rightarrow D = E\left(\frac{1 + (S - \hat{S})W_{\mathrm{i}} + S \cdot W_{\mathrm{m}}}{1 - \hat{S} \cdot W_{\mathrm{i}}}\right) \tag{A.12}$$

to derive the system's transfer function

$$H_{\mathrm{mi}}(z) = \frac{E(z)}{D(z)} = \frac{1 - \hat{S}(z)W_{\mathrm{i}}(z)}{1 + \big(S(z) - \hat{S}(z)\big)W_{\mathrm{i}}(z) + S(z)W_{\mathrm{m}}(z)}. \tag{A.13}$$

If the condition $\hat{S}(z) = S(z)$ is met, then the system's transfer function simplifies to

$$\hat{H}_{\mathrm{mi}}(z) = \frac{1 - S(z)W_{\mathrm{i}}(z)}{1 + S(z)W_{\mathrm{m}}(z)}. \tag{A.14}$$

A.1.2. IMC effective secondary path

The controller $W_{\mathrm{i}}(z)$ is removed from the diagram and the disturbance is set to zero, i.e. $d(n) = 0$. Now, given the resulting block diagram two equations are derived

$$E = -S(Y'_{\mathrm{m}} + Y'_{\mathrm{i}}) \tag{A.15}$$

$$Y'_{\mathrm{m}} = W_{\mathrm{m}}(\hat{S} \cdot Y'_{\mathrm{i}} + E). \tag{A.16}$$

Using Eq. A.16 to replace Y_m' in Eq. A.15

$$Y = -S\big(W_\mathrm{m}(\hat{S}\cdot Y_\mathrm{i}' + E) + Y_\mathrm{i}'\big) \tag{A.17}$$

$$\rightarrow E = -S\cdot W_\mathrm{m}\cdot\hat{S}\cdot Y_\mathrm{i}' - S\cdot W_\mathrm{m}\cdot E - S\cdot Y_\mathrm{i}' \tag{A.18}$$

$$\rightarrow E(1+S\cdot W_\mathrm{m}) = -S(W_\mathrm{m}\cdot\hat{S}+1)Y_\mathrm{i}', \tag{A.19}$$

the transfer function can be derived

$$\frac{E(z)}{Y_\mathrm{i}'(z)} = -S(z)\frac{1+\hat{S}(z)W_\mathrm{m}(z)}{1+S(z)W_\mathrm{m}(z)}. \tag{A.20}$$

This is further used to define the IMC effective secondary path

$$S_\mathrm{i}^\mathrm{mi}(z) = -\frac{E(z)}{Y_\mathrm{i}'(z)} = S(z)\frac{1+\hat{S}(z)W_\mathrm{m}(z)}{1+S(z)W_\mathrm{m}(z)}. \tag{A.21}$$

In cases in which the constraint $\hat{S}(z) = S(z)$ is fulfilled, this simplifies to

$$\hat{S}_\mathrm{i}^\mathrm{mi}(z) = S(z). \tag{A.22}$$

A.2. MVC-IMC Combination with Dependent Optima

Here the derivations for the system presented in Sec. 5.1.1 are described.

A.2.1. System's Transfer Function

From the Fig. 5.1b the equations

$$Y = -S(Y_\mathrm{i}' + Y_\mathrm{m}'), \tag{A.23}$$

$$Y_\mathrm{i}' = W_\mathrm{i}\cdot E_\mathrm{m}, \tag{A.24}$$

$$Y_\mathrm{m}' = W_\mathrm{m}\cdot E, \tag{A.25}$$

$$E_\mathrm{m} = E + \hat{S}_\mathrm{i}\cdot Y_\mathrm{i}', \tag{A.26}$$

and

$$E = D + Y \tag{A.27}$$

are derived. Using Eq. A.26 in Eq. A.24

$$Y_\mathrm{i}' = W_\mathrm{i}(E + \hat{S}_\mathrm{i}\cdot Y_\mathrm{i}') \tag{A.28}$$

$$\rightarrow Y_\mathrm{i}' = \frac{W_\mathrm{i}}{1-\hat{S}_\mathrm{i}\cdot W_\mathrm{i}}E \tag{A.29}$$

Using Eq. A.29 and Eq. A.25 in Eq. A.23

$$Y = -S\left(\frac{W_\mathrm{i}}{1-\hat{S}_\mathrm{i}\cdot W_\mathrm{i}} + W_\mathrm{m}\right)E \tag{A.30}$$

$$= -S\left(\frac{W_\mathrm{i} + (1-\hat{S}_\mathrm{i}\cdot W_\mathrm{i})W_\mathrm{m}}{1-\hat{S}_\mathrm{i}\cdot W_\mathrm{i}}\right)E \tag{A.31}$$

Using Eq. A.31 in Eq. A.27

$$E = D - S\left(\frac{W_\mathrm{i} + (1-\hat{S}_\mathrm{i}\cdot W_\mathrm{i})W_\mathrm{m}}{1-\hat{S}_\mathrm{i}\cdot W_\mathrm{i}}\right)E \tag{A.32}$$

$$\rightarrow D = E\left(1 + S\frac{W_\mathrm{i} + (1-\hat{S}_\mathrm{i}\cdot W_\mathrm{i})W_\mathrm{m}}{1-\hat{S}_\mathrm{i}\cdot W_\mathrm{i}}\right) \tag{A.33}$$

$$\rightarrow D = E\frac{1-\hat{S}_\mathrm{i}\cdot W_\mathrm{i} + S\big(W_\mathrm{i} + (1-\hat{S}_\mathrm{i}\cdot W_\mathrm{i})W_\mathrm{m}\big)}{1-\hat{S}_\mathrm{i}\cdot W_\mathrm{i}} \tag{A.34}$$

$$\rightarrow D = E\frac{1-\hat{S}_\mathrm{i}(W_\mathrm{i} + S\cdot W_\mathrm{i}\cdot W_\mathrm{m}) + S\big(W_\mathrm{i} + W_\mathrm{m}\big)}{1-\hat{S}_\mathrm{i}\cdot W_\mathrm{i}} \tag{A.35}$$

to derive a system's transfer function

$$\frac{E(z)}{D(z)} = \frac{1-\hat{S}_\mathrm{i}\cdot W_\mathrm{i}}{1-\hat{S}_\mathrm{i}(W_\mathrm{i} + S\cdot W_\mathrm{i}\cdot W_\mathrm{m}) + S\big(W_\mathrm{i} + W_\mathrm{m}\big)} \tag{A.36}$$

Using the substitution

$$\hat{S}_\mathrm{i} = \frac{\hat{S}}{1+\hat{S}\cdot W_\mathrm{m}}, \tag{A.37}$$

the system's transfer function

$$H_\mathrm{mido}(z) = \frac{E(z)}{D(z)} \tag{A.38}$$

can be derived

$$H_\mathrm{mido}(z) = \frac{1-\frac{\hat{S}}{1+\hat{S}\cdot W_\mathrm{m}}\cdot W_\mathrm{i}}{1-\frac{\hat{S}}{1+\hat{S}\cdot W_\mathrm{m}}(W_\mathrm{i} + S\cdot W_\mathrm{i}\cdot W_\mathrm{m}) + S\big(W_\mathrm{i} + W_\mathrm{m}\big)} \tag{A.39}$$

$$= \frac{1+\hat{S}\cdot W_\mathrm{m} - \hat{S}\cdot W_\mathrm{i}}{(1+S\cdot W_\mathrm{i} + S\cdot W_\mathrm{m})(1+\hat{S}\cdot W_\mathrm{m}) - \hat{S}(W_\mathrm{i} + S\cdot W_\mathrm{i}\cdot W_\mathrm{m})} \tag{A.40}$$

$$= \frac{1+\hat{S}\cdot W_\mathrm{m} - \hat{S}\cdot W_\mathrm{i}}{1+(S-\hat{S})W_\mathrm{i} + (S+\hat{S})W_\mathrm{m} + S\cdot\hat{S}\cdot W_\mathrm{m}^2}. \tag{A.41}$$

If the condition $\hat{S}(z) = S(z)$ is fulfilled, then the system's transfer function simplifies to

$$\hat{H}_{\text{mido}}(z) = \frac{1 - \frac{S(z)}{1+S(z)\cdot W_{\text{m}}(z)} W_{\text{i}}(z)}{1 + S(z) \cdot W_{\text{m}}(z)}. \tag{A.42}$$

A.2.2. IMC effective secondary path

The controller $W_{\text{i}}(z)$ is removed from the diagram and the disturbance is set to zero, i.e. $d(n) = 0$. Now, given the resulting block diagram, two equations are derived

$$E = -S(Y'_{\text{m}} + Y'_{\text{i}}) \tag{A.43}$$
$$Y'_{\text{m}} = W_{\text{m}} \cdot E. \tag{A.44}$$

Using Eq. A.44 to replace Y'_{m} in Eq. A.43

$$E = -S(W_{\text{m}} \cdot E + Y'_{\text{i}}) \tag{A.45}$$
$$\rightarrow E(1 + S \cdot W_{\text{m}}) = -S \cdot Y'_{\text{i}} \tag{A.46}$$

the transfer function can be derived

$$\frac{E}{Y'_{\text{i}}} = -S \frac{1}{1 + S \cdot W_{\text{m}}}. \tag{A.47}$$

This is further used to define the IMC effective secondary path

$$S_{\text{i}}^{\text{mido}}(z) = -\frac{E(z)}{Y'_{\text{i}}(z)} = S(z) \frac{1}{1 + S(z) W_{\text{m}}(z)}. \tag{A.48}$$

A.3. MVC-FF Combination with Independent Optima

Here the derivations for the system presented in Sec. 5.2 are described.

A.3.1. System's Transfer Function

From the Fig. 5.2a, the equations

$$E = D + Y, \tag{A.49}$$
$$D = P \cdot X, \tag{A.50}$$
$$Y = -S(Y'_{\text{f}} + Y'_{\text{m}}), \tag{A.51}$$
$$Y'_{\text{f}} = W_{\text{f}} \cdot X, \tag{A.52}$$

and

$$Y'_{\text{m}} = W_{\text{m}} \cdot E \tag{A.53}$$

are derived. By using Eq. A.52 and Eq. A.53 to replace the signals Y_f' and Y_m' in the combined control signal Eq. A.51

$$Y = -S(W_\mathrm{f} \cdot X + W_\mathrm{m} \cdot E) \tag{A.54}$$
$$= -S \cdot W_\mathrm{f} \cdot X + -S \cdot W_\mathrm{m} \cdot E. \tag{A.55}$$

Using this together with Eq. A.50 in Eq. A.49

$$E = P \cdot X - S \cdot W_\mathrm{f} \cdot X - S \cdot W_\mathrm{m} \cdot E \tag{A.56}$$
$$\rightarrow E(1 + S \cdot W_\mathrm{m}) = (P - S \cdot W_\mathrm{f})X \tag{A.57}$$

the system's transfer function

$$H_\mathrm{fm}(z) = \frac{E(z)}{X(z)} = \frac{P(z) - S(z)W_\mathrm{f}(z)}{1 + S(z)W_\mathrm{m}(z)} \tag{A.58}$$

can be derived.

A.3.2. FF Effective Secondary Path

The controller $W_\mathrm{f}(z)$ is removed from the diagram and the disturbance is set to zero, i.e. $d(n) = 0$. Now, taking this into account, Eq. A.53 can be used in Eq. A.51

$$Y = -S(Y_\mathrm{f}' + W_\mathrm{m} \cdot E) \tag{A.59}$$
$$= -S \cdot Y_\mathrm{f}' - S \cdot W_\mathrm{m} \cdot E, \tag{A.60}$$

which is then used in Eq. A.49

$$E = -S \cdot Y_\mathrm{f}' - S \cdot W_\mathrm{m} \cdot E \tag{A.61}$$
$$\rightarrow E(1 + S \cdot W_\mathrm{m}) = -S \cdot Y_\mathrm{f}'. \tag{A.62}$$

This is used to find the FF effective secondary path

$$S_\mathrm{f}^\mathrm{fm}(z) = -\frac{E(z)}{Y_\mathrm{f}'(z)} = \frac{S(z)}{1 + S(z)W_\mathrm{m}(z)}. \tag{A.63}$$

A.4. MVC-FF Combination with Dependent Optima

Here the derivations for the system presented in Sec. 5.2.1 are described.

A.4.1. System's Transfer Function

From the Fig. 5.2b, the equations

$$E = D + Y, \tag{A.64}$$
$$D = P \cdot X, \tag{A.65}$$
$$Y = -S(Y_\mathrm{f}' + Y_\mathrm{m}'), \tag{A.66}$$
$$Y_\mathrm{f}' = W_\mathrm{f} \cdot X, \tag{A.67}$$

and

$$Y_\mathrm{m}' = W_\mathrm{m}(\hat{S} \cdot Y_\mathrm{f}' + E) \tag{A.68}$$

are derived. By using Eq. A.67 and Eq. A.68 to replace the signals Y_f' and Y_m' in the combined control signal Eq. A.66

$$Y = -S\big(W_\mathrm{f} \cdot X + W_\mathrm{m}(\hat{S} \cdot W_\mathrm{f} \cdot X + E)\big) \tag{A.69}$$
$$= -S \cdot W_\mathrm{f} \cdot X - S \cdot W_\mathrm{m} \cdot \hat{S} \cdot W_\mathrm{f} \cdot X - S \cdot W_\mathrm{m} \cdot E \tag{A.70}$$
$$= -S \cdot W_\mathrm{f}(1 + \hat{S} \cdot W_\mathrm{m})X - S \cdot W_\mathrm{m} \cdot E. \tag{A.71}$$

Using this together with Eq. A.65 in Eq. A.64

$$E = P \cdot X - S \cdot W_\mathrm{f}(1 + \hat{S} \cdot W_\mathrm{m})X - S \cdot W_\mathrm{m} \cdot E \tag{A.72}$$
$$\rightarrow E(1 + S \cdot W_\mathrm{m}) = \big(P - S \cdot W_\mathrm{f}(1 + \hat{S} \cdot W_\mathrm{m})\big)X \tag{A.73}$$

the system's transfer function can be derived

$$H_\mathrm{fmdo}(z) = \frac{P(z)}{1 + S(z)W_\mathrm{m}(z)} - S(z)W_\mathrm{f}(z)\frac{1 + \hat{S}(z)W_\mathrm{m}(z)}{1 + S(z)W_\mathrm{m}(z)}. \tag{A.74}$$

If the condition $\hat{S}(z) = S(z)$ is fulfilled, then the system's transfer function simplifies to

$$\hat{H}_\mathrm{fmdo}(z) = \frac{P(z)}{1 + S(z)W_\mathrm{m}(z)} - S(z)W_\mathrm{f}(z). \tag{A.75}$$

A.4.2. FF Effective Secondary Path

The controller $W_\mathrm{f}(z)$ is removed from the diagram and the disturbance is set to zero, i.e. $d(n) = 0$. Now, taking this into account, Eq. A.68 can be used in Eq. A.66

$$Y = -S(Y_\mathrm{f}' + W_\mathrm{m}(\hat{S} \cdot Y_\mathrm{f}' + E)) \tag{A.76}$$
$$= -S \cdot Y_\mathrm{f}' - S \cdot W_\mathrm{m} \cdot \hat{S} \cdot Y_\mathrm{f}' - S \cdot W_\mathrm{m} \cdot E, \tag{A.77}$$

which is then used in Eq. A.64 with $d(n) = 0$

$$E = -S \cdot Y_\mathrm{f}' - S \cdot W_\mathrm{m} \cdot \hat{S} \cdot Y_\mathrm{f}' - S \cdot W_\mathrm{m} \cdot E \tag{A.78}$$

$$\rightarrow E(1 + S \cdot W_\mathrm{m}) = -S(1 + \hat{S} \cdot W_\mathrm{m}) \cdot Y_\mathrm{f}'. \tag{A.79}$$

This is used to find the FF effective secondary path

$$S_\mathrm{f}^\mathrm{fmdo}(z) = -\frac{E(z)}{Y_\mathrm{f}'(z)} = S(z)\frac{1 + \hat{S}(z)W_\mathrm{m}(z)}{1 + S(z)W_\mathrm{m}(z)}, \tag{A.80}$$

which simplifies to

$$\hat{S}_\mathrm{f}^\mathrm{fmdo}(z) = S(z) \tag{A.81}$$

when $\hat{S}(z) = S(z)$ is fulfilled.

A.5. IMC-FF Combination with Independent Optima

Here the derivations for the system presented in Sec. 5.3 are described.

A.5.1. System's Transfer Function

From the Fig. 5.3a, the equations

$$E = D + Y, \tag{A.82}$$

$$D = P \cdot X, \tag{A.83}$$

$$Y = -S(Y_\mathrm{f}' + Y_\mathrm{i}'), \tag{A.84}$$

$$Y_\mathrm{f}' = W_\mathrm{f} \cdot X, \tag{A.85}$$

and

$$Y_\mathrm{i}' = W_\mathrm{i}(\hat{S} \cdot Y_\mathrm{i} + E) \tag{A.86}$$

$$\rightarrow Y_\mathrm{i}'(1 - \hat{S} \cdot W_\mathrm{i}) = W_\mathrm{i} \cdot E \tag{A.87}$$

$$\rightarrow Y_\mathrm{i}' = \frac{W_\mathrm{i}}{1 - \hat{S} \cdot W_\mathrm{i}} E \tag{A.88}$$

are derived. By using Eq. A.85 and Eq. A.88 to replace the signals Y_f' and Y_i' in the combined control signal Eq. A.84

$$Y = -S\left(W_\mathrm{f} \cdot X + \frac{W_\mathrm{i}}{1 - \hat{S} \cdot W_\mathrm{i}} E\right) \tag{A.89}$$

$$= -S \cdot W_\mathrm{f} \cdot X - \frac{S \cdot W_\mathrm{i}}{1 - \hat{S} \cdot W_\mathrm{i}} E. \tag{A.90}$$

Using this together with Eq. A.83 in Eq. A.82

$$E = P \cdot X - S \cdot W_\mathrm{f} \cdot X - \frac{S \cdot W_\mathrm{i}}{1 - \hat{S} \cdot W_\mathrm{i}} E \tag{A.91}$$

$$\rightarrow E\left(1 + \frac{S \cdot W_\mathrm{i}}{1 - \hat{S} \cdot W_\mathrm{i}}\right) = (P - S \cdot W_\mathrm{f})X \tag{A.92}$$

$$\rightarrow E\left(\frac{1 + (S - \hat{S}) \cdot W_\mathrm{i}}{1 - \hat{S} \cdot W_\mathrm{i}}\right) = (P - S \cdot W_\mathrm{f})X \tag{A.93}$$

the system's transfer function can be derived

$$H_\mathrm{fi}(z) = \frac{E(z)}{X(z)} = \frac{\big(P(z) - S(z)W_\mathrm{f}(z)\big) \cdot \big(1 - \hat{S}(z)W_\mathrm{i}(z)\big)}{1 + \big(S(z) - \hat{S}(z)\big)W_\mathrm{i}(z)} \tag{A.94}$$

If the condition $\hat{S}(z) = S(z)$ is fulfilled, then the system's transfer function simplifies to

$$\hat{H}_\mathrm{fi}(z) = \big(P(z) - S(z)W_\mathrm{f}(z)\big) \cdot \big(1 - S(z)W_\mathrm{i}(z)\big). \tag{A.95}$$

A.5.2. FF Effective Secondary Path

The controller $W_\mathrm{f}(z)$ is removed from the diagram and the disturbance is set to zero, i.e. $d(n) = 0$. Now, taking this into account, Eq. A.88 can be used in Eq. A.84

$$Y = -S\left(Y_\mathrm{f}' + \frac{W_\mathrm{i}}{1 - \hat{S} \cdot W_\mathrm{i}} E\right) \tag{A.96}$$

$$= -S \cdot Y_\mathrm{f}' - \frac{S \cdot W_\mathrm{i}}{1 - \hat{S} \cdot W_\mathrm{i}} E, \tag{A.97}$$

which is then used in Eq. A.82 with $d(n) = 0$

$$E = -S \cdot Y_\mathrm{f}' - \frac{S \cdot W_\mathrm{i}}{1 - \hat{S} \cdot W_\mathrm{i}} E \tag{A.98}$$

$$\rightarrow E\left(1 + \frac{S \cdot W_\mathrm{i}}{1 - \hat{S} \cdot W_\mathrm{i}}\right) = -S \cdot Y_\mathrm{f}' \tag{A.99}$$

$$\rightarrow E\frac{1 + (S - \hat{S})W_\mathrm{i}}{1 - \hat{S} \cdot W_\mathrm{i}} = -S \cdot Y_\mathrm{f}' \tag{A.100}$$

This is used to find the FF effective secondary path

$$S_\mathrm{f}^\mathrm{fi}(z) = -\frac{E(z)}{Y_\mathrm{f}'(z)} = S(z)\frac{1 - \hat{S}(z)W_\mathrm{i}(z)}{1 + \big(S(z) - \hat{S}(z)\big)W_\mathrm{i}(z)}, \tag{A.101}$$

which simplifies to

$$\hat{S}_{\mathrm{f}}^{\mathrm{fi}}(z) = S(z)\big(1 - S(z)W_{\mathrm{i}}(z)\big), \tag{A.102}$$

if $\hat{S}(z) = S(z)$ holds.

A.6. IMC-FF Combination with Dependent Optima

Here the derivations for the system presented in Sec. 5.3.1 are described.

A.6.1. System's Transfer Function

From the Fig. 5.3a, the equations

$$E = D + Y, \tag{A.103}$$
$$D = P \cdot X, \tag{A.104}$$
$$Y = -S(Y_{\mathrm{f}}' + Y_{\mathrm{i}}'), \tag{A.105}$$
$$Y_{\mathrm{f}}' = W_{\mathrm{f}} \cdot X, \tag{A.106}$$

and

$$Y_{\mathrm{i}}' = W_{\mathrm{i}}(\hat{S} \cdot Y_{\mathrm{i}}' + \hat{S} \cdot Y_{\mathrm{f}}' + E) \tag{A.107}$$
$$\rightarrow Y_{\mathrm{i}}'(1 - \hat{S} \cdot W_{\mathrm{i}}) = W_{\mathrm{i}} \cdot \hat{S} \cdot Y_{\mathrm{f}}' + W_{\mathrm{i}} \cdot E \tag{A.108}$$
$$\rightarrow Y_{\mathrm{i}}' = \frac{\hat{S} \cdot W_{\mathrm{i}}}{1 - \hat{S} \cdot W_{\mathrm{i}}} Y_{\mathrm{f}}' + \frac{W_{\mathrm{i}}}{1 - \hat{S} \cdot W_{\mathrm{i}}} E \tag{A.109}$$

are derived. By using Eq. A.106 and Eq. A.109 to replace the signals Y_{f}' and Y_{i}' in the combined control signal Eq. A.105

$$Y = -S\left(W_{\mathrm{f}} \cdot X + \frac{\hat{S} \cdot W_{\mathrm{i}}}{1 - \hat{S} \cdot W_{\mathrm{i}}} W_{\mathrm{f}} \cdot X + \frac{W_{\mathrm{i}}}{1 - \hat{S} \cdot W_{\mathrm{i}}} E\right) \tag{A.110}$$
$$= -\frac{S \cdot W_{\mathrm{f}}}{1 - \hat{S} \cdot W_{\mathrm{i}}} X - \frac{S \cdot W_{\mathrm{i}}}{1 - \hat{S} \cdot W_{\mathrm{i}}} E. \tag{A.111}$$

Using this together with Eq. A.104 in Eq. A.103

$$E = P \cdot X - \frac{S \cdot W_{\mathrm{f}}}{1 - \hat{S} \cdot W_{\mathrm{i}}} X - \frac{S \cdot W_{\mathrm{i}}}{1 - \hat{S} \cdot W_{\mathrm{i}}} E \tag{A.112}$$
$$\rightarrow E\left(1 + \frac{S \cdot W_{\mathrm{i}}}{1 - \hat{S} \cdot W_{\mathrm{i}}}\right) = \frac{P(1 - \hat{S} \cdot W_{\mathrm{i}}) - S \cdot W_{\mathrm{f}}}{1 - \hat{S} \cdot W_{\mathrm{i}}} X \tag{A.113}$$
$$\rightarrow E\big(1 + (S - \hat{S}) \cdot W_{\mathrm{i}}\big) = \big(P(1 - \hat{S} \cdot W_{\mathrm{i}}) - S \cdot W_{\mathrm{f}}\big)X \tag{A.114}$$

the system's transfer function can be derived

$$H_{\text{fido}}(z) = \frac{E(z)}{X(z)} = \frac{P(z) \cdot \big(1 - \hat{S}(z)W_{\text{i}}(z)\big) - S(z)W_{\text{f}}(z)}{1 + \big(S(z) - \hat{S}(z)\big)W_{\text{i}}(z)}. \tag{A.115}$$

If the condition $\hat{S}(z) = S(z)$ is fulfilled, then the system's transfer function simplifies to

$$\hat{H}_{\text{fido}}(z) = P(z) \cdot \big(1 - S(z)W_{\text{i}}(z)\big) - S(z)W_{\text{f}}(z). \tag{A.116}$$

A.6.2. FF Effective Secondary Path

The controller $W_{\text{f}}(z)$ is removed from the diagram and the disturbance is set to zero, i.e. $d(n) = 0$. Now, taking this into account, Eq. A.109 can be used in Eq. A.105

$$Y = -S\left(Y_{\text{f}}' + \frac{\hat{S} \cdot W_{\text{i}}}{1 - \hat{S} \cdot W_{\text{i}}} Y_{\text{f}}' + \frac{W_{\text{i}}}{1 - \hat{S} \cdot W_{\text{i}}} E\right) \tag{A.117}$$

$$= -\frac{S}{1 - \hat{S} \cdot W_{\text{i}}} Y_{\text{f}}' - \frac{S \cdot W_{\text{i}}}{1 - \hat{S} \cdot W_{\text{i}}} E, \tag{A.118}$$

which is then used in Eq. A.103 with $d(n) = 0$

$$E = -\frac{S}{1 - \hat{S} \cdot W_{\text{i}}} Y_{\text{f}}' - \frac{S \cdot W_{\text{i}}}{1 - \hat{S} \cdot W_{\text{i}}} E \tag{A.119}$$

$$\rightarrow E\left(1 + \frac{S \cdot W_{\text{i}}}{1 - \hat{S} \cdot W_{\text{i}}}\right) = -\frac{S}{1 - \hat{S} \cdot W_{\text{i}}} Y_{\text{f}}' \tag{A.120}$$

$$\rightarrow E \frac{1 + (S - \hat{S})W_{\text{i}}}{1 - \hat{S} \cdot W_{\text{i}}} = -\frac{S}{1 - \hat{S} \cdot W_{\text{i}}} Y_{\text{f}}' \tag{A.121}$$

This is used to find the FF effective secondary path

$$S_{\text{f}}^{\text{fido}}(z) = -\frac{E(z)}{Y_{\text{f}}'(z)} = S(z) \frac{1}{1 + \big(S(z) - \hat{S}(z)\big)W_{\text{i}}(z)}, \tag{A.122}$$

which simplifies to

$$\hat{S}_{\text{f}}^{\text{fido}}(z) = S(z), \tag{A.123}$$

if $\hat{S}(z) = S(z)$ holds.

Bibliography

[Bai and Lee, 1997] Bai, M. and Lee, D. (1997). Implementation of an active headset by using the H_∞ robust control theory. *The Journal of the Acoustical Society of America*, 102(4):2184–2190.

[Bai and Lin, 1997] Bai, M. R. and Lin, H. H. (1997). Comparison of active noise control structures in the presence of acoustical feedback by using the H_∞ synthesis technique. *Journal of Sound and Vibration*, 206(4):453 – 471.

[Bao et al., 1992] Bao, C., Sas, P., and Van Brussel, H. (1992). A novel filtered-x LMS algorithm and its application to active noise control of sound. In *1992 European Signal Processing Conference (EUSIPCO)*, pages 1709–1712.

[Bjarnason, 1992] Bjarnason, E. (1992). Active noise cancellation using a modified form of the filtered-x LMS algorithm. In *1992 European Signal Processing Conference (EUSIPCO)*, pages 1053–1056.

[Bose, 1985] Bose, A. G. (1985). Feedback control. US Patent 4,494,074.

[Burgess, 1981] Burgess, J. C. (1981). Active adaptive sound control in a duct - A computer simulation. *Acoustical Society of America Journal*, 70:715–726.

[Carme, 1999] Carme, C. (1999). The third principle of active control: The feed forback. *INTER-NOISE and NOISE-CON Congress and Conference Proceedings*, 1999(5):885–896.

[Chong et al., 2005] Chong, Y.-K., Wang, L., Ting, S.-C., and Gan, W.-S. (2005). Integrated headsets using the adaptive hybrid active noise control system. In *2005 5th International Conference on Information Communications Signal Processing*, pages 1324–1328.

[Elliott, 2001a] Elliott, S. J. (2001a). Adaptive feedback controllers. In Elliot, S. J., editor, *Signal Processing for Active Control*, Signal Processing and its Applications, chapter 7. Academic Press, London.

[Elliott, 2001b] Elliott, S. J. (2001b). *Signal Processing for Active Control*. Signal Processing and its Applications. Academic Press, London.

[Elliott, 2008] Elliott, S. J. (2008). *Handbook of Signal Processing in Acoustics*, chapter Feedback Control Systems, pages 1081–1105. Springer New York, New York, NY.

[Elliott et al., 1987] Elliott, S. J., Stothers, I. M., and Nelson, P. (1987). A multiple error LMS algorithm and its application to the active control of sound and vibration. *IEEE Transactions on Acoustics, Speech, and Signal Processing*, 35(10):1423–1434.

[Fletcher, 1987] Fletcher, R. (1987). *Practical Methods of Optimization*. John Wiley & Sons, New York, NY, USA, second edition.

[Foudhaili, 2008] Foudhaili, H. (2008). *Kombinierte feedback- und adaptive Feedforward-Regelung für aktive Lärmreduktion in einem Kommunikations-Headset*. PhD thesis, Leibniz Universitä Hannover, Aachen.

[Franklin et al., 1997] Franklin, G. F., Workman, M. L., and Powell, D. (1997). *Digital Control of Dynamic Systems*. Addison-Wesley Longman Publishing Co., Inc., Boston, MA, USA, 3rd edition.

[Gill et al., 1981] Gill, P. E., Murray, W., and Wright, M. (1981). *Practical Optimization*. Academic Press.

[Håkansson et al., 2002] Håkansson, L., Johansson, S., Dahl, M., Sjisten, P., and Claesson, I. (2002). Noise cancelling headsets for speech communication. In Davis, G. M., editor, *Noise Reduction in Speech Applications*, chapter 12, pages 305–328. CRC Press, London.

[Hansen, 2001] Hansen, C. H. (2001). *Understanding Active Noise Cancellation*. Spon Press, London.

[Johansson et al., 1997] Johansson, S., Winberg, M., Lagö, T., and Claesson, I. (1997). A new active headset for a helicopter application. In *1997 Proceedings of the 5th International Congress on Sound and Vibration*.

[Kong et al., 1998] Kong, X., Liu, P., and Kuo, S. M. (1998). Multiple channel hybrid active noise control systems. *IEEE Transactions on Control Systems Technology*, 6(6):719–729.

[Kuo and Morgan, 2000] Kuo, S. M. and Morgan, D. R. (2000). Review of DSP algorithms for active noise control. In *Proceedings of the 2000. IEEE International Conference on Control Applications. Conference Proceedings (Cat. No.00CH37162)*, pages 243–248.

[Liebich et al., 2016] Liebich, S., Anemüller, C., Vary, P., Jax, P., Rüschen, D., and Leonhardt, S. (2016). Active noise cancellation in headphones by digital robust feedback control. In *2016 24th European Signal Processing Conference (EUSIPCO)*, pages 1843–1847.

[Lueg, 1936] Lueg, P. (1936). Process of silencing sound oscillations. US Patent 2,043,416.

[Morari and Zafiriou, 1989] Morari, M. and Zafiriou, E. (1989). *Robust process control*. Prentice-Hall, NJ.

[Morrow, 1971] Morrow, C. T. (1971). Point-to-point correlation of sound pressures in reverberation chambers. *Journal of Sound and Vibration*, 16(1):29 – 42.

[Nyquist, 1932] Nyquist, H. (1932). Regeneration theory. *The Bell System Technical Journal*, 11(1):126–147.

[Olson, 1961] Olson, H. F. (1961). Electronic sound absorber. US Patent 2,983,790.

[Olson and May, 1953] Olson, H. F. and May, E. G. (1953). Electronic sound absorber. *The Journal of the Acoustical Society of America*, 25(6):1130–1136.

[Pawełczyk, 2002] Pawełczyk, M. (2002). Analogue active noise control. *Applied Acoustics*, 63(11):1193–1213.

[Pawełczyk, 2003] Pawełczyk, M. (2003). A hybrid active noise control system. *Archives of Control Sciences*, 13(2):191–213.

[Pawełczyk, 2005] Pawełczyk, M. (2005). *Feedback Control of Acoustic Noise at Desired Locations*. PhD thesis, Silesian University of Technology, Gliwice, Poland.

[Rafaely, 1997] Rafaely, B. (1997). *Feedback Control of Sound*. PhD thesis, University of Southampton, Southampton, England.

[Rafaely and Jones, 2002] Rafaely, B. and Jones, M. (2002). Combined feedback-feedforward active noise-reducing headset–the effect of the acoustics on broadband performance. *The Journal of the Acoustical Society of America*, 112(3):981–989.

[Rivera Benois et al., 2016] Rivera Benois, P., Bhattacharya, P., and Zölzer, U. (2016). Derivation technique for headphone transfer functions based on sine sweeps and least squares minimization. *INTER-NOISE and NOISE-CON Congress and Conference Proceedings*, 253(4):4263–4272.

[Rivera Benois et al., 2017] Rivera Benois, P., Nowak, P., and Zölzer, U. (2017). Evaluation of a decoupled feedforward-feedback hybrid structure for active noise control headphones in a multi-source environment. In *Proceedings of the 46^{th} International Congress and Exposition on Noise Control Engineering, INTER-NOISE*.

[Rivera Benois et al., 2017] Rivera Benois, P., Nowak, P., and Zölzer, U. (2017). Fully digital implementation of a hybrid feedback structure for broadband active noise control in headphones. In *2017 Proceedings of the 24th International Congress on Sound and Vibration*.

[Rivera Benois et al., 2019] Rivera Benois, P., Nowak, P., and Zölzer, U. (2019). Improving the performance of an active noise cancelling headphones prototype. In *Proceedings of the 48th International Congress and Exposition on Noise Control Engineering, INTER-NOISE*.

[Rivera Benois et al., 2018a] Rivera Benois, P., Nowak, P., Zölzer, U., Eckert, M., and Klauer, B. (2018a). Low-latency FIR filter structures targeting FPGA platforms. In *Proceedings of the 9th International Symposium on Highly-Efficient Accelerators and Reconfigurable Technologies*, HEART 2018, pages 14:1–14:7, New York, NY, USA. ACM.

[Rivera Benois et al., 2018b] Rivera Benois, P., Papantoni, V., and Zölzer, U. (2018b). Psychoacoustic hybrid active noise control structure for application in headphones. In *2018 Proceedings of the 25th International Congress on Sound and Vibration*.

[Rivera Benois and Zölzer, 2019] Rivera Benois, P. and Zölzer, U. (2019). Psychoacoustic optimization of a feedback controller for active noise cancelling headphones. In *Proceedings of the 26th International Congress on Sound and Vibration*.

[Schumacher et al., 2011] Schumacher, T., Krüger, H., Jeub, M., Vary, P., and Beaugeant, C. (2011). Active noise control in headsets: A new approach for broadband feedback ANC. In *2011 IEEE International Conference on Acoustics, Speech and Signal Processing (ICASSP)*, pages 417–420.

[Sen and Morgan, 1996] Sen, K. M. and Morgan, D. R. (1996). *Active Noise Control Systems: Algorithms and DSP Implementations*. Telecommunications and Signal Processing. John Wiley & Sons, Inc, New York.

[Shynk, 1992] Shynk, J. J. (1992). Frequency-domain and multirate adaptive filtering. *IEEE Signal Processing Magazine*, 9(1):14–37.

[Simshauser and Hawley, 1955] Simshauser, E. D. and Hawley, M. E. (1955). The noise cancelling headset—an active ear defender. *The Journal of the Acoustical Society of America*, 27(1):207–207.

[Skogestad and Postlethwaite, 2005] Skogestad, S. and Postlethwaite, I. (2005). *Multivariable Feedback Control: Analysis and Design*. John Wiley & Sons, Inc., USA.

[Song et al., 2005] Song, Y., Gong, Y., and Kuo, S. M. (2005). A robust hybrid feedback active noise cancellation headset. *IEEE Transactions on Speech and Audio Processing*, 13(4):607–617.

[Streeter et al., 2004] Streeter, A. D., Ray, L. R., and Collier, R. D. (2004). Hybrid feedforward-feedback active noise control. In *Proceedings of the 2004 American Control Conference*, volume 3, pages 2876–2881 vol.3.

[Tay and Moore, 1991] Tay, T.-T. and Moore, J. B. (1991). Enhancement of fixed controllers via adaptive-q disturbance estimate feedback. *Automatica*, 27(1):39 – 53.

[Tseng et al., 1998] Tseng, W.-K., Rafaely, B., and Elliott, S. J. (1998). Combined feedback-feedforward active control of sound in a room. *The Journal of the Acoustical Society of America*, 104(6):3417–3425.

[Wang et al., 2012] Wang, T., Gan, W. S., and Chong, Y. K. (2012). Psychoacoustic hybrid active noise control system. In *2012 IEEE International Conference on Acoustics, Speech and Signal Processing (ICASSP)*, pages 321–324.

[Widrow et al., 1975] Widrow, B., Glover, J. R., McCool, J. M., Kaunitz, J., Williams, C. S., Hearn, R. H., Zeidler, J. R., Dong, E., and Goodlin, R. C. (1975). Adaptive noise cancelling: Principles and applications. *Proceedings of the IEEE*, 63(12):1692–1716.

[Widrow et al., 1981] Widrow, B., Shur, D., and Shaffer, S. (1981). On adaptive inverse control. In *15th Asilomar Conference on Circuits, Systems and Computers*, pages 185–189.

[Wu et al., 2015] Wu, L., Qiu, X., Burnett, I. S., and Guo, Y. (2015). Decoupling feedforward and feedback structures in hybrid active noise control systems for uncorrelated narrowband disturbances. *Journal of Sound and Vibration*, 350:1 – 10.

[Zames, 1981] Zames, G. (1981). Feedback and optimal sensitivity: Model reference transformations, multiplicative seminorms, and approximate inverses. *IEEE Transactions on Automatic Control*, 26(2):301–320.

Curriculum Vitae

Personal Details

Name	Piero Iared **Rivera Benois**
Date of birth	21/09/1985
Place of birth	Santiago de Chile, Chile
Nationality	German

Employement History

03/2014 – 02/2020	**Research Assistant** Helmut-Schmidt-University Department of Signal Processing and Communications Hamburg, Germany
03/2011 – 09/2011	**Process Engineer** LAN Airlines S.A. Santiago de Chile, Chile
01/2009 – 02/2009	**Internship** Ingeniería Wiseconn S.A. Viña del Mar, Chile
01/2008 – 02/2008	**Internship** Nestlé Chile S.A. Graneros, Chile

Academic Career

03/2014 – 02/2020	**PhD. Candidate** Helmut-Schmidt-University Department of Signal Processing and Communications Hamburg, Germany
10/2011 – 12/2013	**Master of Science** Information and Communication Systems Hamburg University of Technology Hamburg, Germany
03/2004 – 12/2010	**Ingeniero Civil Electrónico** Ingeniería Civil Electrónica Universidad Técnica Federico Santa María Valparaíso, Chile

School Education

03/1992 – 12/2003 **St. Paul's School**, Viña del Mar, Chile